Bubbles: Sensors for the Micro World

Caroline Jane Harfield

A thesis submitted in partial fulfilment
of the requirements for the degree of
Doctor of Philosophy
(DPhil)
of
St Catherine's College
University of Oxford

IBME
Department of Engineering Science
University of Oxford
Trinity 2014

Abstract

It has been proposed that coated gas microbubbles, currently used as ultrasound contrast agents could also be used as microscale sensors due to the sensitivity of their acoustic response to changes in their environment. However, their behaviour is not fully understood and there remains considerable scope for improving their characterisation. The aim of this thesis is to improve the theoretical description of microbubble dynamics under ultrasound excitation with the ultimate aim of assessing the regimes in which they could be exploited most effectively as sensors.

Previous theoretical and experimental work relating to the confinement and acoustic excitation of microbubbles is reviewed. Specifically, optical trapping as a method for the isolation and manipulation of individual bubbles is studied for use in developing a sensor. An assessment of the existing models' validity is undertaken. This is followed by the development of models for optical trapping of single microbubbles, and the coupled radial and translational motion of a microbubble under ultrasound excitation, which includes time dependent phenomena. The latter model is used to perform a sensitivity analysis to determine the uncertainty associated with using microbubbles as sensors. The potential for uniquely characterising the shell of the microbubble from experimental data is also assessed.

Subsequent chapters present the results from a combination of computer simulations and experimental data, used to develop and assess the validity of the new models for describing microbubble behaviour. Particularly, the model is used to simulate the response of a dilute suspension of microbubbles undergoing large amplitude oscillations and single microbubbles undergoing lipid shedding. The optimal regimes in which microbubbles may be utilised as sensors for liquid physical properties and local pressure variations are then assessed. Finally, a summary of the conclusions and areas for further work is presented.

Acknowledgements

I am forever grateful to my supervisors Dr Phil Jones and especially Dr Eleanor Stride for all their help, support and advice throughout my DPhil, without them this work would not have been possible.

As Theoretical Physicists who doesn't get along well with doing experiments I'd also like to particularly thank Susan Graham, Jacopo Viti and Laun Ying for all giving me data to compare my theories too and kindly explaining what experiments they did.

A big thanks also goes to Dr Nick Ovenden who was more like a third supervisor, all my friends and my lab past and present who all provided support and useful discussions thought my DPhil.

Finally I'd like to like to thank my family who have supported and believed in me and without them I would not have been able to achieve all that I have.

Contents

Publications and Conference Talks

C J Harfield, N C Ovenden, G Memoli, P H Jones and E P J Stride, Theoretical Characterisation of the Radial and Translational Motion of Coated Microbubbles under Acoustic Excitation, 2013 *J. Phys.: Conf. f. Ser*. 457

M. Azmin, C. Harfield, Z. Ahmad, M. Edirisinghe and E. Stride. "How do Microbubbles and Ultrasound Interact? Basic physical, dynamic and engineering principles", Curr. Pharm. Design 18(15): 2118-2134 (2012)

Investigating the Sensitivity of Microbubble Acoustic Response for Biosensing Applications, POMA - ICA 2013 Montreal, Canada, 2 - 7 June 2013

2014- The 19th European symposium on Ultrasound Contrast Imaging Rotterdam, "Theoretical and Experimental Observations of Lipid Shedding"-Poster

2013-ASA- ICA Montreal, Canada, "Investigating the Sensitivity of Microbubble Acoustic Response for Biosensing Applications"- poster and presentation

2013- The 18th European symposium on Ultrasound Contrast Imaging Rotterdam, "Investigating the Potential of Microbubble Contrast Agents as Biosensors"- poster

2012-Workshop Acoustic Waves for the Control of Microfluidics Flows at the Lorentz Center – "Theoretical Characterisation of the Radial and Translational Motion of Coated Microbubbles Under Acoustic Excitation"-Poster + Presentation

2012 -AFPAC-Brighton- "Theoretical Characterisation of Coated Microbubbles Under Acoustic and Optical Trapping"-Presentation

2011 Leeds Microbubble symposium- "Opto-Acoustic Trapping of Microbubbles"-Poster

List of Figures

List of Tables

1 Introduction

1.1 Overview

Microbubbles, consisting of a suspension of gas bubbles stabilised by a surfactant or polymer shell, are used as ultrasound contrast agents, as they produce a very strong nonlinear scattering response to ultrasound excitation. This response is sensitive to changes in the surrounding environment and it is this that gives them the potential to also be used as microscale sensors.

1.2 Diagnostic Imaging

Microbubbles have been used in clinical research now for more than two decades [1]. They scatter ultrasound much more effectively than red blood cells due to their high compressibility. In addition, they undergo nonlinear volumetric oscillations in response to ultrasound excitation, so that the scattered, or more correctly, re-radiated signal, contains frequencies other than that of the incident ultrasound beam. This allows the signal from the microbubbles to be clearly distinguished from that due to tissue and hence the contrast between the blood vessels carrying the microbubbles and the surrounding tissue is greatly improved. This makes contrast enhanced ultrasound a very useful modality for imaging tissue perfusion [2].

The origin of microbubbles as ultrasound contrast agents can be dated to the late 1960's, Dr. Claude Joyner [3] was performing a M-mode echocardiogram while his patient was simultaneously being injected with indocyanine green dye into the left ventricle for a study of cardiac output. After each injection there was a temporary increase in the ultrasound signal from the left ventricle. Initially the nature of the dye was thought to be the reason for the increased contrast between the blood vessels and tissue; however in 1968, Gramiak & Shah [4] suggested that the enhancement was due to the presence of

microbubbles forming at the catheter tip, after the same effect was observed for a number of other fluids. This theory was validated by Kremkau *et al*. in 1970 [5], who increased the ambient pressure to stop bubbles forming and observed no contrast enhancement.

Microbubbles are currently used for a number of diagnostic applications, for example, examining blood flow rates, in blood vessels as well as in organs such as the liver and kidneys and they can also be used to examine the microvasculature, for example, tumour detection and differentiation [2]. However they have not gained widespread usage due to the USA Food and Drugs Administration (FDA) Black box warning (the highest level of warning issued by the FDA) due to safety concerns surrounding the use of microbubbles. This warning is high in comparison to other imaging procedures. The microbubbles are injected into the blood stream and ultrasound is applied to the region of interest. When the microbubbles flow through this region, the pressure variations due to the ultrasound wave cause the bubbles to oscillate and emit a secondary ultrasound field. The nonlinear character of the bubble oscillations allows the blood vessels and the tissue to be distinguished from one another. For a given ultrasound field, the signal emitted will be different for varying sizes of bubble, coating materials and environments, for example changes in local viscosity, temperature or pressure. This means that if the bubbles could be characterised beforehand then the acoustic signals could also be used to obtain quantitative imaging relating to the surrounding tissue (e.g. percentage perfusion or blood pressure) in addition to image contrast enhancement. Microbubbles are also being actively investigated for their use for therapeutic applications but these are not of direct relevance to the work presented in this thesis. However the models developed could be relevant to this field.

1.3 Production of Microbubbles

To meet the requirements of more advanced imaging techniques and therapeutic applications, new microbubble formulations and improved production techniques need to

be developed. The two most common microbubble production methods are sonication and high shear emulsification which both produce a high yield of highly poly-disperse microbubbles. Thus filtration/fractionation processes are needed to remove any bubbles that might potentially cause an embolism or when a certain bubble size is required [6]. More advanced methods such as ink jet printing, coaxial electrohydrodynamic atomisation (CEHDA) and microfluidic processing have been shown to produce near monodisperse bubbles as well as the ability to produce multi layered bubble coatings [6, 7], though they have a low yield compared to the previous methods. As well as being uniform in size it is also desirable for the shell thickness and mechanical properties to be the same for the whole population as inhomogeneities in the population can affect the dynamics of the bubbles and hence their performance in diagnostic and therapeutic applications. It is, however, at present difficult to verify the uniformity of the shell with existing characterisation methods.

1.4 Bubbles as sensors

Bubbles have been used as sensors in a variety of forms, the best known is in Sonar, (Sound Navigation and Ranging), where both passive detection of acoustic emissions and active “pulse-echo” strategies are used for the location and identification of objects under water. In particular, passive sonar is used to locate ships and submarines by listening for the emissions from cavitation bubbles caused by the propellers.

Microbubbles in recent years have also gained renewed interest for use as sensors in blood perfusion and blood pressure. Being able to quantify tissue perfusion rates is desirable in a number of clinical assessments involving changes in local blood flow such as cancer and cardiovascular disease. Using ultrasound in order to quantify tissue perfusion has many advantages in terms of, convenience, cost, real-time imaging and patient safety. [8-11].

To measure blood perfusion rates, injections of microbubbles are staged with a known time difference between injections and this is related to the observed difference in intensity from the image, [12]. The hypothesis for being able to measure changes in the ambient blood pressure is that the local pressure will affect the signals produced by the bubble by altering its equilibrium radius and therefore its resonant frequency and the strength of the scattered signal from the bubbles. In 1977, Fairbank and Scully [13] showed that microbubbles with radii in the range 30-40 μm underwent an observable shift in their resonance behaviour with an ambient pressure change of 20kPa [13]. In 1994, Moravi et al. used a rabbit heart model to demonstrate an intensity decrease in the image owing to a shift in the pressure [14]. Investigations of the emission of different harmonic frequencies as a function of ambient pressure have also been carried out [15-17]. It has also been observed that, upon applying a hydrostatic pressure of ~20kPa, albumin bubbles tend to shrink and disappear, [12], which has been attributed to bubble dissolution. Similar effects have been reported in [18]. It has also been observed that imaged bubbles disappear at a greater rate for higher ambient pressures, and that the contrast reduction is an irreversible process, [19-21].

1.5 Aims and Objectives

1.5.1 Statement of Problem

For microbubbles to be used effectively in the ways described above, it is necessary for their response to ultrasound to be fully characterised. This will facilitate a number of advanced applications such as quantitative imaging and controlled drug release as well as addressing some of the concerns relating to microbubble safety. This thesis, however, is concerned specifically with the assessment of microbubbles as sensors.

For the potential of microbubble sensors to be realised, the response of a bubble to an ultrasound pulse in a given environment must be predictable and it must be possible to quantify and relate any changes in this response to a change in one of the environmental parameters. This imposes a number of requirements: first, an accurate model to predict microbubble dynamics; second, quantification and, as far as possible, minimisation of the uncertainty in the measurement of those dynamics. The subsequent chapters discuss these requirements in more detail and the potential for meeting them.

1.5.2 Objectives

The overall objective of the work described in this thesis is to develop theoretical models to improve the description of microbubble dynamics with the aim of assessing the feasibility of developing a microbubble based sensing device. The specific aims are as follows:

- To review existing theoretical models for predicting the forces involved in the optical trapping of particles and to assess their applicability to microbubbles.
- To derive a model for microbubble trapping and determine the trap parameters required to optimise the strength of the trap, to enable microbubbles to be effectively manipulated during experiments.
- To review existing theoretical models for predicting the behaviour of microbubbles under ultrasound excitation and assess their applicability for use in designing a sensor.
- To derive a new model for microbubble acoustic response that meets the requirements for sensor design and data interpretation.
- To assess the validity of the new models for characterising microbubble behaviour in a range of environments through sensitivity analysis and comparison with experimental data.

- To evaluate the potential for utilising microbubbles as sensors and to identify the optimal operating regimes in terms of both microbubble characteristics and ultrasound exposure conditions.

1.6 Outline

In Chapter 2 the review and assessment of optical trapping models and their applicability to microbubbles is carried out. A model for microbubbles is then formulated and used to assess which parameters would produce the most stable trap for different microbubble sizes.

In Chapter 3 the review and derivation of a generalised model describing the behaviour of microbubbles under acoustic excitation is presented. The new model includes coupled radial and translational bubble motion and also the influence of a rigid boundary upon microbubble response. In addition the effects of variable surface tension, variable shell viscosity and "shedding" from the bubble surface are considered. In Chapter 4 this model is used to perform a sensitivity analysis to better understand which are the dominant factors in determining microbubble response. This is so that they can be exploited in designing a sensor and also predicting the level of experimental uncertainty that would be expected. In addition it is proven that the microbubble response is characterised by a unique set of coating parameters that may be determined through fitting experimental data to the theoretical simulations.

In Chapters 5 and 6 the results from simulations performed with the model are compared to experimental data to assess how well it describes the microbubble response. In Chapter 7 the requirements for an ideal microbubble based sensor are discussed and further simulations presented to identify the optimal combination of microbubble characteristics and ultrasound excitation parameters for use in such a sensor. The conclusions from the work are presented in Chapter 8 followed by a discussion of the areas for further work.

1.7 References

1. Cosgrove, D., *Ultrasound contrast agents: An overview.* European Journal of Radiology, 2006. **60**(3): p. 324-330.
2. Stride, E.P. and Coussios, C.C., *Cavitation and contrast: the use of bubbles in ultrasound imaging and therapy.* Proceedings of the Institution of Mechanical Engineers Part H-Journal of Engineering in Medicine, 2010. **224**(H2): p. 171-191.
3. Feignbaum, H., Stone, J., and Lee, D., *Identification of ultraouns echoes from the left ventricle by use of intracardiac injections of indocynine green.* Circulation, 1970. **41**: p. 615-621.
4. Gramiak, R. and Shah, P.M., *Echocardiography of the Aortic Root.* Investigative Radiology, 1968. **3**(5).
5. Kremkau, F.W., et al., *Ultrasonic detection of cavitation at catheter tips.* The American journal of roentgenology, radium therapy, and nuclear medicine, 1970. **110**(1): p. 177-183.
6. Stride, E. and Edirisinghe, M., *Novel microbubble preparation technologies.* Soft Matter, 2008. **4**(12): p. 2350-2359.
7. Ahmad, Z., et al., *Generation of multilayered structures for biomedical applications using a novel tri-needle coaxial device and electrohydrodynamic flow.* Journal of The Royal Society Interface, 2008. **5**(27): p. 1255-1261.
8. Becher, H.B.P., *Handbook of Echocardiography*. 2000, Frankfurt: Springer Verlag.
9. Wilson, S.R. and Burns, P.N., *Microbubble-enhanced US in Body Imaging: What Role?* Radiology, 2010. **257**(1): p. 24-39.
10. Cosgrove, D. and Lassau, N., *Imaging of perfusion using ultrasound.* European Journal of Nuclear Medicine and Molecular Imaging, 2010. **37**(1): p. 65-85.

11. Sboros, V., et al., *The assessment of microvascular flow and tissue perfusion using ultrasound imaging.* Proceedings of the Institution of Mechanical Engineers, Part H: Journal of Engineering in Medicine, 2010. **224**(2): p. 273-290.

12. de Jong, N., et al., *Quantification of transpulmonary echocontrast effects.* Ultrasound in Medicine & Biology, 1993. **19**(4): p. 279-288.

13. Fairbank, W.M. and Scully, M.O., *A New Noninvasive Technique for Cardiac Pressure Measurement: Resonant Scattering of Ultrasound from Bubbles.* Biomedical Engineering, IEEE Transactions on, 1977. **BME-24**(2): p. 107-110.

14. Moravi, V., et al., *Effects of left ventricular pressure on sonicated albumin microbubbles: evaluation using an isolated rabbit heart model.* Journal of the American College of Cardiology, 1994. **24**(7): p. 1779-85.

15. Shi W, T., et al., *Pressure dependence of subharmonic signals from contrast microbubbles.* Ultrasound in Medicine & Biology, 1999. **25**(2): p. 275-283.

16. Leodore, L.M., Forsberg, F., and Shi, W.T. *P5B-6 In Vitro Pressure Estimation Obtained from Subharmonic Contrast Microbubble Signals*. in *Ultrasonics Symposium, 2007. IEEE*. 2007.

17. Andersen, K.S. and Jensen, J.A. *Non-invasive estimation of blood pressure using ultrasound contrast agents*. 2009. Proceedings of the International Congress on Ultrasonics (ISBN:), pages: 59, part of.

18. Shapiro, J.R., et al., *Intravenous contrast echocardiography with use of sonicated albumin in humans: Systolic disappearance of left ventricular contrast after transpulmonary transmission.* Journal of the American College of Cardiology, 1990. **16**(7): p. 1603-1607.

19. Vuille, C., et al., *Effect of static pressure on the disappearance rate of specific echocardiographic contrast agents.* J Am Soc Echocardiogr, 1994. **7**(4): p. 347-54.

20. Gottlieb, S., A. Ernst, and Meltzer, R.S., *Effect of pressure on echocardiographic videodensity from sonicated albumin: an in vitro model.* Journal of Ultrasound in Medicine, 1995. **14**(2): p. 109-16.

21. Brayman, A.A., et al., *Effect of static pressure on acoustic transmittance of Albunex microbubble suspensions.* J Acoust Soc Am, 1996. **99**(4 Pt 1): p. 2403-8.

2 Optical Trapping Theories of Microbubbles

Optical trapping offers a method for the contactless manipulation of microscopic particles [1] which utilises the potential energy gradient experienced by a polarisable particle in a laser beam to hold and move them. This makes it an ideal technique for manipulating microbubbles in experiments, as a single bubble can be selected and moved into a desired location, e.g. away from influences that might affect its dynamics [2, 3]. In this chapter the forces involved in bubble trapping are investigated by comparing different theoretical models to see which best describe them and investigating how changing the trap parameters affects the equilibrium trapping position of the bubble and trap strength. This is to ascertain which trapping parameter would produce the most efficient and stable trap for a specifically sized microbubble.

2.1 Overview of Laser Trapping

Optical Tweezers were first reported in 1986 by Ashkin [4], and have since been exploited in many fields, including trapping of aerosols [5], metal nanoparticles [6] and their aggregates [7], carbon nanotubes [8], graphene flakes [9] through to the trapping of single cells [10]. This technique has been applied to microbubbles to trap, manipulate and investigate their properties [2, 3, 11-15], and these studies will be discussed further later.

Optical tweezers generate forces, typically in the piconewton range, that are sufficiently high to trap micrometre sized particles using a tightly focused laser beam which produces an extremely high gradient in the electric field near the beam waist. This requires the objective lens to have a high numerical aperture (*NA*). The *NA* is a dimensionless number that describes the spread of the beam and is defined by $NA=n\ sin\theta$, where n is the

refractive index of the medium and θ is the half-angle of the maximum convergence angle of light brought to a focus by the lens.

Optical Tweezers allow particles to be trapped in three dimensions enabling contactless manipulation. Dielectric particles experience a radiation force which can be divided into two components: scattering and gradient. The origin of the scattering force is the momentum transfer involved in the scattering of photons and acts in the direction of beam propagation. The gradient force arises from interaction of the particle with the electric field gradient of the laser beam and for a high relative refractive index particle, i.e. $n_{particle}/n_{medium}>1$ is directed towards the region of the highest light intensity. For a particle to be fully trapped in three dimensions the backward directed gradient force in the axial direction must exceed the forward directed scattering force in the axial direction [16, 17]. Therefore simply increasing the power of a laser beam is not sufficient to form a trap as both forces scale linearly with light intensity. Instead the intensity gradient of the beam needs to be maximised, hence the need for high *NA* focusing to trap in the (axial) direction of beam propagation.

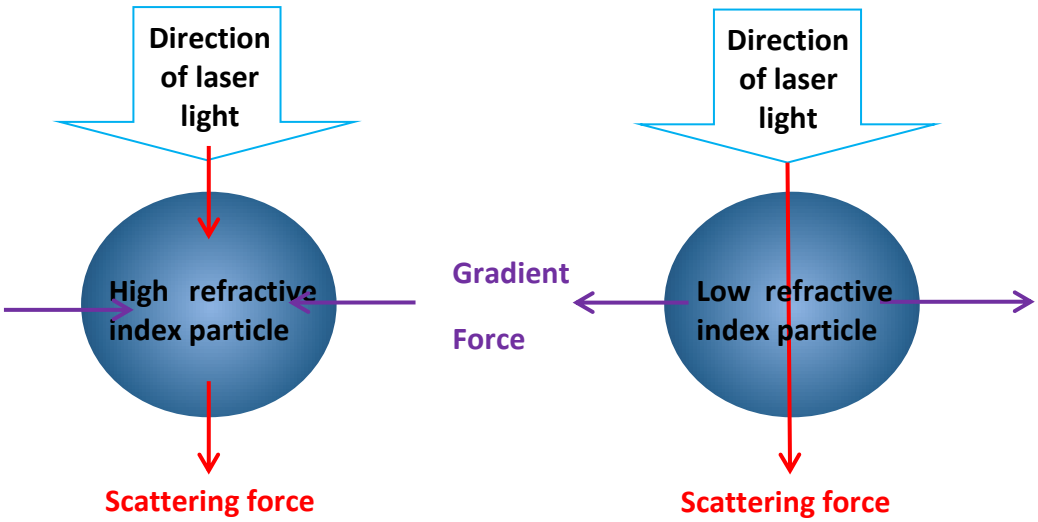

Figure 2.1. Diagram showing the direction of the laser gradient and scattering forces for high and low refractive index particles.

The gradient force acts perpendicularly to the incident ray and the scattering force acts parallel to the incident ray. For particles that have a high refractive index relative to their surrounding medium, such as polystyrene beads suspended in water, the particles are drawn toward the highest amplitude of the electromagnetic field, making a Gaussian beam ideal for trapping them [4, 16, 18], see

Figure *2.1*. For low refractive index particles, such as microbubbles, the direction of the gradient force is reversed. This means that instead of being attracted to the region of high intensity, the particles are repelled from it [19], as shown in Figure 2.1. Microscopic metallic particles are also repelled by a high optical scattering force, due to their high reflection coefficient [20], though metal nanoparticles have been trapped successfully [21-23]. Therefore, to trap a low index or highly reflective particle, an area of low intensity surrounded by a region of high intensity is required. This means that a dark core needs to be formed around the particle to trap it. There are several techniques to trap low index particles including (i) time averaged optical potential, [14], (ii) computer generated holography Laguerre-Gaussian beam arrays [3, 12, 24, 25], (iii) dark fringes of two beam interference [25] or (iv) Bessel beams [26, 27]. Only the first two have been used to trap microbubbles, however. The other methods have been used to trap low refractive index (iii-iv) hollow spheres. Methods (i) & (ii) are described below.

The time averaged potential method requires a laser beam, usually a Gaussian beam, to be scanned around the circumference of the particle; the scanning speed needs to be faster than the rate at which the particle can diffuse away due to its Brownian motion. The particle then experiences a time averaged optical potential, which allows for both 2D and 3D trapping [20]. Multiple trapping also becomes possible with scanning tweezers, although this requires that the laser is scanned around each trapping site sufficiently fast to stop them diffusing away. Since this reduces the time that the laser spends at each site the

number of particles that can be trapped and manipulated with one beam via this method is limited by the maximum speed that the laser can be scanned and the laser power [19]. Microbubbles have been trapped in this way by Jones *et al.* [14] who found that the maximum axial force that the microbubbles experience was proportional to the square of the radius of the bubble, a^2 and had a magnitude of the order of piconewtons [13], with a maximum power of 150mW being used.

Optical vortices are present in Laguerre-Gaussian[1] (LG) beams, which are beams with a spiral like wave front that have a phase discontinuity on the axis resulting in a zero intensity region, giving a dark spot at the centre of the beam [3]. When used to trap absorptive particles, rotational motion can be induced due to the angular momentum of the laser beam [3]. Computer generated holograms (CGH) can be used to create higher order Laguerre-Gaussian beams, by simulating appropriately designed diffractive optical elements (DOEs). Phase only DOEs can be used to modulate the phase of the input beam by imposing a pattern of phase delays to obtain the desired wave front [3]. This pattern is created by a phase singularity which is a point in an optical field around which the phase of the field changes by an integer multiple of 2π (the integer is the topological charge of the vortex), creating a point that shows up as a dark spot against a bright background [24]. Computer algorithms may be formulated to generate LG beams with a desired topological charge, *l*. A computer driven spatial light modulator (SLM) can then be used to produce the required interference pattern, including ones possessing several phase singularities, which are useful for trapping multiple objects [28]. Computer controlled holograms are very versatile and can be changed at video frame rates or faster making them very useful for 3D manipulation [2]. This technique has been used as a method to position microbubbles for experiments [2, 3, 11] as well as trapping multiple microbubbles [12].

[1] The terms Gaussian and Laguerre-Gaussian refer to the mathematical functions that describe the beam intensity profile.

2.2 Overview of Beam modes

A laser beam type is usually described by its Transverse Electro Magnetic modes, $TEM_{nm,}$ where n and m are integers that denote a given mode. For a circular geometry, denoted by a *, the indices p and l are typically used referring respectively to radial and azimuthal modes. Where l refers to the number of 2π phase cycles around the mode circumference. The two main types of mode used for trapping microbubbles are the Gaussian beam, TEM_{00}, which is employed for scanning tweezers, and Laguerre-Gaussian beams, TEM_{pl}* , that can be created by CGH. Figure 2.2. shows how the beam intensity profile varies for four TEM mode.

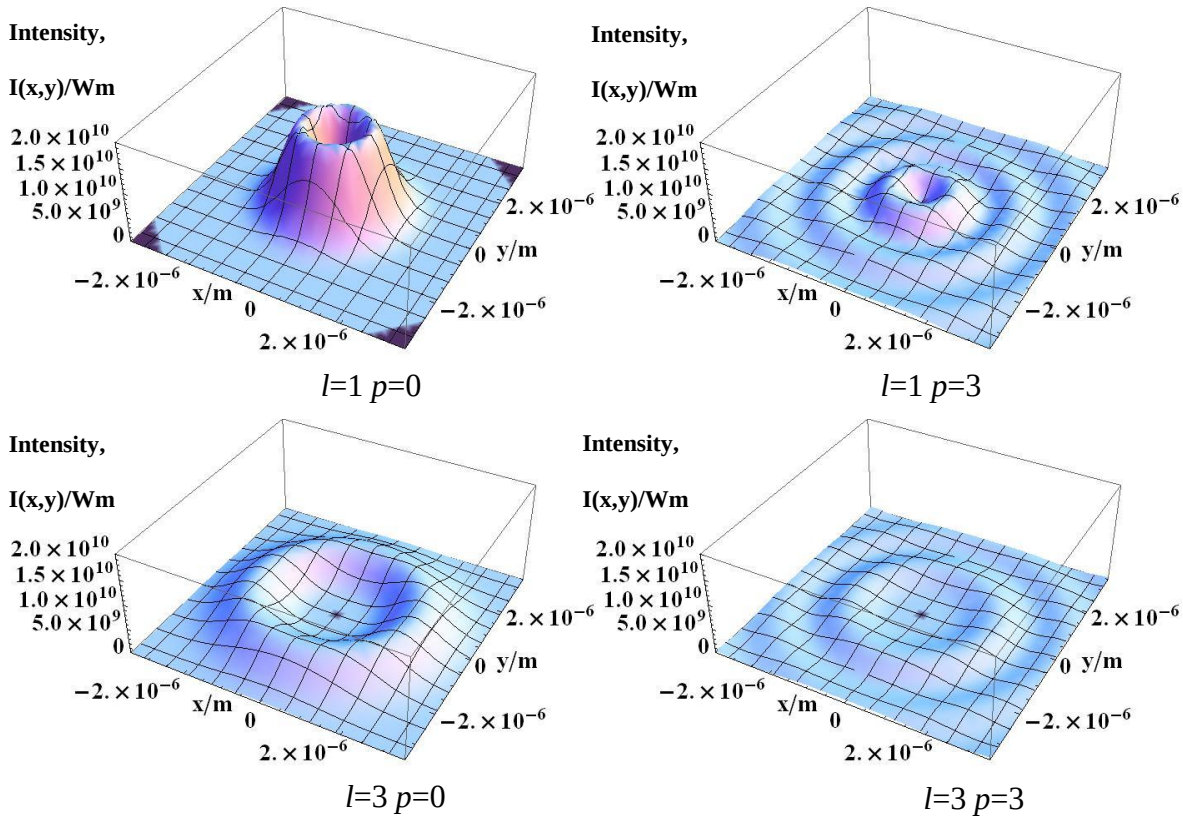

Figure 2.2 how the Laguerre-Gaussian beam intensity profiles change for different modes, where I(x,y) is Equation 2.3

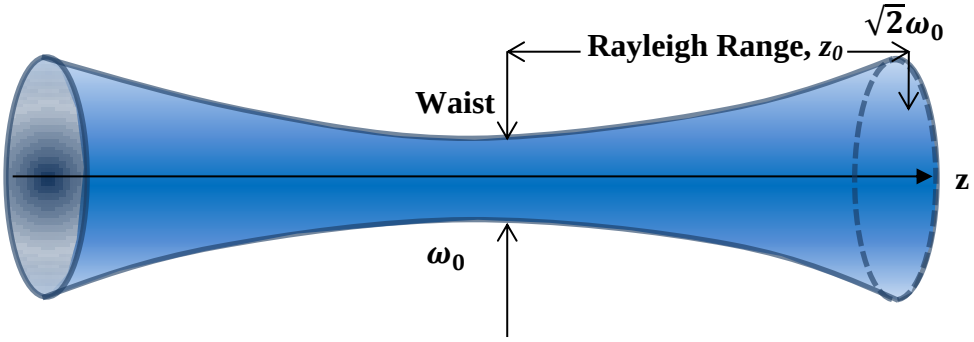

Figure 2.3 the beam waist, ω_0 of a Gaussian beam, and the Rayleigh Range

The time averaged intensity profile of a Gaussian beam in the plane transverse to the propagation direction [29], is given by:

$$I(r) = I_0 \left(\frac{\omega_0}{\omega(z)}\right)^2 e^{-2r^2/\omega(z)^2} \qquad (2.1)$$

Where r is the radial distance, ω_0 is the spot size at the beam waist or focus (.i.e. when $z=0$ in Figure 2.3) and $\omega(z)$ is the spot size at z which evolves as [29]:

$$\omega^2(z) = \omega_0^2 \left(1 + \frac{z^2}{z_0^2}\right) \qquad (2.2)$$

where the Rayleigh range $z_0 = \frac{\pi\omega_0^2}{\lambda} = \frac{k\omega_0^2}{2}$, shown in Figure 2.3, the wavenumber $k = \frac{2\pi}{\lambda}$, and λ is the wavelength of the laser beam. The intensity profile and burn profile, which is the image seen on burn (light sensitive) paper which is used to permanently recording the beam shape from a laser, observed at the beam waist of a Gaussian beam, TEM_{00}, are shown in Figure 2.4 .

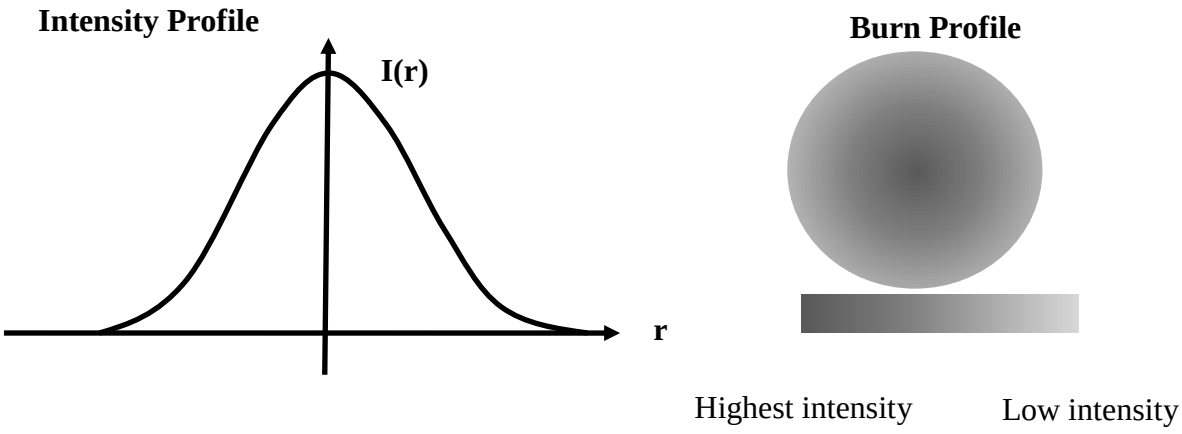

Figure 2.4 the intensity profile of a Gaussian beam with a burn profile of the beam

For a Laguerre-Gaussian, TEM_{lp}*, the Intensity profile of the beam is described by [30]:

$$I(r) = I_0 \frac{(2p+l+1)}{2} \frac{p!}{(l+p)!} exp\left(-\frac{2r^2}{\omega(z)^2}\right)\left(\frac{2r^2}{\omega(z)^2}\right)^{|l|}\left(L_p^l\left(\frac{2r^2}{\omega(z)^2}\right)\right)^2 \quad (2.3)$$

Where L_p^l is a Laguerre polynomial, which gives the characteristic *p+1* radial mode. At higher order Gaussian modes such as that of the Laguerre-Gaussian beam the spot size has been observed to spread more widely [31]. Equation (2.2) only describes the spot size of the fundamental modeL_0^0 and does not capture the physical intensity spot size of a higher order mode. Equation (2.2) therefore gives an inaccurate picture of the beam divergence and no longer describes the spot size accurately. Philips *et al.* [32] proposed the following expression, Equation (2.4), to provide a more accurate description of the spot size, that fulfils the criteria of being large enough to contain the intensity peaks for the beams characterised by all values of *l* and *p,* with the definition that the square of the radius is twice the variance of the intensity distribution.

$$\omega(z)^2 = \omega_0^2(2p+l+1)\left(1+\left(\frac{\lambda z}{\pi\omega_0^2}\right)^2\right) \quad (2.4)$$

The profile of a Laguerre-Gaussian TEM_{01}* beam is shown in Figure 2.5.

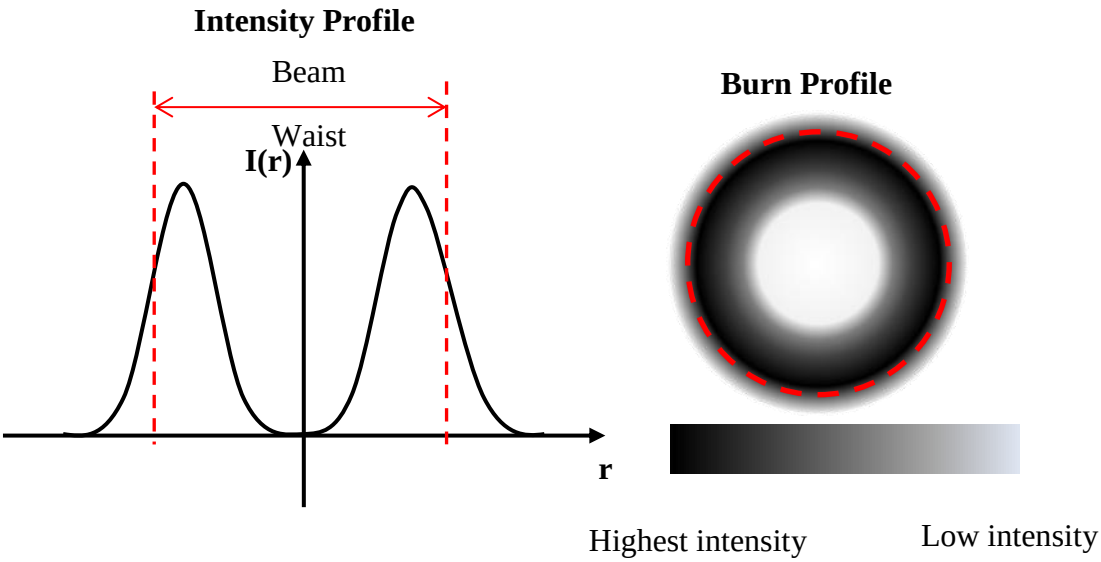

Figure 2.5 the intensity profile of a Laguerre-Gaussian beam, TEM01 with a burn profile of the beam, where the red dotted line indicates the spot size.*

2.3 Experimental Set Up

The aim of this chapter is to develop theoretical models that describe the trapping forces on a microbubble, so that the trapping mode and power can be selected to give the strongest trap for a given microbubble. Therefore the calculations are based on parameters provided by the project collaborators performing the experimental work that was proposed to take place in parallel with the work described in this thesis. A CGH was selected to produce the LG beams to trap the microbubbles, as this would provide the option of trapping isolated and multiple bubbles with the same set up. The trapping beam is formed using a single mode Nd:YAG laser, which has a wavelength, λ, of 1064nm, which was selected for its good beam pointing stability, power output, beam quality (of a single mode) and low absorption coefficient in water. The beam is collimated prior to reaching the Spatial Light Modulator (SLM) (Boulder Non-Linear systems Inc. XY Series). The SLM then alters the phase profile along the cross section of the beam by a user defined value. This simulates the effect of the beam encountering specific optical elements such as lenses,

diffraction gratings, wedges or combinations of these. The imparted phase change on the beam is delivered via a hologram, an example of which can be seen in Figure 2.6 which is a spiral plus a linear ramp to separate the LG beam from the zero order (undiffracted) beam. The beam is then passed through an objective lens (Nikon PLAN APO IR) which has a *NA* of 1.27.

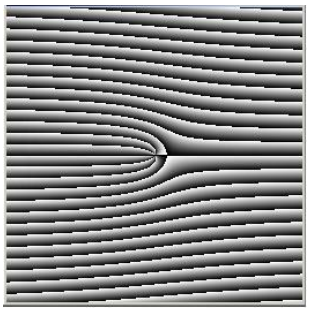

Figure 2.6 an example of the computer generated hologram used to create a LG beam.

The maximum output power of the laser is 5W; however, to stay below the damage threshold of the SLM, it was decided that maximum power of 0.5W would be used for the experiments. This was found to stably trap the microbubble for a prolonged period of time without causing excessive heating in the surrounding liquid. It is assumed that only 20% of the maximum power emitted will reach and interact with the bubble, due to attenuation and scattering in the experimental path, leading to a lower power , P~0.1W at the trap location. This is assumed to be the maximum power for all the following calculations, unless otherwise stated, used to find the maximum force on a microbubble. The refractive indices of the bubble's gas core and surrounding medium are assumed to be those of water and air (n_1= 1.33 and n_2=1.000 respectively) as the bubble coating has a thickness ~1-10 nm, which is much smaller than the optical wavelength and its effect upon the refractive index is therefore negligible [13]. The distance between the objective lens and the focal plane, l_t was 200μm. The parameters used for the modelling are summarised in Table 2.1.

Parameter	*Value*
Wavelength, λ	*1064nm*
Refractive index of the medium, n_1	*1.33*
Refractive index of the particle, n_2	*1.00*
Numerical Aperture, NA	*1.27*
Focal length, l_t	*200μm*

Table 2.1 parameters used for modelling

The axial and radial spring constants, relate to the stiffness of the optical trap in their respective directions, and the equilibrium trapping position of the bubble, can both be predicted theoretically and measured experimentally. These parameters were therefore selected as the key outputs from the simulations. The spring constants give a more accurate means of characterising the trap and the optical forces acting on the microbubble at the equilibrium position than simply determining its escape velocity [16].

2.4 Optical Trapping Theory: Introduction

To effectively manipulate a microbubble using an optical trap, the forces upon it in need to be known. However, a problem arises when trying to calculate these forces as the wavelengths, $\lambda \approx 1\mu m$, typically used in optical trapping are of the same order of magnitude as the radius of the bubble, $a \approx 1\text{-}10\mu m$. Microbubbles are thus classed as "intermediate sized" particles and fall in-between the two regimes normally used for modelling optical scattering, the Ray Optics and Rayleigh regimes [13, 33]. This makes microbubble trapping somewhat difficult to characterise theoretically. The assumptions underlying the dipole approximation used for particles in the Rayleigh regime are not fully met but neither is the condition $2\pi\ a\ n_1/\lambda >> 1$ required by the ray optics model for particles in the Ray Optics regime [34]. Ray Optics models for high index particles predict a force independent of the radius of the bubble a, whilst the force on particles in the Rayleigh regime is dependent on a^3 due to the gradient force dominating. Experimentally [13], the forces upon a microbubble caused by scanning optical tweezers have been found to scale with a^2.

Optical trapping of microbubbles, which are low index particles when immersed in water, is an under researched area with most theoretical studies concentrating on high index particles. In the next sections models will be developed and implemented to investigate the forces acting upon a microbubble when it is trapped, first via the dipole approximation then by the Ray Optics method. The aim will be to see which gives the best description of the trends that have been previously observed experimentally and hence to define the optimum parameters for trapping. It should be noted that a analytical model could be developed using Mie theory, but this would be a phD in it's own right and wasn't deemed necessary for this work.

2.5 The Dipole approximation

A particle which has a radius much smaller than the wavelength of a laser beam can be treated using the dipole approximation [33], under which the particle can be treated as an induced point dipole. As above, this is not strictly valid in the case of microbubble at optical wavelengths, but the model may still provide useful qualitative insights into the behaviour of a microbubble under optical trapping.

2.5.1 Overview of Theory

The optical scattering force is given in Equation (2.5) and the instantaneous gradient force is given by Equation (2.6) [35], where n is the ratio of refractive indices, $n=\frac{n_2}{n_1}$, n_1 is the refractive index of the medium and n_2 is the refractive index of the particle, $I(r)$ is the intensity distribution of the laser beam and a is the radius of the microbubble.

$$F_{scat}(r,t) = \frac{n_1 8}{3c_l}\pi(ka)^4 a^2 \left(\frac{n^2-1}{n^2+2}\right) I(r)\,\hat{z} \tag{2.5}$$

$$F_{grad}(r,t) = \frac{2\pi n_1^3 a^3}{c_l}\varepsilon_0 \left(\frac{n^2-1}{n^2+2}\right) \nabla I(r) \tag{2.6}$$

From Equation (2.6), as per section 2.1, it can be seen that the force is directed towards the region of highest intensity for high refractive index particles, (where n>1), and directed away for low refractive index particles (n<1) [1, 19]. The coordinate system for these equations can be seen in Figure 2.7. The origin is located at the centre of the beam waist, *Ob* (x,y,z)=(0,0,0) for all cases, *Op* is located at the centre of the particle and ***r*** is the vector difference between *Op* and *Ob*.

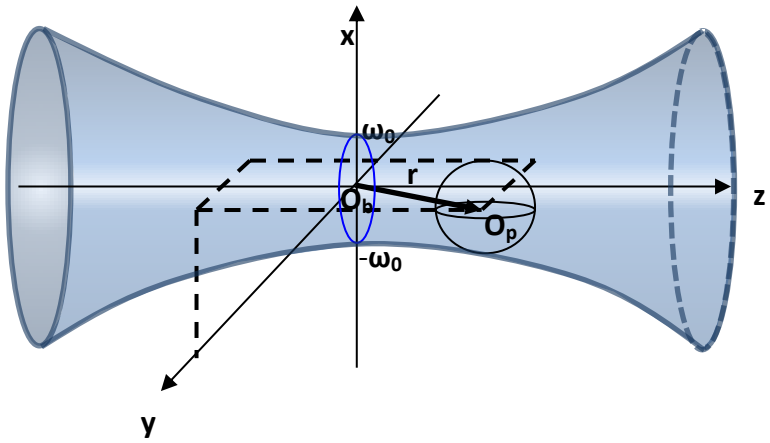

Figure 2.7 shows the coordinate system for a bubble in a beam for dipole approximation, where O_b is the centre of the beam waist and O_p is the centre of the particle.

2.5.2 Method

The forces were calculated using purpose written code in Wolfram Mathematica 9 ® implementing equations 2.5 and 2.6. The parameters used for the laser beam are shown in Table 2.1, and the other parameters used are beam power, P_0=1mW, the permittivity of free space ε_0 =8.85× 10^{-12} F/m, the speed of light c_l =299798548 m/s, and bubble radius a=1μm. The last of these is the average radius of microbubbles in the commercial contrast agent SonoVue® [36].

The forces were calculated using Equations (2.5) & (2.6). The *axial* force is made up of the *z*-gradient force, F_{zg} and the scattering force, F_s (F_s acts solely in the *z*-direction).

The radial force is only made up of the *r*-gradient force, F_{rg}. To determine the stiffness of the trap in arbitrary trap locations, the corresponding spring constants for were calculated respectively as $k_z = -\frac{d(F_{zg}+F_s)}{dz}$, $k_r = -\frac{dF_{rg}}{dr}$.

2.5.3 Results & Discussion

To investigate the relevant range of parameters, the code was run for a TEM_{lp}* mode when *l=1* and *p=0*, and for *l=3* and *p=0*, (see Figure 2.2 to see the beam intensity profiles). The axial, *z*, and radial, *r*, forces and spring constants were then calculated.

In the absence of experimental data for LG beams the values published in [13] microbubbles trapped in scanning optical tweezers were used for comparison. In these experiments the trapping forces were measured to be of the order of 10^{-12}N with spring constants of the order of 10^{-6}N/m.

The predicted axial and radial force distributions and corresponding spring constants are shown in Figure 2.8 and Figure 2.9. It can be seen that the model provides an accurate prediction of where the maximum forces and spring constants occur, (based on comparison with [16], where the maximum force is found one radii away from the beam axis), but not of their magnitudes. The predicted axial force is ~10^{-8}N and the radial force~ 10^{-11}N which is higher than indicated by the experimental results of ~10^{-12}N. As above, the reason for this is that, in the dipole approximation, the force depends on the third power of the bubble radius size (as the gradient force dominates). Thus the model over-predicts the force and consequently the spring constants. The model also predicts that the axial force will be zero all the way along on the axis, which is clearly not the case for a bubble of finite size.

To conclude, this model produces a good qualitative description of the spatial variation in the trapping force and spring constants, but the predicted magnitudes are

incorrect. Therefore a Ray Optics model was pursued to see if it would provide a more accurate quantitative description for the equilibrium trapping position and magnitude of the spring constant.

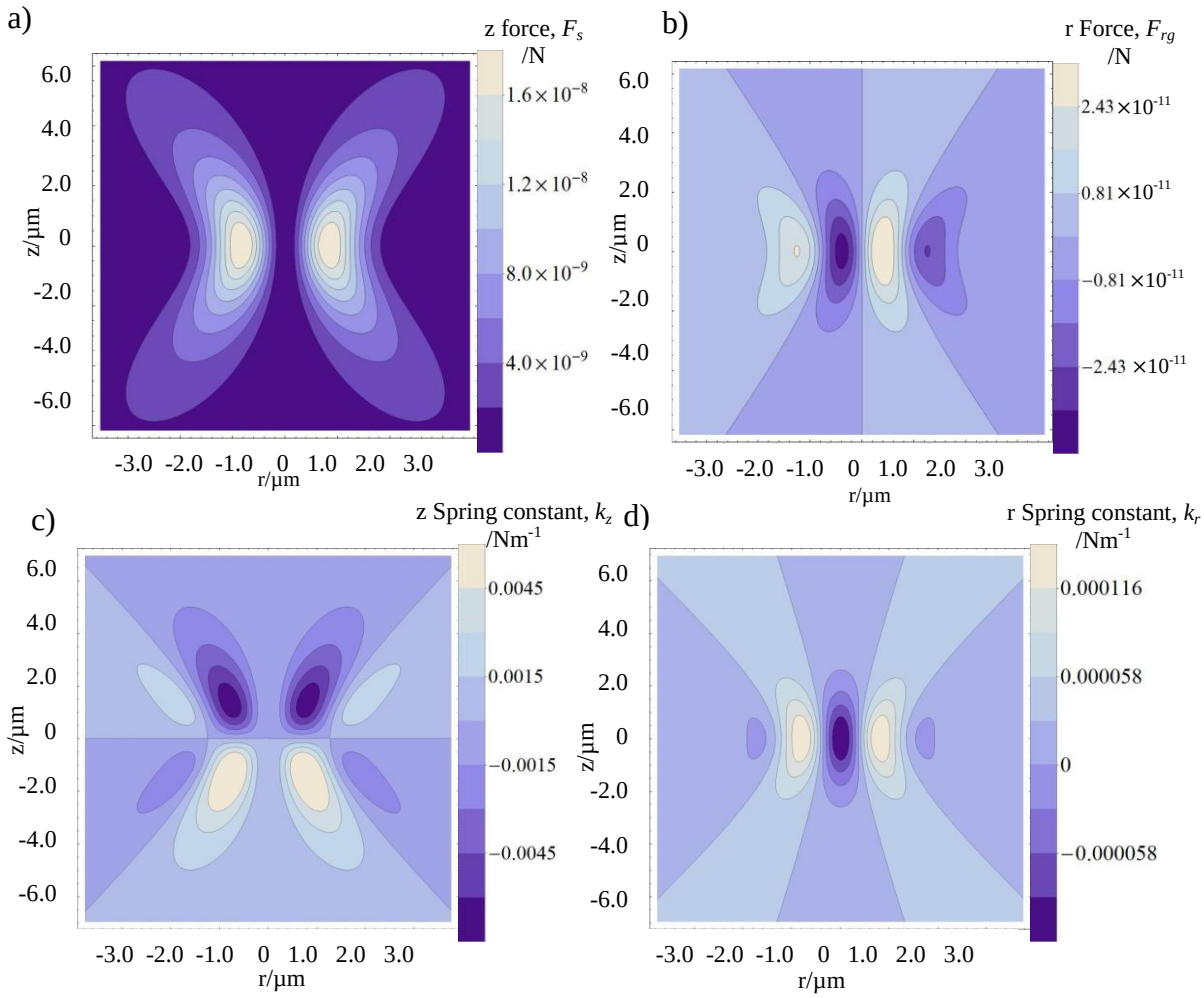

Figure 2.8 All graphs are for a TEM_{01} beam for a 1µm gas-air bubble. a-b) the total force in the z direction and r direction respectively, on the bubble when displaced from the centre of the trap in the z and r direction, c-d) is the spring constant for the axial force and the radial force respectively.*

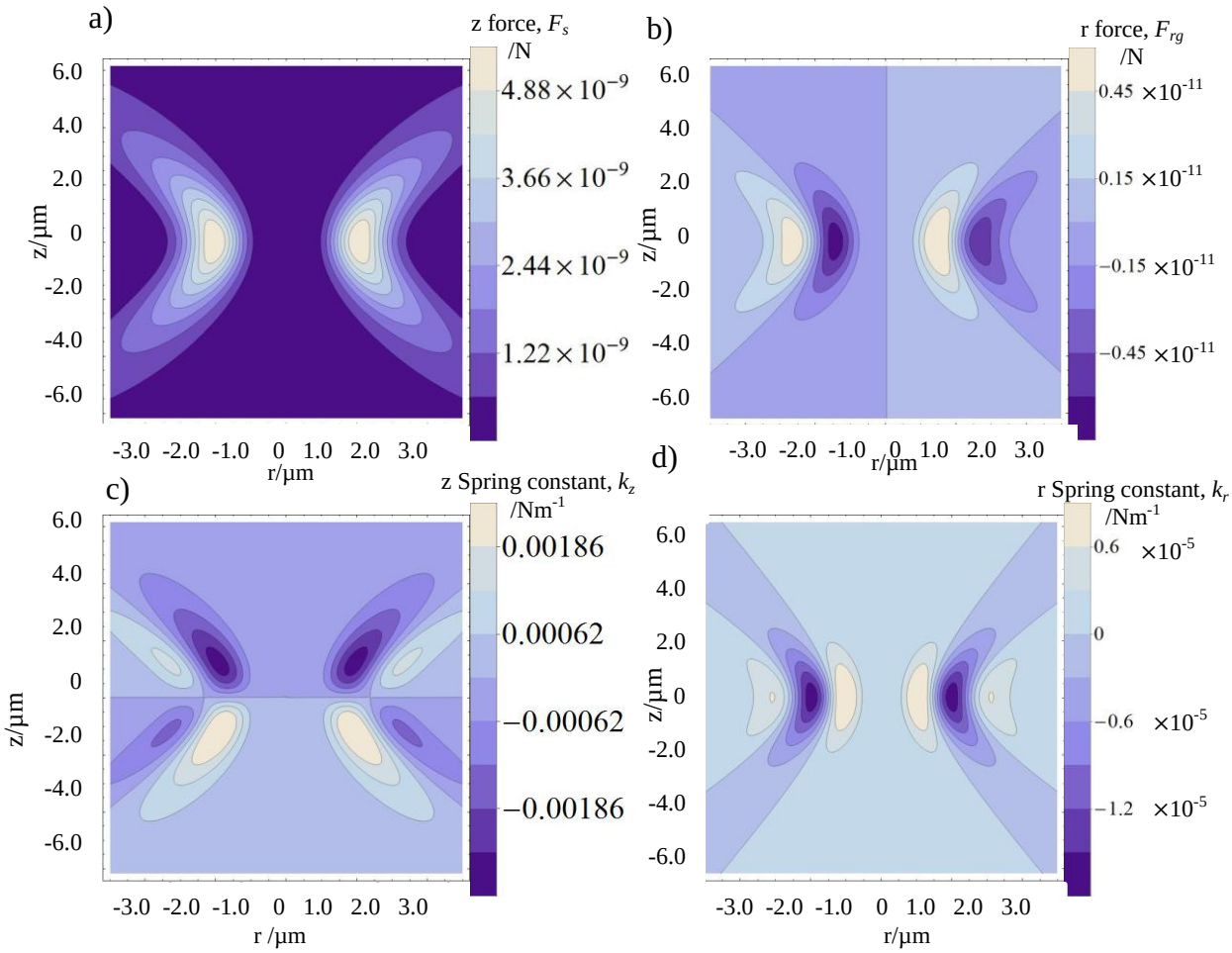

Figure 2.9 All graphs are for a TEM_{03} beam for a 1µm gas-air bubble. a-b) the total force in the z direction and r direction respectively, on the bubble when displaced from the centre of the trap in the z and r direction, c-d) is the spring constant for the axial force and the radial force respectively*

2.6 Ray Optics Implementation

Particles that are much larger in diameter than the wavelength of the laser beam can be treated by a Ray Optics approach [13]. This model assumes that the beam is decomposed into numerous individual rays, each with an appropriate intensity, direction and state of polarization.

2.6.1 Overview of Ray Optics Theory

Each ray is considered to be a plane wave that changes direction when it refracts according to Snell's Law, $n_1 Sin(\theta) = n_2 Sin(\theta r)$, where θ is the angle of incidence and θr is the angle of refraction. It then follows that θ can be used to find the Fresnel coefficients of reflection, R, and transmission, T of light, Equation (2.7a-b) [29, 38], in which the relative refractive index is $n=n_2/n_1$. The calculation of R and T depends on the polarisation of the incident ray. The subscript s denotes that the ray is polarised with an electric field that is perpendicular to the plane of incidence and the subscript p that it is polarised with an electric field that is parallel to the plane of incidence. Here a circularly polarised input beam is assumed with half the power in the s and p orientated polarisation components, thus the reflection and transmission coefficients are:

$$R = \frac{R_s + R_p}{2} \qquad (2.7a)$$

$$T = 1 - R \qquad (2.7b)$$

where

$$R_p = \left(\frac{-n^2 \cos\theta + \sqrt{n^2 - \sin\theta^2}}{n^2 \cos\theta + \sqrt{n^2 - \sin\theta^2}} \right)^2 \qquad (2.8a)$$

$$R_s = \left(\frac{\cos\theta - \sqrt{n^2 - \sin\theta^2}}{\cos\theta + \sqrt{n^2 - \sin\theta^2}} \right)^2 \qquad (2.8a)$$

Each ray is considered to carry a certain amount of incident momentum, $n_1 P/c_l$, where P is the power of the ray, n_1 is the refractive index of the medium and c_l is the speed of light in the medium. The force felt by the particle is caused by the change in momentum of the ray when it interacts with the particle [39].

For a sphere, the total force is found by vectorial summation of each contribution due the power of the reflected rays PR and the infinite number of emergent refracted rays of consecutively decreasing power $(PT^2, PT^2R, \ldots PT^2R^n, \ldots\ldots)$ [16], shown in Figure 2.10. The forces are again decomposed into two components, in the parallel F_s, and perpendicular direction F_g as given by Roosen *et al.* [40, 41]. F_s is the scattering force and F_g is the gradient force for the total beam [16].

$$F_s = \frac{n_1 P}{c_l}\left(1 + R\cos(2\theta) - \frac{T^2(\cos(2\theta - 2\theta r) + R\cos(2\theta))}{1 + R^2 + 2R\cos(2\theta r)}\right) \tag{2.9}$$

$$F_g = \frac{n_1 P}{c_l}\left(R\sin(2\theta) - \frac{T^2(\sin(2\theta - 2\theta r) + R\sin(2\theta))}{1 + R^2 + 2R\cos(2\theta r)}\right) \tag{2.10}$$

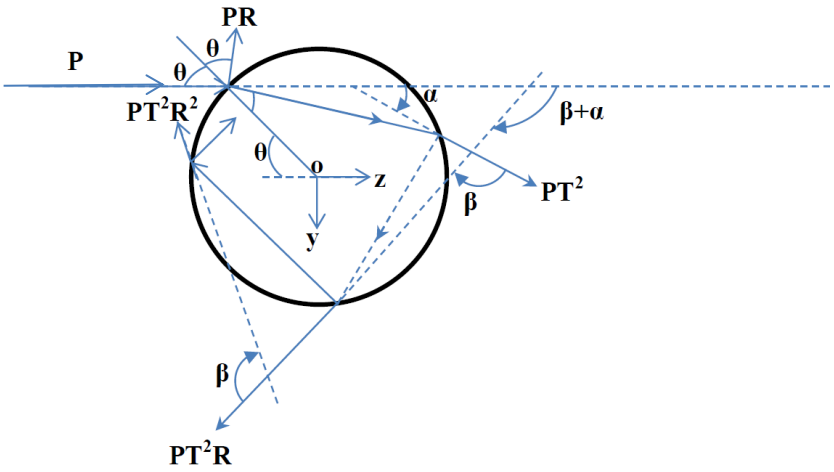

Figure 2.10 Geometry for calculating the force due to the scattering of a single incident ray of power P by a dielectric sphere.

This can also be written in the form $F = Q\frac{n_1 P}{c}$, where Q is the trapping efficiency of the beam and is found by integrating q_s and q_g, respectively the scattering and gradient momentum fractions for each ray, over the area of the objective lens, see Figure 2.11.

$$Q_i = \frac{2}{\pi}\int_0^{r_{max}}\int_0^{2\pi}\frac{r}{{r_{max}}^2}(q_i\hat{\imath})\sin\alpha\, dr d\beta \;\; where\; i = s, g \tag{2.11}$$

$$q_s = \left(1 + R\cos(2\theta) - \frac{T^2(\cos(2\theta - 2\theta r) + R\cos(2\theta))}{1 + R^2 + 2R\cos(2\theta r)}\right) \tag{2.12}$$

$$q_g = \left(R\sin(2\theta) - \frac{T^2(\sin(2\theta - 2\theta r) + R\sin 2\theta)}{1 + R^2 + 2R\cos(2\theta r)}\right) \tag{2.13}$$

The trap force can be calculated by again decomposing the force generated by each incident ray into the scattering and gradient force components, correspondingly given by

$$d\boldsymbol{F}_s = \hat{s}\frac{n_1}{c}q_s dP \tag{2.14}$$

$$d\boldsymbol{F}_g = \hat{g}\frac{n_1}{c}q_g dP \tag{2.15}$$

Where dP is the incremental power of the ray and $\hat{s}$ and $\hat{g}$ are the unit vectors in the directions $d\boldsymbol{F}_s$ and $d\boldsymbol{F}_g$ respectively with each having an axial and radial component. Equation (2.16) gives dP over the area of the objective lens.

$$dP = Ir dr d\beta = \frac{2P}{\pi{\omega_0}^2}\left(\frac{\omega_0}{r_{max}}\right)^2\sin(\alpha)\, r dr d\beta \tag{2.16}$$

2.6.2 Derivation for an Arbitrary Trap Location

This derivation is the same as that found in [16], however a typographical error was discovered in the paper. The corrected derivation of this model has been briefly summarized below.

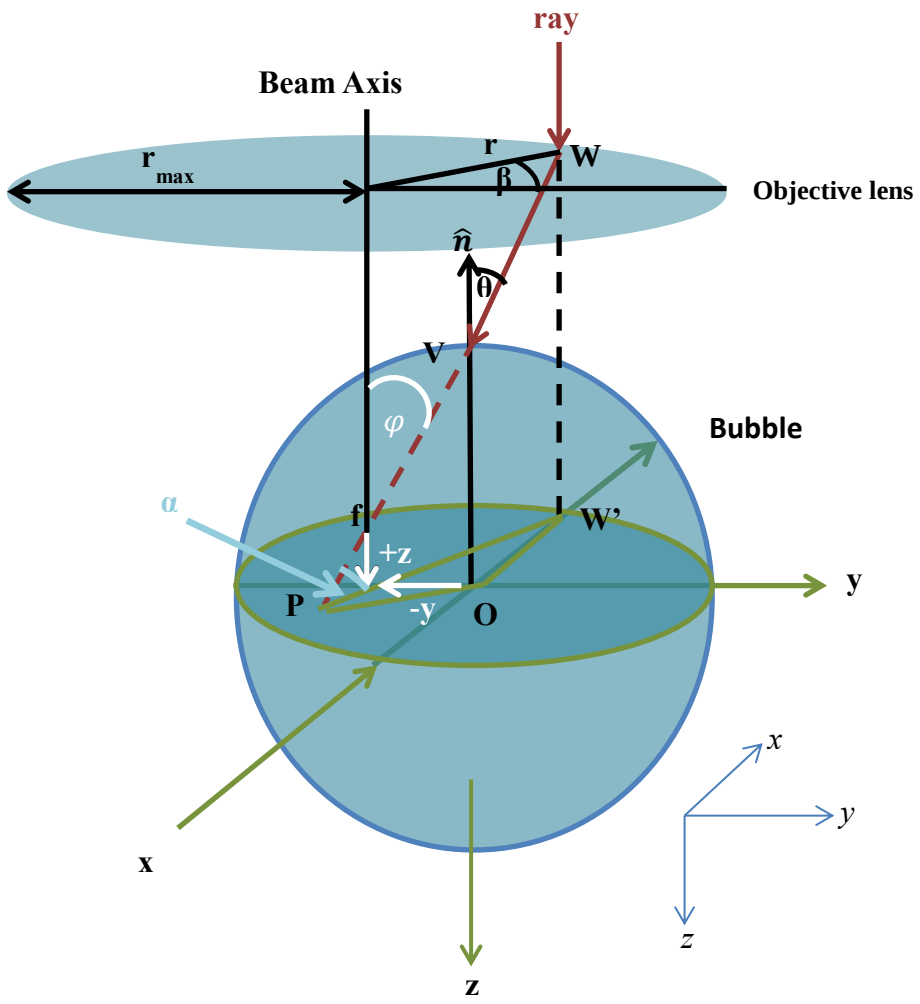

Figure 2.11 Trap geometry showing the relative positions of microbubble centre and beam focus .

A schematic of the trap geometry is shown in Figure 2.11, where the ray enters a lens at distance r from the laser beam axis and angle β with respect to the y-axis, and exits the lens interacting with the bubble at point V making an interaction angle of θ with the z-axis The ray is then extended down to the xy plane to a point P, where the angle α is the angle between the xy plane and the ray. The plane of incidence of the ray is POV, which contains both the incident ray and the normal to the sphere, OV. The gradient force, F_g, acts in direction OV' and is perpendicular to the incident ray VP in the plane of OPV.

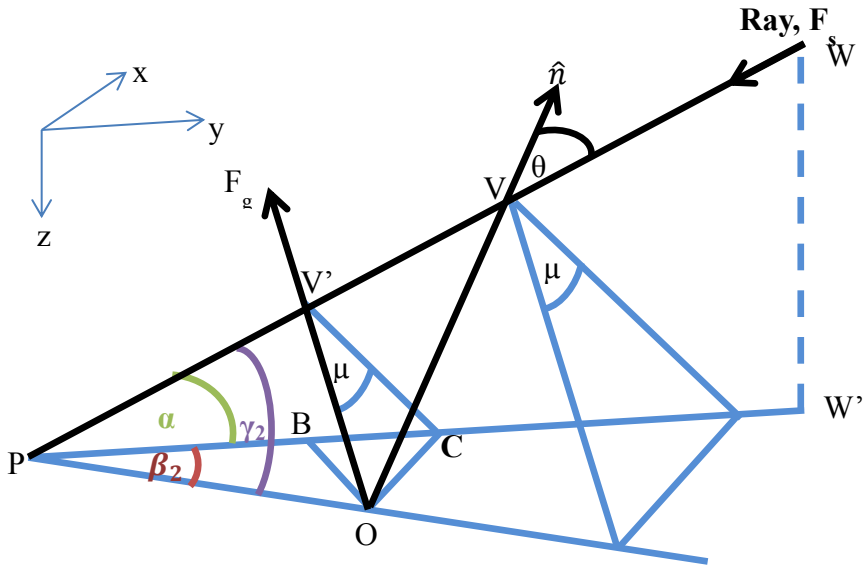

Figure 2.12 Another view of the arbitrary trap geometry, showing the angles more clearly

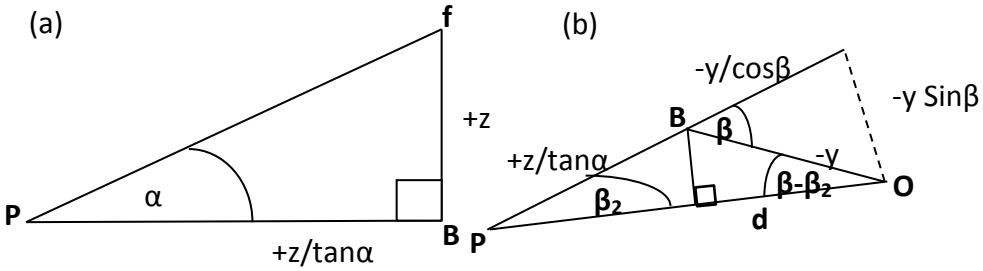

Figure 2.13 (a) Geometry of the triangle fPB (b) geometry of POB used to calculate β2 and d

The angle β_2 can be found via simple geometry, Figure 2.13

$$\beta_2 = \tan^{-1}\left(\frac{-y\sin\beta}{-y\cos\beta + z/\tan\alpha}\right) \qquad (2.17)$$

γ_2 from Figure 2.12 is similarly found as:

$$\gamma_2 = \cos^{-1}(\cos\alpha\cos\beta_2) \qquad (2.18)$$

Then using the Sine Rule and Figure 2.14:

$$\theta = \sin^{-1}\left(\frac{d\sin\gamma 2}{r0}\right) \tag{2.19}$$

And from Figure 2.13(b)

$$d = \frac{z\cos\beta 2}{\tan\alpha} - \mathrm{y}\cos(\beta - \beta 2) \tag{2.20}$$

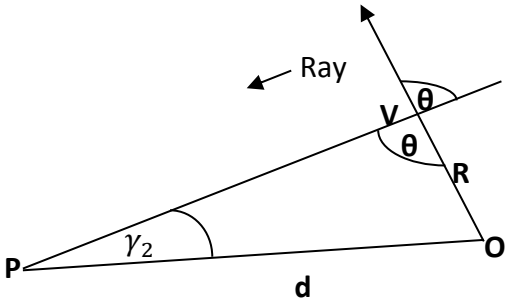

Figure 2.14 Geometry of POV

And from Figure 2.12

$$\mu = \cos^{-1}\left(\frac{\tan\alpha}{\tan\gamma 2}\right) \tag{2.21}$$

Deriving the *z* component forces in the trap, as seen in Figure 2.15 consider the *V'OC* plane, which is perpendicular to the plane with angle *γ2* in plane *POV*. The angles *OCV'*, *OCP* and *CV'P* are all right angles.

From triangle *WPW'*, Figure 2.15(a), the component of the scattering force, F_s with respect to the *z*-axis *WW'* is $F_{sz}=F_s \sin\alpha$. Then from *V'OC*, Figure 2.15(b), the component of F_g on *CV'* is $F_g \cos\mu$ and from *V'PC*, Figure 2.15(c), the gradient component in the *z*-axis is $F_{gz}=F_g\cos\mu\cos\alpha$. Giving the total force of the ray in the *z* direction as:

$$F(z) = F_s \sin\alpha + F_g \cos\mu\cos\alpha \tag{2.22}$$

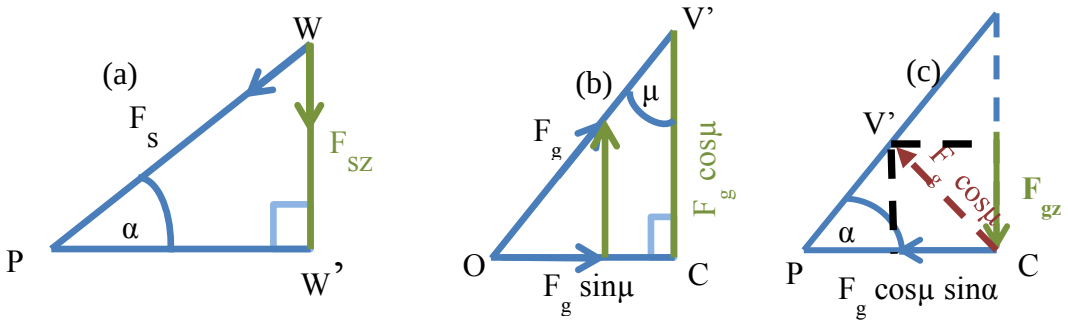

Figure 2.15 geometries used to derive the z component of the scattering and gradient forces (a) is triangle WPW' (b) V'OC and (c)V'PC

For the *y*-axis forces in the laser trap: from *PCV*, Figure 2.16(a), the component of the scattering force, F_s in the *PC* direction is $-F_s \cos\alpha$ and using *PCO*, Figure 2.16(b), the component of the scattering in the *y* direction *BO* is $F_{sy}=-F_s \cos\alpha \cos\beta$

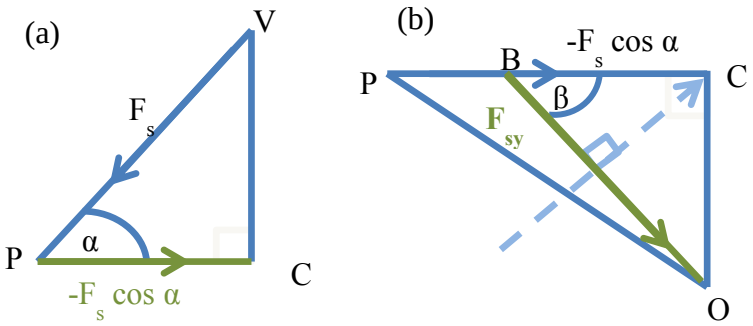

Figure 2.16 geometries to find the scattering force in the y-direction, (a) triangle PCV (b) PCO

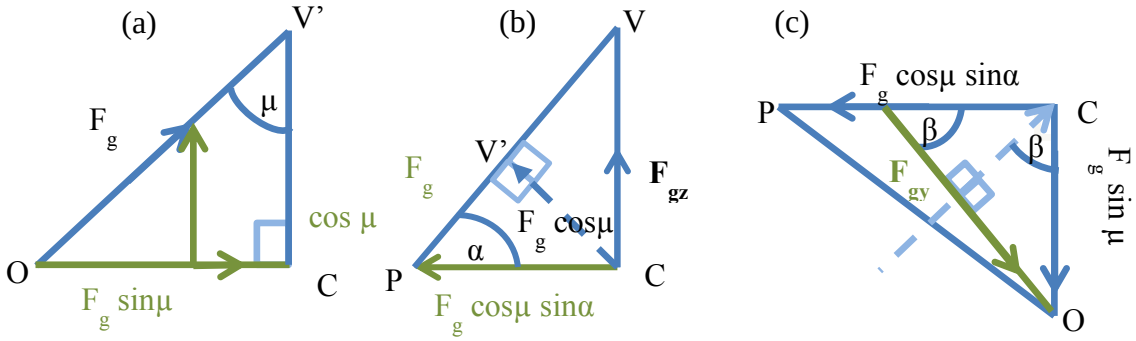

Figure 2.17 geometries to find the gradient force in the y-direction, (a) triangle V'OC (b)VPC and (c) PCO

It may be seen in Figure 2.17 (a) that the component of the gradient force, F_g in the *OC* direction is $F_g \sin\mu$, and in Figure 2.17 (c) that the component of the gradient force in the *y* direction *BO* is F_{gy}= -$F_g \sin\mu \sin\beta$. The second part of the gradient-force component is found from Figure 2.17 (a), triangle V'OC, which gives the component of F_g on *CV'* which is $F_g \cos\mu$. Then from *VPC*, Figure 2.17 (b), the component to *PC* in the *z*-axis is F_{gz}=$F_g \cos\mu \sin\alpha$ and finally Figure 2.17(c) *PCO*, the component of the gradient in the *y*-direction to *BO* is $F_{gy} = F_g \cos\mu \sin\alpha \cos\beta$. Giving the total force of the ray in the *y*-direction as:

$$F(Y) = -F_s \cos\alpha \cos\beta + F_g(\cos\mu \sin\alpha \cos\beta - \sin\mu \sin\beta) \qquad (2.23)$$

It should be noted that this result differs from that of Ashkin [16] as the third term was found to be negative instead of positive. However as already stated this does not change the calculation of the total force, as the term is odd and therefore when integrated will be unchanged.

The *x*-components of the force are found via triangle *PCO*, Figure 2.18 (a), the component of the scattering in the *x*-direction *BO* is F_{sx}=-$F_s \cos\alpha \sin\beta$ and from Figure 2.18 (b), the component of the gradient in the *x*-direction *BO* is $F_{gx} = F_g(\cos\mu \sin\alpha \sin\beta - \sin\mu \cos\beta)$. Giving the total force of the ray as:

$$F(X) = -F_s \cos\alpha \sin\beta + F_g(\cos\mu \sin\alpha \sin\beta - \sin\mu \cos\beta) \qquad (2.24)$$

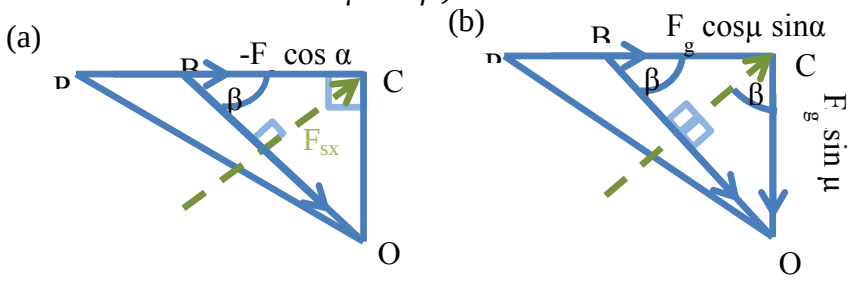

Figure 2.18 geometries to find the x components of the force(a) for the scattering component (b) the gradient component

This means that the unit vectors $\hat{s}$ and gradient $\hat{g}$ can be written as:

$$\hat{s} = \hat{s}_z + \hat{s}_y + \hat{s}_x \quad (2.25)$$
$$= \sin\alpha\,\hat{z} - \cos\alpha\cos\beta\hat{y} - \cos\alpha\sin\beta\hat{x}$$
$$\hat{g} = \hat{g}_z + \hat{g}_y + \hat{g}_x \quad (2.26)$$
$$= \cos\mu\cos\alpha\,\hat{z} + (\cos\mu\sin\alpha\cos\beta + \sin\mu\sin\beta)\hat{y}$$
$$+ (\cos\mu\sin\alpha\sin\beta + \sin\mu\cos\beta)\hat{x}$$

2.6.3 Implementation of the Model

To implement this model some geometric relations were used to simplify the equations. Namely when $\varphi=\varphi_{max}$ the maximum angle of divergence, $tan\,\varphi_{max} = \frac{r_{max}}{l_t}$, which is obvious from the symmetry seen in Figure 2.11. Similarly, from Figure 2.11 $\alpha = tan^{-1}\frac{l_t}{r}$ where r is the radius of the aperture, l_t is the distance between the lens and the focus and is 200μm as stated in Table 2.1 and r_{max} is found from the above relation.

Using the geometric relations $r = l_t\,\tan\varphi$ and $\omega(z) = l_t\tan^2(\varphi_{max}) = r_{max}$, Equation (2.16) becomes:

$$dP = \frac{2P}{\pi}\frac{r}{{r_{max}}^2}\sin(\alpha)\,drd\beta \quad (2.27)$$

Therefore the trapping efficiencies Q_i where i=x,y,z are calculated by integrating over the surface of the lens.

$$Q_i = \frac{2}{\pi}\int_0^{r_{max}}\int_0^{2\pi}\frac{r}{{r_{max}}^2}(q_s\hat{s} + q_g\hat{g})\sin\alpha\,drd\beta \quad (2.28)$$

This means that the scattering component of the trapping efficiency is:

$$Q_s = \frac{2}{\pi}\int_0^{r_{max}}\int_0^{2\pi}\frac{r}{{r_{max}}^2}(q_s\hat{s})drd\beta \quad (2.29)$$

And the gradient component is:

$$Q_g = \frac{2}{\pi}\int_0^{r_{max}} \int_0^{2\pi} \frac{r}{{r_{max}}^2}(q_g \hat{g}) dr d\beta \tag{2.30}$$

It should be noted that there is symmetry about the *y*- axis for the *z* and *y* forces, as angle β from 0-π has the same contribution as the β from π -2π. Therefore theses forces only need to be integrated for β from 0-π, and the result multiplied by 2 to get the net force.

When the angle θ is larger than 90° the trapping efficiencies Q_s and Q_g are taken to be zero as the ray will not interact with the bubble. When $n_2 < n_1$ (e.g. water to air) the critical angle, θ_c, where total reflection occurs also needs to be taken into consideration. In the Fresnel relations when $\sin\theta_c > n$ then the term $\sqrt{n^2 - \sin^2\theta}$ becomes negative and *R* becomes complex; its magnitude however is easily shown to be unitary in this range owing to total reflection for $\theta > \theta_c$. Therefore when $\sin\theta > n, R$ is taken to equal 1 and *T* (transmission) =0.

2.6.4 Model Verification

Before using this model to predict and evaluate the equilibrium position and spring constants involved in trapping a microbubble, the purpose written code was verified against figures 5 and 7 in [16] which depict the scattering and gradient trapping efficiencies along the *z*- and *y*- axis respectively for a uniform beam incident upon a high index particle with a numerical aperture of 1.2, a relative refractive index $n = n_2/n_1 = 1.2$, where n_1 =1.33, the refractive index of water, and n_2=1.6, that of a polystyrene bead. The other constants used were l_t=200μm, r_{max}=*549μm* and particle radius, *a*=1μm. The graphs, shown in Figure 2.19, were produced by calculating the trapping efficiencies Q_s and Q_g (Equations (2.29) - (2.30)) when varying the position of the particle centre –*y* along the y-axis, (keeping *z*=0), and +*z* along the *z*-axis, (keeping -*y*=0). These figures exactly match those produced in [16] , figures 5 & 7 ,thereby validating the code for this case.

As the model was derived for high index particles, however, a check needed to be carried out to see if it would still describe the behaviour of low index particles, such as microbubbles in water. For these particles it is expected that the gradient force would reverse direction, but the scattering force would not, as shown in

Figure 2.1. It was also expected that the magnitude of the trapping force would be comparable to that of the high index particle. For this computation the same set up was used for the high index particle except that $n_2 = 1$, the refractive index of air, which is assumed to be similar to the filling gas of a microbubble. It can be seen from Figure 2.20, the expected behaviour of the gradient and scattering trapping efficiencies were observed and that the model holds for a low index particle as well as a high index particle.

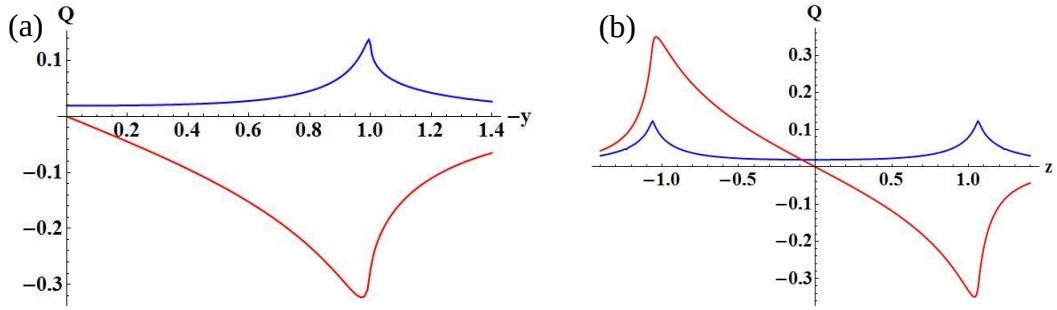

Figure 2.19 the scattering (blue) and gradient (red) components along the (a) y-axis (left) and (b) z-axis (right) for a uniform high-index particle and uniform beam

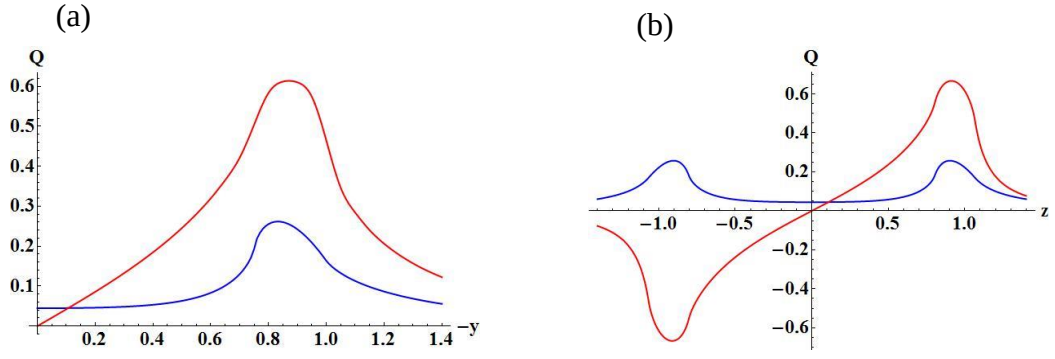

Figure 2.20 the scattering (blue) and gradient (red) components along the (a)y-axis (left) and (b) z-axis (right) for a uniform low-index particle and a uniform beam.

2.6.5 Numerical Implementation

To compare the model with experimental data, the outputs from the model required were the trapping position of the bubble in the *z*-axis and the spring constants in the *x, y* and *z* directions. The calculations were carried out for the parameters in Table 2.1, assuming that the microbubble is being trapped by a Laguerre Gaussian beam for a range of laser powers, *P*=10mW-100mW with modes *l*=1-10 for the bubble radii, *a*, of 2.5μm, 5μm, 7.5μm, 10μm.. The parameters were chosen to correspond to the experimental set up, so that the strongest trap could be found for a given bubble size by varying the mode, *l*, and power, *P*. For the purposes of the numerical calculations all lengths were non-dimensionalized by *a* and the equations were implemented as follows.

First the Equations for *dP* and Q_i, were found for a Laguerre-Gaussian (LG) beam, TEM_{lp}*, which possesses the irradiance profile given by Equation (2.3). Where L_p^l is the associated Laguerre Polynomial, where *l* is the azimuthal index and *p* is the radial index:

$$dP = \frac{2P_0}{\pi {\omega_0}^2}\left(\frac{p!}{(l+p)!}\right) e^{-\left(\frac{2r^2}{({r_{max}}^2)}\right)} \left(\frac{2r^2}{r_{max}^2}\right)^{|l|} \left(L_p^l\left(\frac{2r^2}{r_{max}^2}\right)\right)^2 \times \sin(\alpha)\, r dr d\beta \tag{2.31}$$

$$Q_i = \frac{2}{\pi}\int_0^{r_{max}}\int_0^{2\pi} \frac{r}{{r_{max}}^2}\left(\frac{p!}{(l+p)!}\right) e^{-\left(\frac{2r^2}{({r_{max}}^2)}\right)} \times \left(\frac{2r^2}{r_{max}^2}\right)^{|l|} \left(L_p^l\left(\frac{2r^2}{r_{max}^2}\right)\right)^2 (q_s \hat{s}_i + q_g \hat{g}_i) \sin(\alpha)\, dr d\beta \tag{2.32}$$

Where i=x,y and z.

The steps to find all of the four parameters were as follows. First the *z* equilibrium trapping positon and the spring constant were found. The equilibrum trapping position is assumed to occur at *y =0* (*.i.e.* along the *z*-axis) and is where the bubble is held in a stable position in the trap. This position occurs when the laser force in the *z*-axis balances the

weight and buoyancy force of bubble Figure 2.21 and occurs when F_{z_total}, the total z force, shown in Equation (2.33) equals zero.

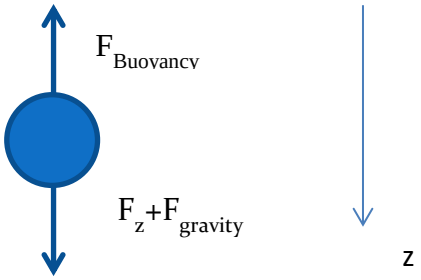

Figure 2.21 Shows the forces which act on the bubble in the z-axis direction

$$F_{z_{total}} = F_z + F_{gravity} - F_{buoyancy} \qquad (2.33)$$

Where $F_z = \frac{n_1 P_0}{c_l} Q_z$. Equation (2.33) was run for z=*0-5*, which covers a sufficiently large range to cover all positions where an equilibrium trapping location may occur for the bubbles. For some of the parameter values the bubble escaped the trap as the buoyancy of the bubble was much larger than the maximum force in the trap. As can be seen from Figure 2.22(a) there can sometimes be two points in this range where the force equals zero. However the equilibrium trapping position would occur when the z spring constant , k_z, is positive (i.e the gradient of the force is negative) as this is where the force of the laser would be pushing the bubble away from the focus of the beam (positive z direction) counteracting the buoyancy of the bubble which acts towards the focus of the beam (negative z direction). To find the equilibrium position, the location corresponding to the

maximum force was found and only points after this in the *z*- axis were considered as they possessed a positive spring constant.

The equilibrium trapping position and the spring constant were found by locating the point at which the net force changes sign. The step sizes between the points found either size of where F_{z_total}=0 occurs, were then decreased, so that the points could be considered to be a straight line through the axis, Figure 2.22 (b). The straight line formula $F_{z\_total}=m\,z+c$ where *m* is the gradient and *c* is a constant was fitted to these data points. As the spring constant in the *z*-axis is $k_z = -\frac{dF_{z\_total}}{dz}$, it can be taken to be the negative of the gradient of the line at the equilibrium trapping position, in other words –*m*, the equilibrium trapping position was found by making $F_{z\_total} = 0$ and solving for *z*. If $F_{z\_total} \neq 0$ at any point the bubble was taken to have escaped.

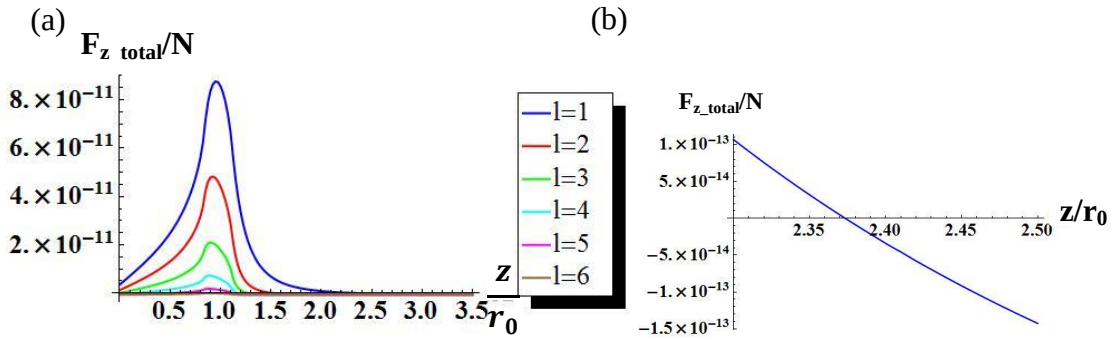

Figure 2.22 (a) showing how the F_{z_total} force varies with z at P=60mW and (b) a zoomed image of l=1,where it F_{z_total}=0, with the negative gradient of the force pushing the bubble towards the centre (downwards in the positive z direction). The bubble is held in equilibrium trapping position when F_{z_total}=0 .

The equilibrium trapping position found was then used to define the axial position at which $F_z = \frac{n_1 P_0}{c_l} Q_y$. This was determined for 0 < -y < 0.1, Figure 2.23, to find the *y*-spring constant $k_y = -\frac{dF_y}{dy}$. The *x* spring constant in the x-direction would be identical to the y spring constant due to symmetry.

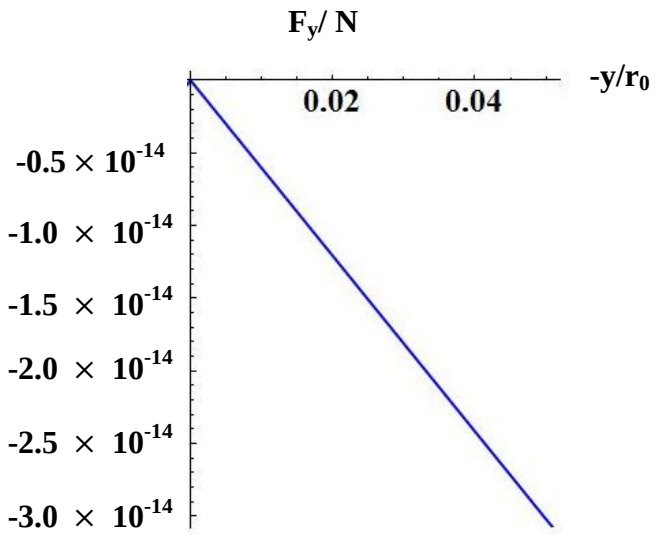

Figure 2.23 the direction of F_y (the y force) around y=0 at the z equilibrium trapping position for l=1 and P=60mW

2.6.6 Results

The equilibrium trapping positions were found to be further from the focus as the bubble size increased, Figure 2.24 and increasing the laser power moved the bubbles to a trapping position (further away from the focus), since as the power increases the force becomes larger and linearly scales the shape of the graph (Figure 2.25). It was also observed that there existed a larger range of *l* over which the smaller bubbles could be trapped than the larger bubbles, with the position of the equilibrium trapping occurring nearer the focus as *l* increased in value. This can be seen in Figure 2.22a which shows the equilibrium position for increasing *l*.

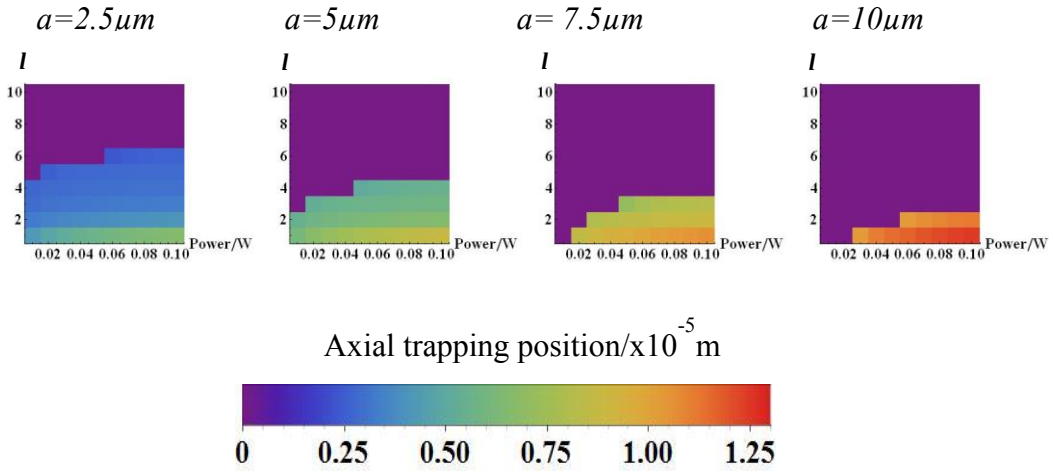

Figure 2.24 the equilibrium trapping positions for varying bubble size, power and l. When the axial trapping position= 0 (purple), the bubbles is assumed to have escaped from the trap.

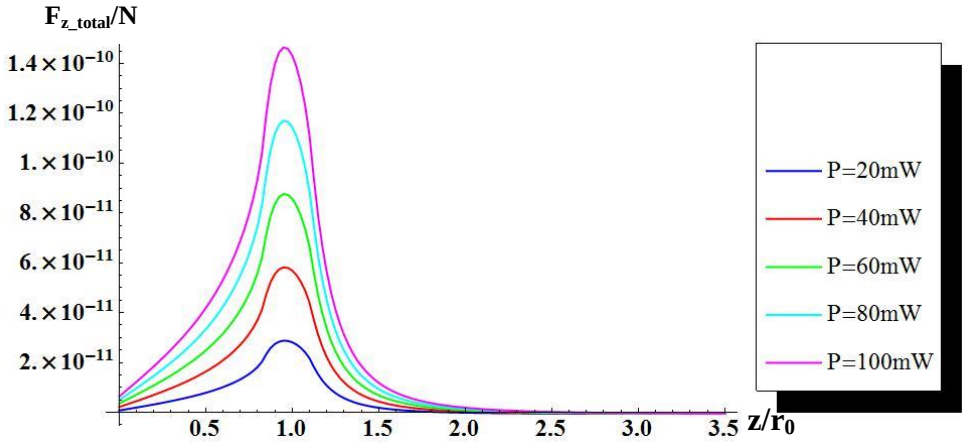

Figure 2.25 demonstrates how the axial force as a function of displacement in the z direction changes with increasing power

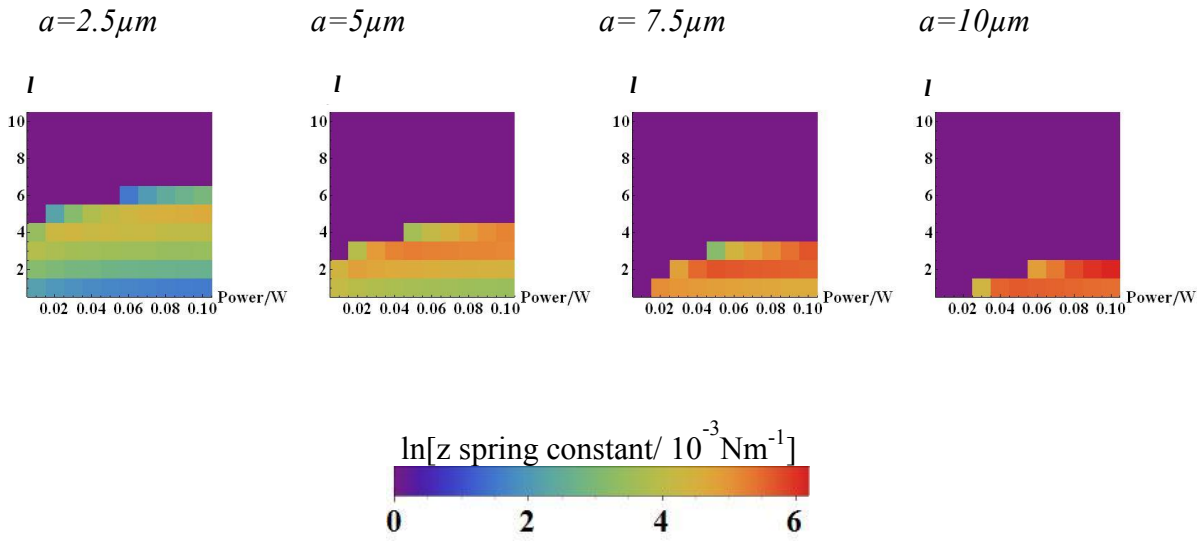

Figure 2.26 the z-spring constants for varying size and power. When the z- spring constant= 0 the bubble is assumed to have escaped

Figure 2.26 shows the effect of varying bubble size and the laser power on the spring constants. As the bubble's size increases so does the spring constant for a certain *l* and power. However for any given power or *l*, the effect of increasing them has a more complex trend on the value of the spring constant. As can be seen, the spring constant may increase or decrease from the previous value when increasing power for a certain *l* and vice versa. This can be explained by looking at the curvature of trapping force. Figure 2.27 shows that for the trapping modes *l=1-3*, an inversely proportional behaviour is observed between the spring constant, as it decreases, and the power, which increases. At *l=4* this relationship becomes less clear and at *l=5-6* the relationship has completely reversed with the spring constant being proportional the power. At *l=7* and above the bubble escapes. The change in behaviour becomes obvious from looking at $\frac{a^2 Q_z}{dz^2}$ for *l=1* and *l=6* for power at 60mW, shown in Figure 2.28(c)-(d). This shows how the curvature of *l=1* is straight with a negative gradient, whereas the curvature at *l=6* is seen to be negative and changing at a faster rate than *l=1*.

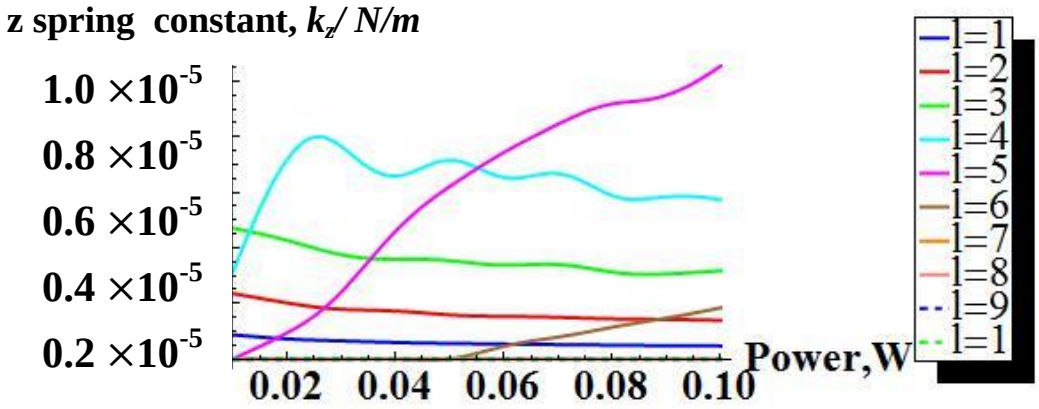

Figure 2.27 the z spring constant vs power for varying mode l, where the modes l=7-10 cannot be seen as the bubble escapes

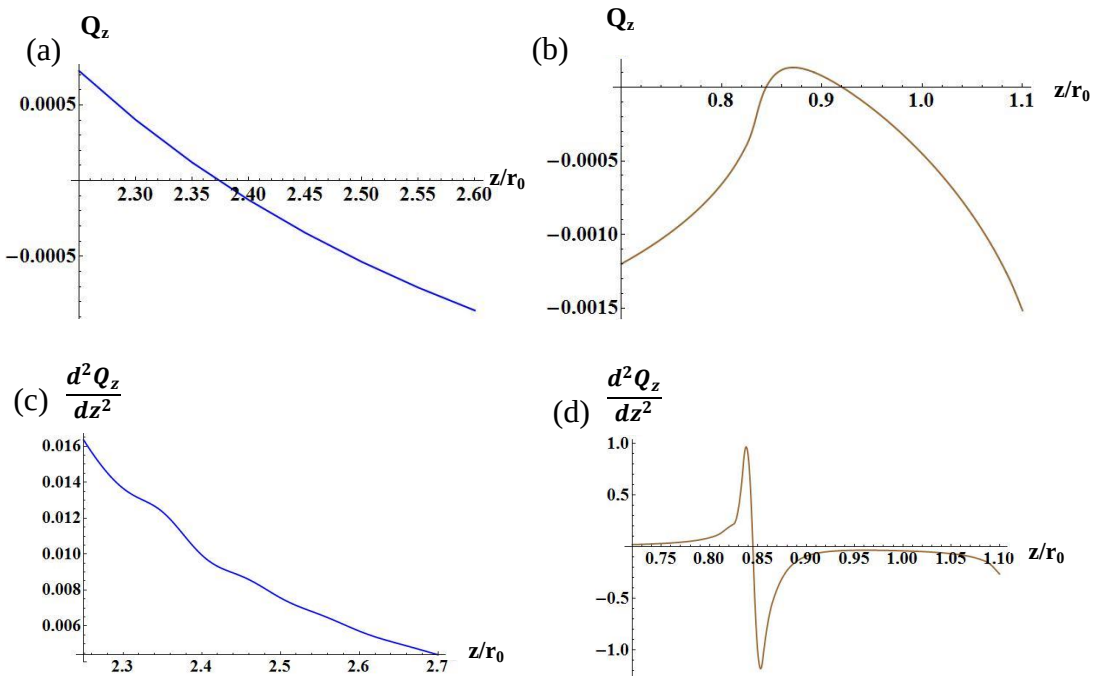

Figure 2.28 the zoomed in crossing point of the equilibrium position of a 2.5 µm radius bubble (a) for l=1 and (b) for l=6 this shows the different position and curvature of the position. This becomes more apparent when looking at $\frac{d^2Q_z}{dz^2}$ *pictured in (c) for l=1 and (d)=l=6.*

The transverse spring constants, shown in Figure 2.29, were observed to have a linear relationship with size and power, with them all increasing. As the mode increased the

spring constants decreased. The strongest *y*-spring constants were observed for the lowest trapping mode, i.e. *l=1*, and the highest power and the largest bubble.

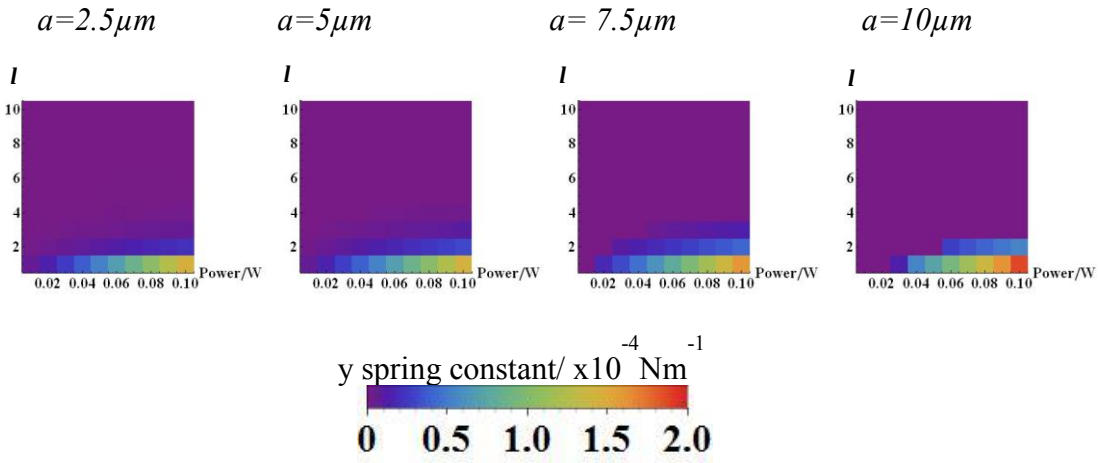

Figure 2.29 the y-spring constants for different bubble radii for varying trapping mode and power.

In conclusion, the forces and spring constants predicted using the ray optics approach are in the pN and pN/μm ranges respectively expected from [13]. The equilibrium trapping position moves further away from the focus with increasing power and radius until the point at which the bubble escapes. This is because as the power increases it has the effect of "stretching" the $F_{\_ztotal}$ vs z curve parallel to the $F_{\_ztotal}$ axis, shifting the equilibrium position to a higher z. The gradient of $Q(z)$ (i.e. the spring constant) at this new equilibrium position may be either lower or higher than at the previous equilibrium depending on whether the curvature is positive or negative. The *y*-spring constant increases both with increasing radius and power. This has interesting implications for experimental implementation as the strongest *z*-trapping position does not have a clear relationship with either power or the LG mode. In practice, both the axial and radial forces need to be maximized to ensure the bubbles are stably trapped, which is particularly important in the presence of external forces, e.g. acoustic radiation pressures or fluid drag.

2.7 Summary

In this chapter the forces involved in trapping a low index particle (microbubble) whose size falls into the intermediate range between the Ray optics and Rayleigh scattering regimes were investigated. A dipole model and a ray optics model were both implemented. However it was observed that the dipole method overestimated the force upon the bubble and also did not adequately describe the expected behaviour, e.g. location of the axial equilibrium. This is thought to be because the theory predicts an a^3 dependence of the force on the radius of the bubble, therefore using a radius in the micrometer regime (where the dipole approximation is not valid) rather overestimates the force[13]. This method was nevertheless useful in indicating the position and the shape of the maximum and minimum forces in the trap, which correspond to the ray optics result, with both models finding the maximum force occurring roughly one bubble radius away from the beam focus.

The ray optics method was found to predict a force which is closer to that expected from experimental results. It further demonstrated how changing the mode and power of the trap effects the trapping position and the spring constants. The spring constants were found to increase and decrease depending on the mode of the LG beam used, which has interesting implications for the use of optical trapping in bubble experiments. However due to the lack of experimental data covering the whole parameter space, it is difficult to conclusively ascertain how accurate the model is.

It can also be seen from Figure 2.22 that this type of trapping is not the same as that in “true” optical tweezers, as the bubble is not confined in three dimensions by the optical gradient, instead this kind of trap is actually (counter) levitation, as the buoyancy of the bubble helps stabilise the trap in the z-axis, whereas in the y-axis the bubble is stabilised by the gradient force in both positive and negative directions.

2.8 References

1. Neuman, K.C. and Block, S.M., *Optical trapping.* Review of Scientific Instruments, 2004. **75**(9): p. 2787-2809.
2. Garbin, V., *Optical Tweezers for the Study of Microbubble Dynamics in Ultrasound*, in *Department of Physics* 2007, University of Trieste, Italy: University of Trieste, Italy.
3. Garbin, V., et al., *Optical micro-manipulation using Laguerre-Gaussian beams.* Japanese Journal of Applied Physics, Part 1: Regular Papers and Short Notes and Review Papers, 2005. **44**(7 B): p. 5773-5776.
4. Ashkin, A., et al., *Observation of a single-beam gradient force optical trap for dielectric particles.* Optics Letters, 1986. **11**(5): p. 288-290.
5. Burnham, D.R. and McGloin, D., *Holographic optical trapping of aerosol droplets.* Optics Express, 2006. **14**(9): p. 4175-4181.
6. Messina, E., et al., *Manipulation and Raman Spectroscopy with Optically Trapped Metal Nanoparticles Obtained by Pulsed Laser Ablation in Liquids.* The Journal of Physical Chemistry C, 2011. **115**(12): p. 5115-5122.
7. Messina, E., et al., *Plasmon-Enhanced Optical Trapping of Gold Nanoaggregates with Selected Optical Properties.* ACS Nano, 2011. **5**(2): p. 905-913.
8. Maragò, O.M., et al., *Optical trapping of carbon nanotubes.* Physica E: Low-dimensional Systems and Nanostructures, 2008. **40**(7): p. 2347-2351.
9. Maragò, O.M., et al., *Brownian Motion of Graphene.* ACS Nano, 2010. **4**(12): p. 7515-7523.
10. Zhang, H. and Liu, K.K., *Optical tweezers for single cells.* Journal of the Royal Society Interface, 2008. **5**(24): p. 671-90.

11. Prentice, P., et al., *Membrane disruption by optically controlled microbubble cavitation.* Nature Physics, 2005. **1**(2): p. 107-110.

12. Prentice, P., et al., *Manipulation and filtration of low index particles with holographic Laguerre-Gaussian optical trap arrays.* Optics Express, 2004. **12**(4): p. 593-600.

13. Jones, P.H., Maragò, O.M., and Stride, E., *Parametrization of trapping forces on microbubbles in scanning optical tweezers.* Journal of Optics A: Pure and Applied Optics, 2007. **9**(8): p. S278.

14. Jones, P.H., Stride, E., and Saffari, N., *Trapping and manipulation of microscopic bubbles with a scanning optical tweezer.* Applied Physics Letters, 2006. **89**(8).

15. Skelton, S.E., et al., *Trapping and deformation of microbubbles in a dual-beam fibre-optic trap.* Journal of Optics, 2012. **14**(7): p. 075706.

16. Ashkin, A., *Forces of a single-beam gradient laser trap on a dielectric sphere in the ray optics regime.* Biophysical Journal, 1992. **61**(2): p. 569-582.

17. Gahagan, K.T. and Swartzlander, G.A., *Trapping of low-index microparticles in an optical vortex.* Journal of the Optical Society of America B: Optical Physics, 1998. **15**(2): p. 524-534.

18. Ye, J.Y., et al., *Trapping cavitation bubbles with a self-focused laser beam.* Optics Letters, 2004. **29**(18): p. 2136-2138.

19. Molloy, J.E. and Padgett, M.J., *Lights, action: Optical tweezers.* Contemporary Physics, 2002. **43**(4): p. 241-258.

20. Sasaki, K., et al., *Optical trapping of a metal particle and a water droplet by a scanning laser beam.* Applied Physics Letters, 1992. **60**(7): p. 807-809.

21. Hansen, P.M., et al., *Expanding the Optical Trapping Range of Gold Nanoparticles.* Nano Letters, 2005. **5**(10): p. 1937-1942.

22. Maragò, O., et al. *Plasmon-enhanced optical trapping of metal nanoparticles: force calculations and light-driven rotations of nanoaggregates*. in *SPIE NanoScience+ Engineering*. 2010. International Society for Optics and Photonics.

23. Bendix, P.M., et al., *Optical Trapping of Nanoparticles and Quantum Dots.* Selected Topics in Quantum Electronics, IEEE Journal of, 2014. **20**(3): p. 1-12.

24. He, H., Heckenberg, N.R., and Rubinsztein-Dunlop, H., *Optical particle trapping with higher-order doughnut beams produced using high efficiency computer generated holograms.* Journal of Modern Optics, 1995. **42**(1): p. 217-223.

25. Macdonald, M.P., et al., *Trapping and manipulation of low-index particles in a two-dimensional interferometric optical trap.* Optics Letters, 2001. **26**(12): p. 863-865.

26. Arlt, J., et al., *Optical micromanipulation using a Bessel light beam.* Optics Communications, 2001. **197**(4-6): p. 239-245.

27. Garcés-Chávez, V., et al., *Transfer of orbital angular momentum to an optically trapped low-index particle.* Physical Review A, 2002. **66**(6): p. 063402.

28. Reicherter, M., et al., *Optical particle trapping with computer-generated holograms written on a liquid-crystal display.* Optics Letters, 1999. **24**(9): p. 608-610.

29. Pedrotti, F.L., *Introduction To Optics, 3/E*. 2008: Pearson Education India.

30. Kennedy, S.A., et al., *Creation of Laguerre-Gaussian laser modes using diffractive optics.* Physical Review A, 2002. **66**(4): p. 043801.

31. Carter, W.H., *Spot size and divergence for Hermite Gaussian beams of any order.* Applied Optics, 1980. **19**(7): p. 1027-1029.

32. Phillips, R.L. and Andrews, L.C., *Spot size and divergence for Laguerre Gaussian beams of any order.* Applied Optics, 1983. **22**(5): p. 643-644.

33. Felgner, H., Muller, O., and Schliwa, M., *Calibration of light forces in optical tweezers.* Applied Optics, 1995. **34**(6): p. 977-982.

34. van de Hulst, H.C., *Light Scattering by Small Particles*. 1957: Dover Publications.

35. Harada, Y. and Asakura, T., *Radiation forces on a dielectric sphere in the Rayleigh scattering regime.* Optics Communications, 1996. **124**(5-6): p. 529-541.

36. Gorce, J.M., Arditi, M., and Schneider, M., *Influence of bubble size distribution on the echogenicity of ultrasound contrast agents: a study of SonoVue.* Investigative Radiology, 2000. **35**(11): p. 661-71.

37. Fury, C., et al., *Experimental characterisation of holographic optical traps for microbubbles*, in *SPIE Photonics Europe 2014*2014: Brussels, Belgium.

38. Fox, F.E. and Herzfeld, K.F., *Gas Bubbles with Organic Skin as Cavitation Nuclei.* The Journal of the Acoustical Society of America, 1954. **26**(6): p. 984-989.

39. Gahagan, K.T. and Swartzlander, G.A., *Optical vortex trapping of particles.* Optics Letters, 1996. **21**(11): p. 827-829.

40. Roosen, G. and Imbert, C., *Optical levitation by means of two horizontal laser beams: A theoretical and experimental study.* Physics Letters A, 1976. **59**(1): p. 6-8.

41. Roosen, G., *Optical Levitation of spheres.* Canadian Journal of Physics, 1979. **57**(9): p. 1260-1279.

3 Modelling Microbubble Translational & Radial Motion

The acoustic response of a microbubble can be sensitive to changes in its immediate environment. Microbubbles thus have the potential to be used for quantitative interrogation of their surroundings for example to determine tissue perfusion and also for non-invasive measurement of hydrostatic pressure, both of which have been the subject of research for some years [1]. This dependence can potentially be exploited for the microscale interrogation of a liquid; for example, to detect changes in viscosity, pressure or the presence of particular chemical species in biosensing applications. However to utilize bubbles as sensors, they must be accurately characterised and the sensitivity of their response to changing conditions quantified. To achieve this, a theoretical model describing bubble dynamics under acoustic excitation which accounts for radial and translational motion of the microbubble, as well as time dependent phenomena and a variety of environments is developed and analysed in this chapter.

A literature review of bubble dynamics is given in sections 3.1-3.3. In sections 3.4-3.6 a model is developed for coupled radial and translational motion including gas diffusion and time dependent surface tension and viscosity terms. In addition, in section 3.5 the model is further developed to include the effects of bubble-wall/bubble-bubble interactions via an image bubble method.

3.1 Overview of Single Bubble Radial Motion Theories

In 1859 Besant [2] published an equation describing the collapse of a spherical cavity, Equation (3.1), which applies the principle of conservation of momentum to the motion of the bubble wall, equating the wall acceleration to the difference in pressure across it.

$$R\ddot{R} + \frac{3}{2}\dot{R}^2 = \frac{p_L - p_0}{\rho_L} \qquad (3.1)$$

Where R is the instantaneous bubble radius and the overdot denotes a time derivative, making $\dot{R}$ the velocity of the bubble wall and $\ddot{R}$ its acceleration, p_L is the pressure of the liquid at the wall, p_0 is the hydrostatic pressure, and ρ_L is the density of the liquid. Besant's equation formed the basis for Lord Rayleigh's subsequent work on the analysis of a collapsing cavity which he published in 1917 [3].

This was later developed by Plesset in 1949 [4], Noltingk & Neppiras in 1950 & 1951 [5, 6] and Poritsky in 1952 [7], with the resulting equation including the effects of internal gas pressure, interfacial tension, liquid viscosity and vapour pressure. This is commonly known as the Rayleigh-Plesset equation, though a more correct term for this equation would be the Rayleigh-Plesset-Noltingk-Neppiras-Poritsky equation (RPNNP), Equation (3.2) [8]:

$$R\ddot{R} + \frac{3}{2}\dot{R}^2 = \frac{1}{\rho_L}\left(\left(p_0 + \frac{2\sigma}{R} - p_v\right)\left(\frac{R_0}{R}\right)^{3\gamma} + p_v - \frac{2\sigma}{R} - \frac{4\mu_L\dot{R}}{R} - p_0 - p_{ac}(t)\right) \qquad (3.2)$$

Where R_0 is the initial radius, p_v is vapour pressure, γ is the polytropic constant, σ is the surface tension, μ_L is the viscosity of the liquid, and p_{ac} is the pressure due to the acoustic wave.

The above equation assumes that the ultrasound wavelength, λ_a, is larger than the radius of the bubble, that there is no transfer of heat or mass during oscillation, the gas behaves ideally, the liquid is much more dense than the gas, that the liquid is incompressible and therefore the velocity of the bubble wall never approaches the speed of

sound in the liquid. However, when the microbubble is exposed to higher ultrasound pressures such as those used for therapeutic applications, the assumptions start to break down and to fully describe the dynamics, the conservation equations for mass, energy and momentum must be solved simultaneously [9], which in the majority of cases is extremely expensive in terms of computational time.

The assumption of liquid compressibility has a particular tendency to be invalidated. This occurs when the velocity of the bubble wall is comparable to that of the speed of sound in the liquid, and several models have been developed to take this into account. Equation (3.2) was re-derived by Herring [10] and Trilling [11] to include approximations for the effects of liquid compressibility and the resulting energy dissipation due to acoustic re-radiation. However this treatment assumed that the speed of sound in the liquid was constant and thus was still limited in terms of the maximum amplitude of oscillation for which it was valid. Gilmore [12] addressed this by using the Kirkwood-Bethe hypothesis which suggests that a bubble surrounded by the flow of an compressible liquid reduces to a single total differential equation for the bubble wall velocity, this allowed it to predict bubble behaviour up to a wall velocity 2.2 times the speed of sound. Keller and Miksis [13] published a more complete model in 1980, for the treatment of large amplitude bubble oscillations, including terms to describe surface tension and liquid viscosity which had previously been ignored by Herring [10] and Trilling [11]. This was developed further by Prosperetti in 1988 [9] by removing the assumption of the ideal gas law and coupling the equation of motion with those for the conservation of mass and energy.

The case of a bubble surrounded by an outer shell was first investigated by Fox and Herzfeld [14] for coated bubbles in the ocean. de Jong *et al.* [15-17] were the first to describe a coated contrast agent microbubble, using the RPNNP equation as the basis for the model, and then including two additional terms to describe the shell as a viscoelastic

solid characterised by two material parameters; the shell elasticity and shell friction. This model also includes approximate correction terms for thermal and radiative dissipation based on the work by Devin [18]. Church [19] was the first to publish a model for a ultrasound contrast agent, that was derived from first principles, for a finite thickness viscoelastic shell on the microbubble surface. Church's model does not include thermal/ radiative dissipation effects, but the paper does show how they could be incorporated.

Hoff *et al*. [20] took the limit of Church's model for an infinitely thin shell:

$$R\ddot{R} + \frac{3}{2}\dot{R}^2 = \frac{1}{\rho_L}\left(p_0 - p_{ac} - p_G(R) - \frac{4\dot{R}\mu_L}{R} - \frac{12\mu_s d_s R_0^2 \dot{R}}{R^4} - \frac{12G_s d_s R_0^2}{R^3}\left(1 - \frac{R_0}{R}\right)\right) \quad (3.3)$$

Where G_s is the shear modulus, d_s is the thickness of the shell, μ_s is the viscosity of the shell, $p_G(R)$ is the pressure due to the gas inside the bubble. This is, in fact, similar in form to the equation proposed by de Jong *et al.* [15, 17], although different functional relationships are used to describe the shell's viscoelastic response.

Glazman [21] and Morgan *et al*. [22] built on previous studies of oceanic bubbles, to develop a model to consider the vibrations of surfactant coated microbubbles, which treated the shell as an adsorbed surface layer instead of a discrete shell. However there was a mistake in Glazman's derivation which was corrected by Marmottant *et al.* [23] who produced a model that described the effect of the shell through an area dependent interfacial tension with a constant surface viscosity. This model also defines three distinct regimes for the surface tension based upon experimental observations, shown in Figure 3.1. This assumes that there is an lower and upper radius limit: R_{buck}, below which the bubble shell buckles and the surface tension falls to zero; and R_{rupt}, above which the surface tension becomes that of water (an uncoated bubble), the regime in between these limits is described as the elastic region in which radial displacement and elastic resistance are linearly related.

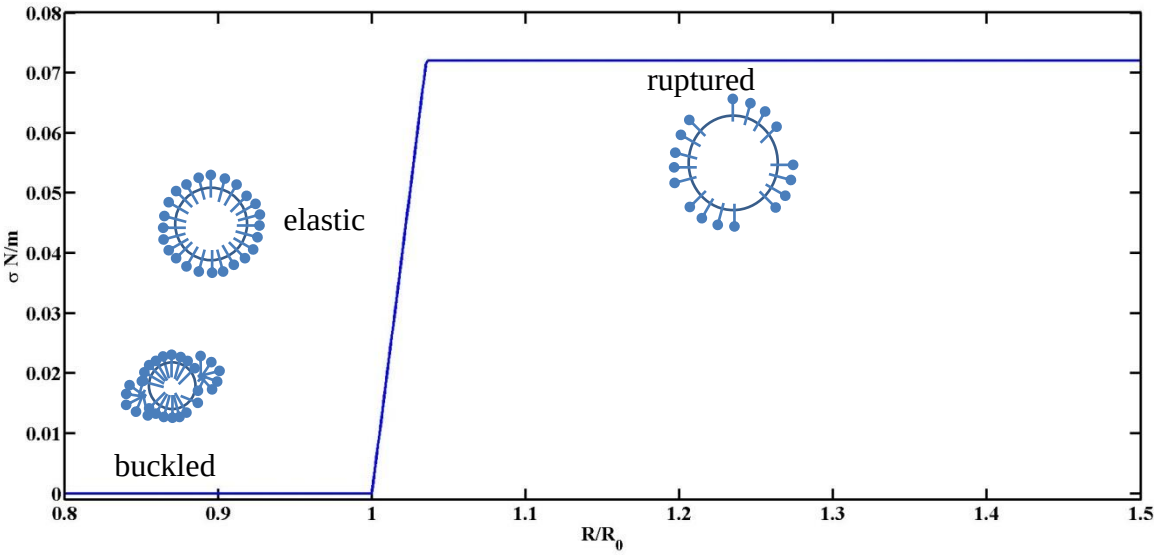

Figure 3.1 Figure demonstrating how surface tension varies with bubble radius according to Marmottant et al. [23].

Stride [24] developed a model, Equation (3.4), in which interfacial tension and viscosity are modelled as continuous functions of surface molecular concentration, Γ, based on functional relationships defined from surface chemistry experiments. These variable terms replace the more conventional elastic terms seen in the above equations.

$$R\ddot{R} + \frac{3}{2}\dot{R}^2 = \frac{1}{\rho_L}\left(p_0 - p_{ac} - p_G(R) - \frac{4\dot{R}\mu_L}{R} - \frac{4\dot{R}}{R^2}\eta_{s0}e^{\frac{zR_y^2}{(R^2-R_y^2)}} - \frac{2}{R}\left(\sigma_0 + \frac{K\Gamma_0^{y+1}}{(y+1)}\left(1 - \left(\frac{R_0}{R}\right)^{2(y+1)}\right)\right)\right) \quad (3.4)$$

Where Γ_0 inital molecular concentration, σ_0 surface tension at equilibrium, K is the power law constant, y power law exponent, Z surface viscosity exponent, η_{so} surface viscosity constant and R_y is the limiting bubble radius beneath which the surface buckles.

Chatterjee & Sarkar [25], considered a liquid shell and derived separately an equation that has an identical viscous term to that of de Jong *et al*. which was further

extended by the same group to include a time dependent elastic term based on surface concentration [26]. This model was developed further by Paul [27] to include a nonlinear elastic term and Tsiglifis *et al.* [28] investigated the effect of a different nonlinear viscoelastic shell models on bubble behaviour. Alternative constitutive equations have also been considered, for example hyperelastic shells [29] and viscoelastic fluids [30-32].

These types of models cannot describe the non-spherical behaviour of microbubbles as they are based on the assumption that the bubble remains spherical during oscillation. Experimentally, microbubbles can become non-spherical due to number of factors, for example the bubble being close to another bubble or wall, or inhomogeneity in the shell in the case of a coated bubble. The second Bjerknes force, the radiation force between two objects, is responsible for causing the shape deformations in bubble-bubble and bubble-wall interactions. This force is usually attractive causing the bubbles to come together or go towards the wall [33]. Due to the complex nature of the non-spherical oscillations, numerical methods are usually more applicable than analytical methods [34]. In particular, Boundary Element Modelling (BEM) and Finite Element Modelling (FEM) are usually used to investigate theses boundary interactions and bubble-bubble interactions as well as the mechanism behind the collapsing of bubbles and jet development.

BEM is a numerical time integration method coupled to a boundary integral spatial solution, which allows for modelling in both 2 and 3 dimensions near other structures including rigid boundaries [35-38], free surfaces [39-42] and tissue interfaces [43-45]. BEM is considered to be both stable and efficient, although it is much more difficult to model coated microbubbles with this method than FEM. In FEM, the solution domain is described by a covering of non-uniform triangular mesh with the domains covering the bubble surface and the structural interfaces in the liquid regions using a higher resolution

mesh. The Arbitrary Lagrangian-Eulerian (ALE) Algorithm is typically used for solving this type of model [45].

FEM can accommodate modelling the fluid viscosity which BEM cannot. FEM can also include the finite thickness of a shell, though the model is prone to buckling for elastic structures with rapid motion, which to be accurate, requires the modelling of a high resolution mesh. Though BEM does not suffer from buckling, it does suffer from a separate issue, in which the model can accumulate errors, causing a roughness of the mesh for which a smoothing method is applied such as the Longuet-Higgins & Cokelet [46], Dold [47] which were used in Blake *et al* [35, 40] and Best & Kuceara [36] for 2D models, as this smoothing technique is not suitable for 3D models. However another problem arises if these smoothing techniques are over used as they themselves can generate errors [34].

Although BEM and FEM can model the behaviour of a bubble deforming either near a wall or another bubble, they do not allow for the easy incorporation of a shell with time dependent properties, in particular one undergoing surfactant "shedding", which is thought to have a larger effect on the behaviour of the bubble than non-spherical deformation. This is because it is the spherical oscillations that contribute more substantially to the acoustic response than the non-spherical oscillations [48]. Therefore as BEM and FEM would also be computationally very expensive to run in comparison to the radially symmetric models, it was decided that a one dimensional model would be used for the investigation described in the subsequent sections.

3.2 Overview of Time Dependent Single Bubble Radial Motion Models

SonoVue® and Definity ® are two of the most commonly used microbubble contrast agents and have a 'lipid' (phospholipid) shell. This coating acts both to reduce the surface tension that drives the dissolution of the bubble and inhibit the diffusion of gas

across the boundary, thereby increasing the bubble's lifetime. Lipids are a preferred coating material as they are bio-compatible and allow the bubbles to remain acoustically sensitive thus giving better contrast compared to polymer bubbles, whose shell is more rigid. However the drawback of using a lipid coating is that the shell properties change over the course of a pulse. This change is not just due to a repeating change in surface area and hence molecular concentration due to the bubbles' expansion and contraction during oscillation, but also to loss of surfactant over the acoustic pulse. The models mentioned above all assume that the surfactant mass on the surface of the bubble remains constant during and in between pulses.

Borden *et al*. [49] and Viti *et al.* [50] have experimentally observed that several insonations of the same contrast agent microbubble give differing responses and that the bubble shrinks. They found that a bubble excited off resonance remained relatively stable, and those near resonance experienced the greatest change in both size and response. The shrinking observed has been previously hypothesised to be due to gas diffusion, however some studies have shown that the time scale on which this shrinkage arises is too small for gas diffusion to occur [51]. Borden *et al*. [49] have high-speed camera images that show that bubbles tend to shrink until they reach a stable size, and this is in agreement with the results obtained by Viti *et al*. [50]. Moreover the images also show some form of material shedding during or/and after the pulse. Hence suggesting that the bubbles under certain circumstances shed material, violating the assumption of a constant mass assumed in the previous models. However a relatively new model [51], Equation (3.5) has attempted to model lipid "shedding" from microbubbles over many pulses.

$$R\ddot{R} + \frac{3}{2}\dot{R}^2 = \frac{1}{\rho_L}\left(\left[p_0 + \frac{2\sigma_0}{R_0} - p_v\right]\left(\frac{R_0}{R}\right)^{3\gamma} - p_0 - p_{ac} + p_v - \frac{2\sigma(\Gamma)}{R} - \frac{4\mu_L\dot{R}}{R} - \frac{4\kappa_s(\Gamma)\dot{R}}{R^2}\right) \tag{3.5}$$

Where σ_0 is the clean surface tension, $\sigma(\Gamma)$ is the variable surface tension, $\kappa_s(\Gamma)$ is the variable surface viscosity. Both σ and κ_s are treated as functions of surface molecular concentration Γ, which is defined as the total mass of surfactant divided by surface area. These relations are well known from the surface chemistry literature [52]. There are 3 distinct concentration regimes in which the surfactant behaves differently. The first regime is when Langmuir absorption takes place. This occurs for concentrations close to equilibrium up to the maximum concentration, Γ^*. The second regime is when the surfactant becomes insoluble in the surrounding liquid. This occurs for concentrations higher than Γ^* up to the maximum packing concentration Γ^{max}. Finally the third regime occurs when $\Gamma=\Gamma^{max}$, when the surface is unable to hold any more surfactant molecules and the film collapses [51]. The equations for the variable surface tension are given in more detail in Section 3.6.2, and the implementation of the variable viscosity in Section 3.6.3. It should be noted that this model only describes the behaviour of lipid coated microbubbles, but this is relevant to a large class of bubbles used as image contrast agents, for example SonoVue and Definity.

3.3 Overview of Coupled Translational and Radial Models

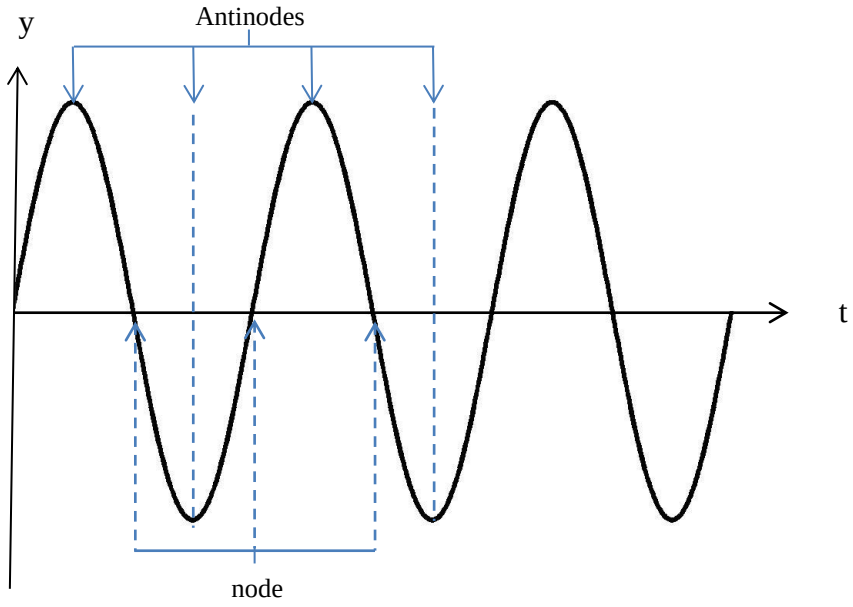

Figure 3.2 Diagram showing the location of the nodes and antinodes of a standing wave

As well as radial oscillatory motion, bubbles may also undergo translational motion due to the steady pressure gradient produced by the propagating wave. In a standing wave, for example, a bubble will travel to the nearest node or antinode depending on its size and the acoustic frequency.

Interest in bubble translational motion initially started with a study by King [53] into the effect of acoustic radiation pressure on a rigid sphere in a standing wave, this revealed that the sphere is driven to the node or antinode of the acoustic field (Figure 3.2) which was found to depend on the ratio between the density of the sphere and the ambient fluid. Yosioka & Kawasima [54] furthered this by showing that the compressibility of the sphere amplified the acoustic radiation pressure. Crum [55] first studied the effect of the Primary Bjerknes (acoustic radiation) force on an oscillating bubble, and with Prosperetti

[9], found the ratio between the Bjerknes force and the buoyant force, which would enable them to study the harmonic pulsation of the bubble in an acoustic standing wave.

Watanabe and Kukita [56] solved the radial and translational equations simultaneously for a uncoated bubble, using the RPNNP Equation (3.2) for the radial and Equation (3.6) for the translational motion.

$$m_b\ddot{x} = -V\frac{dP_{ac}}{dx} - \frac{1}{2}\rho_L\frac{d}{dt}(Vu_r) - \frac{1}{2}\rho_L|u_r|u_r A\, C_d \qquad (3.6)$$

Where the first term on the right hand side is the acoustic radiation force, also known as the Primary Bjerknes forces, and the third term accounts for the drag of the bubble in the liquid, the other terms combine to account for the added mass of the bubble as it moves through the liquid. The mass of the bubble is m_b, x is the translation of the bubble centre from the origin, $\dot{x}$ is the velocity of the bubble, $\ddot{x}$ is the acceleration of the bubble, V is the volume of the bubble, u_r is the relative velocity of the liquid where u_r=u_b-u_L, where u_b is the bubble velocity which in this case equal to $\dot{x}$ and u_L is the liquid velocity, A=πR^2 is the projected area of the bubble, and the drag coefficient

$$C_d = 27Re^{-0.78} \qquad (3.7)$$

Where Re is the Reynolds number which is

$$Re = \frac{2\rho_L u_r R}{\mu_L} \qquad (3.8)$$

From this it was found that a bubble would translate to a different position in a standing wave depending on its size compared to the resonant size. Bubbles that are larger than the resonant size corresponding to the driving frequency will translate to the nearest node, bubbles that are much smaller than the resonant size move to the antinode, whilst bubbles that are equal to or slightly smaller may undergo chaotic motion. They concluded

that the nonlinearity in the radial oscillations caused the chaotic motion in the translational direction [56].

Doinikov [57] used a Lagrangian approach to derive coupled Equations (3.9 & 3.10) for the radial and translational motion of an uncoated bubble. This derivation ignores the added mass due to the displaced liquid of the bubble, although unlike Watanabe and Kukita's [56] approach it did include the term, $\frac{\dot{x}^2}{4}$, in the radial equation which coupled the equations. This term also appears in Doinikov's later model [58], although other of his publications have included this term with using the relative velocity of the bubble, u_r [59]. This term is usually ignored because it is often negligibly small, however this is not always the case. Doinikov [57], concluded that if the acoustic driving pressure, p_A, was high enough a bubble driven below resonance could exhibit chaotic behaviour around the pressure node instead of moving towards the antinode, behaviour often missed due to the coupling term being ignored.

$$R\ddot{R} + \frac{3}{2}\dot{R} = \frac{1}{\rho_L}\left(\left(P_0 + \frac{2\sigma}{R_0}\right)\left(\frac{R_0}{R}\right)^{3\gamma} - \frac{2\sigma}{R} - \frac{4\mu_L\dot{R}}{R} - p_0 - p_{ac}\right) + \frac{\dot{x}^2}{4} \qquad (3.9)$$

$$\ddot{x} + \frac{3\dot{R}\dot{x}}{R} = \frac{3F_{ex}}{2\pi\rho_L R^3} \qquad (3.10)$$

F_{ex} denotes the external forces accounting for the Primary Bjerknes force and the drag.

Later with Dayton [58], the coupled equations were re-derived by Doinikov using the same method as above, but for a shelled bubble for which the Church equation was used to describe the radial dynamics including the coupling term and the translational equation (3.11). This is equivalent to the treatment of Watanabe and Kukita [56] if the added mass

term described above is included and relative motion between the liquid and the bubble is ignored.

$$\ddot{x} = \frac{1}{\left(m_b + \frac{2}{3}\pi R^3 \rho_L\right)}\left(\frac{4\pi R^3}{3}\frac{dp_{ac}(x,t)}{dx} - 6\pi\mu_L R\dot{x} - 2\pi\rho_L\left(R^2\dot{R}\dot{x}\right)\right) \quad (3.11)$$

Dayton *et al.[60]* subsequently published a model using the translational equation from Meyer *et al.*[61], which included some unnecessary terms (given the one dimensional nature of the treatment), but did include the added mass.

Several similar models have also been derived in varying forms, [59, 62-64] though there is some inconsistency with regard to the frame of reference used, as some use the relative velocity between the bubble wall and the liquid, while others do not and some include the inertial term of the bubble with m_b which is incorrect as all the models claim to take the centre of the bubble as the origin of the translational motion .

Some translational models also include a term called the "history force" which describes the cumulative effect of the relative acceleration between the bubble and the fluid. It has been used by many authors [62, 63, 65, 66] in varying forms to more accurately describe the translational motion of the bubble. For example in Garbin *et al.* [62] a term based on that of Takemura and Magnaudet [67] which is the case of the bubble that obeys a no-slip condition for the condition *Re<1*, where *Re* is the Reynolds number. In the report they found that not including the term leads to an underestimation of translational motion which increased with time. Park *et al.* [65] who investigated the effects for *Re>13* found that not including the term only overestimates the trajectory by 5%. These models also assume that there are no boundaries nearby and assume that the bubbles remain perfectly spherical, thus not allowing for any nonlinear viscous effects. The form the History force

takes in the model is unique for each situation the bubble is placed and has a negligible effect on the radial motion of the bubble. Consequently, this term will be neglected in the following derivation.

3.4 New Model Development

In reviewing the previous Equations given by Watanabe and Kukita [56] , Doinikov and *et al*. [58] a number of errors were discovered. In Watanabe and Kukita the model considers the bubble's mass to be the mass of the gas $m_g = \frac{4}{3}\pi R_0^3 \rho_g$, where $\rho_g$is the density of the gas, which does not include the more significant added mass which would be required for their frame of reference, $m_{added} = \frac{2}{3}\pi R_0^3 \rho_L$, a well known effect in fluid dynamics [68] which is caused by the inertia of the volume of the surrounding liquid displaced by the bubble accelerating / decelerating. The Doinikov *et al*. model ignores the relative velocity of the bubble in the liquid and considers the bubble to be travelling through a stationary liquid, which is incorrect if an acoustic field is applied to the bubble, because this sets the liquid surrounding the bubble into motion, giving it a velocity which will be different to the bubble's velocity due to drag. Hence a new model is derived from first principles with a consistent frame of reference in the following section, after a discussion of the underlying assumptions.

3.4.1 Assumptions

The assumptions made in the derivation of the model are as follows:

1. Spherical symmetry is maintained during microbubble oscillation and translation.
2. External forces such as gravity and buoyancy can be ignored as they are very small in comparison to other forces experienced by the bubble.

3. There are no changes in the bubble properties during oscillation, i.e. the equilibrium radius and shell properties will remain constant (this assumption will however be amended later to account for time dependent shell effects). This includes the assumption that the bubble remains intact and there is negligible gas diffusion over the oscillation period [51].
4. The average temperature of the bubble remains constant throughout the oscillation, *i.e*. thermal damping is negligible
5. Due to the gas having very low density and viscosity compared with that of the surrounding liquid, the inertial and viscous contributions of the gas can be taken to be negligible.
6. The acoustic wavelength of the ultrasound in the liquid is much larger than the radius of the bubble. Hence pressure variations across the bubble can be regarded as negligible.
7. Vapour inside the bubble is negligible; i.e. it is filled purely with gas. This is because the majority of microbubbles are manufactured under gas saturated conditions [34] and it is assumed that the shell would inhibit inwards diffusion of vapour after bubble formation.
8. Ideal and polytropic behaviour of the filling gas can be assumed.
9. The thermal diffusivity of the filling gas must remain constant during oscillation as pressure and temperature are uniform throughout the bubble at all times and there is negligible heat transfer across the wall.
10. The surrounding fluid is taken to be infinite unless otherwise stated, initially static, homogeneous, incompressible and Newtonian.

3.4.2 Derivation of Coupled Radial and Translational Equations

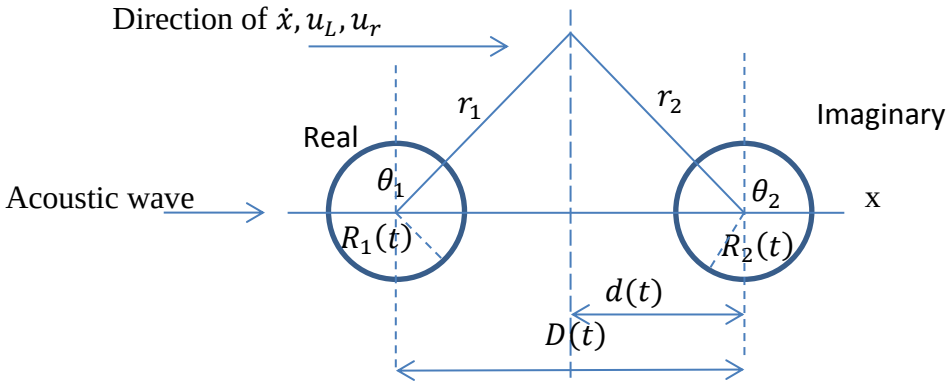

Figure 3.3 Geometry of system where the distance between the two bubbles is D, and d is the distance between the wall and the bubble, with the initial coordinate of the real bubble being $(R, \dot{\boldsymbol{R}}, \boldsymbol{x}, \dot{\boldsymbol{x}}) = (R_0, 0, -d, 0)$ *and the imaginary bubble* $(R, \dot{\boldsymbol{R}}, \boldsymbol{x}, \dot{\boldsymbol{x}}) = (R_0, 0, d, 0)$*. The angle* $\boldsymbol{\theta}$ *is the polar angle of the bubble.*

Consider a system of one bubble initially at rest with an initial radius R_0 a distance d from a rigid wall. In this system it shall be assumed that translational motion can only occur along one axis, in this case the x-axis as shown in Figure 3.3, and that it can be set into motion in this direction via the application of an acoustic pressure wave with or without incorporating an imposed flow in the liquid. Though for simplicity of the derivation it shall be assumed that only an acoustic pressure wave is imposed, an enforced flow can be easily incorporated via changing the velocity of the bubble and that of the liquid.

The acoustic pressure wave causes the surrounding liquid to move with velocity u_L and the bubble to have a velocity, $\dot{x}$, as well as radial motion. If the initial condition of the bubble is taken to be $(R, \dot{R}, x, \dot{x}) = (R_0, 0, d, 0)$, then the bubble is seen to be moving with a relative velocity $u_r = \dot{x} - u_L$. This motion imposes boundary conditions on the bubble surface.

The "image bubble" method has been used by many authors [62, 69] and can be used for modelling either the interaction between two bubbles or a bubble and a rigid free surface by altering the phase difference between the bubbles' responses. It is used here to determine the relative influence of a rigid boundary upon the bubble response. The wall is accounted for by the inclusion of an image bubble as pictured in Figure 3.3 in which the second imaginary bubble of radius, R_2, is considered to be identical to the real bubble and the two are assumed to be oscillating in phase with each other.

First, if d is considered to be so large that the effects from the wall can be ignored, then following the approach adopted by Doinikov [57, 58], starting from the Lagrangian Equation

$$\frac{d}{dt}\frac{\partial L}{\partial \dot{q}_i} - \frac{\partial L}{\partial q_i} = -\frac{\partial F}{\partial \dot{q}_i} \tag{3.12}$$

Where L is the Lagrangian function defined by $L=T-U$, where T is the kinetic energy and U is the potential energy, q_i and $\dot{q}_i$ are the generalised coordinates and velocities respectively, and F is the dissipative function which will take account of the dissipative effects of the liquid viscosity.

The kinetic energy T of the liquid

$$T = \frac{\rho_L}{2}\int_V |\nabla\varphi|^2 dV \tag{3.13}$$

Where dV is the volume element. The velocity potential of the liquid, φ, using spherical coordinates (r,θ,ϕ), where θ is the polar angle and taking the origin to be at the centre of the bubble with the boundary condition being

$$\frac{\partial\varphi}{\partial r} = \dot{R} + u_r \cos\theta \;\; at\; r = R(t) \tag{3.14}$$

Where the first term depends upon the radial oscillations, and the second upon the motion of the bubble though the liquid. φ is the velocity potential of the liquid, $R(t)$ and $x(t)$ are the time dependent radius and position of the centre of the bubble. An overdot represents a time derivative. The relative velocity of the bubble is given by $u_r = u_b - u_L$, with the velocity of the bubble $u_b = \dot{x}$ and the liquid velocity being

$$u_L = \frac{p_A}{\rho_L c_s} \cos(\omega\, t) \cos(k\, x) \tag{3.15}$$

With the angular frequency $\omega = 2\pi f$, where f is the frequency of the driving wave, the wavenumber $k = \frac{2\,\pi\, f}{c_s}$, where c_s is the speed of sound in water and the acoustic driving pressure is be taken to be

$$p_{ac}(x,t) = p_A \sin(\omega t\,) \sin(k\, x) \tag{3.16}$$

The velocity potential must satisfy the Laplace equation $\Delta\varphi = 0$, which gives

$$\varphi = \frac{b(t)}{r} + \frac{d(t)\, cos\, \theta}{r^2} \tag{3.17}$$

From Equation (3.14) and Equation (3.17) the coefficients are found to be

$$b(t) = -\dot{R}R^2, d(t) = -\frac{u_r R^3}{2} \tag{3.18}$$

Substituting φ into Equation(3.13),

$$T = 2\pi\rho_l R^3 \left(\dot{R}^2 + \frac{{u_r}^2}{6}\right) \tag{3.19}$$

The potential energy is given by:

$$U = U_g + U_{st} + U_{ex} \tag{3.20}$$

Where U_g is the potential energy of the gas, U_{st} is the potential energy due to surface tension and U_{ex} is the potential energy due to the external pressure. Assuming that the internal gas follows the polytropic relation then:

$$U_g = \frac{p_{g0}V_o}{\gamma - 1}\left(\frac{R_0}{R}\right)^{3(\gamma-1)} \quad (3.21)$$

Where $p_{g0} = \left(p_0 + \frac{2\sigma_0}{R_0}\right)$ and is the equilibrium pressure of the gas and $V_o = \frac{\frac{4\pi}{3}}{R_0^3}$. The effect of surface tension at the gas liquid interface is given by

$$U_{st} = 4\pi R^2 \sigma \quad (3.22)$$

And the work done by the external pressure is:

$$U_{ex} = \frac{4\pi}{3}R^3[p_0 + p_{ac}(x,t)] \quad (3.23)$$

This gives the potential function as:

$$U = \frac{p_{g0}V_o}{\gamma - 1}\left(\frac{R_0}{R}\right)^{3(\gamma-1)} + 4\pi R^2\sigma + \frac{4\pi}{3}R^3[p_0 + p_A\, sin(t\omega)\, sin(k\, x)] \quad (3.24)$$

The dissipative function for the liquid is:

$$F = F_L + F_S = \int_{V_L} f_L dV + \int_{V_s} f_s dV \quad (3.25)$$

Where V_s is the volume of the shell, f_s is the density of the dissipative function of the shell, V_L is the volume occupied by the liquid and f_L is the density of the dissipative function which can be written as.

$$f_L = \mu_L\left(v_{ij} - \frac{1}{3}\delta_{ij}v_{kk}\right)^2 + \frac{1}{2}\xi_L v_{kk}^2 \quad (3.26)$$

ξ_L is the bulk viscosity coefficient of the liquid and v_{ij} is the stress strain tensor of the liquid,

$$v_{ij} = \frac{1}{2}\left(\frac{\partial v_i}{\partial x_j} + \frac{\partial v_j}{\partial x_i}\right) \qquad (3.27)$$

With *v* denoting the liquid velocity. Since the liquid is incompressible, $v_{kk} = \boldsymbol{\nabla v} = 0$. Therefore Equation(3.26) becomes:

$$f_L = \mu_L \left(v_{ij}\right)^2 \qquad (3.28)$$

The boundary condition at the liquid and bubble interface is:

$$v = \dot{R}e_r + u_r = \left(\dot{R} + u_r cos\,\theta\right)e_r - u_r\, sin\,\theta e_\theta\,, \qquad at\ r = R \qquad (3.29)$$

The liquid velocity can be represented as $v = \boldsymbol{\nabla}\varphi + \boldsymbol{\nabla} \times \psi$, where φ, the scalar potential obeys the Laplace Equation , $\Delta\varphi = 0$, applying these conditions gives:

$$\varphi = -\frac{R^2\dot{R}}{r} + \frac{R^3 u_r\, cos\,\theta}{4r^2} \qquad (3.30)$$

$$\psi = \frac{3}{4} R u_r\, sin\,\theta\, e_\varepsilon \qquad (3.31)$$

Then the liquid velocity is calculated as:

$$v = \left[\frac{R^2\dot{R}}{r^2} + \frac{u_r}{2}\left(\frac{3R}{r} - \frac{R^3}{r^3}\right) cos\,\theta\right] e_r - \frac{u_r}{4}\left(\frac{3R}{r} + \frac{R^3}{r^3}\right) sin\,\theta e_\theta \qquad (3.32)$$

$\left(v_{ij}\right)^2$ can be written as given in [58]:

$$\begin{aligned}\left(v_{ij}\right)^2 &= v_{rr}^2 + v_{\theta\theta}^2 + v_{\epsilon\epsilon}^2 + 2v_{r\theta}^2 \\ &= \left(\frac{\partial v_r}{\partial r}\right)^2 + \frac{1}{r^2}\left(v_r + \frac{\partial v_\theta}{\partial \theta}\right)^2 + \frac{1}{r^2}\left(v_r + v_\theta \frac{cos\,\theta}{sin\,\theta}\right)^2 \\ &\quad + \frac{1}{2}\left(\frac{1}{r}\frac{\partial v_r}{\partial \theta} + \frac{\partial v_\theta}{\partial r} - \frac{v_\theta}{r}\right)^2\end{aligned} \qquad (3.33)$$

Substituting Equation(3.32) into Equation(3.33) gives:

$$\left(v_{ij}\right)^2 = \frac{6R^4\dot{R}^2}{r^6} + \frac{9R^6u_r^2}{8r^8} + \frac{9R^2\dot{R}u_r}{r^4}\left(\frac{R}{r} - \frac{R^3}{r^3}\right)cos\,\theta + \frac{u_r^2}{8}\left(\frac{27R^2}{r^4} - \frac{54R^4}{r^6} + \frac{18R^6}{r^8}\right)cos^2\,\theta \quad (3.34)$$

Finally, by integrating Equation(3.34) over V_L, it is found that:

$$F_L = 8\pi\mu_L R\dot{R}^2 + 3\pi\mu_L R{u_r}^2 \quad (3.35)$$

$$f_s = \frac{\kappa_s}{3}\left(v_{ij}\right)^2 = \frac{\kappa_s}{3}\left[\left(\frac{\partial v_s}{\partial r}\right)^2 + \frac{2v_s^2}{r^2}\right]$$

Where the acceleration of the bubble shell is v_s:

$$v_s = \frac{R^2\,\dot{R}}{r^2}$$

This gives after integrating:

$$F_S = 8\pi\kappa_s\dot{R}^2$$

Substituting Equations (3.19),(3.24) and Equation(3.35) into Equation (3.12) for q =R and x respectively gives:

$$\rho_L\left(R\ddot{R} + \frac{3}{2}\dot{R}^2\right) = \left(p_0 + \frac{2\sigma}{R_0}\right)\left(\frac{R_0}{R}\right)^{3\gamma} - \frac{2\sigma}{R} - p_0 - p_{ac} + \frac{\rho_L u_r^2}{4R} - \frac{4\mu_L\dot{R}}{R} - \frac{4\kappa_s\dot{R}}{R^2} \quad (3.36)$$

$$\dot{u}_r = -\frac{3\dot{R}u_r}{R} - \frac{2}{\rho_L}\frac{\partial p_{ac}(x,t)}{\partial x} - \frac{9\mu_L u_r}{\rho_L R^2} + u_r\frac{\partial u_r}{\partial x} \quad (3.37)$$

As can be seen, this gives the RPNNP equation with an added coupling term, that includes the slip velocity, $\frac{u_r^2}{4}$, (the fifth term on the right hand side), which is now dependent on the relative velocity instead of the bubble velocity, and an equation for the translational motion that is the same as that derived by Doinikov and Dayton apart from the

relative motion being used to describe the velocity of the bubble in the flow and including one extra term at the end of Equation (3.37) , the significance of which shall be discussed in Chapter 4. For Equation (3.37) it should be noted that the derivation produces a drag term based on Stokes law, which only holds for $Re<<1$ and therefore should be changed if using the model for higher Reynolds numbers.

The newly derived Equations(3.36) - (3.37) include the slip velocity in the radial equation as a coupling term between the translational and radial motion and both have a consistent frame of reference. Previously it has been shown in [69] that the slip velocity only becomes dominant at high pressures and affects both the radial and the translational motion. This effect is shown in Figure 3.4 with a low driving pressure of 10kPa where no difference is seen and at a higher driving pressure of 200kPa in Figure 3.5 showing the effect it has. This effect is also described in more quantitative terms in Chapter 4. The effect of changing the frame of reference is thought to be negligible, as the mass of the bubble is very small and the velocity of the liquid is smaller than that of the bubble meaning that there would be little effect seen from these changes. The graphs Figure 3.4 and Figure 3.5 were obtained using MatLab 2012b ® using the inbuilt function ode45 for the variables shown in Table 3.1, and for 20 cycles, solving the Equations (3.36) -(3.37) simultaneously and comparing the full Equation and then omitting the slip velocity.

Parameter	Value
Resting Radius, R_0	2μm
Density of the liquid, ρ_l	1000 kg/m^3
Hydrostatic Pressure, p_0	100kPa
Surface Tension, σ_0	0.07 N/m
Polytropic constant, γ	1.4
Speed of sound, c_s	1400 m/s
Viscosity , κ_s	0.0 Kg/s
Frequency, f	1MHz
Liquid Viscosity, μ_l	1.5x10^{-3} Pa.s

Table 3.1.Values used for simulations

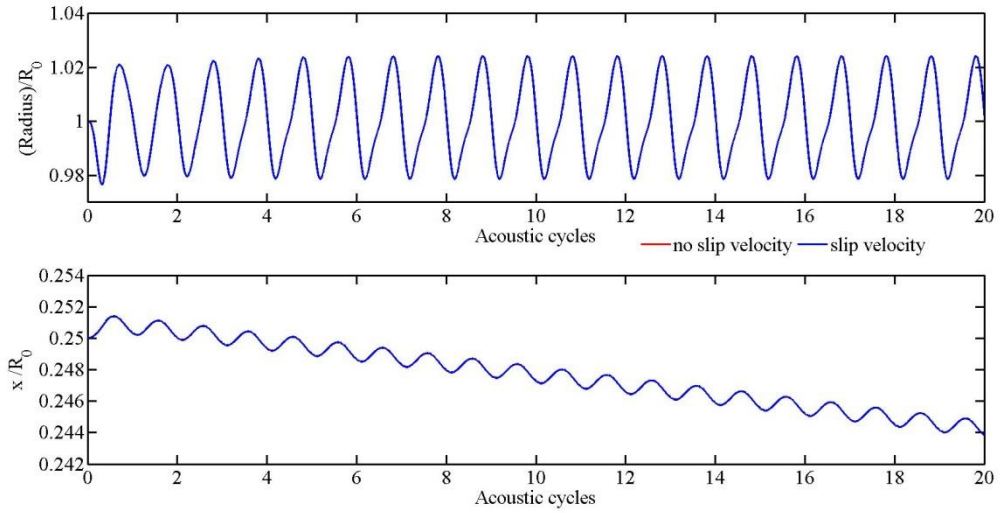

Figure 3.4 The effect of the slip velocity on the equations at a driving pressure of 10 kPa. As can be seen there is a negligible difference between them at this pressure.

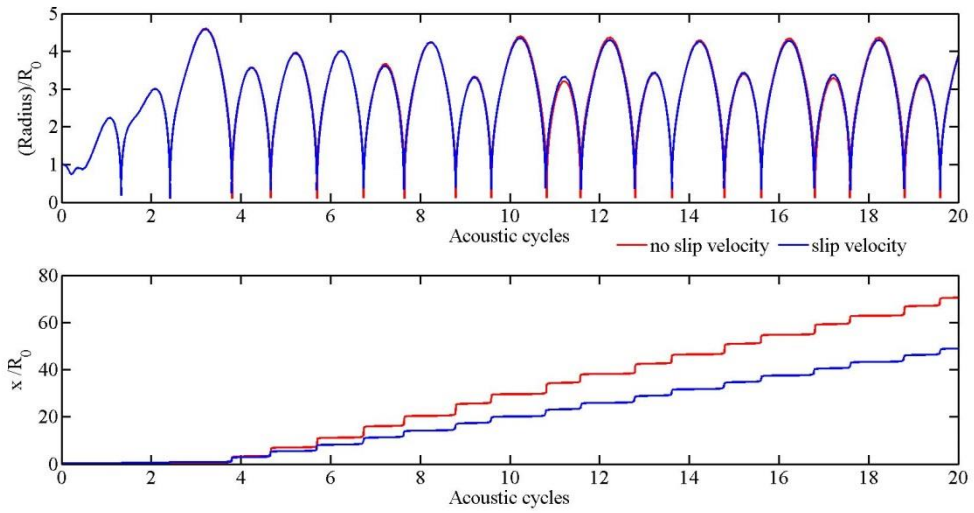

Figure 3.5 The effect of the slip velocity on the model at a driving pressure of 200kPa.

3.5 Derivation of Coupled Radial and Translational Equations near a Rigid Wall

In the previous section a new model for coupled translational and radial motion for a coated microbubble was derived from first principles and has been validated against other models, See Appendix B. Now this model will be extended to consider the effect of a nearby rigid wall, and of time dependent shell parameters. It should be noted that the model

can also be used to consider the effect of another bubble nearby as well, but for simplicity the subsequent derivation, analysis and discussion shall only consider the effect of a rigid wall.

Using spherical coordinates (r_j,θ,ϕ), where $j=1,2$ for the real and image bubble respectively and taking the origin of movement in both directions to be from the centre of the bubble the boundary condition at the bubbles surfaces is :

$$\frac{\partial \varphi}{\partial r_j} = \dot{R}_j + u_{rj}\cos\theta_j \; at \; r_j = R_j(t) \; for \; j = 1,2 \qquad (3.38)$$

Where φ is the velocity potential of the liquid. For two bubbles we can expand this as $\varphi = \varphi_1 + \varphi_2$ where φ_j the scattered potential of the jth bubble can be given by:

$$\varphi_j = \sum_{n=0}^{\infty} A_n^{(j)}(t) r_j^{-n-1} P_n(\cos\theta_j) = \sum_{n=0}^{\infty} B_n^{(j)}(t) r_{3-j}^{n} P_n(\cos\theta_{3-j}) \qquad (3.39)$$

A relation between $A_n^{(j)}$ and $B_n^{(j)}$ is obtained using the polynomial identity [70]

$$P_n(\cos\theta_j) r_j^{-n-1} = \frac{(-1)^{n(j-1)}}{D^{n+1}} \sum_{m=0}^{\infty} \frac{(-1)^{jm}(n+m)!}{n!\,m!} \left(\frac{r_{3-j}}{D}\right)^m P_m \cos\theta_{3-j} \qquad (3.40)$$

Where $D(t)$ is the distance between the centre of the bubbles. Substituting Equation (3.40) into Equation (3.39) gives:

$$\sum_{n=0}^{\infty} B_n^{(j)}(t) r_{3-j}^{n} P_n(\cos\theta_{3-j}) = \sum_{n=0}^{\infty} A_n^{(j)}(t) \frac{(-1)^{n(j-1)}}{D^{n+1}} \sum_{m=0}^{\infty} \frac{(-1)^{jm}(n+m)!}{n!\,m!} \left(\frac{r_{3-j}}{D}\right)^m P_m \cos\theta_{3-j} \qquad (3.41)$$

After rearranging, Equation (3.41) ,gives

$$B_n^{(j)}(t) = \frac{(-1)^{n(j-1)}}{D^{n+1}} \sum_{m=0}^{\infty} \frac{(-1)^{jm}(n+m)!}{n!\,m!\,D^m} A_m^{(j)}(t) \qquad (3.42)$$

Using both equations to give φ

$$\varphi = \varphi_1 + \varphi_2 = \sum_{n=0}^{\infty} \left[A_n^{(j)}(t) r_j^{-n-1} + B_n^{(3-j)}(t) r_j^n\right] P_n(\cos\theta_j) \tag{3.43}$$

Now applying the boundary condition Equation (3.38)

$$\frac{d\varphi}{dr_j} = \left[A_n^{(j)}(-n-1) r_j^{-n-2} + B_n^{(3-j)} n r_j^{n-1}\right] P_n(\cos\theta_j) \tag{3.44}$$

Therefore matching terms in both equations. When n=0, $\frac{d\varphi}{dr_j} = \left[\boldsymbol{A_0^{(j)}(-1) r_j^{-2}}\right]$.

Which matches to $\frac{\partial \varphi}{\partial r_j} = \dot{R}_j$ giving **:**

$$A_0^{(j)} = -\dot{R}_j R_j^2 \tag{3.45}$$

Otherwise

$$\left[A_n^{(j)}(-n-1) r_j^{-n-2} + B_n^{(3-j)} n r_j^{n-1}\right] P_n(\cos\theta_j) = u_{rj}\cos\theta_j \tag{3.46}$$

Rearranging Equation (3.46) gives Equation (3.41):

$$A_n^{(j)} = -\frac{u_{rj} R_j^3}{2}\delta_{n1} + \frac{n R_j^{2n+1}}{n+1} B_n^{(3-j)} \tag{3.47}$$

Therefore following the same approach as before, using the Lagrangian function in Equation(3.12), where the Kinetic, potential and dissipative energy can now be written in the form $T = T_1 + T_2$, $U = U_1 + U_2, F = F_1 + F_2$. Where the potential energy is given by

$$U_j = \frac{p_0 V_o}{\gamma - 1}\left(\frac{R_{0\,j}}{R_j}\right)^{3(\gamma-1)} + 4\pi R_j^2 \sigma + \frac{4\pi}{3} R_j^3 \left[p_0 + p_A \sin(t\omega)\sin(k\, x_j)\right] \tag{3.48}$$

Where j=1,2. The dissipative energy is found to be

$$F_j = 8\pi\mu_L R_j \dot{R}_j^2 + 3\pi\mu_L R_j u_{r\,j}{}^2 + 8\pi k_s \dot{R}_j^2 \tag{3.49}$$

The kinetic energy is determined by the kinetic energy of the liquid

$$T = \frac{\rho_L}{2}\int |\nabla\varphi|^2 dV \tag{3.50}$$

This can be rearranged to give:

$$T_j = -\pi\rho_L R_j^2 \int_{-1}^{1} \left(\varphi \frac{\partial\varphi}{\partial r_j}\right)_{r_j=R_j} d\left(\cos\theta_j\right) \tag{3.51}$$

Substituting Equation (3.43) and Equation (3.38) into the above gives

$$\begin{aligned} T_j = -\pi\rho_L R_j^2 \int_{-1}^{1} \Big(\sum\nolimits_{n=0}^{\infty} \Big[A_n^{(j)}(t) r_j^{-n-1} \\ + B_n^{(3-j)}(t) r_j^n\Big] P_n\left(\cos\theta_j\right)\Big)\left(\dot{R}_j \right. \\ \left. + u_{rj}\cos\theta_j\right) d(\cos\theta) \end{aligned} \tag{3.52}$$

So looking inside the integral if n=0

$$\begin{aligned} \int_{-1}^{1} \left(\left(A_0^{(j)}(t) r_j^{-1} + B_0^{(3-j)}(t)\right) P_0\left(\cos\theta_j\right)\right)\left(\dot{R}_j \right. \\ \left. + u_{rj}\cos\theta_j\right) d\left(\cos\theta_j\right) = 2B_0^{(3-j)}\dot{r}_j + \frac{2A_0\dot{r}_j}{r_j} \end{aligned} \tag{3.53}$$

If n=1

$$\begin{aligned} \int_{-1}^{1} \left(\left(A_1^{(j)}(t) r_j^{-2} + B_1^{(3-j)}(t) r_j\right) P_1\left(\cos\theta_j\right)\right)\left(\dot{R}_j \right. \\ \left. + u_{rj}\cos\theta_j\right) d\left(\cos\theta_j\right) = \frac{2A_1 u_{rj}}{3r_j^2} + \frac{2B_1^{(3-j)} r_j u_{rj}}{3} \end{aligned} \tag{3.54}$$

This gives an accuracy up to the third order in D^{-1} giving:

$$T_j = -\pi\rho_L R_j^2 \left(2B_0^{(3-j)}\dot{r}_j + \frac{2A_0\dot{r}_j}{r_j} + \frac{2A_1 u_{rj}}{3r_j^2} + \frac{2B_1^{(3-1)} r_j u_{rj}}{3}\right) \tag{3.55}$$

Now substituting back in A_0 and rewriting in terms of $B_1^{(3-j)}$, T_j becomes

$$T_j = -2\pi\rho_L\left(R_j^3\dot{R}_j^2 - \frac{1}{3}R_j^3u_{rj}^2 - R_j^2\dot{R}_j\ B_0^{(3-j)} - A_1u_{rj}\right) \tag{3.56}$$

So from Equation (3.47) and finding A_1:

$$A_n^{(j)} = -\frac{u_{rj}R_j^3}{2}\delta_{n1} + \frac{nR_j^{2n+1}}{n+1}\frac{(-1)^{n(2-j)}}{D^{n+1}}\sum_{m=0}^{\infty}\frac{(-1)^{(3-j)m}(n+m)!}{n!\,m!\,D^m}A_m^{(3-j)}(t) \tag{3.57}$$

Where D is the distance between the two bubbles and letting $n=1$ gives

$$A_1^{(j)} = -\frac{u_{rj}R_j^3}{2} + \frac{R_j^3(-1)^{(2-j)}}{D^2}\sum_{m=0}^{\infty}\frac{(-1)^{(3-j)m}(n+m)!}{n!\,m!\,D^m}A_m^{(3-j)}(t) \tag{3.58}$$

Then letting $m=0$ and $m=1$ as we are only taking D to 3rd order gives:

$$A_1^{(j)} \approx -\frac{R_j^3}{2}\left(u_{rj} - \frac{(-1)^jR_{2-j}^2\dot{R}_{3-j}}{D^2} - \frac{R_{3-j}^3u_{r(3-j)}}{D^3}\right) \tag{3.59}$$

$B_0^{(3-j)}$ is found from

$$B_0^{(3-j)}(t) = \frac{(-1)^{n(2-j)}}{D^1}\sum_{m=0}^{\infty}\frac{(-1)^{(3-j)m}(m)!}{m!\,D^m}A_m^{(3-j)}(t) \tag{3.60}$$

Which gives from applying $m=0,1$

$$B_0^{(3-j)}(t) \approx -\frac{R_{3-j}^2}{2D}\left(2\dot{R}_{3-j} + \frac{(-1)^jR_{3-j}u_{r(3-j)}}{D}\right) + O(D^{-4}) \tag{3.61}$$

This gives:

$$T = 2\pi\rho_L\left(\frac{1}{6}u_{r1}^2r_1^3 + \frac{1}{6}u_{r2}^2r_2^3 + r_1^3\dot{r}_1^2 + r_2^3\dot{r}_2^2 + \frac{2r_1^2r_2^2\dot{r}_1\dot{r}_2}{D} + \frac{r_1^2r_2^2(u_{r1}r_1\dot{r}_2 - u_{r2}r_2\dot{r}_1)}{D^2} - \frac{u_{r1}u_{r2}r_1^3r_2^3}{D^3}\right) \tag{3.62}$$

The full dissipative term is

$$F = 8\pi\mu_L r_1\dot{r}_1 + 3\pi\mu_L r_1 u_{r1} 8\pi\mu_L r_2\dot{r}_2 + 3\pi\mu_L r_2 u_{r2} + 8\pi\kappa_s\dot{r}_1^2 + 8\pi\kappa_s\dot{r}_2^2 \quad (3.63)$$

The full potential energy term is

$$U = -\frac{P_{g01}V_{01}\left(\frac{r_{10}}{r_1(t)}\right)^{-1+3\gamma}}{-1+\gamma} + 4\pi\sigma r_1^2 + \frac{P_{g02}V_{02}\left(\frac{r_{20}}{r_2(t)}\right)^{-1+3\gamma}}{-1+\gamma} + 4\pi\sigma r_2^2 + \frac{4}{3}\pi r_1^3\left(p_0 + p_a\sin(\omega t)\sin(kx_1) + \frac{4}{3}\pi r_2^3(p_0 + p_a\sin(\omega t)\sin(kx_2))\right) \quad (3.64)$$

Where $P_{g0i} = \left(p_0 + \frac{2\sigma_0}{R_{0i}}\right)$ $with\ i = 1,2$. Making the Lagrangian $L=T_1+T_2-U_1-U_2$:

$$\mathrm{L}=2\pi\rho_L\left(\frac{1}{6}u_{r1}^2 r_1^3 + \frac{1}{6}u_{r2}^2 r_2^3 + r_1^3\dot{r}_1^2 + r_2^3\dot{r}_2^2 + \frac{2r_1^2 r_2^2\dot{r}_1\dot{r}_2}{D} + \frac{r_1^2 r_2^2(u_{r1}r_1\dot{r}_2 - u_{r2}r_2\dot{r}_1)}{D^2} - \frac{u_{r1}u_{r2}r_1^3 r_2^3}{D^3}\right) - \left(\frac{P_{g01}V_{01}\left(\frac{r_{10}}{r_1(t)}\right)^{-1+3\gamma}}{-1+\gamma} + 4\pi\sigma r_1^2 + \frac{P_{g02}V_{02}\left(\frac{r_{20}}{r_2(t)}\right)^{-1+3\gamma}}{-1+\gamma} + 4\pi\sigma r_2^2 + \frac{4}{3}\pi r_1^3\left(p_0 + p_a\sin(\omega t)\sin(kx_1) + \frac{4}{3}\pi r_2^3(p_0 + p_a\sin(\omega t)\sin(kx_2))\right)\right) \quad (3.65)$$

This gives the coupled radial and translational equations as:

$$R_1\ddot{R}_1 + \frac{3}{2}\dot{R}_1^2 = \frac{1}{\rho_L}\left(\left(p_0 + \frac{2\sigma}{R_{01}}\right)\left(\frac{R_{01}}{R_1}\right)^{3\gamma} - \frac{2\sigma}{R_1} - p_0 - p_{ac}(t) - \frac{4\dot{R}_1\mu_L}{R_1} - \frac{4\kappa_s\dot{R}_1}{R_1^2}\right) + \frac{u_{r1}^2}{4} - \frac{R_2}{D}\left(2\dot{R}_2^2 + R_2\ddot{R}_2\right) + \frac{R_2^2}{2D^2}\left(\dot{u}_{r2}R_2 + 3u_{r1}\dot{R}_2 + 3u_{r2}\dot{R}_1 + 2\dot{D}\dot{R}_2\right) - \frac{u_{r2}R_2^3}{D^3}\left(\frac{3}{2}u_{r1} + \dot{D}\right) \quad (3.66)$$

$$R_2\ddot{R}_2 + \frac{3}{2}\dot{R}_2^2 = \frac{1}{\rho_L}\left(\left(p_0 + \frac{2\sigma}{R_{02}}\right)\left(\frac{R_{02}}{R_2}\right)^{3\gamma} - \frac{2\sigma}{R_2} - p_0 - p_{ac} - \frac{4\dot{R}_2\mu_L}{R_2} - \frac{4\kappa_s\dot{R}_2}{R_2^2}\right) + \frac{u_{r2}^2}{4} - \frac{R_1}{D}\left(2\dot{R}_1^2 + R_1\ddot{R}_1\right) - \frac{R_1^2}{2D^2}\left(\dot{u}_{r1}R_1 + 3u_{r2}\dot{R}_1 + 3u_{r1}\dot{R}_2 + 2\dot{D}\dot{R}_1\right) - \frac{u_{r2}R_1^3}{D^3}\left(\frac{3}{2}u_{r2} + \dot{D}\right) \quad (3.67)$$

$$\dot{u}_{r1} = -\frac{3u_{r1}\dot{R}_1}{R_1} + u_{r2}\frac{du_{r1}}{dx_1} + \frac{2}{\rho_L}\frac{dp_{ac}}{dx_1} + \frac{3R_2}{D^2}\left(R_2\ddot{R}_2\frac{du_{r1}}{dx_1} - \frac{3R_2\dot{R}_1\dot{R}_2}{R_1} - 2\dot{R}_2^2 - R_2\ddot{R}_2\right) + \frac{3R_2}{D^3}\left(\dot{u}_{r1}R_2 - u_{r2}R_2\frac{du_{r1}}{dx_1} + 3u_{r2}\dot{R}_2 + \frac{3u_{r2}R_2\dot{R}_1}{R_1} + 2\dot{D}\dot{R}_2\right) - \frac{9\mu_L u_{r1}}{\rho_L R_1^2} \quad (3.68)$$

$$\dot{u}_{r2} = -\frac{3u_{r2}\dot{R}_2}{R_2} + u_{r1}\frac{du_{r2}}{dx_2} + \frac{2}{\rho_L}\frac{dp_{ac}}{dx_2} - \frac{3R_1}{D^2}\left(R_1\ddot{R}_1\frac{du_{r2}}{dx_2} - \frac{3R_1\dot{R}_1\dot{R}_2}{R_2} - 2\dot{R}_1^2 - R_1\ddot{R}_1\right) + \frac{3R_1}{D^3}\left(\dot{u}_{r2}R_1 - u_{r1}R_2\frac{du_{r2}}{dx_2} + 3u_{r1}\dot{R}_1 + \frac{3u_{r1}R_1\dot{R}_2}{R_2} + 2\dot{D}\dot{R}_1\right) - \frac{9\mu_L u_{r2}}{\rho_L R_2^2} \quad (3.69)$$

3.6 Implementation of Variable Shell Parameters

The above Equations (3.66-3.69), however, assume constant shell parameters and consequently cannot describe certain experimentally observed phenomena, in particular changes in the bubble equilibrium radius and non-linear character which may occur over the course of a single pulse. As such, they are unsuitable for modelling bubbles for bio-sensing where the time dependent changes in bubble dynamics due, for example, to adsorption of molecules on to the bubble surface, need to be captured. However O'Brien *et al's*. model [51] does include the effects of both surfactant and gas diffusion over time and the more rapid phenomenon of surface shedding from single isolated microbubbles. In this

section a brief overview of the mathematical model for the dynamics of a lipid-coated microbubble, used by O'Brien *et al*. [51], which uses *ad hoc* surface terms to incorporate the effects of gas and lipid diffusion is presented.

3.6.1 Implementation of Gas & Surfactant Diffusion

It is known that the composition of the shell has a significant effect on the dynamic response and the stability of a bubble. To accurately model the problem two types of diffusion are considered: that of gas between the bubble and the bulk liquid and that of surfactant from the bubble surface into and throughout the bulk liquid.

Contrast agents in a liquid possess a permeable shell, through which gas can diffuse in and out of the bubble. Thus the bubble can either grow, which is known as "rectified diffusion" or dissolve when oscillating. The rate of dissolution depends on bubble size, liquid gas concentration the frequency and the acoustic pressure of the acoustic driving wave. This relationship can be described by the well-known convection-diffusion Equation and the boundary condition stating that the rate of change of mass of the gas inside the bubble m is equal to the flux of gas through its boundary, where $D_g(\Gamma)$ is the diffusivity .

$$\frac{\partial c}{\partial t} + \frac{R^2 \dot{R}}{r^2}\frac{\partial c}{\partial r} = \frac{D_g}{r^2}\frac{\partial}{\partial r}\left(r^2 \frac{\partial c}{\partial r}\right) \qquad (3.70)$$

$$\frac{dm}{dt} = 4\pi R^2 D_g(\Gamma)\frac{\partial c(r = R, t)}{\partial r} \qquad (3.71)$$

The radial equation contains a term that is dependent on the equilibrium gas pressure inside the bubble, which will obviously change dependent on the gas mixture inside of the bubble. Therefore each gas compound will contribute proportionally to the partial pressure based on its concentration in the mixture and Henry's constant k_H,

$$c = k_H p \qquad (3.72)$$

Assuming a constant temperature and pressure throughout the bubble, a value for the concentration of the gas can be found using the relation between its mass and partial pressures via the ideal gas law, which gives a boundary condition at, *c(0,t)*.

$$pV = \frac{mGT}{M}$$

$$pV = m\alpha$$

Where *V* is the volume of the bubble, *G* is the universal gas constant, *M* is the molar mas of the gas and *T* is the temperature. This means that the equilibrium gas pressure term of the radial Equations (3.66-3.67) can now be written in the form below, where *A* and *B* can denote any gas and any number of gases may be considered.

$$p_0 + \frac{2\sigma_0}{R_0} = \frac{1}{V}(m^A\alpha^A + m^B\alpha^B) \qquad (3.73)$$

The diffusion equations governing the surfactant behaviour can be split into two problems occurring on different time scales, one is the fast time scale of an oscillation of a bubble and the second is the long time scale of diffusion.

Fyrillas and Szeri [71-73] derived the thresholds necessary for rectified diffusion to occur by modelling the effect of surfactant-dependent diffusivity on the gas diffusion into and out of the bubble. The time scales involved transpired to be on the same timescale as the transport of gas molecules through the liquid, which is much slower than that of a microbubble oscillation at medical ultrasound frequencies (i.e. MHz). They proved this by using a series expansion for large values of the gas and surfactant Pèclet numbers $Pe = \frac{R_0^2\omega}{D_g}$ for typical values of $R_0 \sim 10^{-6}m$ and $\omega = 10^6 Hz$ with $D_g \sim 10^{-9}m^2s^{-1}$ gives a $Pe \sim 10^3$. Consequently, over the time scale of an ultrasound pulse the effects of diffusion in the bulk liquid can be ignored. Importantly, the order of magnitude *Pe* suggests that diffusion becomes important on the timescale of milliseconds, or a pulse repetition frequency of

~1kHz. Therefore for short oscillation cycles, diffusion can be assumed to only occur in-between the pulses but not during, meaning that the full gas equations do not need to be implemented, (it is worth noting that some therapeutic applications use long oscillation cycles and this assumption may not hold). O'Brien e*t al.*'s [51] model differs from this in the treatment of the boundary conditions, as it includes a mechanism for surfactant shedding to occur and therefore uses a multiscale approach to modelling the gas diffusion and the surfactant shedding.

3.6.2 Implementation of Lipid Shedding and Variable Surface Tension

In this section a brief overview of the mathematical model for the dynamics of a lipid-coated microbubble, used by O'Brien *et al*. [51], is given as the same approach has been adopted here. As described earlier, the variable nature of the surface tension can all be described through the use of terms dependent on surface concentration. Three distinct concentration regimes in which the surfactant behaves differently. These regimes are described by Equation (3.74):

$$\frac{d(A\Gamma)}{dt} = \begin{cases} A[k_1 C^{surf}(R,t)(\Gamma^* - \Gamma) - k_2\Gamma] & if\ \Gamma < \Gamma^* \\ 0 \quad if\ \Gamma^* < \Gamma < \Gamma_{max} & \\ \Gamma_{max}\dfrac{dA}{dt} \quad if\ \Gamma_{max} < \Gamma & \end{cases} \tag{3.74}$$

Here C^{surf} is the concentration of surfactant in the surrounding liquid, k_1 and k_2 are the absorption and desorption coefficients respectively. During the phase transition from the Langmuir to the insoluble regime a simplistic assumption is made that the values of these two coefficients drop discontinuously and are allowed to reduce to zero $\Gamma=\Gamma^*$ [52] . Morris *et al*. [74] refer to this as "pseudo-film collapse" so called this since it exhibits the same characteristics, i.e. that the σ remains relatively constant as the interfacial area is reduced, as the true film collapse.

However, even with this amendment, under specific conditions a pseudo-film collapse is still observed, and is the result of the bubble being unable to reach sufficient interfacial surfactant concentration to enter the insoluble regime. For this behaviour to be exhibited the rate of change of the interfacial concentration must be negative for some Γ during the compression cycle. When Γ approaches Γ^* molecules are being ejected via desorption which lowers the interfacial concentration during which the interfacial film is being compacted as the bubble compresses which raises the interfacial concentration. Therefore in order to avoid this numerical artefact k_i can be written as:

$$\beta(\Gamma) = \begin{cases} 1 \; \Gamma < 0.96 \times \Gamma^* \\ 25k_i\left(1 - \dfrac{\Gamma}{\Gamma^*}\right) \; 0.96 \times \Gamma^* < \Gamma < \Gamma^* \\ 0 \; \Gamma < \Gamma^* \end{cases}$$

. From Equation (3.74) the equilibrium surface concentration Γ_{eq} at *t=0*, is:

$$\Gamma_{eq} = \frac{\Gamma^* k_1 C_\infty}{k_1 C_\infty + k_2}$$

When the bubble oscillates, the surface surfactant concentration changes with the size of the bubble, hence the shell properties vary with respect to time. Therefore, if the bubble is going to be properly described, time dependent shell parameters will have to be incorporated into the radial Equations (3.66-3.67). This has been done previously [23, 24, 51]. As described earlier, Marmottant *et al.'s* model considers surface tension into three regimes :

$$\sigma(R) = \begin{cases} 0 \text{ if } R \le R_{buckling} \\ \chi\left(\dfrac{R^2}{R_{buckling}^2} - 1\right) \text{if } R_{buckling} \le R \le R_{rupture} \\ \sigma_{water} \text{ if ruptured } R \ge R_{ruptured} \end{cases} \tag{3.75}$$

Where $R_{rupture} = R_{buckling}\left(1 + \frac{\sigma(R_0)}{\chi}\right)^{1/2}$ and $R_{buckling} = R_0$

This type of surface tension model has discontinuities in the model and can be replaced by a smooth sigmoid curve as previously shown by Stride [24] and O'Brien [51]. This sigmoid curve used by the latter gives the surface tension based on surfactant concentration. The coefficients Q,U,W and Y are found from fitting the curve to the experimentally based discontinuous model of Marmottant *et al*.[23].

$$\sigma(\Gamma) = \sigma_0 + \frac{\sigma_{min} - \sigma_0}{\left(1 + Q\ exp\left(-U(\Gamma - W)\right)^{(1/Y)}\right)} \tag{3.76}$$

3.6.3 Implementation of Variable Viscosity

The viscosity term in the radial equation of motion for the bubble has a restricting effect on the oscillation of the bubble. Similar to surface tension, over the course of an oscillation the viscosity changes as the bubble's shell is expanded and constricted, this is due to the surfactant concentration of the shell changing. As the radius increases the surfactant concentration reduces, causing the shell viscosity to decrease, and as the radius decreases the surfactant concentration increases, increasing the viscosity. Moreover in [75] it has been investigated how the curvature of the shell affects its properties. The variable effect of viscosity is ignored in most models. This is due to many reasons, one being that most models consider that the bubble's properties remain constant throughout the oscillation pulse, thus the variation in viscosity over an oscillation is considered so small that it has a negligible effect on the model and therefore it is justified to take an average value for the viscosity. However when considering the effect of lipid shedding and gas diffusion, during and in-between acoustic pulses, the change in viscosity potentially has a more of a marked effect upon the oscillation [51].

There are two problems, but separate ones: (1) mathematical description at a molecular scale and (2) experimentally measuring viscosity. Furthermore it is difficult to describe the shell viscosity in conventional mechanical terms. In classical Newtonian

mechanics the bubble's shell is considered to have 3 intrinsic interfacial properties, surface tension, shear viscosity, μ_s, and dilatational viscosity, κ_s, where all these properties can be treated as functions of monolayer concentration [76]. However studies have found that classical Newtonian descriptions of monolayers that consist of coexisting phase domains are inadequate when undergoing compression or expansion, which occurs during a bubble oscillation [76].

Existing models include either dilatational or shear viscosity depending on the description of the shell employed. If the shell is considered as a surfactant monolayer then the viscosity can be described as dilatational viscosity which governs the damping motion, an example of this is Marmottant's model [23]. If instead an incompressible viscoelastic shell description is applied then the shear viscosity of the shell material is required, an example of this kind of model is Hoff [20].

Another issue is that viscosity on this scale is difficult to measure experimentally. Currently there is no method that directly measures the viscosity of the shell, the closest method to achieving this is a new technique, FLIM (fluorescence lifetime imaging microscopy) [77] that exploits the viscosity sensitive properties of a fluorescent probe known as a molecular rotor to measure viscosity. This measurement gives an indication of the energy dissipated by the molecular interaction which in effect produces viscosity on a large scale and therefore gives a quantitative measure of the viscosity [77]. However, it is unclear what kind of viscosity it is, as it does not fall into the category of shear or dilatational viscosity and has no clear link to either. Consequently it has been described as "microviscosity" [78]. Crucially though it still does not give any definitive relationship for $\kappa_s(\Gamma)$.

It is unclear what mechanism causes the dissipative effects of the bubble's shell and whether or not it can be defined as a form of viscosity. Additionally it is unknown what the process causes this effect whether it is due to the monolayer, the domains of the surfactant, and other dissipative effects in the membrane or a combination of these effects. Thus with it being experimentally unattainable at the present time to measure the viscosity, the form of the time dependent viscosity term shall be based on the nearest known equivalent, that of the monolayers of molecules, which have been shown to follow an exponential type of behaviour [79]. Though it is not known if this behaviour holds when the curvature of the shell is taken into account, or at the deformation rates corresponding to the oscillation of a bubble during an ultrasound pulse.

As the viscosity is expected to be dependent upon the surfactant concentration of the shell, a boundary condition is imposed. As $\Gamma \rightarrow 0$, the viscosity must also tend to zero giving the boundary condition as:

$$\kappa_s = 0 \; as \; \Gamma = 0 \qquad (3.77)$$

As far as the author knows only two models have included time dependent viscosity previously, O'Brien's [51] and Stride [24]. In [51] a dilatational viscosity function dependent on the surfactant concentration on the bubble surface assuming a linear dependence between $0 \leq \Gamma < \Gamma^{max}$, based upon two radii where $\Gamma = \Gamma^{eq}$, κ_s=7x10^{-9} at R_0=4.5μm and κ_s=1.6x10^{-8} at R_0=1μm. This term produces the expected trend of viscosity but it does not have any physical basis, and assumes that the bubble's viscosity scales linearly with bubble radius which is unknown. Stride's [24] treatment of viscosity is based upon Sacchetti *et al*. [79] which correlates shear viscosity, η_s, to area and is based upon empirical measurements of a molecular monolayer at an air/water interface [79], giving the function.

$$\eta_s = \eta_{s0}\, exp\left(\frac{ZR_x^2}{R^2 - R_x^2}\right) \tag{3.78}$$

Where η_{s0} and Z are constants and R_x is radial bucking limit, in other words for radii below this the bubble's shell buckles. It is therefore suggested that here the function for shell viscosity κ_s should be based on a term similar to this. Using $R^2 = \frac{m_s}{4\,\pi\,\Gamma}$ where, ${R_x}^2 = \frac{m_s}{4\,\pi\,\Gamma^{max}}$ to give the Equation (3.77) in terms of surfactant concentration for a shell viscosity. It should be noted that in the case of a finite thickness shell shear and dilatational viscosity are clearly different quantities, but for an infinitely thin monolayer the assumption is made that there is a single surface viscosity arising from changes in molecular concentration, thus $\frac{4\kappa_s\dot{R}}{R^2} \approx \frac{4\eta_s\dot{R}}{R^2}$, where

$$\kappa_s = \kappa_{s0}\, exp\left(\frac{Z\Gamma}{\Gamma^{max} - \Gamma}\right) \tag{3.79}$$

This can be modified to obtain the equation in the form :

$$\kappa_s = \kappa_{s0} A\, exp\left(\frac{\Gamma}{\Gamma^{max} - \Gamma}\right) \tag{3.80}$$

Where A is a constant. Now applying the boundary condition Equation (3.77) and also assuming an equilibrium condition:

$$\kappa_s = \kappa_{s0}\, when\, \Gamma = \Gamma^{eq} \tag{3.81}$$

It becomes apparent from Equation (3.77) that the Equation (3.80) needs to be revised to take the form:

$$\kappa_s = \kappa_{s0} B\left(1 - exp\left(\frac{\Gamma}{\Gamma^{max} - \Gamma}\right)\right)$$

Where B is again a constant. Then applying the equilibrium condition Equation (3.81) yields an Equation of the form.

$$\kappa_s = \frac{\kappa_{s0}\left(1 - exp\left(\frac{\Gamma}{\Gamma^{max} - \Gamma}\right)\right)}{\left(1 - exp\left(\frac{\Gamma^{eq}}{\Gamma^{max} - \Gamma^{eq}}\right)\right)} \qquad (3.82)$$

Figure 3.6 below shows the behaviour of the function up to maximum concentration.

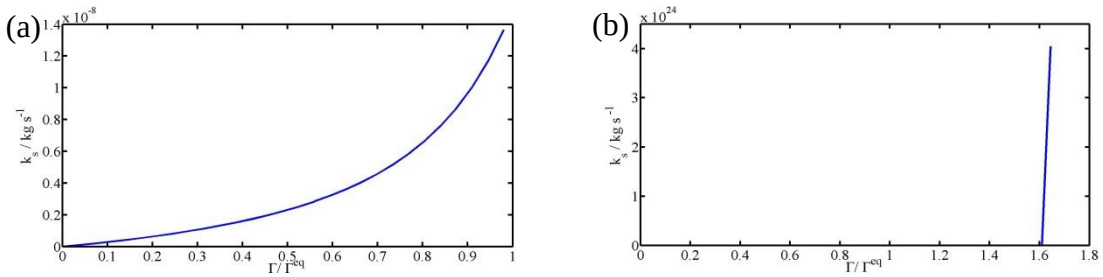

Figure 3.6 (a) showing the viscosity in Equation (3.82) up to Γ^{eq} (b) continuing the graph up to Γ^{max} which shows the extreme behaviour of the viscosity tending to infinity.

It can be seen from Figure 3.6(b) that this form of the equation goes to infinity at Γ^{max} which is unphysically and would result in instability upon solving the equation numerically. In reality instead of going to infinity at this point the viscosity would in fact start to fall as the shell would buckle. However at this point the assumption of spherical symmetry is lost and there is little or no data currently available to enable a description of shell buckling to be generated. Therefore it is suggested that as $\Gamma \longrightarrow \Gamma^{max}$ the viscosity tends towards a maximum value. A more appropriate function to describe this is tanh, as pictured in Figure 3.7.

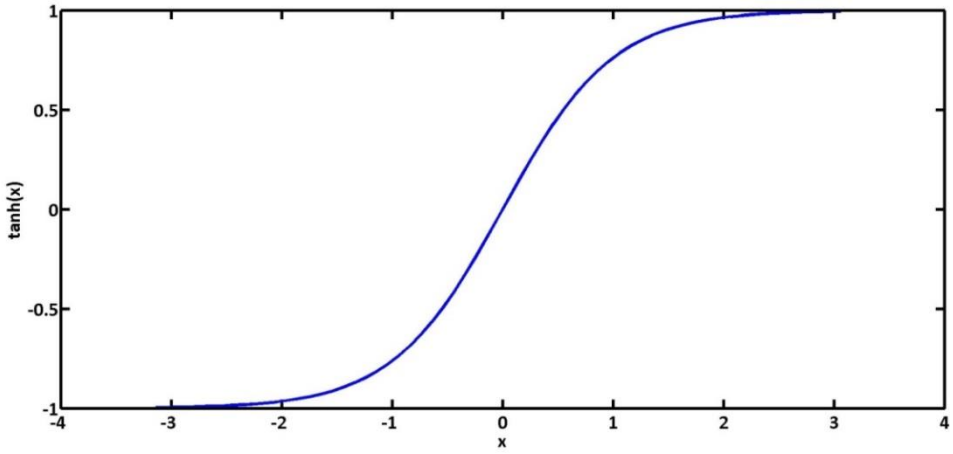

Figure 3.7 Tanh(x) function. It can be seen that at 0 the function equals 0 and that at the maximum its gradient tends to zero.

Therefore Equation 3.82 can be rewritten as:

$$\kappa_s(\Gamma) = \kappa_{s0} A \tanh\left(\frac{\Gamma}{\Gamma^{max} - \Gamma}\right) \tag{3.83}$$

Where A is an unknown found by applying the boundary conditions. The boundary condition at $\Gamma=0$, Equation (3.77), is automatically included due to the nature of tanh. Therefore applying the equilibrium condition, Equation (3.81), it becomes apparent that the function should take the form, shown in Figure 3.8:

$$\kappa_s(\Gamma) = \kappa_{s0} \frac{\tanh\left(\frac{\Gamma}{\Gamma^{max} - \Gamma}\right)}{\tanh\left(\frac{\Gamma^{eq}}{\Gamma^{max} - \Gamma^{eq}}\right)} \tag{3.84}$$

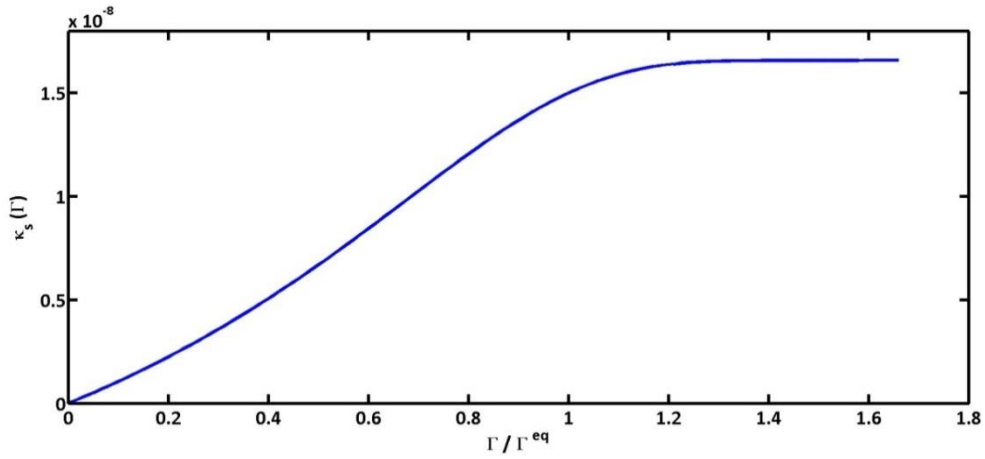

Figure 3.8 The dependence of viscosity on surface concentration.

So in conclusion it can be seen that Equation (3.84) describes a form of viscosity that is dependent on surfactant concentration and based on physically observed effects of viscosity under compression and expansion. This term will be incorporated into the bubble model and investigated to determine whether or not it gives a better description of experimentally observed bubble dynamics.

3.7 Summary

In this chapter a literature review of previous models describing the dynamic behaviour of microbubbles under ultrasound has been carried out. The areas in which the previous model could be enhanced have been discussed. This has led to a new model for coupled radial and translational motion being derived, incorporating the effects of the distance from a rigid wall, with the time dependent shell effects of lipid shedding, variable surface tension and shell viscosity. The model developed here, Equations (3.66-69) with Equations (3.74), (3.76) and (3.84), will be analysed in Chapters 4 & 5.

3.8 References

1. Tang, M.-X., et al., *Quantitative contrast-enhanced ultrasound imaging: a review of sources of variability.* Interface Focus, 2011. **1**(4): p. 520-539.
2. Besant, W., *Hydrostatics and Hydrodynamics*. 1859, Cambridge , UK: Deighton Bell.
3. Rayleigh (J.W. Strutt), Baron, *On the pressure developed in a liquid during the collapse of a spherical cavity.* Philosophical Magazine, 1917(34): p. 94-98.
4. Plesset, M.S., *The dynamics of cavitation bubbles.* Transactions of the Americal Society of Mechanical Engineers: Journal of Applied Mechanics, 1949. **16**(3): p. 227.
5. Neppiras, E.A. and Noltingk, B.E., *Cavitation Produced by Ultrasonics - Theoretical Conditions for the Onset of Cavitation.* Proceedings of the Physical Society of London Section B, 1951. **64**(384): p. 1032-1038.
6. Noltingk, B.E. and Neppiras, E.A., *Cavitation Produced by Ultrasonics.* Proceedings of the Physical Society of London Section B, 1950. **63**(369): p. 674-685.
7. Poritsky, H., *The collapse or growth of a spherical bubble or cavity in a viscous fluid.* Proceedings of the first US National Congress in Applied Mechanics (ASME), 1952: p. 813.
8. Lauterborn, W., *Numerical Investigation of Nonlinear Oscillations of Gas-Bubbles in Liquids.* Journal of the Acoustical Society of America, 1976. **59**(2): p. 283-293.
9. Prosperetti, A., *Nonlinear bubble dynamics.* J.Acoust.Soc.Am., 1988. **83**(2): p. 502.
10. Herring, C., *Theory of the pulsations of the gas bubble produced by an underwater explosion*. 1941: Columbia Univ., Division of National Defense Research.

11. Trilling, L., *The collapse and rebound of a gas bubble.* Journal of Applied Physics,, 1952. **23(1)**: p. 14-17.

12. Gilmore, F.R., *The growth or collapse of a spherical bubble in a viscous compressible liquid.* 1952.

13. Keller, J., *Bubble oscillations of large amplitude.* J.Acoust.Soc.Am., 1980. **68**(2): p. 628.

14. Fox, F.E. and Herzfeld, K.F., *Gas Bubbles with Organic Skin as Cavitation Nuclei.* The Journal of the Acoustical Society of America, 1954. **26**(6): p. 984-989.

15. de Jong, N., Cornet, R., and Lancée, C.T., *Higher harmonics of vibrating gas-filled microspheres. Part one: simulations.* Ultrasonics, 1994. **32**(6): p. 447-453.

16. de Jong, N., Cornet, R., and Lancée, C.T., *Higher harmonics of vibrating gas-filled microspheres. Part two: measurements.* Ultrasonics, 1994. **32**(6): p. 455-459.

17. de Jong, N., et al., *Absorption and scatter of encapsulated gas filled microspheres: Theoretical considerations and some measurements.* Ultrasonics, 1992. **30**(2): p. 95-103.

18. Devin, J.C., *Survey of Thermal, Radiation, and Viscous Damping of Pulsating Air Bubbles in Water.* The Journal of the Acoustical Society of America, 1959. **31**(12): p. 1654-1667.

19. Church, C., *The effects of an elastic solid surface layer on the radial pulsations of gas bubbles.* J. Acoust. Soc. Am., 1995. **97**(3): p. 1510.

20. Hoff, L., Sontum, P.C., and Hovem, J.M., *Oscillations of polymeric microbubbles: Effect of the encapsulating shell.* Journal of the Acoustical Society of America, 2000. **107**(4): p. 2272-2280.

21. Glazman, R.E., *Effects of adsorbed films on gas bubble radial oscillations.* The Journal of the Acoustical Society of America, 1983. **74**(3): p. 980-986.

22. Morgan, K.E., et al. *Experimental and theoretical analysis of individual contrast agent behavior*. in *Ultrasonics Symposium, 1999. Proceedings. 1999 IEEE*. 1999.

23. Marmottant, P., et al., *A model for large amplitude oscillations of coated bubbles accounting for buckling and rupture.* Journal of the Acoustical Society of America, 2005. **118**(6): p. 3499-3505.

24. Stride, E., *The influence of surface adsorption on microbubble dynamics.* Philosophical Transactions of the Royal Society A-Mathematical Physical and Engineering Sciences, 2008. **366**(1873): p. 2103-2115.

25. Chatterjee, D. and Sarkar, K., *A Newtonian rheological model for the interface of microbubble contrast agents.* Ultrasound Med Biol, 2003. **29**(12): p. 1749-57.

26. Sarkar, K., et al., *Characterization of ultrasound contrast microbubbles using in vitro experiments and viscous and viscoelastic interface models for encapsulation.* J Acoust Soc Am, 2005. **118**(1): p. 539-50.

27. Paul, S., et al., *Material characterization of the encapsulation of an ultrasound contrast microbubble and its subharmonic response: strain-softening interfacial elasticity model.* J Acoust Soc Am, 2010. **127**(6): p. 3846-57.

28. Tsiglifis, K. and Pelekasis, N.A., *Nonlinear radial oscillations of encapsulated microbubbles subject to ultrasound: the effect of membrane constitutive law.* J Acoust Soc Am, 2008. **123**(6): p. 4059-70.

29. Allen, J.S. and Rashid, M.M., *Dynamics of a Hyperelastic Gas-Filled Spherical Shell in a Viscous Fluid.* Journal of Applied Mechanics, 2004. **71**(2): p. 195-200.

30. Allen, J.S. and Roy, R.A., *Dynamics of gas bubbles in viscoelastic fluids. I. Linear viscoelasticity.* The Journal of the Acoustical Society of America, 2000. **107**(6): p. 3167-3178.

31. Allen, J.S. and Roy, R.A., *Dynamics of gas bubbles in viscoelastic fluids. II. Nonlinear viscoelasticity.* The Journal of the Acoustical Society of America, 2000. **108**(4): p. 1640-1650.

32. Khismatullin, D.B. and Nadim, A., *Radial oscillations of encapsulated microbubbles in viscoelastic liquids.* Physics of Fluids, 2002. **14**(10): p. 3534-3557.

33. Lauterborn, W. and Kurz, T., *Physics of bubble oscillations.* Reports on Progress in Physics, 2010. **73**(10).

34. Becher, H.B.P., *Handbook of Echocardiography*. 2000, Frankfurt: Springer Verlag.

35. Blake, J.R., Taib, B.B., and Doherty, G., *Transient cavities near boundaries.1. Rigid Boundary.* Journal of Fluid Mechanics, 1986. **170**: p. 479-497.

36. Best, J.P. and Kucera, A., *A numerical investigation of nonspherical rebounding bubbles.* Journal of Fluid Mechanics, 1992. **245**: p. 137-154.

37. Harris, P.J., *A numerical-model for determining the motion of a bubble close to a fixed rigid structure in a fluid.* International Journal for Numerical Methods in Engineering, 1992. **33**(9): p. 1813-1822.

38. Harris, P.J., *A nuerical-method for predicting the motion of a bubble close to a moving rigis structure.* Communications in Numerical Methods in Engineering, 1993. **9**(1): p. 81-86.

39. Blake, J.R. and Gibson, D.C., *Growth and collapse of a vapour cavity near a free surface.* Journal of Fluid Mechanics, 1981. **111**: p. 123-140.

40. Blake, J.R., Taib, B.B., and Doherty, G., *Transient cavities near boundaries .2. Free-Surface* Journal of Fluid Mechanics, 1987. **181**: p. 197-212.

41. Wang, Q.X., et al., *Strong interaction between a buoyancy bubble and a free surface.* Theoretical and Computational Fluid Dynamics, 1996. **8**(1): p. 73-88.

42. Wang, Q.X., et al., *Nonlinear interaction between gas bubble and free surface.* Computers & Fluids, 1996. **25**(7): p. 607-628.

43. Qin, S.P. and Ferrara, K.W., *Acoustic response of compliable microvessels containing ultrasound contrast agents.* Physics in Medicine and Biology, 2006. **51**(20): p. 5065-5088.

44. Miao, H., Gracewski, S.M., and Dalecki, D., *Ultrasonic excitation of a bubble inside a deformable tube: Implications for ultrasonically induced hemorrhage.* Journal of the Acoustical Society of America, 2008. **124**(4): p. 2374-2384.

45. Martynov, S., Stride, E., and Saffari, N., *The natural frequencies of microbubble oscillation in elastic vessels.* Journal of the Acoustical Society of America, 2009. **126**(6): p. 2963-2972.

46. Longuet-Higgins, M.S. and Cokelet, E.D., *Deformation of steep surface-waves on water. 1. numerical-method of computation.* Proceedings of the Royal Society of London Series a-Mathematical Physical and Engineering Sciences, 1976. **350**(1660): p. 1-26.

47. Dold, J.W., *An eficient surface-intergral algortithm applied to unsteady gravity-waves.* Journal of Computational Physics, 1992. **103**(1): p. 90-115.

48. Lamb, H., Sir,, *Hydrodynamics by Horace Lamb*. 4th ed. 1895, Cambridge [Eng.] :: University Press.

49. Borden, M.A., et al., *Influence of lipid shell physicochemical properties on ultrasound-induced microbubble destruction.* Ultrasonics, Ferroelectrics and Frequency Control, IEEE Transactions on, 2005. **52**(11): p. 1992-2002.

50. Viti, J., et al. *Nonuniform oscillations of deflating bubbles - a pilot study.* in *The 16th European Symposium on Ultrasound Contrast Imaging,*. 2011. Rotterdam.

51. O'Brien, J.-P., Ovenden, N., and Stride, E., *Accounting for the stability of microbubbles to multi-pulse excitation using a lipid-shedding model.* The Journal of the Acoustical Society of America, 2011. **130**(4): p. EL180-EL185.

52. Israelachvili, J., *Intermolecular and Surface Forces*. 1992, London: Academic Press.

53. King, L.V., *On the Acoustic Radiation Pressure on Spheres.* Proceedings of the Royal Society of London. Series A, Mathematical and Physical Sciences, 1934. **147**(861): p. 212-240.

54. Yosioka, K., Kawasima, Y, *Acoustic radiation pressure on a compressible sphere.* Acoust. Soc. Am, 1955. **5**: p. 167.

55. Crum, L., *Nonlinear oscillations of gas bubbles in liquids: An interpretation of some experimental results.* J. Acoust. Soc. Am., 1983. **73**(1): p. 121.

56. Watanabe, T. and Kukita, Y., *Translational and Radial Motions of a Bubble in an Acoustic Standing-Wave Field.* Physics of Fluids a-Fluid Dynamics, 1993. **5**(11): p. 2682-2688.

57. Doinikov, A.A., *Translational motion of a spherical bubble in an acoustic standing wave of high intensity.* Physics of Fluids, 2002. **14**(4): p. 1420-1425.

58. Doinikov, A.A.and Dayton, P.A, *Spatio-temporal dynamics of an encapsulated gas bubble in an ultrasound field.* J. Acoust. Soc. Am., 2006. **120**(2): p. 661.

59. Hsiao, C.-T. and Chahine, G., *Prediction of tip vortex cavitation inception using coupled spherical and nonspherical bubble models and Navier–Stokes computations.* Journal of Marine Science and Technology, 2004. **8**(3): p. 99-108.

60. Dayton, P., *The magnitude of radiation force on ultrasound contrast agents.* J. Acoust. Soc. Am., 2002. **112**(5): p. 2183.

61. Meyer, R.S., Billet, M.L., and Holl, J.W., *Freestream Nuclei and Traveling-Bubble Cavitation.* Journal of Fluids Engineering, 1992. **114**(4): p. 672-679.

62. Garbin, V., et al., *History force on coated microbubbles propelled by ultrasound.* Physics of Fluids, 2009. **21**(9): p. 092003-7.

63. Reddy, A.J. and Szeri, A.J., *Coupled dynamics of translation and collapse of acoustically driven microbubbles.* J Acoust Soc Am, 2002. **112**(4): p. 1346-52.

64. Harkin, A., Kaper, T.J., and Nadim, A., *Coupled pulsation and translation of two gas bubbles in a liquid.* Journal of Fluid Mechanics, 2001. **445**: p. 377-411.

65. Park, W.C., Klausner, J.F., and Mei, R., *Unsteady forces on spherical bubbles.* Experiments in Fluids, 1995. **19**(3): p. 167-172.

66. Suslick, K.S., *Sonochemistry.* Science, 1990. **247**(4949): p. 1439-1445.

67. Takemura, F. and Magnaudet, J., *The history force on a rapidly shrinking bubble rising at finite Reynolds number.* Physics of Fluids, 2004. **16**(9): p. 3247-3255.

68. Batchelor, G.K., *An Introduction to Fluid Dynamics*. 2000: Cambridge University Press.p.452-455.

69. Doinikov, A.A., *Translational motion of two interacting bubbles in a strong acoustic field.* Physical Review E, 2001. **64**(2).

70. Hobson, E.W., *The theory of spherical and ellipsoidal harmonics*. Vol. 1. 1931: CUP Archive.

71. Fyrillas, M.M. and Szeri, A.J., *Dissolution or growth of soluble spherical oscillating bubbles.* Journal of Fluid Mechanics, 1994. **277**: p. 381-407.

72. Fyrillas, M.M. and Szeri, A.J., *Dissolution or growth of soluble spherical oscillating bubbles: the effect of surfactants.* Journal of Fluid Mechanics, 1995. **289**: p. 295-314.

73. Fyrillas, M.M. and Szeri, A.J., *Surfactant dynamics and rectified diffusion of microbubbles.* Journal of Fluid Mechanics, 1996. **311**: p. 361-378.

74. Morris, J., et al., *Dynamic Behavior of Lung Surfactant.* Journal of Biomechanical Engineering, 2001. **123**(1): p. 106-113.

75. David, B., *Mechanics of the Cell*. 2001: Cambridge University Press.

76. Lopez, J.M., Vogel, M.J., and Hirsa, A.H., *Influence of coexisting phases on the surface dilatational viscosity of Langmuir monolayers.* Phys Rev E Stat Nonlin Soft Matter Phys, 2004. **70**(5 Pt 2): p. 17.

77. Hosny, N.A., et al., *Mapping microbubble viscosity using fluorescence lifetime imaging of molecular rotors.* Proceedings of the National Academy of Sciences, 2013.

78. Nipper, M.E., et al., *Characterization of changes in the viscosity of lipid membranes with the molecular rotor FCVJ.* Biochimica et Biophysica Acta (BBA) - Biomembranes, 2008. **1778**(4): p. 1148-1153.

79. Sacchetti, M., Yu, H., and Zografi, G., *In-plane steady shear viscosity of monolayers at the air/water interface and its dependence on free area.* Langmuir, 1993. **9**(8): p. 2168-2171.

4 Model Analysis

For a microbubble to be used successfully as a sensor, it is important that the expected behaviour can be modelled accurately to allow for the characterization of its unknown shell parameters in a known environment and vice versa.

This chapter is concerned with the analysis of the model, Equations (3.66-3.69), developed in Chapter 3 and using it to assess the suitability of lipid encapsulated microbubbles as bio-sensors. This analysis includes the examination of the different constitutive terms and under what conditions they become dominant (section 4.2), as well as considering the uniqueness of a given set of parameters in describing the bubble response (section 4.3), the sensitivity of the response to changes in the system parameters (section 4.4) and the propagation of errors in the characterisation inherent in experimental equipment to assess microbubbles' applicability as a sensor (section 4.5).

4.1 Numerical Modelling

To implement the model, the following equations were solved simultaneously using a numerical method via purpose written code (Appendix C.2) implementing a 4th order Runge-Kutta method using MatLab2012 ® inbuilt solver ode45, the equations from Chapter 3 are re-written here for the readers' convenience:

- The equations describing the radial and translational motion of both the real and image bubbles,

$$R_1\ddot{R}_1 + \frac{3}{2}\dot{R}_1^2 = \frac{1}{\rho_L}\left(\left(p_0 + \frac{2\sigma_0}{R_{01}}\right)\left(\frac{R_{01}}{R_1}\right)^{3\gamma} - \frac{2\sigma(\Gamma)}{R_1} - p_0 - p_{ac} - \frac{4\dot{R}_1\mu_L}{R_1} - \frac{4k_s\,(\Gamma)\dot{R}_1}{R_1^2}\right) + \frac{u_{r1}^2}{4} - \frac{R_2}{D}\left(2\dot{R}_2^2 + R_2\ddot{R}_2\right) + \frac{R_2^2}{2D^2}\left(\dot{u}_{r2}R_2 + 3u_{r1}\dot{R}_2 + 3u_{r2}\dot{R}_2 + 2\dot{D}\dot{R}_2\right) - \frac{u_{r2}R_2^3}{D^3}\left(\frac{3}{2}u_{r1} + \dot{D}\right) \tag{4.1}$$

$$R_2\ddot{R}_2 + \frac{3}{2}\dot{R}_2^2 = \frac{1}{\rho_L}\left(\left(p_0 + \frac{2\sigma_0}{R_{02}}\right)\left(\frac{R_{02}}{R_2}\right)^{3\gamma} - \frac{2\sigma(\Gamma)}{R_2} - p_0 - p_{ac} - \frac{4\dot{R}_2\mu_L}{R_2} - \frac{4k_s(\Gamma)\dot{R}_2}{R_2^2}\right) + \frac{u_{r2}^2}{4} - \frac{R_1}{D}\left(2\dot{R}_1^2 + R_1\ddot{R}_1\right) - \frac{R_1^2}{2D^2}\left(\dot{u}_{r1}R_1 + 3u_{r2}\dot{R}_1 + 3u_{r1}\dot{R}_1 - 2\dot{D}\dot{R}_1\right) - \frac{u_{r1}R_1^3}{D^3}\left(\frac{3}{2}u_{r2} + \dot{D}\right) \tag{4.2}$$

$$\dot{u}_{r1} = -\frac{3u_{r1}\dot{R}_1}{R_1} + u_{r1}\frac{du_{r1}}{dx_1} + \frac{2}{\rho_l}\frac{dp_{ac}}{dx_1} + \frac{3R_2}{D^2}\left(R_2^2\dot{R}_2\frac{du_{r1}}{dx_1} - \frac{3R_2\dot{R}_1\dot{R}_2}{R_1} - 2\dot{R}_2^2 - R_2\ddot{R}_2\right) + \frac{3R_2^2}{D^3}\left(\dot{u}_{r2}R_2 - u_{r2}R_2\frac{du_{r1}}{dx_1} + 3u_{r2}\dot{R}_2 + \frac{3u_{r2}R_2\dot{R}_1}{R_1} + 2\dot{D}\dot{R}_2\right) - \frac{9\mu_L u_{r1}}{\rho_l R_1^2} \tag{4.3}$$

$$\begin{aligned}\dot{u}_{r2} = &-\frac{3u_{r2}\dot{R}_2}{R_2} + u_{r1}\frac{du_{r2}}{dx_2} + \frac{2}{\rho_l}\frac{dp_{ac}}{dx_2} \\ &- \frac{3R_1}{D^2}\left(R_1\dot{R}_1\frac{du_{r2}}{dx_2} + \frac{3R_1\dot{R}_1\dot{R}_2}{R_2} + 2\dot{R}_1^2 + R_1\ddot{R}_1\right) \\ &+ \frac{3R_1^2}{D^3}\left(\dot{u}_{r1}R_1 - u_{r1}R_1\frac{du_{r2}}{dx_2} + 3u_{r1}\dot{R}_1\right. \\ &\left. + \frac{3u_{r1}R_1\dot{R}_2}{R_2} - 2\dot{D}\dot{R}_1\right) - \frac{9\mu_L u_{r2}}{\rho_l R_2^2}\end{aligned} \tag{4.4}$$

- the equation for gas diffusion

$$\frac{dm}{dt} = 4\pi R^2 D_g(\Gamma)\frac{\partial c(r=R,t)}{\partial r} \tag{4.5}$$

- the conditions for different surfactant behaviour

$$\frac{d(A\Gamma)}{dt} = \begin{cases} A\left[k_1 C^{surf}(R,t)(\Gamma^* - \Gamma) - k_2\Gamma\right] & if\ \Gamma < \Gamma^* \\ 0 & if\ \Gamma^* < \Gamma < \Gamma_{max} \\ \Gamma_{max}\dfrac{dA}{dt} & if\ \Gamma_{max} < \Gamma \end{cases} \tag{4.6}$$

- the equations describing the surfactant concentration dependent surface tension (4.7) and viscosity (4.8).

$$\sigma(\Gamma) = \sigma_0 + \frac{\sigma_{min} - \sigma_0}{\left(1 + Q\ exp(-U(\Gamma - W))\right)^{(1/Y)}} \tag{4.7}$$

$$k_s(\Gamma) = k_{s0}\frac{\tanh\left(\frac{\Gamma}{\Gamma^{max} - \Gamma}\right)}{\tanh\left(\frac{\Gamma^{eq}}{\Gamma^{max} - \Gamma^{eq}}\right)} \tag{4.8}$$

This model was run via a non-dimensionalisation via the following scheme:

[mass]=[p_0R_0/ω^2] [length]=[R_0] [time]=[$1/\omega$]

The code was validated by comparing the radial response to the linearized analytical code (Appendix B), and the response over many cycles was observed to give the same

gradient as that found in O'Brien [1], the translational motion was compared to that found in literature which gave similar responses. When using ode45 in MatLab the time step is not fine enough to capture all the activity of the bubble oscillation. Therefore the time step used was determined via lowering the time step until the response in the radial motion over 20 acoustic cycles no longer changed, this was discovered to be a time step of 0.0001 in non-dimensional time.

As the model will be run for multiple pulses, with pulse repetition frequency of 1kHz, the following approximation could be made due to the significant differences in scale between diffusion rates and the pulse repetition rates, for both gas and surfactant diffusion to reduce the computation time required. These comprised of neglecting the explicit finite difference diffusion calculations during the interval between pulses, .i.e Equation (4.5), but still capturing their effect following surfactant shedding during the pulse. For medical imaging a repetition pulse is used which lasts in the order of 10^{-6}s with the time in-between pulses of the order of 10^{-3}s, which is much longer [2].This disparity allows for simplifications to be made [1], considering the Pèclet number, $Pe=R_0^2\, f/D_i$, for gas diffusion with $D_g \sim 10^{-9}\text{m}^2\text{s}^{-1}$ giving a $Pe_g \approx 10^3$ and for surfactant diffusion which has been indicated [3] to have a diffusion in the order of $D_s \sim 10^{-13}\text{m}^2\text{s}^{-1}$ giving a $Pe_s \approx 10^7$. This means that for $\Gamma < \Gamma^*$, absorption & desorption occur on a timescale in the order of ~10s, which is much longer than the time between pulses. Consequently after the surfactant has been ejected during the pulse, it can be assumed that it is not absorbed back onto the shell in any significant degree [4]. Therefore the gas diffusion can be modelled in the following way; Figure 4.1 gives a graphical representation corresponding to the steps below:

1. Bubble is in initial equilibrium state, where $\Gamma=\Gamma^{eq}$ with inputs of the ODE being: Radius=R_0, *d*istance to wall=d_0, mass of gas=m_{0g} *and m*ass of surfactant =m_{0s}

2. Bubble is exposed to pulse and equations (4.1) and (4.6) are solved simultaneously in the ode45 in MatLab ®.

3. At the end of the pulse, the mass of the surfactant left , m_{0s}^{new} , and the new position of the bubble, d_0^{new}, are calculated as the last values in the run.

4. In the interval between pulses the bubble is assumed to reach a new equilibrium state in which $\Gamma=\Gamma^{eq}$ .The new bubble radius is found via

$$R_0^{new} = \sqrt{\frac{m_{0s}^{new}}{4\,\pi\,\Gamma^{eq}}} \tag{4.9}$$

From this the new gas mass, m_{0g}^{new} , is calculated from the ideal gas law.

5. The radius, mass of gas, the mass of the surfactant and the distance moved are all updated and the procedure is repeated.

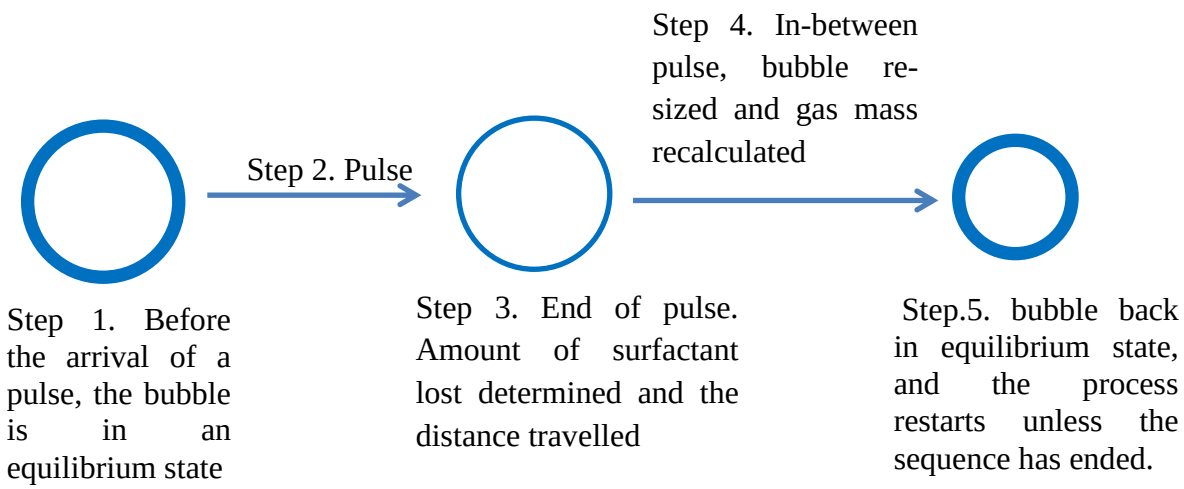

Figure 4.1 Diagram showing graphically how the code is implements gas diffusion and lipid shedding. Step numbers correlate to the step numbers in the text.

4.2 Analysis of the New Model

The new model derived in Chapter 3 for coupled radial and translational motion, was analysed to assess the importance of the different constitutive terms and under what conditions they become dominant e.g., under higher pressures, larger radii, higher frequencies or when the bubble is close to a rigid boundary.

4.2.1 Orders of Magnitude

This preliminary study was carried out to identify under what conditions certain terms might become negligible, in particular the new terms based on D and u_r. At large distances from the wall, any term which includes D is known to become negligible. Thus for this analysis, the bubble was considered to be near a rigid wall so that the new terms dependent upon D could be investigated. The values used for this analysis were chosen because they covered the relevant range used in medical imaging, these were as follows:

$R_0=1\mu m$	$\ddot{x}=10^6 ms^{-2}$	$D=5\mu m$	$u_r=10^{-2}\ ms^{-1}$
$\dot{R}=0.1ms^{-1}$	$p_0=100\ kPa$	$\mu_l=10^{-3}\ Nsm^{-2}$	$\dot{u}_r=10^6\ ms^{-2}$
$\ddot{R}=10^6\ ms^{-2}$	$p_A=100\ kPa$	$c_s=10^3 ms^{-1}$	$\frac{du_r}{dx}=10^2\ m^2s^{-1}$
$x=10^{-6}\ m$	$\rho l=1000kgm\text{-}3$	$\omega=1MHz$	$k_s=10^{-8}\ kg/s$
$\dot{x}=0.01\ ms^{-1}$	$\sigma=10^{-2}\ Nm^{-1}$	$k=10^3 m^{-1}$	$u_l=10^{-1}\ ms^{-1}$

It is obvious that the magnitudes of the R and x components of the real and imaginary bubble will be the same; consequently the equations can be rewritten with bubble 1 components equalling those of bubble 2. Accordingly the radial and translational motion can be rewritten, as shown below, where the terms have been labelled:

$$\ddot{R} = \underbrace{-\frac{3}{2}\frac{\dot{R}^2}{R}}_{\{\ddot{R}\}=-\{R_A\}} + \underbrace{\frac{1}{\rho_L R}\left(\left(p_0+\frac{2\sigma_0}{R_0}\right)\left(\frac{R_0}{R}\right)^{3\gamma} - \frac{2\sigma(\Gamma)}{R} - p_0 - p_{ac} - \frac{4\dot{R}\mu_L}{R} - \frac{4k_s(\Gamma)\dot{R}}{R^2}\right)}_{\{R_B\}} + \underbrace{\frac{u_r^2}{4R}}_{+\{R_C\}}$$

$$\underbrace{-\frac{1}{D}\left(2\dot{R}^2+R\ddot{R}\right)}_{-\{R_D\}}+\underbrace{\frac{R}{2D^2}\left(\dot{u}_rR+6u_r\dot{R}+2\dot{D}\dot{R}\right)}_{\{R_E\}}-\underbrace{\frac{u_rR^2}{D^3}\left(\frac{3}{2}u_r+\dot{D}\right)}_{\{R_F\}}$$

With the magnitudes below having the corresponding positions to the terms in the equation:

$$10^8=-10^5+10^3(10^5-10^4-10^5-10^5-10^{-2}-10^2)+10^3-10^6(10^{-2}+1)$$
$$+10^5(10^{-1}+10^{-3}+10^{-3})-10^4(10^{-1}+10^{-1})$$

$$10^8=-10^5+(10^8-10^7-10^8-10^8-10^1-10^5)+10^3-(10^4+10^6)$$
$$+(10^4+10^2+10^2)-(10^3+10^3)$$

$$10^8=-10^5+(10^8)+10^3-(10^6)+(10^4)-(10^3)$$

$$\ddot{x}=\underbrace{+\frac{1}{c_s\rho_L}(p_a\omega+kp_a\dot{x})}_{\{T_A\}}+\underbrace{u_r\frac{du_r}{dx}}_{\{T_B\}}+\underbrace{\frac{2}{\rho_l}\frac{dp_{ac}}{dx}}_{\{T_C\}}-\underbrace{\frac{3u_r\dot{R}}{R}}_{\{T_D\}}-\underbrace{\frac{9\mu_Lu_r}{\rho_lR^2}}_{\{T_E\}}$$

$$\ddot{x}=\{T_A\}+\{T_B\}+\{T_C\}-\{T_D\}-\{T_E\}$$

$$+\underbrace{\frac{3R}{D^2}\left(R^2\dot{R}\frac{du_r}{dx}-5\dot{R}^2-R\ddot{R}\right)}_{\{T_F\}}+\underbrace{\frac{3R^2}{D^3}\left(\dot{u}_rR-u_rR\frac{du_r}{dx}+6u_r\dot{R}+2\dot{D}\dot{R}\right)}_{\{T_G\}}$$

$$\underbrace{-\frac{9u_rR^3\dot{D}}{D^4}}_{-\{T_H\}}$$

With the magnitudes again in the same position as in the equation:

$$10^6 = 10^{-6}(10^{11} + 10^6) + 10 - 10^5 - 10^4 - 10^4 + 10^6(10^{-12} - 10^{-2} - 1) + 10^6(10^{-1} + 10^{-9} + 10^{-8} + 10^{-3}) - 10^3$$

$$10^6 = (10^5 + 1) + 10 - 10^6 - 10^5 - 10^5 + (10^{-6} - 10^4 - 10^5) + (10^5 + 10^{-3} + 10^{-2} + 10^3) - 10^3$$

$$10^6 = (10^5) + 10 - 10^6 - 10^5 - 10^5 + (10^5) + (10^5) - 10^3$$

From the above analysis it can be seen that term T_B in the translational equation is 5 orders of magnitude smaller than $\ddot{x}$, suggesting that it can be ignored, as it has no dependence on the driving pressure or frequency. Term T_H, the $\frac{1}{D^4}$ term, is considerably smaller in comparison to other terms (ignoring T_B) and is 3 orders of magnitude smaller than $\ddot{x}$. This indicates that it also has little effect on the bubble dynamics, as this analysis was carried out near the rigid boundary where it is expected to have its largest effect. This term is also expected to change proportionally with respect to T_E, T_F, T_G and therefore is expected to remain negligible. In the radial equation, terms R_C, the slip velocity and R_F, $\frac{1}{D^3}$, are both 3 orders of magnitude smaller than $\ddot{R}$, thus these terms too have only a very small effect on the bubble dynamics. However in the translational equation T_G, the $\frac{1}{D^3}$ term, is only one order of magnitude smaller than $\ddot{x}$, and therefore indicates that R_F should be included to be consistent with the expansion of D used in both equations. The term R_C should also be investigated further as other studies have indicated that it increases in influence with increasing driving pressure [6].

It was therefore necessary to continue this analysis for different conditions to further investigate the constitutive terms to determine whether or not they are negligible under

different conditions; specifically different initial resting radius of the bubble, R_0, different acoustic exposures (driving pressure, p_A, driving frequency, f) and/or environmental factors (initial distance from the wall, D). This analysis was carried out by calculating the maximum magnitude of each term when varying one of the parameters to two different values, which were chosen to cover the range usually used in medical imaging.

4.2.2 Change in Driving Pressure

The relative influence of the driving pressure was increased and decreased to see how this would affect the terms. It is seen in Figure 4.2 that decreasing the pressure decreased the effect of all the translational terms except T_F which had no effect and T_B and T_H having the smallest effect overall. For the radial terms it was found that changes in pressure affect R_C the most and indicated that at higher pressures this term does become more influential and will start to affect the dynamics of the bubble. Hence it should be included in the model. R_F however was observed to be relatively insignificant at all driving pressures.

(a)

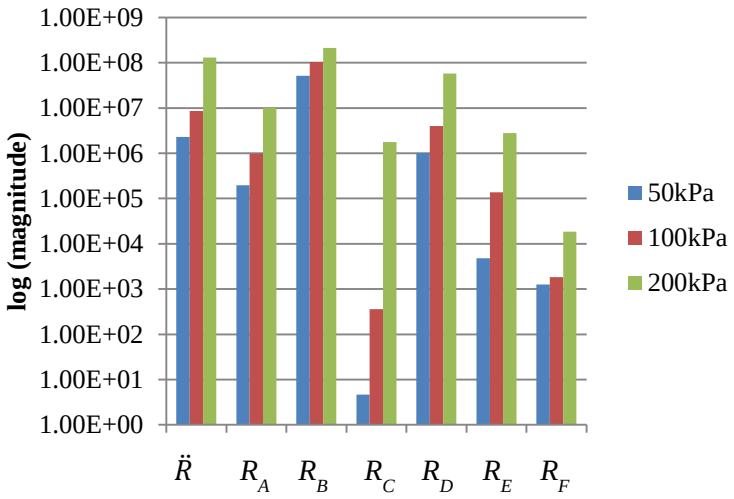

(b)

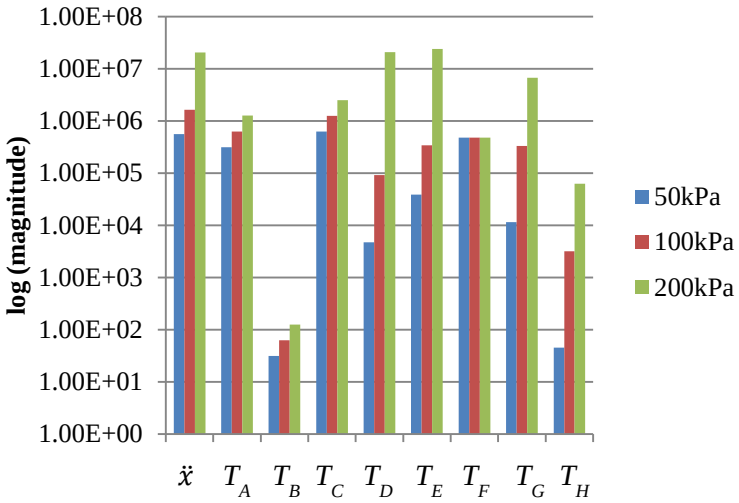

Figure 4.2 (a) shows the magnitudes of the radial terms and (b) shows the magnitudes of the translational terms for varying driving pressures, P_A

4.2.3 Change in Frequency

The frequency was varied to observe how it would affect the relative influence of the terms. It was discovered this had little effect on T_B and T_H, though T_E and T_G increase in dominance and T_F was again insensitive to changes. In the radial equation it was found that R_C does become more influential at the highest frequency, 5MHz. R_D was also found to be more sensitive to changes in frequency than the other terms.

(a)

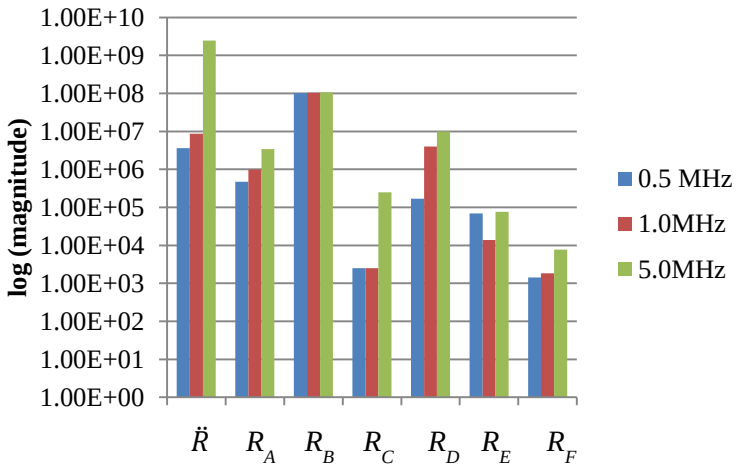

(b)

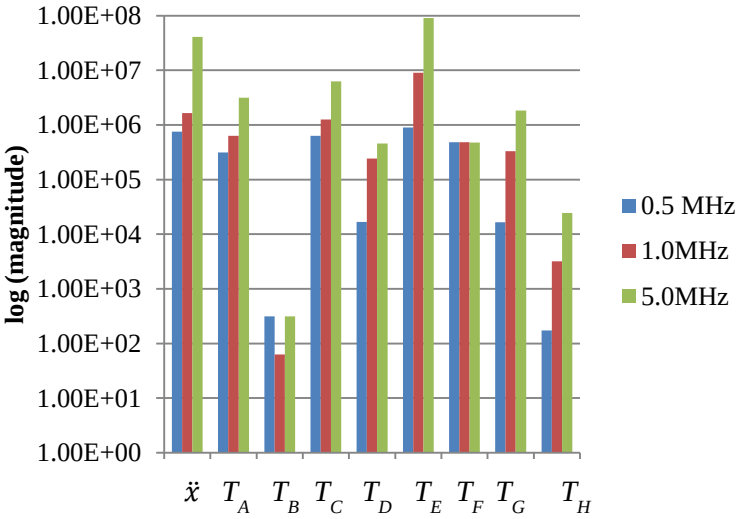

Figure 4.3 (a) shows the magnitudes of the radial terms and (b) shows the magnitudes of the translational terms for variable driving frequency, f

4.2.4 Change in distance from the wall

The initial distance from the wall was increased, (in terms of the initial resting radius, R_0, which in this case is 1μm), to see how this would affect the relative influence of the terms. As expected, any term inversely dependent on D, (R_D, R_E, R_F, T_F, T_G, T_H), decreased in magnitude as the distance from the wall increased (see Figure 4.4). The change in D had no effect on any of the other terms, as expected.

(a)

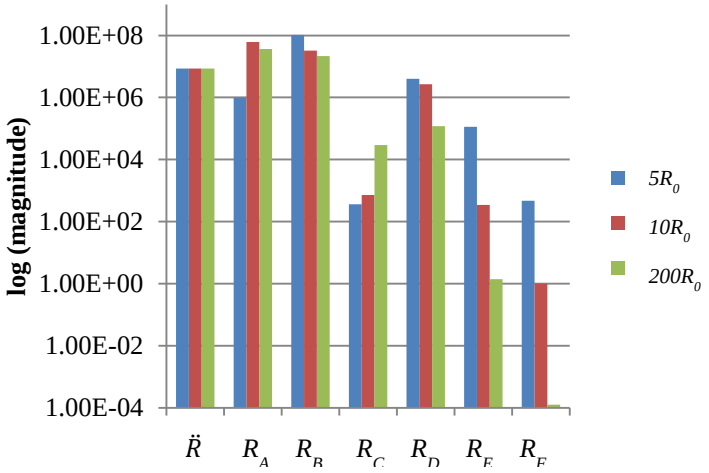

(b)

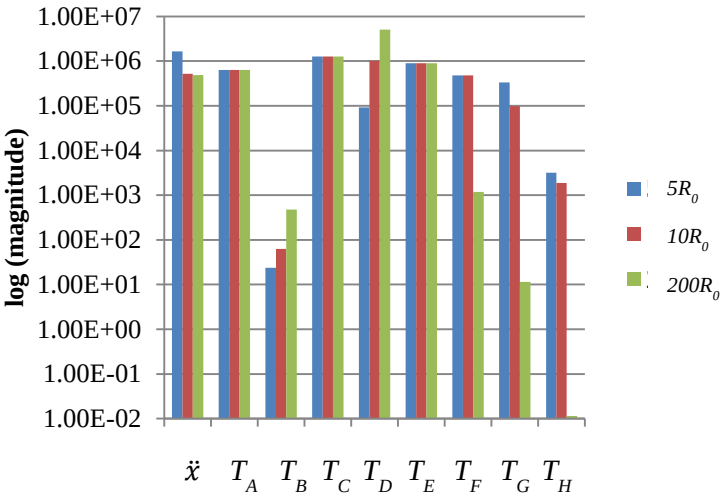

Figure 4.4 (a) shows the magnitudes of the radial terms and (b) shows the magnitudes of the translational terms for variable initial distance from the wall, D

4.2.5 Change in Resting Radius

The initial resting radius was increased, and driven at their natural frequency ω_0, to observe how this influenced the terms in the model; it was found from Figure 4.5 that the translational and radial motion terms dependent on D had similar effects except T_F which is most likely due to its dependence on R. T_A and T_C were are insensitive to changes in resting radius, when they are driven at their natural frequency ω_0, and terms T_B, T_D, T_E in the

translational and R_B, R_C in the radial all change magnitude at a similar same rate in their respective equation.

(a)

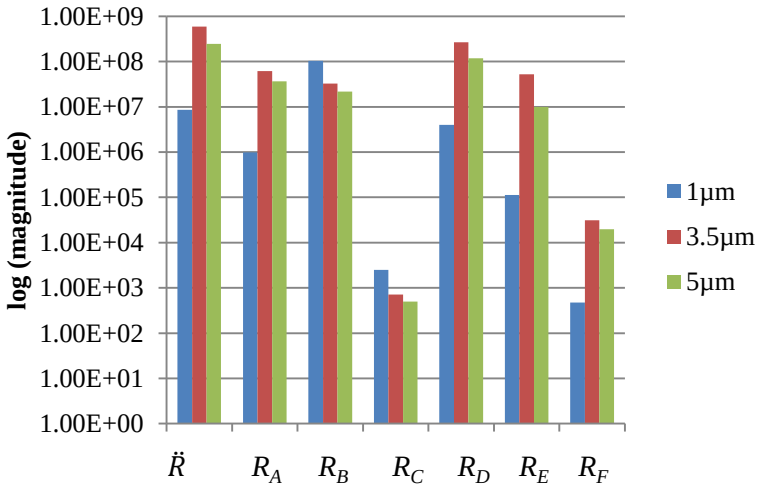

(b)

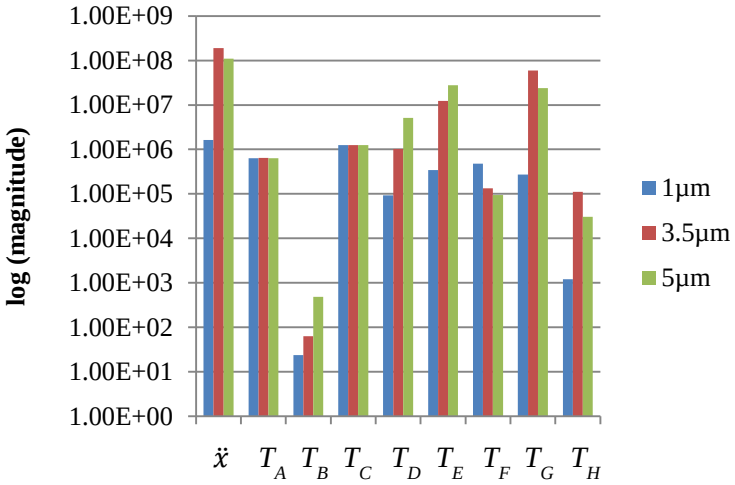

Figure 4.5 (a) shows the magnitudes of the radial terms and (b) shows the magnitudes of the translational terms for variable initial resting radius, R_0

4.2.6 Final form of Model

In conclusion, T_B (a coupling term) and T_H ($\frac{1}{D^4}\ term$) were assumed to be negligible for all the different parameter changes above and therefore can be removed from the model. Giving the final equations:

$$R_i\ddot{R}_i + \frac{3}{2}\dot{R}_i^2 = \frac{1}{\rho_L}\left(\left(p_0 + \frac{2\sigma_0}{R_{0i}}\right)\left(\frac{R_{0i}}{R_i}\right)^{3\gamma} - \frac{2\sigma(\Gamma)}{R_i} - p_0 - p_{ac}\right.$$
$$\left. - \frac{4\dot{R}_i\mu_L}{R_i} - \frac{4k_s(\Gamma)\dot{R}_i}{R_i^2}\right) + \frac{u_{ri}^2}{4} - \frac{R_j}{D}\left(2\dot{R}_j^2 + R_j\ddot{R}_j\right)$$
$$\pm\frac{R_j^2}{2D^2}\left(\dot{u}_{rj}R_{\boldsymbol{j}} + 3u_{ri}\dot{R}_{\boldsymbol{j}} + 3u_{rj}\dot{R}_j + 2\dot{D}\dot{R}_j\right)$$
$$-\frac{u_{rj}R_j^3}{D^3}\left(\frac{3}{2}u_{ri} + \dot{D}\right) \tag{4.10}$$

$$\dot{u}_{ri} = -\frac{3u_{ri}\dot{R}_i}{R_i} + \frac{2}{\rho_l}\frac{dp_{ac}}{dx_i}$$
$$\pm\frac{3R_2}{D^2}\left(R_j^2\dot{R}_j\frac{du_{ri}}{dx_i} - \frac{3R_j\dot{R}_i\dot{R}_j}{R_{\boldsymbol{i}}} - 2\dot{R}_j^2 - R_j\ddot{R}_j\right)$$
$$+\frac{3R_j^2}{D^3}\left(\dot{u}_{rj}R_{\boldsymbol{j}} - u_{rj}R_j\frac{du_{ri}}{dx_{\boldsymbol{i}}} + 3u_{rj}\dot{R}_{\boldsymbol{j}} + \frac{3u_{rj}R_{\boldsymbol{j}}\dot{R}_i}{R_i}\right.$$
$$\left. + 2\dot{D}\dot{R}_j\right) - \frac{9\mu_L u_{ri}}{\rho_l R_i^2} \tag{4.11}$$

Where *i*=1, *j*=2, or *i*=2 ,*j*=1 and the +/- is used for the real or imaginary bubble. The sensitivity of the model will be analysed later in section 4.4, to observe more fully the effects of changes in the environment and the effects this has on the translational & radial motion and the lipid shedding. First, however, it is important to determine whether or not the microbubble response is described by a unique set of material parameters; and hence whether these parameters can be determined through via fitting the model to experimental data.

4.3 Uniqueness of the Relationship Between Shell Parameters and Microbubble Dynamics

Currently no method exists that can directly measure the shell parameters of a microbubble. Instead the shell parameters that are quoted in many papers, [7-10], have been found via fitting experimental data to theoretical models. However, the implicit assumption for this to be a valid method for indirectly measuring the shell parameters is that only one set of them exist for each bubble. This is an important point as it is the basis of any microbubble characterisation. To the best of the author's knowledge, however this has never been proven theoretically. This is the aim of the following section.

To begin the proof it is first assumed, for simplicity, that the microbubble is far away from a wall and the shell parameters have no time dependence, giving the radial and translational equations as:

$$\rho_L\left(R\ddot{R}-\frac{3}{2}\dot{R}^2\right) = \left(p_0+\frac{2\sigma_0}{R_0}\right)\left(\frac{R_0}{R}\right)^{3\gamma}-\frac{2\sigma}{R}-p_0-p_{ac}+\frac{\rho_L u_r^2}{4R} - \frac{4\mu_L\dot{R}}{R}-\frac{4\kappa_s\dot{R}}{R^2} \tag{4.12}$$

$$\dot{u}_r=-\frac{3\dot{R}u_r}{R}-\frac{2}{\rho_L}\frac{dp_{ac}(x,t)}{dx}-\frac{9\mu_L u_r}{\rho_L R^2}+u_r\frac{du_r}{dx} \tag{4.13}$$

Then assuming for instance that the variation in radius *R(t)* of an encapsulated bubble driven by a known external ultrasound pressure field $p_{ac}(t)$ can be accurately measured during an experiment. If everything about the bubble and the surrounding medium is known aside from the properties of the shell, then, the surface tension σ and the shell viscosity κ_s, can be found by fitting the theoretical and experimental *R(t)* profiles. However, the question remains over whether such parameter values are unique for a given bubble. To answer the uniqueness question, equation (4.12) is written in the following way

$$\rho_L\left(R\ddot{R}+\frac{3}{2}\dot{R}^2\right)+\left(-\left(p_0+\frac{2\sigma_0}{R_0}\right)\left(\frac{R_0}{R}\right)^{3\gamma}+p_0+p_{ac}\right)+\frac{4\dot{R}}{R}\mu_L \qquad (4.14)$$

$$-\frac{\rho_L u_r^2}{4}=-\frac{2\sigma}{R}-\frac{4\kappa_s\dot{R}}{R^2}$$

Where only terms containing the unknown shell parameters are retained on the right-hand side. This leaves just two unknowns, σ and κ_s. For this proof it shall be assumed that these parameter values are constant over an oscillation and their uniqueness will be proved by contradiction. Hence, it is initially assumed that σ and κ_s are not unique and thus there must exist at least two sets of values σ_1, κ_{s1} and σ_2, κ_{s2} that, when substituted into (4.14), identically replicate the experimental measurement of *R(t)*. Redefining the left hand side of equation (4.14) to be equal to a function $F\left(\ddot{R},\dot{R},R\right)$, gives:

$$\begin{aligned}F\left(\ddot{R},\dot{R},R\right)&=-\frac{2}{R}\sigma_1-\frac{4\dot{R}}{R^2}\,k_{s1}\\F\left(\ddot{R},\dot{R},R\right)&=-\frac{2}{R}\sigma_2-\frac{4\dot{R}}{R^2}\,k_{s2}\end{aligned} \qquad (4.15)$$

Eliminating $F\left(\ddot{R},\dot{R},R\right)$ from these equations and rearranging then yields the ordinary first-order differential equation for *R(t)*,

$$\dot{R}(k_{s1}-k_{s2})+\frac{R(\sigma_1-\sigma_2)}{2}=0 \qquad (4.16)$$

Rearranging the above and letting $\frac{(\sigma_1-\sigma_2)}{(k_{s1}-k_{s2})}=\beta$ and solving subsequently reveals the general solution to be

$$R(t)=\frac{C}{\beta}e^{-\beta t} \qquad (4.17)$$

Where *C* is an unknown constant, which can be set by the initial condition. Therefore for Equation (4.16) to equal zero either *R(t)* has to have an exponential decay to

the value R_0, which from experiments is known not to be the case, or that $\sigma_1 = \sigma_2$and $k_{s1} = k_{s2}$, assuming that R and $\dot{R}$ are non-zero.

As a consequence, any data-fitted parameter values must be unique. This proof also holds true for both Marmottant et al.'s [7] and Stride's [11] models (see below) or in fact any model that has two time independent shell parameters.

Following similar logic it can also be proven that if values of parameters η_{so} and $K\Gamma_0$ are fitted to experimental data of $R(t)$ in equation (2.3) with power-law exponent y=0 and surface viscosity exponent z=0, then those fitted values are unique. In this case the governing equation is given by:

$$\rho_L\left(R\ddot{R}+\frac{3}{2}\dot{R}^2\right)+p_0-p_{ac}-p_G(R)+\frac{4\dot{R}}{R}\mu_L=-\frac{4\dot{R}}{R^3}\eta_{so}-\mathrm{K\Gamma_0}\frac{3}{\mathrm{R^2}}\left(1-\frac{\mathrm{R_0^2}}{\mathrm{R^2}}\right) \quad (4.5)$$

Hence, as before by taking $\alpha_1=\eta_{so}$, $\beta_1=K\Gamma_0$ and $\alpha_2=\eta_{so}$, $\beta_2=K\Gamma_0$ as two sets of parameter values that accurately fit the experimental data, these two sets can be substituted into (4.5) and, on eliminating the common left-hand side of the equation in each case, yields

$$R(\alpha_1-\alpha_2)\frac{dR}{dt}+\frac{3(\beta_1-\beta_2)}{4}R^2=\frac{3(\beta_1-\beta_2)}{4}\mathrm{R_0^2}$$

for $\Omega=\frac{3(\beta_1-\beta_2)}{4(\alpha_1-\alpha_2)}$. The general solution to this differential equation is then $R(t)=\sqrt{(R_0^2+2Ce^{-2\Omega t})}$ and hence unless R^2(t) exponentially decays in this manner to R_0^2 in the experimental data then the fitted parameter values must be unique.

Thus it can be proven via contradiction that for time independent shell parameters a unique set exists. These proofs would also remain true for a bubble by a rigid wall, as all the extra terms in the radial and translational motion are again known and both the real and imaginary bubble give identical responses (they just travel in opposite directions), therefore the problem simplifies to the same as shown above. Furthermore, for a model with time

dependent shell parameters, for example those seen in Equation (4.1) , it can be argued that both parameters are unique, even if they are changing with respect to time, as at any single point in time, only one set will exist.

4.4 Sensitivity Analysis

The previous section demonstrates that microbubbles have the theoretical potential to be used as sensors due to them having a dynamic response that can be related to a unique set of shell properties. Therefore it is important to assess how much of a change in any of the input parameters in the model is required to cause significant observable (measurable) alterations in the dynamic response. This will indicate which properties need to be measured precisely to make sure that the shell parameters determined are as accurate as they can. It will also indicate how sensitive the model is to changes in the shell properties and/or environment and hence the effectiveness of bubbles as sensors of different parameters.

4.4.1 Methodology

The purpose of the sensitivity analysis was to investigate the effect of varying the input parameters on:

1. Lipid shedding via observing the equilibrium resting radius, R_{0new} in-between pulses,
2. Distance travelled during the pulse via noting x_{new} at the end of a pulse,
3. The response of the bubble during an oscillation by noting the maximal radius, R_{max}, during a pulse.

This investigation was carried out by running the model as stated in section 4.1 but using the radial and translational equations finalised in section 4.2.6, Equations (4.10)-(4.11) which also use Equations (4.6)-(4.8), varying the initial radius R_0, driving frequency, f, the driving pressures of the acoustic pulse, p_A, the starting distance from the wall, d, the equilibrium shell viscosity, κ_{s0}, the liquid viscosity, μ_l ,the absorption coefficient, k_1 and maximum concentration of the lipid on the shell, Γ^*. These parameters were varied over 3 values which covered the range usually used in medical imaging, shown in Table 4.1.

When a variable was not being varied it was kept at the middle value, except when varying R_0 in which case the natural resonant frequency, ω_0 was used, (see Appendix A for this). This was done to observe the maximum effect that changing the radius would cause, as off resonance the oscillations would be small.

The model was run for 1 and 3 cycle Gaussian pulses for 10 pulses. The values of x, R_0 and R_{max} were recorded after the 1st and the 10th pulse, and a comparison between how they change with respect to changes in different parameters is made. For example does the bubble with the largest oscillation shed the most?

Variable	Unit	Input value 1, IV_1	Input value 2, IV_2	Input value 3, IV_3
R_0	μm	1.0	2.2	4.0
f	MHz	1	2	5
p_A	kPa	10	100	250
d	R_0	5	10	50
k_1	$m^3kg^{-1}s^{-1}$	10 000	40 000	400 000
Γ^*	$kg.m^{-2}$	$1x10^{-8}$	$3x10^{-8}$	$1x10^{-7}$
κ_{s0}	$kg.s^{-1}$	$0.5e^{-9}$	$1.5e^{-9}$	$2.5e^{-8}$
μ_L	$Pa.s$	$0.5x10^{-3}$	$1.5x10^{-3}$	$3x10^{-3}$

Table 4.1 Values used in the sensitivity analysis

To easily analyse the responses in a consistent way, the following ratios were calculated.

$$Ratio1 = \frac{\left(\frac{\Delta\, IV_1\ response}{\Delta\, IV_2 response}\right)}{\left(\frac{IV_1}{IV_2}\right)} = \frac{\%\ in\ reponse}{\%\ in\ input\ value}$$

$$Ratio2 = \frac{\left(\frac{\Delta\, IV_2\ response}{\Delta IV_3\ response}\right)}{\left(\frac{IV_2}{IV_3}\right)} = \frac{\%\ in\ reponse}{\%\ in\ input\ value}$$

Where Δ means a change from the starting value and the IV_i is the input value, where *i=1,2or3*, Table 4.1. These ratios make it possible to observe how the change in the response compares to the relative change in that parameter. If the ratio is equal to one then the change in response is proportional to the change seen in the input value, if the ratio < 1 then the response is relatively sensitive to the change in the parameter and if the ratio > 1 then the response is relatively insensitive to the change in parameter.

4.4.2 Effect on "Lipid Shedding"

For this the value of R_0 was compared after the first pulse and after the 10th pulse to see how the parameters changed, as shown in Table 4.2. From this it can be seen that for the first pulse, that R_0, k_1 and p_A have the greatest effect upon lipid, and by the 10th pulse this has settled down into a common order, where R_0 has the greatest effect upon the lipid shedding followed by k_l, then p_A. This is expected, as when k_1 increases it allows more shedding to occur as it is linked to k_2 the desorption coefficient and when increasing p_A and R_0 the radial oscillations that the bubble experiences increases which increases the amount of shedding that occurs, as shown in Figure 4.8 (a)-(b).

The other parameters had little effect on the shedding, though a slight increase in the amount of shedding was observed when the bubble was closer to the wall, this is due to the fact that a bubble close to the wall lowers the maximum amplitude of oscillation, as

observed in experiments[12] and as seen in Figure 4.6 (b), due to the wall affecting the resonance of the bubble. This effect in Figure 4.8 (f) is difficult to see due to the scale and the distance from the wall. However in Figure 4.6 (a) the observed effect of lipid shedding increasing when closer to the wall is clearer. Although, the bubble oscillating close to the wall will also be likely to undergo non-spherical oscillations due to secondary radiation forces, which are likely to affect the rate of shedding, however this effect is not incorporated in the model. The effect of the wall also had a consistent effect over the whole 10 cycles with both ratios for the 1st and last cycle being the same. The frequency seems to have less of an effect at higher frequencies than smaller frequencies. Though this is due to the fact that IV_1 and IV_2 are closer to the resonace frequency of about 1.8MHz than IV_3 which is off resonance as can be seen by the R_{max} graph in Figure 4.8 (c). Changes in the parameters κ_s and μ_L showed that they have very little effect on the rate of shedding.

Variable	ΔR_0 IV_1 x10^2		ΔR_0 IV_2 x10^2		ΔR_0 IV_3 x10^2		Ratio 1		Ratio 2	
	1st pulse	10th pulse	1st pulse	10th pulse	1st pulse	10th pulse	1st pulse	10th pulse	1st pulse	10th pulse
R_0	0.05	0.51	0.38	3.68	1.10	10.20	0.30	0.31	0.63	0.66
f	0.52	5.02	0.35	3.41	0.03	0.29	2.96	2.94	5.45	29.42
P_A	0.04	0.43	0.35	3.41	54.60	43.00	1.24	1.27	0.02	1.97
d	99.60	96.60	99.60	96.60	115.00	114.00	2.00	2.00	5.01	5.01
k_1	0.01	0.09	0.35	3.41	2.98	23.20	1.02	1.06	1.18	1.47
κ_{s0}	0.54	5.14	0.35	3.41	8.51	8.18	4.56	4.53	2.21	2.19
μ_L	0.38	3.66	0.35	3.41	12.10	11.60	3.23	3.22	2.21	2.20

Table 4.2 Showing the response change in R_0 for a 3 Gaussian pulse.

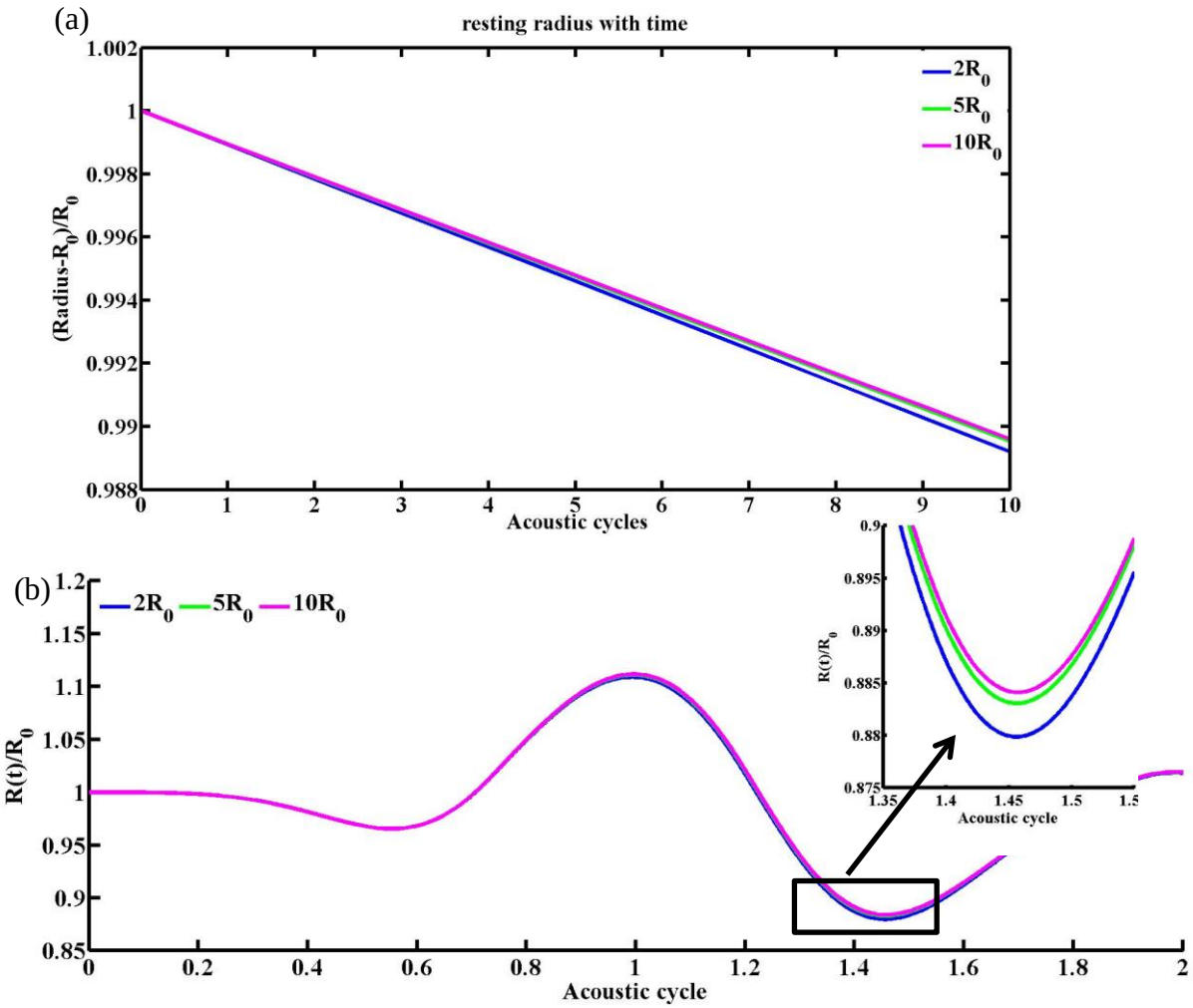

Figure 4.6 showing the dynamic effect from varying the bubbles distance from the wall for 1 cycle Gaussian pulse (a) the equilibrium resting radius over 10 cycles and (b)the R-t curve for the first pulse

4.4.3 Effect on the Bubble Oscillation

Again the greatest effect on the bubble oscillation was caused by changes in R_0 and p_A. This is expected for R_0 as the bubbles are driven at their resonance frequency and so it is expected that as the bubble sizes increase the amplitude of their oscillation would also increase, see Figure 4.8 (a). Again, as p_A increases the bubble is driven harder and receives more energy and so will expand and contract more, see Figure 4.8 (b). The next parameter that caused the largest effect on the bubble oscillations is f , when near to the resonance the

maximum amplitude of oscillation increases, compared to when the *f* is off resonance. The expected change upon varying the viscosities was that when they decreased the bubble would oscillate more and when they increased they would dampen the oscillation, which is seen in Figure 4.8 (e). However the results indicate that the bubble oscillations are more sensitive to an increase in both κ_s and μ_L than a decrease. Again the closer to the wall the lower the amplitude of bubble oscillation and the larger the effect it has on the model predictions. It can be observed that k_1 has hardly any effect on the oscillation of the bubble which is to be expected as it only influences how likely the lipid is likely to shed via its ratio with k_2, the desorption coefficient.

Variable	$\Delta R_0\ IV_1$		$\Delta R_0\ IV_2$		$\Delta R_0\ IV_3$		Ratio 1		Ratio 2	
	1st pulse	10th pulse	1st pulse	10th pulse	1st pulse	10th pulse	1st pulse	10th pulse	1st pulse	10th pulse
R_0	0.02	0.02	0.16	0.14	0.50	0.40	0.33	0.13	0.57	0.65
f	0.12	0.10	0.78	0.14	0.02	0.02	1.62	1.51	2.79	16.69
p_A	0.01	0.01	0.15	0.14	0.55	0.43	0.91	0.31	0.67	0.81
d	0.15	0.14	0.15	0.14	0.15	0.14	1.99	1.98	4.97	4.98
k_1	0.15	0.15	0.15	0.14	0.14	0.08	40.20	42.25	10.44	18.34
κ_{s0}	0.01	0.05	0.00	0.03	0.00	0.03	6.38	10.69	2.86	2.83
μ_L	0.17	0.16	0.15	0.14	0.12	0.12	3.44	3.41	2.41	2.39

Table 4.3 Showing the response change in R_{max} for a 3 Gaussian pulse

4.4.4 The Effect on Translation

The effect on translation alone (ignoring shedding) is seen from the effects of the first pulse, as seen in Table 4.4. Here it is observed that the largest effect was for *D*, when it is close to the wall on the first pulse, which is to be expected. Though it is not an observable effect in the Figure 4.8 (f) taken closer to the wall. The other parameters that affect the translational motion are R_0, p_A and *f*, which is expected. As p_A increases the more

the bubble will translate as the primary Bjerknes force increases, which is the main force which moves the bubble, and this effect is more prevalent at larger values of p_A than smaller values, as seen in Figure 4.8 (b), which is logical given the nature of the term. As R_0 increases the bubble will translate more but it is most sensitive to changes when R_0 is small, as can be seen in Figure 4.8 (a). The change in translation is more sensitive nearer the resonance than off of it Figure 4.8 (c). The translational distance is seen to be affected by changes in μ_L with the lower the liquid viscosity the further the bubble translates. However this effect is less than the other parameters mentioned. The other parameters, mentioned in Table 4.1, cause little change in the distances travelled.

Looking at the results from the last pulse gives a more complex picture as the bubble size is changing over the pulse due to the lipid shedding. This change in size over the pulses will affect the direction and the amount the bubble translates, this is most starkly seen in Figure 4.8(a) for the translation of R_0= 4.0μm, which changes translational direction. This direction change shows the effect of the resonate frequency of the bubble changing over the course of the pulses. However from Figure 4.8(d) it can also be seen that the larger the bubble remains the more it translates. With these changes coupled to other parameter changes it becomes difficult to assess which effect is having the largest effect on the translation, whether it is the actual parameter changing or the effect the parameter change has on the lipid shedding.

Variable	$\Delta R_0\ IV_1$		$\Delta R_0\ IV_2$		$\Delta R_0\ IV_3$		Ratio 1		Ratio 2	
	1st pulse	10th pulse	1st pulse	10th pulse	1st pulse	10th pulse	1st pulse	10th pulse	1st pulse	10th pulse
R_0	-0.10	-1.02	0.29	3.16	-1.88	3.43	0.79	0.71	0.28	1.67
f	0.22	1.82	-0.15	-0.47	-1.15	-6.80	3.03	0.51	0.05	36.35
p_A	-0.02	-0.22	-0.15	-0.47	-12.10	-51.20	1.48	4.59	0.03	0.02
d	-0.15	-0.46	-0.15	-0.47	0.11	0.38	0.21	1.97	6.48	6.22
k_1	-0.17	-1.60	-0.15	-0.47	-0.07	1.36	44.78	137.19	20.18	3.44
κ_{s0}	-1.12	-4.47	-0.15	-0.47	-0.12	-0.84	22.75	28.67	2.00	0.92
μ_L	-0.44	-2.04	-0.15	-0.47	-0.06	-0.23	3.44	3.41	2.41	2.39

Table 4.4 Showing the response change in translation, x, for a 3 Gaussian pulse

4.4.1 Effect of Pulse Length

As expected, decreasing the pulse length reduced the amount the bubble shed and translated but did not affect the maximum radius initially reached. This is clearly demonstrated when comparing Figure 4.8 (c) with Figure 4.7, which is for varying driving frequency.

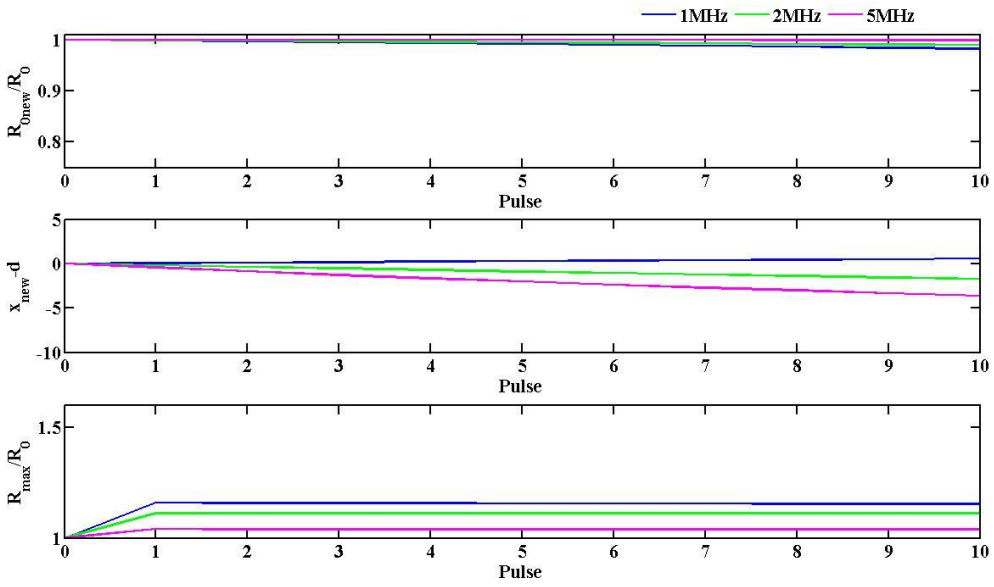

Figure 4.7 This graph is the sensitivity analysis results, for a 1 Gaussian cycle pulse shown over 10 consecutive pulses for varying driving frequency. The results show R_{0new}, x_{new} and R_{max} in dimensionless units.

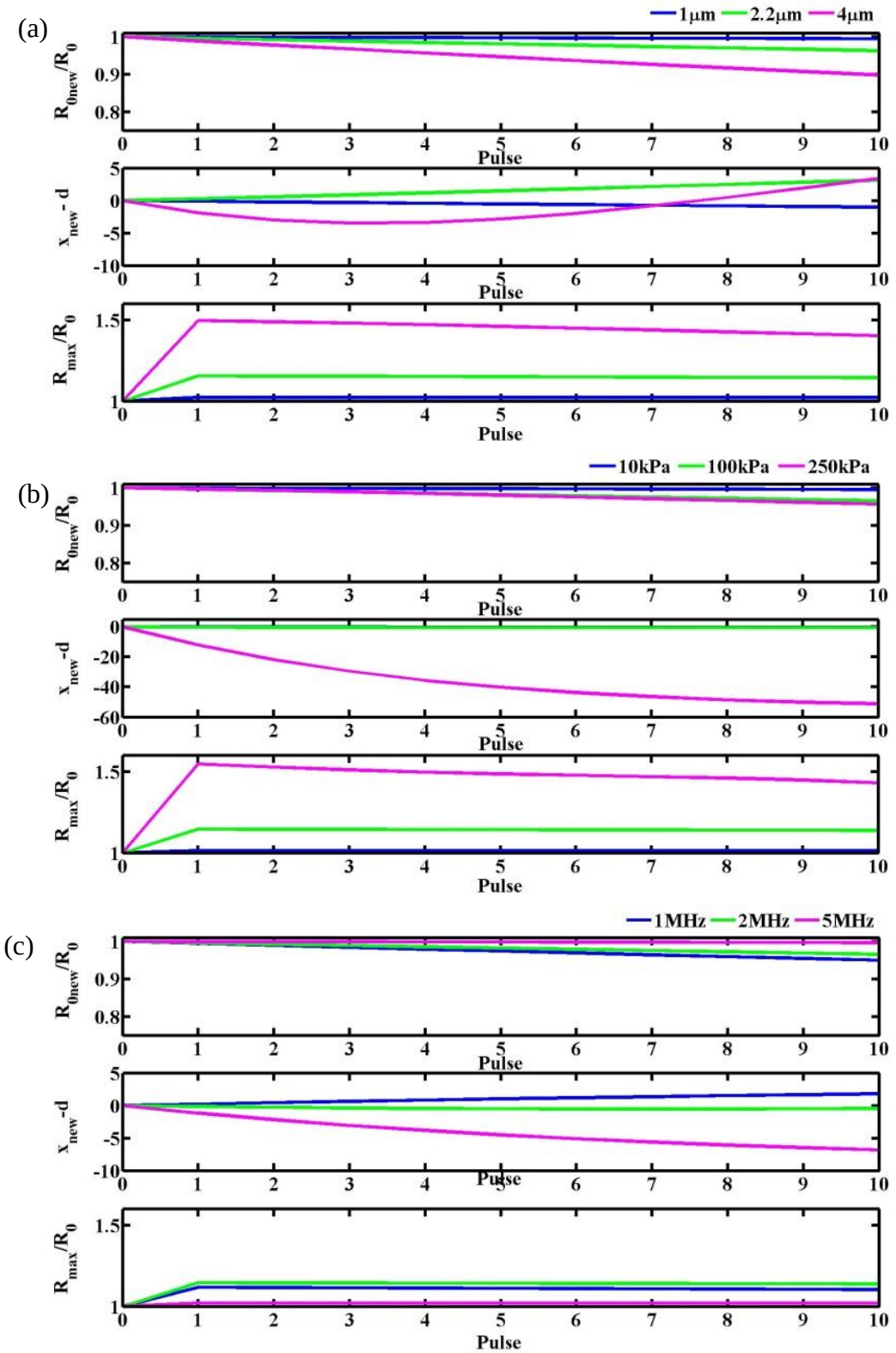

Figure 4.8 The graphs here are a selection of the sensitivity analysis results, for a 3 Gaussian cycle pulse shown over 10 consecutive pulses. The results show R_{0new}, x_{new} and R_{max} in dimensionless units. The results are shown for varying (a) R_0 , (b) p_A ,(c) f ,(d) k_1 ,(e) κ_{s0}, (f) d

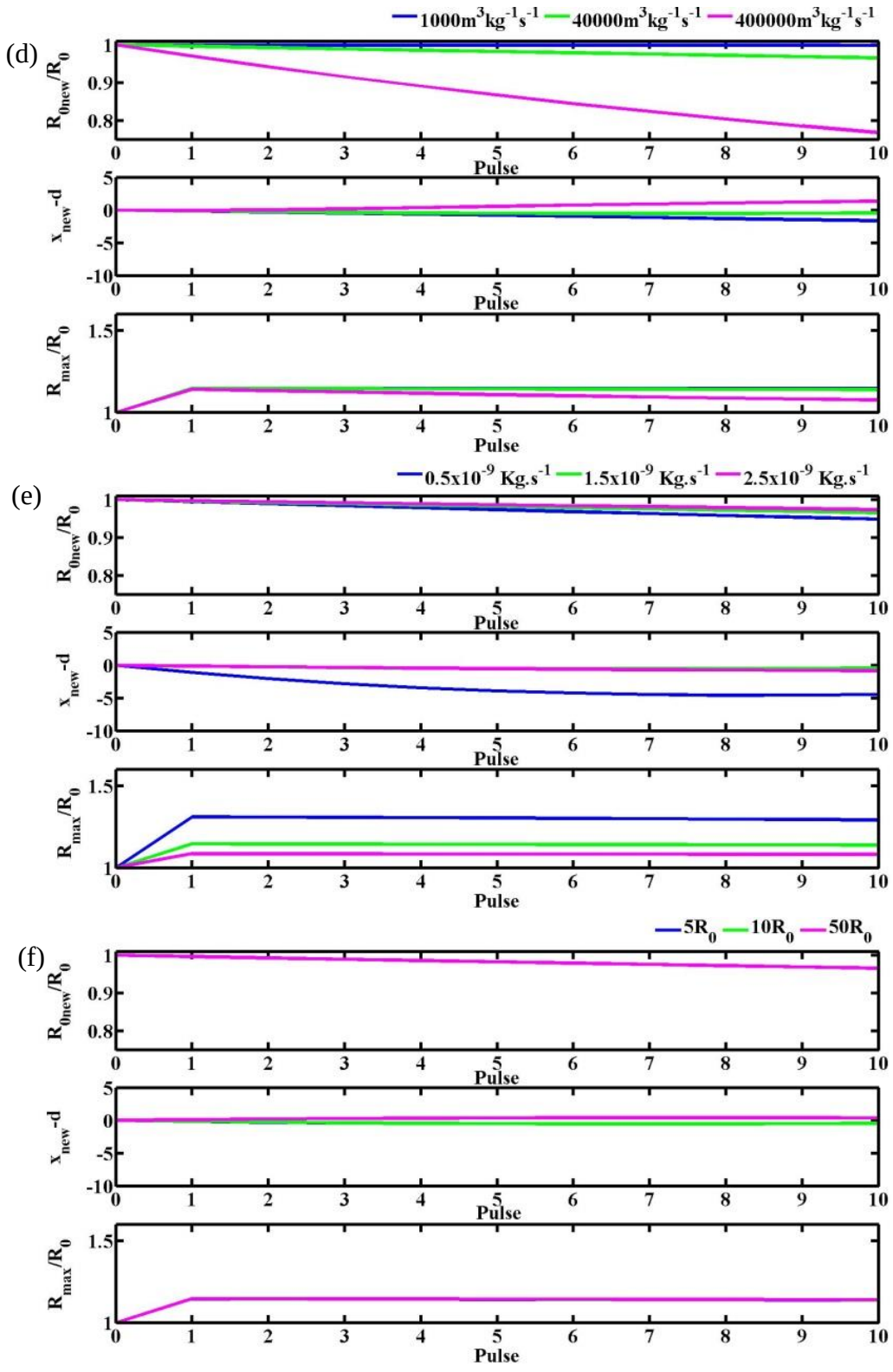

Figure 4.8 The graphs here are a selection of the sensitivity analysis results, for a 3 Gaussian cycle pulse shown over 10 consecutive pulses. The results show R_{0new}, x_{new} and R_{max} in dimensionless units. The results are shown for varying (a) R_0 , (b) p_A ,(c) f ,(d) k_1 ,(e) $\kappa_{s0,}$ (f) d

4.4.2 Conclusion

In conclusion, changes in R_0 and p_A have the most effect on the bubble's dynamic response and hence are the parameters that need to be measured the most accurately. D needs to be measured very accurately if the bubble is near to the wall otherwise there is little effect on the dynamic responses from about $10R_0$. f has more of a prominent effect closer to the resonance frequency and therefore near this frequency measurements should be as accurate as possible. k_1 has a large effect on the shedding of the bubble so needs to be found as accurately as possible if this is not the parameter being measured. Therefore the measurements the effect of errors in of R_0 and p_A will be investigated in the following section.

4.5 Uncertainty in Predicting the Shell Parameters

As this thesis is concerned with using microbubbles as sensors, it is important to know how accurately their behaviour can be measured and in this chapter the emphasis has been on how accurately the unknown shell parameters can be obtained. Therefore the following analysis will give the maximum uncertainty associated with the unknown shell parameters κ_{s0} and k_1 due to experimental errors in the measurement of the input values associated with R_0 and p_A the parameters to which the bubble response was found to be most sensitive in section 4.4.

In experiments the minimum uncertainty in R_0 is roughly ±0.25μm, as the accuracy on the diameter is ±0.5μm when measured by an optical microscope or camera, owing to the resolution of the image and the whether the bubble is in focus or not. The maximum uncertainty on p_A, as measured by a hydrophone is ± 15% [13]. This uncertainty would also occur if the radial response was being measured via the radiated pressure from a transducer, however for simplicity and to gain an indication of the errors on the measurement of the

shell parameters via fitting them to experimental data only the error on the input values shall be considered.

4.5.1 Methodology of Assessing Errors

To assess the errors on fitting the unknown shell parameters, the model was run over 10 cycles for a sinusoidal pulse for the input parameters shown in Table 4.5, with p_A or R_0 run with their associated errors. Then a fitting program was used, running the code for the expected input, R_0=1.1μm and p_A=100kPa and the unknown shell parameters determined. This is done by using purpose written code in MatLab 2012a ® using a program called spec1d which allows two values to be varied simultaneously and run over at least 40 iterations or until the value of best fit has been reached, i.e. when the Chi squared value is minimized. When the 40 iterations have been reached the values from this have been put back in as the initial guess and the run repeated.

Parameter	Value	Units
R_0	*1.1±0.25*	*μm*
p_A	*100±15*	*kPa*
D	*5*	R_0
μ_L	$1x10^{-3}$	*Pa.s*
κ_{s0}	$1.5x10^{-9}$	$Kg.s^{-1}$
k_1	*10000*	$m^3kg^{-1}s^{-1}$
f	*4.1*	*MHz*
γ	*1.4*	
P_0	*100*	*kPa*

Table 4.5 Parameters used to investigate errors made in finding the shell parameters from the errors found in the inputs of R_0 and p_A

4.5.2 Results

It was found that the change in k_1 was quite large, as can be seen in Table 4.6, however this can be better fitted via the equilibrium resting radius in-between pulses and as seen from the sensitivity analysis done in section 4.4, large differences in this value cause little change in the oscillation over a cycle. The equilibrium shell viscosity, $\kappa_{s0,}$ on the other hand varied between 15-25% on both the parameters which is rather large.

Actual value	Fitted κ_{s0}/ $Kg.s^{-1}$	%change in κ_{s0}	Fitted k_1/ $m^3kg^{-1}s^{-1}$	% change in k_1
p_A=115kPa	$1.28x10^{-9}$	15	9000	10
p_A=85kPa	$1.83x10^{-9}$	22	$4.5x10^{4}$	450
R_0=1.35μm	$1.15x10^{-9}$	24	10	99.9
R_0=0.85μm	$2.15x10^{-9}$	14	$1.65x10^{5}$	16.5

Table 4.6 Summarising the results of fitting the unknown shell parameter using p_A=100kPa and R_0=1.1

4.6 Summary

In this chapter a finalised version of the new model has been found, neglecting those terms that were found to be negligible. It was then mathematically proven that this model can be used to find the unknown shell parameters, $\sigma(\Gamma)$ the time dependent surface tension and $\kappa_s(\Gamma)$ the time dependent shell viscosity, and that a unique set can be derived by fitting to experimental data. A sensitivity analysis was then carried out that suggested that R_0 and p_A were the parameters to which the bubble response was most sensitive in terms of their effect on lipid shedding, translation and oscillation during a pulse. It was also found that k_1 was one of the most important parameters involved in shedding which is unsurprising as it is linked to the desorption coefficient and therefore to how likely the lipid is to shed. The experimental errors on the inputs, R_0 and p_A were then assessed to see how they would affect the measurement of the parameters κ_{s0} and k_1. It was discovered that both produced considerable variation in the derived values.

4.7 References

1. O'Brien, J.-P., Ovenden, N., and Stride, E., *Accounting for the stability of microbubbles to multi-pulse excitation using a lipid-shedding model.* The Journal of the Acoustical Society of America, 2011. **130**(4): p. EL180-EL185.
2. Hill, C.R., Bamber, J.C., and ter Haar, G.R., *Physical Principles of Medical ultrasonics*. 2005, Chichester, UK: John Wiley and Sons.
3. Morris, J., et al., *Dynamic Behavior of Lung Surfactant.* Journal of Biomechanical Engineering, 2001. **123**(1): p. 106-113.
4. Jean-Pierre O'Brien, Eleanor Stride and Nicholas Ovenden, et al., *Surfactant shedding and gas diffusion during pulsed ultrasound through a microbubble contrast agent suspension.* The Journal of the Acoustical Society of America, 2013. **134**(2): p. 1416-1427.
5. Batchelor, G.K., *An Introduction to Fluid Dynamics*. 2000: Cambridge University Press.
6. Doinikov, A.A., *Translational motion of a spherical bubble in an acoustic standing wave of high intensity.* Physics of Fluids, 2002. **14**(4): p. 1420-1425.
7. Marmottant, P., et al., *A model for large amplitude oscillations of coated bubbles accounting for buckling and rupture.* Journal of the Acoustical Society of America, 2005. **118**(6): p. 3499-3505.
8. Afanasiev, K.E. and Stukolov, S., *Simulation of problems with free surfaces by a boundary element method*, in *Computational Science and High Performance Computing*, E.S.Y.I.R.M.S.N. Krause, Editor. 2005. p. 307-337.

9. Tu, J., et al., *Estimating the shell parameters of SonoVue[sup [registered sign]] microbubbles using light scattering.* The Journal of the Acoustical Society of America, 2009. **126**(6): p. 2954-2962.

10. Tu, J., et al., *Real-Time Measurements and Modelling on Dynamic Behaviour of SonoVue Bubbles Based on Light Scattering Technology.* Chinese Physics Letters, 2008. **25**(1): p. 172.

11. Stride, E., *The influence of surface adsorption on microbubble dynamics.* Philosophical Transactions of the Royal Society A-Mathematical Physical and Engineering Sciences, 2008. **366**(1873): p. 2103-2115.

12. Garbin, V., et al., *Changes in microbubble dynamics near a boundary revealed by combined optical micromanipulation and high-speed imaging.* Applied Physics Letters, 2007. **90**(11): p. -.

13. Precision Acoustics, *Certificate of calibration hydrophone serial number C1502-092*, National Physics Laboratory.

5 Theoretical and Experimental Observations of Lipid Shedding

A number of recent studies have demonstrated that the properties of the coating of phospholipid-coated bubbles may change significantly, even on the timescale of a single ultrasound pulse [1, 2]. This may have considerable implications for the utility of microbubbles for both diagnostic and therapeutic applications, since the subsequent acoustic response of the bubble may be altered and/or therapeutic molecules attached to the bubble surface may also be released. In Chapters 3 and 4 a model was developed to describe the behaviour of a microbubble under ultrasound excitation that included the time dependent phenomena of variable surface tension, viscosity and "lipid shedding", whereby material is expelled from the bubble surface when it oscillates under ultrasound exposure. The sensitivity of the microbubble response to the model parameters and the influence of shedding were then investigated.

In the work described in this chapter the results from simulations performed with the new model, Equations (4.10)-(4.11), were compared to experimental data[1] to see how well the model describes the dynamic response of the microbubble and in particular, lipid shedding. This was done initially via varying k_1 (the absorption coefficient) to determine whether the composition of the bubble coating affects the probability of shedding and the quantity of material shed for a range of ultrasound exposure conditions. This included the influence of a nearby rigid boundary upon shedding behaviour since the bubbles in the experimental set up were adjacent to a boundary. The experimentally derived radius-time (R-t) curves were then fitted to the simulation results and the fitting error assessed. In

[1] High speed fluorescence microscopy footage of single bubbles undergoing lipid shedding was kindly provided by colleagues at Erasmus University, Rotterdam, The Netherlands 3. Gelderblom, E.C., *Ultra-high-speed fluorescence imaging*, 2012: Enschede. p. 144..

addition, in a previous study [1] a threshold for shedding was hypothesized in terms of a reduction in bubble surface area during compression. The validity of this prediction was also assessed.

5.1 Overview of the Model and the Experimental Limitations in Observing Lipid Shedding

In the model the effects of lipid shedding are seen through the mass of the surfactant lost, which in turn changes the equilibrium size of the bubble as discussed in Chapter 4. Experimentally it is impossible currently to directly quantify the amount of the lipid lost over the course of a pulse. The only way to observe lipid shedding directly is optically, via high speed florescence microscopy, where a fluorescent dye has been attached to the lipid, Figure 5.1. It is assumed that the dye and the lipid stay attached when the bubble oscillates and the shell sheds material. It still remains difficult, however, to determine the amount of lipid that has been lost, due to diffusion in the liquid and the fact that the microscope can only be focused in one (or possibly two) planes in any one experiment. In addition to fitting the R-t curves, this leaves two options for comparing data between theory and experiment: the first is the equilibrium radius, R_0, in between successive pulses and the second is to try and relate the behaviour predicted by the model to the distance over which shed lipid was found to be distributed during the experiments.

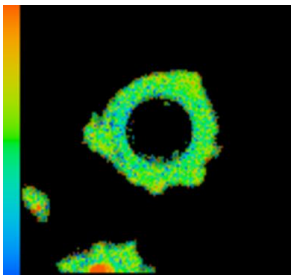

Figure 5.1 Image showing florescent lipid attached to a bubble (image kindly provided by Dr N A Honsy).

5.2 Model Comparison to Lipid Transportation Distance

The first method of comparing the equilibrium radius was also adopted by O'Brien *et al.* [1][4], who used experimental data published by Borden *et al*. [2]. This demonstrated that a reasonable estimate for the change in equilibrium radius due to lipid shedding could be obtained theoretically. This method is applied here and in addition the experimentally measured transportation distance of the lipid, d_e, see Figure 5.2, over the course of a pulse which is compared to the theoretically predicted maximum amplitude of oscillation, ΔR, Figure 5.3. These two parameters should be related as the amplitude of oscillation recorded corresponds to a subsequent compression in which the bubble sheds the lipid. The maximum amplitude of oscillation is linked to the acceleration of the bubble wall and thus affects how far the lipid is transported. There are other factors affecting the bubble oscillations in these experiments as it is performed with the bubble close to the cover slip. When a bubble is close to a boundary it affects the characteristic frequency of the microbubble oscillation [5] and can cause effects such as micro streaming. Micro streaming occurs for microbubbles undergoing steady oscillations causing acoustic streaming to occur around the bubble, including eddying flows that cause shear stresses on the nearby surfaces and helps circulate the shed lipid and also induces shape oscillations to occur. This is thought to help in the mechanism of lipid shedding where the lipid is often observed to be catapulted away from the bubble as a single mass.

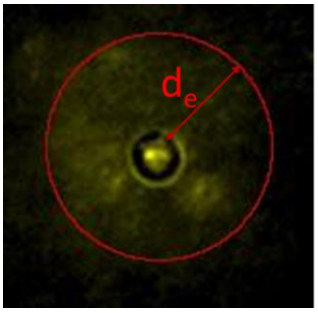

Figure 5.2 Image showing the transportation distance of the lipid

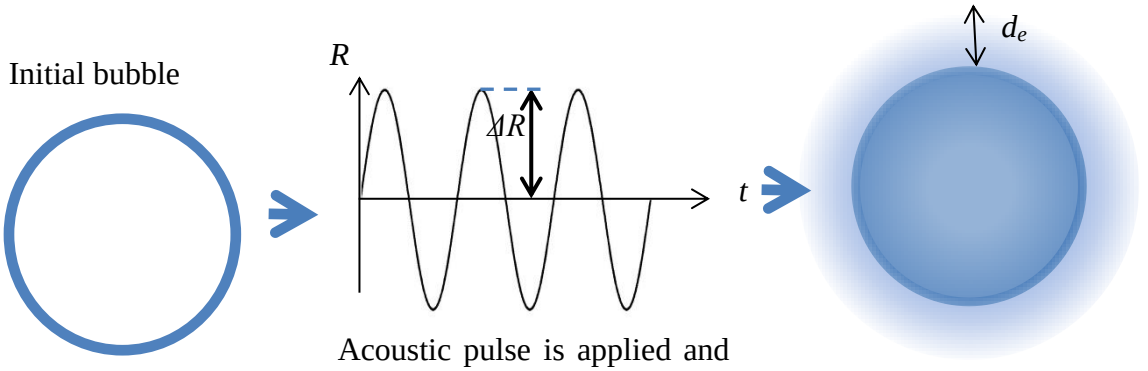

Figure 5.3: Schematic indicating the measurements taken during the experiments.

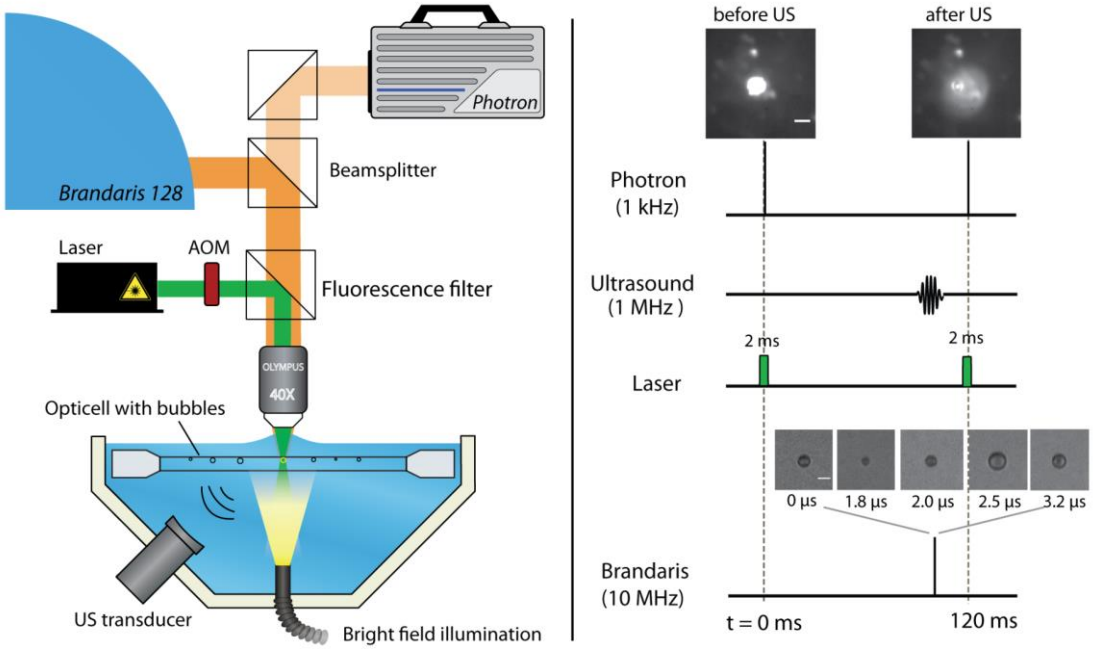

Figure 5.4 Schematic of the experimental set up and method. (Image kindly provided by Ying Luan.)

The experiments were carried out by selecting a microbubble that had come to rest at the microscope cover slip, and hence all oscillations occurred by a rigid boundary where no translational motion was observed or could occur. An overview of the experimental set-up and method is shown in Figure 5.4. This means that the Equations (4.10)-(4.11)

presented in Chapter 4, need to be altered as the translational equations and any term in the radial equation that included the relative velocity of the bubble, u_r, or $\dot{D}$ would become negligible as the bubble is considered to be stationary. It should be noted that the bubble being this close to a rigid boundary violates some of the assumptions in the model, as already mentioned it causes micro streaming to occur, inducing shape oscillations, meaning that the bubble will not remain spherical during the oscillation. However, the approach presented here has been used previously and is proven to give a reasonable estimate of the bubble dynamics [6, 7]. This led to the equations describing the radial motion being modified as follows:

$$R_1\ddot{R}_1 + \frac{3}{2}\dot{R}_1^2 = \frac{1}{\rho_L}\left(\left(p_0 + \frac{2\sigma_0}{R_{01}}\right)\left(\frac{R_{01}}{R_1}\right)^{3\gamma} - \frac{2\sigma(\Gamma)}{R_1} - p_0 - p_{ac} - \frac{4\dot{R}_1\mu_L}{R_1} - \frac{4k_s\,(\Gamma)\dot{R}_1}{R_1^2}\right) - \frac{R_2}{D}\left(2\dot{R}_2^2 + R_2\ddot{R}_2\right) \tag{5.1}$$

$$R_2\ddot{R}_2 + \frac{3}{2}\dot{R}_2^2 = \frac{1}{\rho_L}\left(\left(p_0 + \frac{2\sigma_0}{R_{02}}\right)\left(\frac{R_{02}}{R_2}\right)^{3\gamma} - \frac{2\sigma(\Gamma)}{R_2} - p_0 - p_{ac} - \frac{4\dot{R}_2\mu_L}{R_2} - \frac{4k_s(\Gamma)\dot{R}_2}{R_2^2}\right) - \frac{R_1}{D}\left(2\dot{R}_1^2 + R_1\ddot{R}_1\right) \tag{5.2}$$

The experiments were carried out using 2 high speed cameras: the Brandaris (10 Mfps) [8] to capture the bubble dynamics and a Photron (1 kfps), to estimate the distance that the fluorescent material travelled. The bubbles were driven at a frequency, *f*, of 1MHz, peak negative pressure, p_A, 100 - 300 kPa, for a continuous sinusoidal burst of 100 cycles. The experiments were carried out for 46 microbubbles in the range of initial resting radius R_0=2-4μm. To compare to this data, the theoretical model, implemented as described in

Chapter 4 with the radial Equations (5.1) and (5.2) with a constant shell viscosity, was run for the parameters shown in Table 5.1 and for a sinusoidal pulse of 100 cycles. These were run for a variety of k_1 values to model different adsorption characteristics. The distance from a rigid surface was considered to be, $d = 3R_0$ (where $D=2d$) to satisfy the assumption of spherical symmetry, but the model was also run far away from the wall, $d=100R_0$, to see what effect this would have on the shedding. The value of κ_s was taken from the experimentally found value in Marmottant et al.[9] and the values of Γ^*, Γ^{max}, C_∞^{surf}, have been taken to be the same as those used previously by O'Brien in [1] which gave a good correlation with experimental data, in the case of , C_∞^{surf}.

Parameter	**Value**
Desorption coefficient, k_2, s^{-1}	$\frac{k_1}{C_\infty^{surf}}$ 0.05
Maximum concentration, Γ^*, (kg m^{-2})	$3x10^{-8}$
Maximum packing concentration, Γ^{max}, (kg m^{-2})	$\Gamma^{eq}/0.59$
Shell viscosity, κ_s, (kg/s), (non-variable)	$15x10^{-9}$
Driving Frequency, f, (MHz)	1
Liquid viscosity,μ_L,(Pa s)	0.001
Hydrostatic Pressure, p_0,(kPa)	100
Bulk surfactant concentration, C_∞^{surf} , (kgm^{-3})	1
Initial Resting Radius, R_0	2-4µm in 0.5µm steps
peak negative acoustic pressure, P_A	100-300kPa in 50kPa steps

Table 5.1 the parameters chosen to run the model for.

The experimental results are shown in Figure 5.5 and indicate that when the ratio of maximum amplitude of oscillation, ΔR, to the equilibrium radius R_0, $\frac{\Delta R}{R_0}$ reaches 0.3, then a threshold is reached at which lipid shedding becomes observable. This is different to the value of 0.41 suggested by O'Brien [1]. One possible explanation for this is that a different bubble formulation was used in the experiments [10][11]. The model was therefore run for a range of different coating parameters (k_1) to investigate this. k_1 was varied as it changes the equilibrium lipid concentration Γ due to its relationship with k_2 the desorption coefficient, see Equation(4.6), and thus varies the effective surface tension which is dependent on Γ. The results are shown in Figure 5.6 which shows that a "plateau" in the theoretical results for the proportion of material shed from the bubble over the insonation period and that as k_1 is increased more shedding occurs. It can also be seen from Figure 5.6(a) that the amount of material shed increased slightly when the bubbles were closer to the wall, confirming the need to account for this in comparing theory and experiment. However, all the theoretical results show that at approximately $\Delta R/R_0 = 0.3$ corresponds to a "plateau" in the theoretical results for the proportion of material shed from the bubble over the insonation period. It can be seen in Figure 5.6(b) that varying k_1 changes the shedding behaviour and thus the estimate found for k_1 in [1] is only an estimate specific to the data set used.

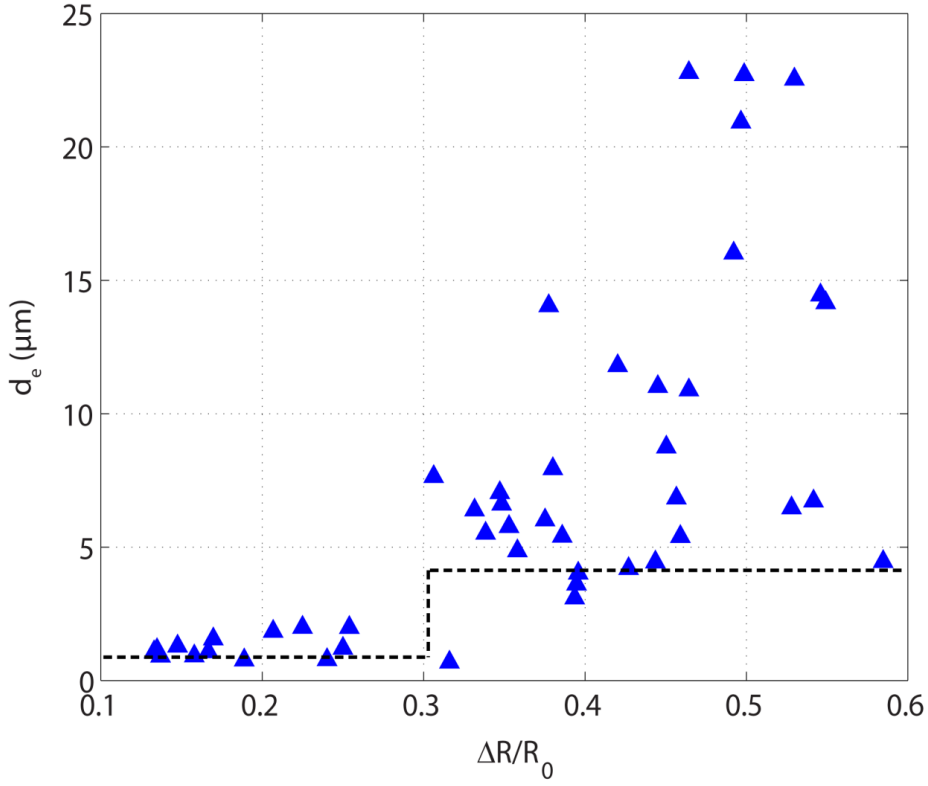

Figure 5.5 Experimental data kindly provided by Ying Luan, showing the estimated transportation distance of the lipid, d_e vs. the ratio $\Delta R/R_0$. The black dotted line shows where measurable shedding occurs

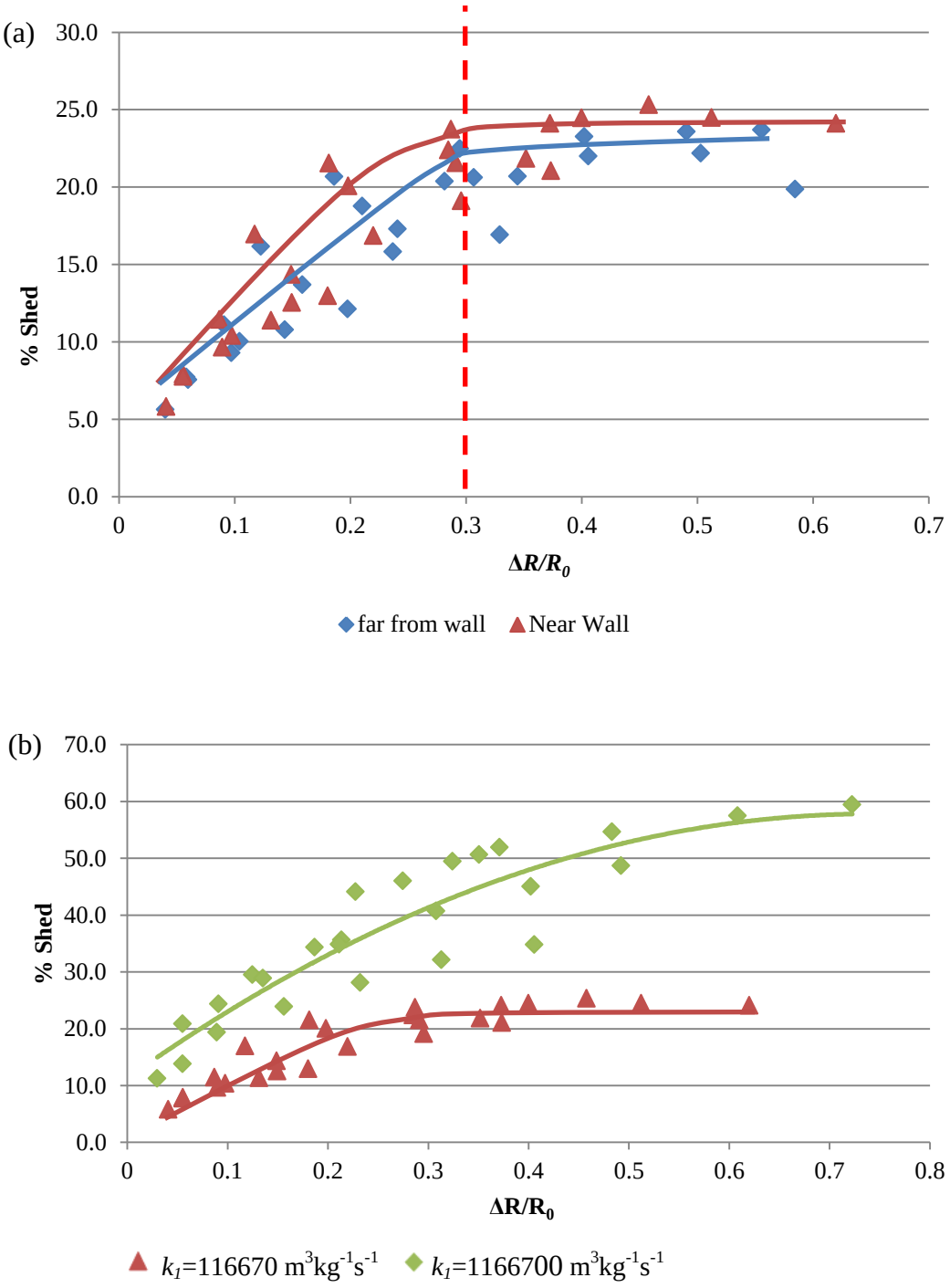

Figure 5.6Theoretical results indicating the total mass of lipid shed as a % of the initial shell mass (a) the effect of the bubble being close to a rigid wall, (b) the effect of different shell composition (varying k_1)

It demonstrates that varying the bubble shell composition does affect the occurrence and degree of shedding, so any threshold for the onset of shedding will be entirely bubble composition dependent. The presence of a wall also affects the onset and degree of shedding by shifting the effective resonance frequency and changing the net change in surface area during oscillation, so this must be taken into account when comparing theory and experiment. The total mass of lipid shed appears to plateau in the theoretical results at a ratio of oscillation amplitude to initial bubble size corresponding to the experimentally observed "threshold" – possibly shedding is only observed when this saturation point is reached, although the dependence upon bubble composition should be considered in this regard.

Therefore in order to get a better understanding of how much lipid is shed, the model was fitted to some radius time curves of the bubble oscillations used to produce this set of experimental data, to try and obtain better estimates of κ_{s0} and k_1. Two sets of data are fitted in the following sections, one in with R-t curves for 10 cycles with varying pressure and initial radius and the other with the resting equilibrium radius of the bubble for 210 pulses.

5.3 Fitting Procedure

R-t curves (unpublished data) were kindly provided by Ms. Ying Luan, from similar experiments, in which the same set up was used in Figure 5.5 and the bubbles were of varying initial size and driven at 1MHz f over three pressures, 255, 170, 85kPa. This was to observe how the parameters might change when different amounts of shedding occurred as lipid shedding became more visible with increasing pressure. From the 100 cycle pulse, 10 cycles were randomly recorded. The following steps were used to fit and select the experimental data, all of this was done via purpose written code in MatLab 2012a ®, using

the variable viscosity term first and then comparing some of the fittings to a constant viscosity term to assess which gives the best fit, code can be found in Appendix C.2.

Only R-t curves in which the start of the pulse is visible were selected, so that R_0 could be obtained. R_0 was assumed to be the last point before the ultrasound pulse was turned on, R_0 was then changed between +/- 0.1μm to optimise the fit. A rough fit to check the initial radius size and the initial guess values of κ_{s0} and k_1 for the fitting were produced as shown in Figure 5.7. The number of points in the experimental data set was increased by interpolating, giving four extra points in-between the originals. This was done so that the fitting program would work more accurately and not discount any peaks as outliers. This then gave the data set seen in Figure 5.7. As it can be seen in this graph, there is a time lag present in the experimental data, from when the optical observation starts and the acoustic signal interacts with the bubble, with a phase difference between the first few cycles caused by the transient in the oscillation. These were subsequently removed from the experimental data during the fitting procedure, by discounting the first 2 cycles to neglect any error from the transient and then for the first 8 peaks after the transient, matching the peaks between the experimental and theoretical data to remove the time lag. An extra peak can also be seen in the experimental data in Figure 5.7, this is thought to be due to a harmonic as shown in Figure 5.8, though asymmetric oscillations due to the presence of the cover slip could also be enhancing the effect. The data were then split into either 3 sections, for an estimate fitting, or 9 sections, for a finer fitting, an example of which is shown in Figure 5.9.

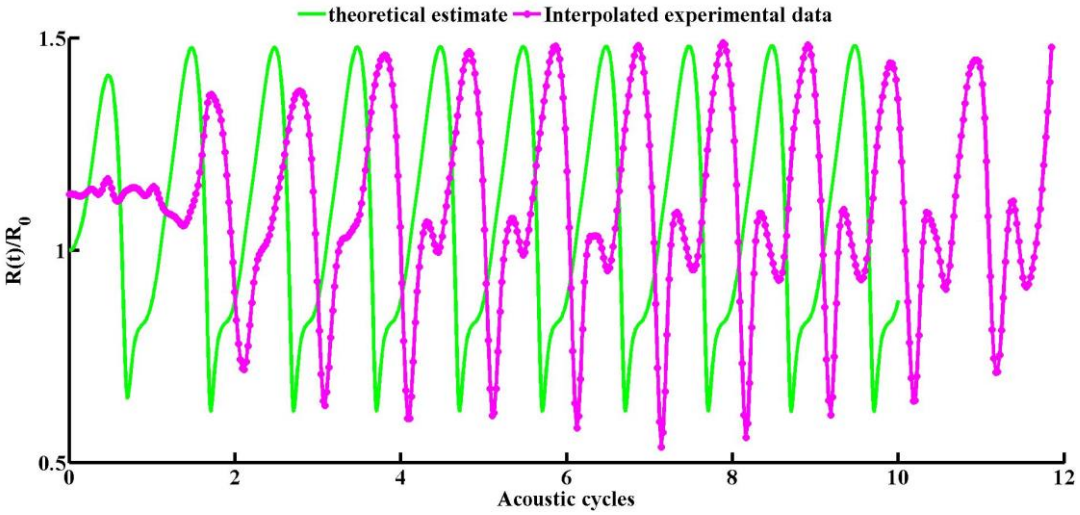

Figure 5.7 *Interpolated data used for fitting (pink) and the estimated fit(in green)*

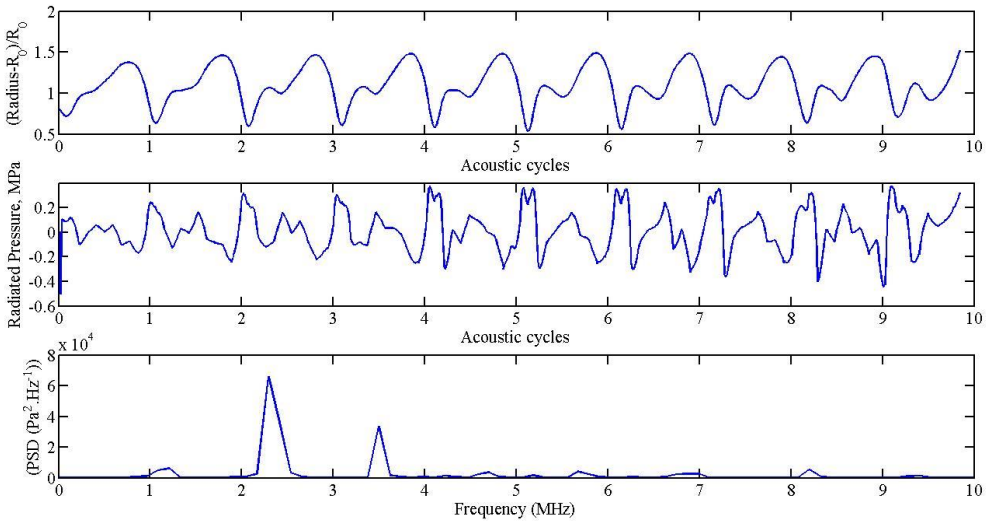

Figure 5.8 Three graphs, R-t curve, Radiated Pressure time curve and pressure- frequency plot of the same bubble. Based on the experimental data of a bubble with R_0 =1.9μm, f=1MHz and p_A=170kPa. (for equations used please see Section 6.3). This shows a fundermenntal peak just off 1MHz and a harmonic just off 2MHz. The reason that peaks are not exactly at 1MHz and 2MHz is due to the transducer centre frequency being off as there's usually an error on the manufacturer specification of 0.1-0.2 MHz.

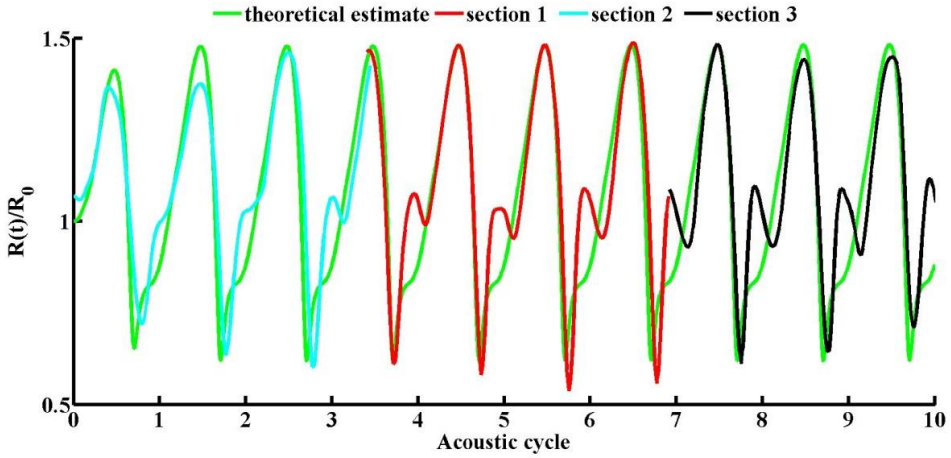

Figure 5.9 showing the estimated fit, in green and the sections used for fitting, including the time lag.

Finally, these sections were fitted to obtain the κ_{so} and k_1, Figure 5.10. This was done by using purpose written code in MatLab 2012a ® and a modified version of the Spec1d program developed Des McMorrow and Henrik Rønnow [12]. It was created to fit Gaussian peaks to neutron scattering data, it has be adapted here to fit sinusoidal waves, this program allows two values to be varied simultaneously and run over at least 40 iterations or until the values of best fit has been reached, in other words where the Chi squared value is minimized. In the cases where 40 iterations have been reached the values from this have been put back in as the initial guess and the run repeated until the value of the parameters stayed constant for 3 significant figures.

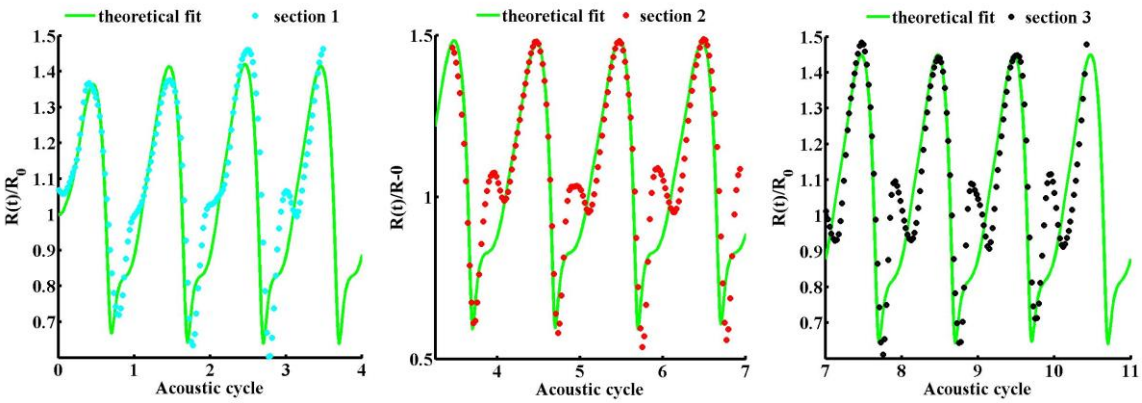

Figure 5.10 this shows the 3 sections of the fitted experimental data for R_0= 1.9 and p_A=170kPa

5.4 Fitting to Experimental Data

Seven experimental R-t curves were selected for fitting in 3 sections, covering a range of initial sizes, $R_{0,}$ and peak negative driving pressures, p_A, as seen in Table 5.2. These were fitted using the model with a variable viscosity. From these fittings where the results are shown in Table 5.2 it can be see for bubbles 1,2,6 and 7 the value of k_1 is initially large and then decreases to a constant value. This suggests that the bubble may not be in an equilibrium state at the beginning of the pulse and that there is extra surfactant on the bubbles surface. This is something that has been observed under a microscope, in the form of a visible fuzzy shelled bubble during FLIM studies [13], see Figure 5.1. Bubbles 3-5 tended to have fairly constant k_1 values.

The model itself fitted well, in terms of peak amplitude (within ±3% of the actual maximum peak R(t) value) and the gradient (going from peak to trough was fitted within a ±3% error as well), to the experimental data. Though, the model under predicted the harmonics, with the theoretical harmonic being less apparent than the experimental one, which could be due to asymmetric oscillations being present in the experiments but not accounted for in the model. The values of the viscosity are consistent with those often

quoted for the viscosity values which is usually $15x10^{-9}kgs^{-1}$ [9]. It should be noted that the bubbles used in these experiments had a different shell composition and so variation in the viscosity values is expected. The viscosity was seen to vary over the 3 sections but no clear trend in how they varied was observed.

Bubble number	R_0, *μm*	P_A,*kPa*	1st section		2nd section		3rd section	
			$\kappa_{s0,}$ $x10^{-9}$ kg/s	$k_{1,}$ $x10^{-5}$ $m^3kg^{-1}s^{-1}$	$\kappa_{s0,}$ $x10^{-9}$ kg/s	$k_{1,}$ $x10^{-5}$ $m^3kg^{-1}s^{-1}$	κ_{s0} $x10^{-9}$ kg/s	k_{1} ,$x10^{-5}$ $m^3kg^{-1}s^{-1}$
1	2.23	255	19.5	49.80	17.9	90.00	25.0	10.00
2	1.9	170	17.2	10.00	16.5	0.70	19.0	0.04
3	1.8	170	16.9	1.00	16.1	1.00	15.0	69.80
4	2.5	170	16.0	0.47	14.0	0.50	20.0	0.50
5	2.5	85	10.0	3.00	10.0	4.00	7.9	5.00
6	3.1	85	9.5	40.00	15.9	4.00	17.0	4.00
7	2.6	85	30.3	8640000.00	13.5	8.64	20.0	6.87

Table 5.2 showing how the fitted values of k_1 and κ_{so} change for different bubble sizes and pressures over 10cycles

Two bubbles were selected, to fit over a single cycle and therefore get a higher quality and closer fit, this was done by splitting the experimental data into 9 sections, and the fitting was done for both a variable and a constant viscosity to see how they affect the fitted values. The first two sections were discounted as they incorporated the transient part of the pulse. The results for the bubble of initial R_0= 1.9 and p_A=170kPa are shown in Table 5.3, and the fitted curves for the variable viscosity are shown in Figure 5.11, and the constant viscosity in Figure 5.12. It can be seen that there is little difference in between the two fits, but the constant viscosity does predict the harmonic slightly better than the variable viscosity. This suggests that the variable viscosity might be over dampening the bubble oscillation during compression, suggesting that a term which increases the viscosity during compression should change more gradually. However as already mentioned asymmetric oscillations of the bubble caused by the presence of the cover slip could also be present which are not accounted for in the model. The results for the bubble of initial R_0=

2.8and p_A=85kPa are shown in Table 5.4, and the fitted curves for the variable viscosity are shown in Figure 5.13, and the constant viscosity in Figure 5.14. These figures also support the fact that during the compression the viscosity is too high, with the curves either being fitted to the maximum or the minimum peak. Again variable viscosity fitted values are higher than that for the constant viscosity where the constant viscosity fitting produced viscosity values close to those seen previously, [9].

Section	Variable $\kappa_s(\Gamma)$		Constant κ_{s0}	
	κ_{s0} x10^{-9} , kg/s	k_1, $m^3kg^{-1}s^{-1}$	κ_{s0} x10^{-9} , kg/s	k_1, $m^3kg^{-1}s^{-1}$
3	17.71	10x10^5	13.50	1.00x10^6
4	16.09	6.69x10^5	12.53	6.87x10^4
5	15.99	7x10^4	12.51	7.00x10^5
6	15.50	7x10^4	12.02	7.00x10^5
7	16.73	6x10^4	12.51	7.95x10^5
8	19.50	45000	15.63	7.99x10^5
9	*19.26*	*45000*	*14.00*	*8.00x10^5*

Table 5.3 fitting results for non-variable and variable fitting parameters

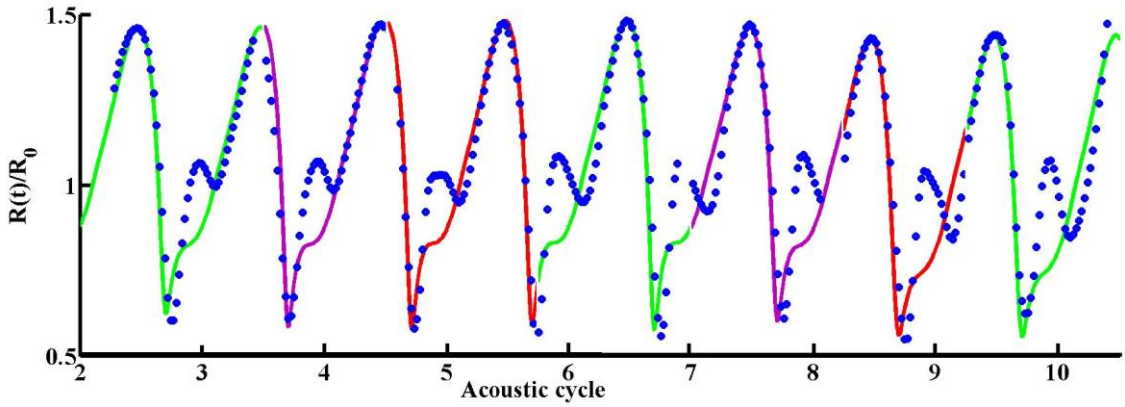

Figure 5.11 This shows the variable viscosity fit done over 9 cycles, the blue dots are the experimental data and the coloured lines show the different fits for each cycle

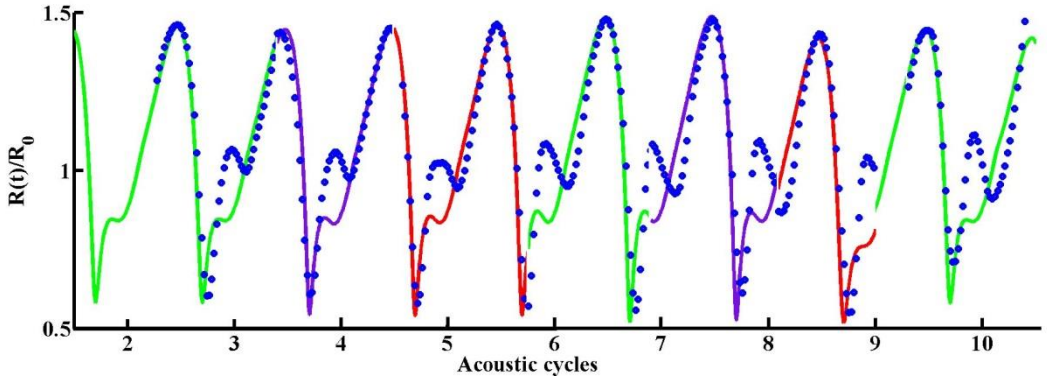

Figure 5.12 This shows the constant viscosity fit done over 9 cycles, the blue dots are the experimental data and the coloured lines show the different fits for each cycle

Section	Variable $\kappa_s(\Gamma)$		Constant κ_{s0}	
	κ_{s0} x10^{-9} , kg/s	k_1, $m^3kg^{-1}s^{-1}$	κ_{s0} x10^{-9} , kg/s	k_1 , $m^3kg^{-1}s^{-1}$
3	7.5	3.00x10^6	17.0	3.94x10^4
4	3.00	3.99x10^6	15.07	3.00x10^4
5	3.00	3.86x10^6	6.39	2.61x10^4
6	10.96	4.00x10^4	6.40	3.00x10^4
7	9.98	3.96x10^5	21.99	2.80x10^4
8	10.80	2.00x10^4	21.14	2.96x10^5
9	7.69	3.00x10^5	10.5	3.00x10^5

Table 5.4 fitting results for non-variable and variable fitting parameters

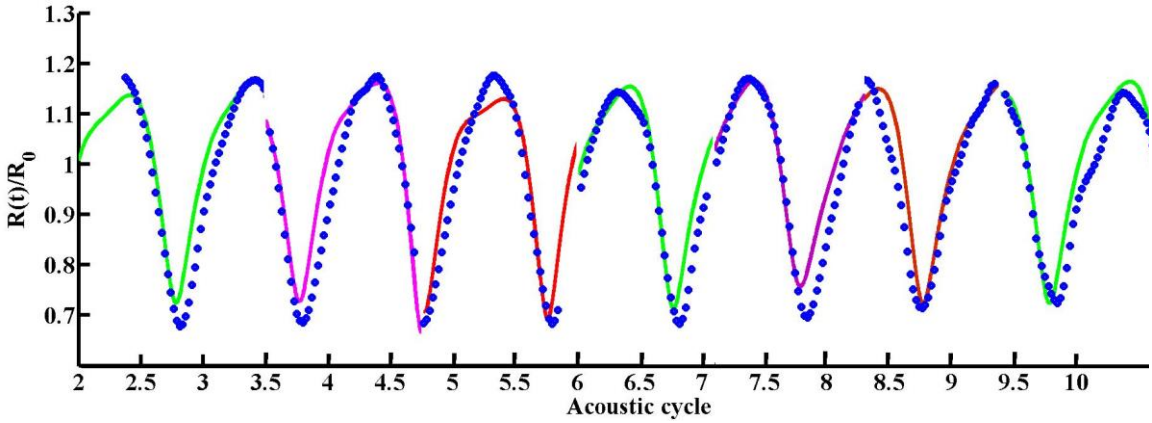

Figure 5.13 This shows the variable viscosity fit done over 9 cycles, the blue dots are the experimental data and the coloured lines show the different fits for each cycle

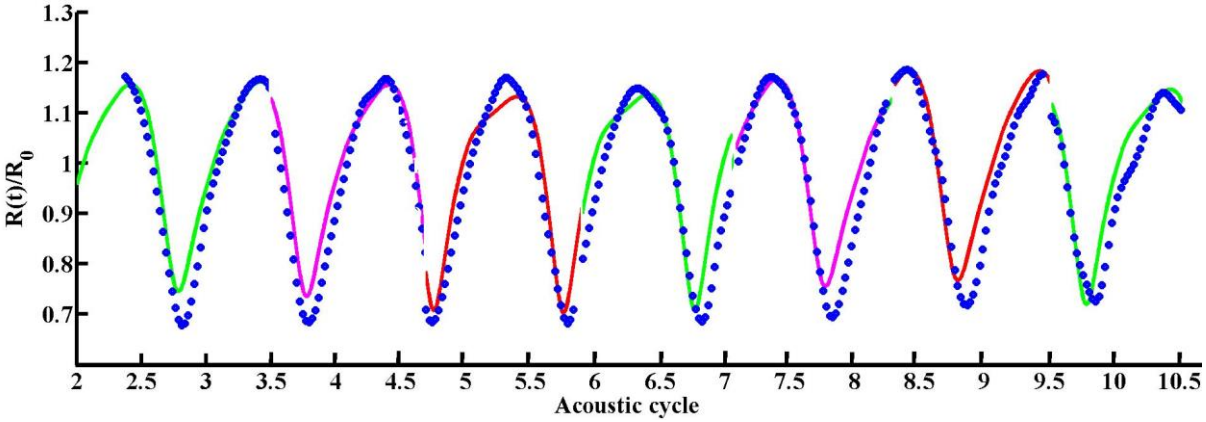

Figure 5.14 This shows the constant viscosity fit done over 9 cycles, the blue dots are the experimental data and the coloured lines show the different fits for each cycle

However during fitting it was discovered that changing the value of k_1 by $\sim\pm 2\text{x}10^3$ had an insignificant effect on the fit, though as the values of k_1 are of the order 10^4 and above this is still a valid parameter to include in the optimisation . This is because k_1 affects the bubble more over the whole cycle and the subsequent re-sizing in between pulses. Therefore fitting of the equilibrium radius with data from Viti (unpublished) has been performed.

Viti's experiment had a similar set up as the one performed by Ying, except this time the bubbles were hit by a driving frequency, f=2MHz, for 15 cycles, with a pulse repetition frequency of 0.5kHz which relates to a $2\text{x}10^{-5}$s gap in-between pulses and a peak negative driving pressure of 70kPa. The recordings happened in a series of 6 in which 30 pulses occurred with every 5^{th} one being recorded. There was then a 2 minute gap between each batch of 6, in total there were 7 batches. The model was run for 210 pulses of 15 cycles with a f=2MHz and p_A =70kPa. In the two minute gap in-between batches rectified diffusion can occur in which the bubble size can increase which is not taken into consideration with the model currently being used. Thefore, the experiments performed by Viti are not completely reproduced theoretically and therefore the values gained here from

the fitting are only being used to give an estimated value of k_1 to use in the comparisons with Ying's data.

Results from fitting 210 pulses to the data, for both a constant and a variable viscosity are shown in Figure 5.15. It was found that for the variable viscosity a value of k_1=7000 $m^3kg^{-1}s^{-1}$ gave a good estimate, and for the constant viscosity k_1= 7000 $m^3kg^{-1}s^{-1}$. The model was run for the 210 pulses for the viscosity values shown in Table 5.5, these are the minimum and maximum values found and the mean value, to show how the viscosity changes the shape of the graph over this number of cycles. It can be seen from Figure 5.15 that the shedding term also needs to have a limit put on to it when the bubble has reached its steady value towards the end at which point no more shedding occurs, which occurs experimentally at about 120 pulses, in which the experimental curve flattens out.

	min	mean	max
Variable, $\kappa_s(\Gamma)$, x10^{-9} Kgs^{-1}	3.0	14.8	20
Constant, κ_{s0} ,x10^{-9} kgs^{-1}	6.4	13.65	22.0

Table 5.5 showing the values of viscosity used for the fitting

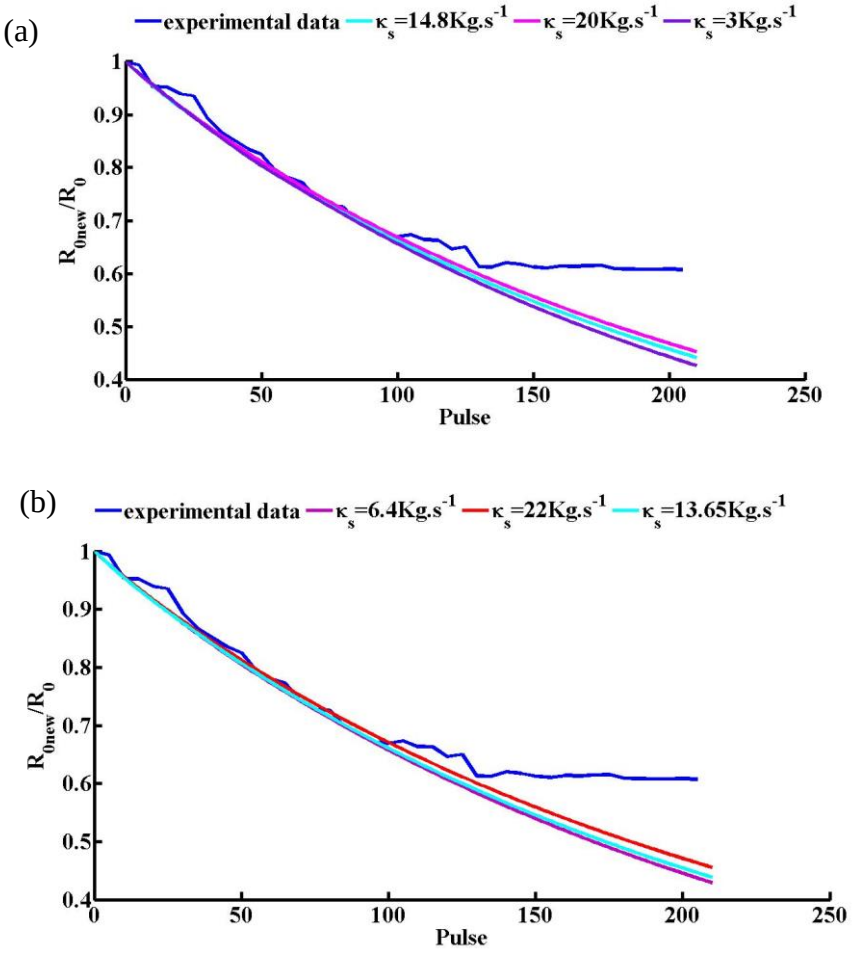

Figure 5.15 showing the experimental data with k_1=7000 $m^3kg^{-1}s^{-1}$ *with the values of κ_{s0} inTable5.5 for (a) a variable viscosity and (b) a constant viscosity*

5.5 Results of Threshold

The Figure 5.6a for near a wall simulation found in section 5.2, is rerun here for a variable viscosity and constant viscosity with the shedding rates and the mean viscosity found in Section 5.4 and the other simulation parameters found in Table 5.1. This is to allow comparison to Yings experimental data, Figure 5.5. Figure 5.16 shows the % of lipid shed from the shell over continuous 100 cycles vs the ratio of maximum amplitude of oscillation, ΔR, to the equilibrium radius $R_{0,}$, for the variety of situations described in Table 5.1. As can be seen in Figure 5.16 the variable viscosity over 100 cycles allows the bubble to over expand with higher $\Delta R/R_{0,}$ in comparison to the constant viscosity which matches

the $\Delta R/R_0$ ratio found in the experiments. This shows that the variable viscosity does not work well for long pulses. However the trend of an increase in shedding as that ratio approaches $\Delta R/R_0 \approx 0.6 - 0.7$ and then decreases. This can be explained physically, with the bubble initially expanding and contracting more, then at a certain point, when the surfactant concentration has decreased the bubble expands more than it contracts reducing the amount of shedding occurring. As shedding can only occur in the compression phase of the bubble oscillation. In conclusion it can be seen that the constant viscosity gives a better experimental prediction of the lipid shedding behaviour of the bubble over a long pulse.

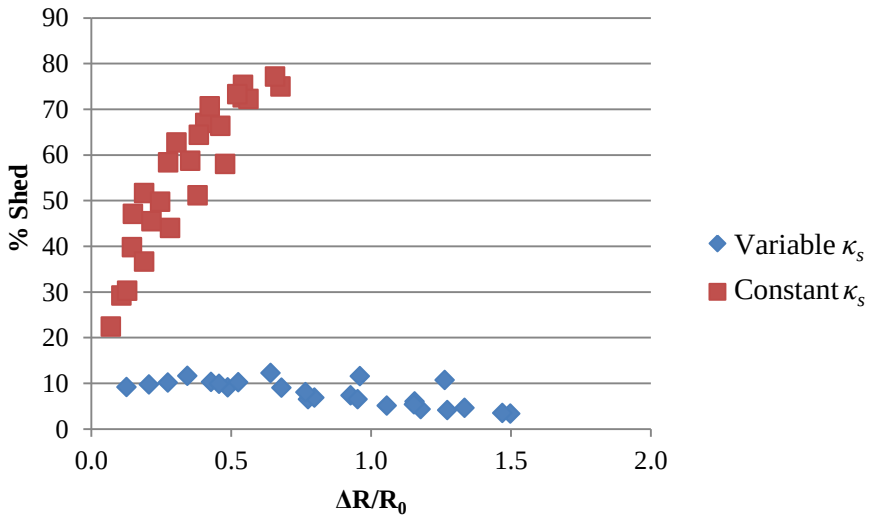

.

Figure 5.16 This figure shows the difference of running Figure 5.6a near a wall simulation with the expected k_1 and κ_s values from the fitting of experimental data in the previous sections. As it can be seen the constant κ_s fits better to what is observed in Ying's initial experiments, shown in Figure 5.5.

5.6 Summary

In this chapter the model had been compared to 3 types of experimental data, lipid transportation, radial time curves and equilibrium radii after repeated pulses. The model fitted the experimental data investigated here well, showing similar behaviour for both R-t

curves over a few acoustic cycles, equilibrium radius after many pulses and correlation with the transportation of lipid shedding. It was found that this model does a good job at describing lipid shedding behaviour when using a constant shell viscosity. However there is still room for improvements which have become obvious over this chapter. The variable viscosity term was found to over dampen the bubble responses when compared to the radial time curves, and over predicted the expansion of the bubble over 100 cycles, relating to poor correlation to the lipid transportation data. The same model with the constant viscosity performed better correlating well with lipid transportation data, but it still failed to predict the harmonics seen at higher pressures. Though, this affect may also have been due to asymmetric oscillation being present in the experiment and not capture in the model. This means that an alternative viscosity term is still needed to predict the behaviour of the bubble response more accurately. However it may also be due to a constant shell elasticity determining the surface tension which also needs to be changed.

The shedding behaviour incorporated into the model could also be improved by including a different rate of shedding at the beginning of the pulse that incorporates the bubble having extra surfactant on it in the first few cycles. Further improvement may come from incorporating a limit on how much surfactant can be lost until the bubble reaches its steady oscillating radius, in which no more shedding is observed. The physical explanation for this behaviour could be explained by the bubble being off resonance or it could be due to a form of lipid restructuring changing the viscosity.

5.7 References

1. O'Brien, J.-P., Ovenden, N., and Stride, E., *Accounting for the stability of microbubbles to multi-pulse excitation using a lipid-shedding model.* The Journal of the Acoustical Society of America, 2011. **130**(4): p. EL180-EL185.
2. Borden, M.A., et al., *Influence of lipid shell physicochemical properties on ultrasound-induced microbubble destruction.* Ultrasonics, Ferroelectrics and Frequency Control, IEEE Transactions on, 2005. **52**(11): p. 1992-2002.
3. Gelderblom, E.C., *Ultra-high-speed fluorescence imaging*, 2012: Enschede. p. 144.
4. O'Brien, J.-P., *Improved Characterisation and Modelling of Microbubbles in Biomedical Applications*, in *Mathematics*2013, University College London: London. p. 193.
5. Longuet-Higgins, M.S., *Bubble noise spectra.* The Journal of the Acoustical Society of America, 1990. **87**(2): p. 652-661.
6. Garbin, V., et al., *Unbinding of targeted ultrasound contrast agent microbubbles by secondary acoustic forces.* Physics in Medicine and Biology, 2011. **56**(19): p. 6161-6177.
7. Marmottant, P., et al., *High-speed imaging of an ultrasound-driven bubble in contact with a wall: "Narcissus" effect and resolved acoustic streaming.* Experiments in Fluids, 2006. **41**(2): p. 147-153.
8. Chin, C.T., et al., *Brandaris 128: A digital 25 million frames per second camera with 128 highly sensitive frames.* Review of Scientific Instruments, 2003. **74**(12): p. 5026-5034.

9. Marmottant, P., et al., *A model for large amplitude oscillations of coated bubbles accounting for buckling and rupture.* Journal of the Acoustical Society of America, 2005. **118**(6): p. 3499-3505.

10. Sirsi, S. and Borden, M., *Microbubble Compositions, Properties and Biomedical Applications.* Bubble Sci Eng Technol, 2009. **1**(1-2): p. 3-17.

11. Luan, Y., et al., *Lipid Shedding from Single Oscillating Microbubbles.* Ultrasound in Medicine & Biology, 2014.**40**(8):p. 1834-46

12. McMorrow, D. and Rønnow, H. *Spec1d*. [Website] 2001 Febuary 2001; Version 2.0:[MatLab Code]. Available from: http://www.ill.eu/instruments-support/computing-for-science/cs-software/all-software/matlab-ill/spec1d/.

13. Hosny, N.A., et al., *Mapping microbubble viscosity using fluorescence lifetime imaging of molecular rotors.* Proceedings of the National Academy of Sciences, 2013.

6 Characterisation of Large Oscillations in a Population

Microbubbles are conventionally used as ultrasound contrast agents (UCA) for imaging, though they are also being investigated for their therapeutic applications, in particular drug delivery, gene therapy and thrombolysis [1-4]. For therapeutic applications microbubbles can be used as drug carriers and/or cavitation nuclei to increase drug transport from blood vessels to the surrounding tissue, [5-7]. This latter effect is often associated with unwanted bio-effects including damage to blood vessel walls [4, 8], leading to many studies trying to maximise the drug dose while minimising excessive or substantial vascular injury [9]. The precise mechanism behind the vascular and cellular damage is still unknown, but a link has been made between the level of inertial cavitation detected and the associated bioeffects, both *in vitro* and *in vivo* [8, 10]. Inertial cavitation refers to the situation when a bubble undergoes violent oscillations, rapidly collapsing during compression. It is defined in more detail later in this chapter. Consequently, it is desirable to have a means of predicting the onset and extent of inertial cavitation from a given population of microbubble nuclei; and this is the subject of this chapter.

First a brief overview of inertial cavitation phenomena will be given. This will be followed by the derivation of a model for a coated microbubble that is valid for large amplitude oscillations and takes into account time dependent shell behaviour. The model will then be used to investigate how different sized microbubbles contribute to the overall acoustic emission from a microbubble population and hence the signal received in cavitation experiments. The extent to which a single bubble model can be used to predict a population response will be assessed and also the influence of the microbubble coating upon the dynamics with increasing excitation pressure.

6.1 Overview of Cavitation Models

A more in-depth literature review about single bubble models can be found in Chapter 3 Section 3.1 but a brief overview of the components for different types of oscillation are summarised below. As previously stated in Chapter 3, to model the dynamics of a microbubble, three conservation equations need to be solved simultaneously for mass, momentum and energy. However in deriving the equation(s) of motion, certain assumptions can be made which allow the model to be simplified, depending on what conditions the model is required to simulate. The consistent assumptions made are that the bubble remains spherical during the oscillations, that there is negligible heat transfer and diffusion of the gas across the bubble surface and that the effect of changes in density of the surrounding liquid can be neglected. Treating the liquid as incompressible, however, means that the energy loss caused by the acoustic radiation from the bubble needs to be reintroduced into the equation(s) of motion via a correction term. The RPNNP Equation 3.2 can be written with a variable surface tension in the form:

$$\ddot{R} = -\frac{3\dot{R}^2}{2R} + \frac{1}{\rho_L R}\left[p_G(R,t) + p_v(R,t) - p_\infty(R,t)\right] + f_L + f_s \qquad (6.1)$$

Where R is the instantaneous radius of the bubble and an over-dot represents a differentiation with respect to time, ρ_L is the density of the liquid, p_G is the pressure from the gas acting on the bubble surface, p_v is the vapour pressure inside the bubble, p_∞ is the far field pressure in the liquid (including the sound field exciting the bubble) and f_L and f_S are the resistance from the surrounding liquid and the shell. Where μ_L is the liquid viscosity, κ_s is the shell viscosity and $\sigma(R)$ is the variable surface tension. Additional terms for energy dissipation due to heat conduction f_{Th} and acoustic re-radiation f_{Rad} can also be included, as

seen in Equation (6.5). Though the appropriate form of these depends on the situation. For example at low pressures and medical diagnostic frequencies f_{Th} and f_{Rad} can be neglected [7, 11, 12], as viscous damping is dominant in this range. The same assumptions made in Chapter 3 Section 3.4.1 still apply here.

$$f_L = -\frac{4\mu_L \dot{R}}{\rho_L R^2} \tag{6.2}$$

$$f_s = \frac{2\sigma(R)}{\rho_L R^2} + \frac{4\kappa_s}{\rho_L R^3} \tag{6.3}$$

During these low pressure driven oscillations coated microbubbles undergo approximate linear oscillations where the resonant frequency, ω_R Equation (6.4), (see Appendix A for the derivation), is strongly dependent on the size of the initial radius R_0 and the properties of the shell.

$$\omega_R^2 = \frac{1}{\rho_L R_0^2}\left(3\gamma\left(P_0 - \frac{2\sigma(R_0)}{R_0}\right) - \frac{2\sigma(R_0)}{R_0}\right) + \frac{8(\mu_L + \kappa_s/R_0)^2}{(\rho_L R_0^2)^2} \tag{6.4}$$

The type of equation is suitable for small amplitude oscillations in which it assumes that the ultrasound wavelength, λ_a, is larger than the radius of the bubble, that there is no transfer of heat or mass during oscillation, the gas behaves ideally, the liquid is much more dense than the gas, the velocity of the bubble wall never approaches the speed of sound in the liquid and that the liquid is incompressible. However, when the microbubble is exposed to higher ultrasound pressure such as those used for therapeutic applications and in which inertial cavitation becomes dominant; the assumptions start to break down. For these larger amplitude oscillations thermal and acoustic damping re-radiation become more significant than the viscous dampening that dominates in the range for small amplitude oscillations. Therefore they need to be incorporated into the model.

As described previously, it is the assumption of liquid compressibility that has a particular tendency to be invalidated, as the velocity of the bubble wall becomes comparable to the speed of sound in the liquid. Models taking this into account were reviewed earlier in Chapter 3.

Prosperetti [17] derived terms for the thermal f_{Th} and acoustic re-radiation f_{Rad} damping for larger initial radii and/or moderate amplitudes of oscillation for an uncoated microbubble, Equations (6.6)-(6.7).

$$\ddot{R} = -\frac{3\dot{R}^2}{2R} + \frac{1}{\rho_L R}[p_G(R,t) + p_v(R,t) - p_\infty(R,t)] + f_L + f_s + f_{Th} + f_{Rad} \tag{6.5}$$

$$f_{Th} = -\frac{4\mu_{Th}\dot{R}}{\rho_L R^2} \tag{6.6}$$

$$f_{Rad} = -\frac{R_0^2\dot{R}}{R^2}\left[\frac{\omega^2 R_0/c_s}{1 + \left(\frac{\omega R_0}{c_s}\right)^2}\right] \tag{6.7}$$

Where μ_{Th} is the effective "thermal" viscosity (a term derived by Prosperetti in [17]) , ω is the angular driving frequency and c_s is the speed of sound in the surrounding liquid. A more rigorous treatment of the term f_{Rad} is required for an uncoated microbubble undergoing large amplitude oscillations, for example as that derived by Keller and Miksis [16] and modified by Prosperetti [17]

$$f_{Rad} = \frac{\dot{R}}{c_s}\left(\ddot{R} + \frac{\dot{R}^2}{2R} + \frac{1}{\rho_L R}[p_G(R,t) + p_v(R,t) - p_\infty(R,t)] + f_L + f_s\right) + \frac{1}{c_s}\frac{d}{dt}\left(\frac{p_G(R,t)}{\rho_L} + f_L R + f_s R\right) \tag{6.8}$$

Under these large oscillations the bubbles behaviour becomes non-linear and the radial amplitude of expansion becomes larger than that of contraction [7, 18]. This leads to the bubble undergoing repetitive oscillations, the periodicity of which may only be observed over several cycles [7]. During this type of behaviour the Equations (6.1) and (6.4) are no longer valid and the frequency at which the maximal radial response of the bubble becomes dependent on the driving pressure. This type of behaviour is commonly referred to as stable or non-inertial cavitation.

As the pressure increases, the amplitude of oscillation continues to increase until the periodic nature of the oscillations is completely lost and the oscillations can become chaotic and/or the bubble undergoes violent collapse, during which the bubble may fragment into smaller bubbles [19].This type of behaviour is often described as unstable, inertial or transient cavitation. However the terms “transient” or “unstable” are misleading terms to use to describe this behaviour as the bubble can collapse many times without fragmenting [20].

The terms “inertial” or “non-inertial” refer to the mathematical characterisation of the bubble collapse developed by Flynn [21]. Here an approximate criterion for predicting when this violent collapse occurs can be found by comparing the magnitude of two terms from Equation (6.1), f_I, which describes the influence of the surrounding liquid on the bubble, i.e. the inertial term, and f_P the influence of the internal pressure of the bubble. In this description it is said that inertial cavitation occurs when the liquid inertia dominates the collapse process, which occurs when the magnitude of f_I is greater than the magnitude of f_P at the point when f_P reaches a minimum, as seen in Figure 6.1.

$$f_I = -\frac{3\dot{R}^2}{2R} \tag{6.9}$$

$$f_P = \frac{1}{\rho_L R}\left[p_G(R) - \frac{2\sigma_0}{R} - p_\infty\right] \tag{6.10}$$

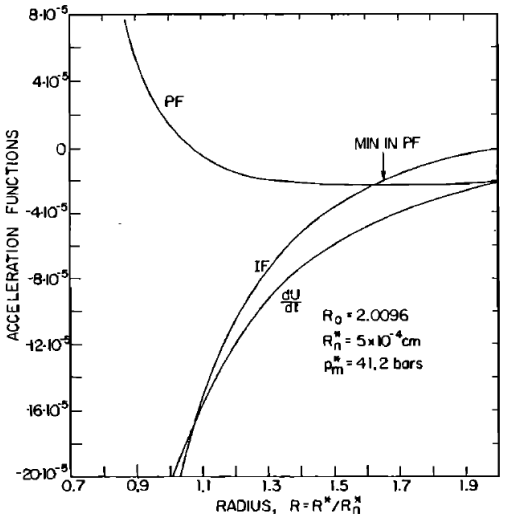

Figure 6.1 reproduction from Flynn [21], showing IF and PF , which relates to f_I and f_p respectively, as a function of radii vs acceleration functions

The threshold at which the collapse becomes controlled by liquid inertia, occurs when the ratio, $\frac{R_{max}}{R_0}$, between the maximum radial oscillation, $R_{max,}$ and the equilibrium radius, R_0 , becomes bigger than some critical limit. This takes place approximately when $\frac{R_{max}}{R_0} > 2$ [20, 21]. Other authors have claimed that this criterion should actually be $\frac{R_{max}}{R_0} > 2.3$ [22], which is when the bubble wall velocity goes faster than the speed of sound [18] i.e. $\dot{R} > c_s$. Both criteria were derived directly from Flynn's analysis and were obtained by linearizing the equations of radial motion.

6.2 Equation of Motion

In this section a theoretical model is formulated for a single, spherical encapsulated bubble undergoing purely spherical radial motion. Previous authors have used the Keller-

Miskis Equation (6.11) [16, 23-25] to describe the behaviour of a bubble undergoing large amplitude oscillations, which is the assumed behaviour of the bubble at high acoustic driving pressures and megahertz frequencies.

$$\left(1-\frac{\dot{R}}{c_s}\right)R\ddot{R}+\frac{3}{2}\left(1-\frac{\dot{R}}{3c_s}\right)\dot{R}^2=\left(1+\frac{\dot{R}}{c_s}\right)\frac{P}{\rho_l}+\frac{R}{\rho_l c_s}\frac{dP}{dt} \tag{6.11}$$

$$\text{Where } P=\frac{1}{\rho_l}\left(p_0+\frac{2\sigma}{R_0}\right)\left(\frac{R_0}{R}\right)^{3\gamma}-p_0-\frac{4\mu_l\dot{R}}{R}-\frac{2\sigma}{R}-p_{ac} \tag{6.12}$$

Where p_{ac} is the acoustic pressure. However, Equation (6.11) does not fully describe the behaviour of an oscillating bubble especially the effect of a shell. As the bubble expands and contracts over an acoustic cycle the surface tension will also change. Although it is common in models, describing inertial cavitation behaviour of microbubbles, for the shell to be neglected, term f_s in Equation (6.5). This is because the shell is assumed to have either physically broken or that the concentration of the shell at the expansion has become so low that it has no influence on the motion of the surface.

In Chapter 3 different methods for incorporating shell effects, with both constant and variable shell parameters for small amplitude oscillations were described. Here a model is being developed to describe the behaviour of the microbubble before and during inertial cavitation, for large amplitude oscillations. A variable surface tension shell model was therefore adopted as this could take into consideration the fact that surface tension at large expansions (when the shell becomes negligible) will be that of air/ water but also that on the subsequent contraction, when the surfactant concentration increases surface tension will vary significantly. Such a term has been derived previously by Marmottant et al. [23]. Therefore a large amplitude oscillation model based on that of Keller and Miksis was used but rederived to include variable surface tension as described in Equation (6.13).

$$\left(1-\frac{\dot{R}}{c_s}\right)R\ddot{R}+\frac{3}{2}\left(1-\frac{\dot{R}}{3c_s}\right)\dot{R}^2=\left(1+\frac{\dot{R}}{c_s}\right)\frac{P}{\rho_l}+\frac{R}{\rho_l c_s}\frac{dP}{dt} \tag{6.13}$$

Where $P=\frac{1}{\rho_l}\left(p_0+\frac{2\sigma(R_0)}{R_0}\right)\left(\frac{R_0}{R}\right)^{3\gamma}-p_0-\frac{4\mu_l\dot{R}}{R}-\frac{2\sigma(R)}{R}-p_{ac}$ (6.14)

The angular frequency of the incident sound field is $\omega=2\pi f$ where f is the frequency in Hertz. The surface tension is based upon three regimes as described in Chapter 3 Equation (3.75) with an overview of the model included here for the readers' convenience. The first regime is a buckled state which is consistent with experimental findings on the fast compression of pulmonary phospholipid monolayers, in which it assumes a near vanishing surface tension in the buckled state. $R_{buckling}$ is the radius at which buckling of the bubble shell occurs. The next regime is the elastic state in which the shell is assumed to have an elastic behaviour and follow a regime with a linear function of surface tension and $R_{rupture}$ is the radius at which the shell ruptures and χ is the shell elasticity. Finally the last regime is the ruptured state, where the shell is assumed to have ruptured and the bubble has become a pure gas bubble with no encapsulation.

6.3 Radiated Pressure and Energy

In trying to relate the acoustic emissions detected experimentally from a bubble population to results from a single bubble model such as Equation (6.13) it is important to know to what extent differently sized bubbles in the population contribute to the overall signal for a given set of conditions. As previously discussed, it is known that at lower pressures the resonant bubbles at a given frequency undergo the largest amplitude oscillations [7]; however it is not known if this is still the case at higher pressures or at which pressure the linear resonance frequency is no longer a useful indicator of the maximum bubble response. To investigate this theoretically the radiated pressure from the

bubble, $P_s^a(r,t)$, and the total scattered energy over the time span, $E_{sc,}$ were calculated. From a bubble undergoing a volumetric oscillation driven by a pressure wave p_A. The scattered pressure, $P_s(r,t)$, can be considered to be made up of two parts: (i) the active emission, $P_s^a(r,t)$, of the sound caused by the oscillations of the bubble (i.e. the change in volume of the bubble) and (ii) the passive, $P_s^p(r,t)$, contribution which is due to the presence (maybe non-oscillating) of the bubble in the incident field.

$$P_S(r,t) = P_s^a(r,t) + P_s^p(r,t) \tag{6.15}$$

Provided the detection of the emitted waves will occur at some distance, r, which greatly exceeds that of the radius of the bubble, R. The resulting far field pressure emitted by the bubble can be written as [26]:

$$P_s^a(r,t) = \frac{\rho_L R}{r}\left(R\ddot{R} + 2\dot{R}^2\right) \tag{6.16}$$

The passively scattered sound due to the presence of the bubble, can similarly be written as [26]:

$$P_s^P(r,t) = \frac{1}{3rc_s^2} R^3 \ddot{P}_A \tag{6.17}$$

The corresponding power can be found as:

$$W_{sc} = \frac{4\pi}{\rho_L c_L}\langle r^2 P_s^2\rangle_t \tag{6.18}$$

The total scattered energy E_{sc} can then be found by integrating the scattered power with respect to time over an interval, τ, *[26, 27]*:

$$E_{sc} = \frac{4\pi r^2}{\rho_L c_L}\int_0^\tau (P_s^2)\ dt \tag{6.19}$$

6.4 Experimental Method and Comparison to Theory

In this section a brief overview of the experiments carried out by Susan Graham are described and the collected (to date unpublished) data presented. In the experiments SonoVue bubbles were characterised in a cylindrical Delrin phantom holder (volume = 6.3 ml) with Mylar sheets attached to the front and back face which are optically and acoustically transparent. 300 µL SonoVue were injected into the phantom holder and diluted with PBS and the samples were immediately aligned at the focus and insonated for 30 seconds. A needle hydrophone (ONDA 1056, Onda Corporation, Sunnyvale, CA, USA) was used to calibrate the absolute pressure and characterise the beam profile. The acoustic emissions were detected passively using a 7.5 MHz single element focused transducer (SN 671678, Panametrics, Waltham, MA, USA) referred to as the passive cavitation detector (PCD). Voltage signals were filtered using a 2 MHz analogue high pass filter (FILT-HP2-A, Allen Avionics Inc., NY, USA) to exclude reflections of the driving frequency, amplified by a factor of 5 (SR445A, Stanford Research Systems, Sunnyvale, CA, USA), and then acquired using a DAQ card. Electrical energy associated with cavitation events was calculated as the sum across all frequencies between 0 and 15 MHz and across time points over 30 seconds for each sample. See Figure 6.2 for how the radius and radiated pressure time curves and the frequency components are related to one another.

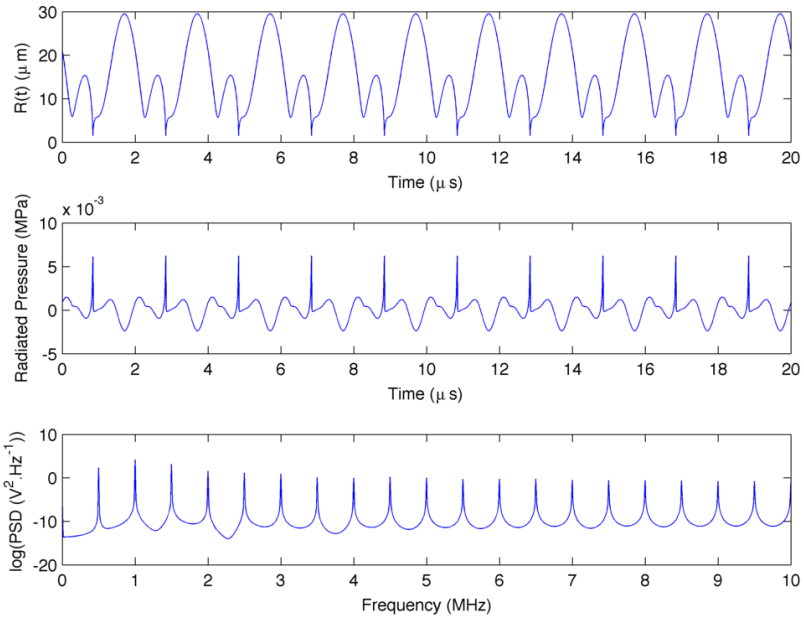

*Figure 6.2 Three graphs showing the theoretical calculations of how the R-t curve, Radiated Pressure time curve and the pressure- frequency plot of the same bubble all relate to one another. This plot is of a bubble with R_0=10μ**m**, p_A=5.9MPa and a frequency of 0.1MHz.(Image kindly provided by Dr J. Collin)*

This gave the total energy emitted by the Sonovue bubble population for 30 seconds for a variety of pressures in the range from 0.2MPa to 4MPa for two frequencies 0.5MHz and 1.614MHz. This data was then compared to the theoretical maximum Wall Mach number, (defined by the fraction $\frac{\dot{R}_{max}}{c_s}$, where $\dot{R}_{max}$ is the maximum wall velocity), found during an oscillation of a single bubble at the given frequency and pressure for a 20 cycle Gaussian pulse. When the wall Mach number goes above 1, the maximum bubble wall velocity will be travelling at or above c_s and therefore it is assumed, as previously discussed, that inertial cavitation will take place. This is being compared to the total energy emitted by a Sonovue population for 30 seconds, for a range of pressures for certain

frequencies, to relate any changes in behaviour, to inertial cavitation becoming dominate signal. This correlation between energy emitted and $\dot{R}$ is also obvious from looking at the Equations (6.16)-(6.19), where it is seen that $E_{sc} \propto {P_s^a}^2 \propto \dot{R}^4$. Therefore in the next section comparisons between the total energy emitted, E_{sc}, the maximum active pressure, P_s^a, and the wall Mach number shall be investigated and their behaviour compared to the experimental data. Before the experiment took place a sample of the bubbles were removed and an image taken under the microscope to use for characterising the sizes of the bubble in the population, to aid in the selecting of the bubble size used from the theoretical model.

6.5 Numerical Implementation

Two versions of the model were run, one for a bubble with a shell described by Equations (6.13)-(6.17) and for an uncoated bubble described by Equations (6.11)-(6.12), so that a comparison between the two could be made to see which one best described the behaviour of the bubbles. To implement the models the equations were non-dimensionalised (in the same manner as described in Chapter 4) and solved simultaneously, using a numerical method via purpose written code implemented using MatLab2012 ® inbuilt solver ode15s, which is a multistep solver that uses a backward differentiation formulas known as Gear's method. Ode15s was used instead of ode45 due to the problem being stiff and taking a very long time to be solved via ode45. From this the Radius, *R(t)* and radial velocity $\dot{R}(t)$ were calculated over 20 cycle Gaussian enveloped pulse. The radiated pressure was then found using Equation (6.16) and the total energy via Equation (6.19). The maximum wall Mach number was calculated by taking the maximum value of $\dot{R}$ and dividing it by the speed of sound in the liquid c_s. The parameters used for all the calculations are shown in Table 6.1, here κ_s and χ have been taken to be the values found in Marmottant *et al.* [28], as these were the values for SonoVue that were observed

experimentally. Also in the following sections specific bubble radii have been investigated, the reasons that these radii have been used are given in Table 6.2.

Parameter	Value
Liquid density, ρ_l , kg m^{-3}	1000
hydrostatic Pressure, p_0,(kPa)	100
Surface tension of water/air, σ_{water} , (N/m)	0.07
Polytropic constant of gas, γ	1.4
liquid viscosity(bulk) , μ_L,(Pa s)	0.001
Shell viscosity (dilatational) , k_s, (kg/s)	1.5×10^{-9}
Speed of sound in a liquid, c_s , (ms^{-1})	1
Shell elasticity, χ, (N/m)	0.3

Table 6.1 The parameter values used for the simulations

Radius value, μm	Reason chosen
0.25	Smallest bubble radius found in population experimentally
0.935	Mean sized bubble
6.9	linear resonant bubble size at 0.5MHz
2.2	exhibited interesting behaviour at 0.5MHz
1.3	linear resonant bubble size at 1.614MHz
3,4,5	selected to investigated the behaviour of bubbles with radii between 2.2μm and 6.9μm

Table 6.2 Table explaining selection of bubble sizes simulated

6.6 Effect of Bubble Size

The first question that needed to be answered from the simulations was which bubble size(s) in a given population would dominate the acoustic emissions at different excitation pressures. It is known that for low amplitude oscillations that there exists a

resonant bubble size for a given excitation frequency that will exhibit the largest radial amplitude of oscillation and produce the largest radiated pressure this can be seen from Equation (6.16).

As the excitation pressure increases, the amplitude of oscillation of the bubble wall will increase, as will the velocity and acceleration, which in turn relates to an increase in the radiated pressure. It can be seen from Figure 6.3 that as the pressure increases the smaller bubbles start to exhibit larger amplitudes of oscillation with respect to their resting radius than the larger bubbles. For example, Figure 6.3(a), for a driving frequency of 0.5MHz and driving pressure of 70kPa, a resonant radius of, R_0 = 6.9μm, can be clearly observed. At p_A = 200kPa, a peak is still observed at 6.9μm but it can be seen that the smaller bubbles have started oscillating at proportionally larger amplitudes. When the pressure is increased to 2MPa, the smallest bubble has the largest R_{max} and as the bubble size increases, R_{max} exponentially decreases. This behaviour is again seen in Figure 6.3(b), for a driving frequency of 1.614MHz. This point is demonstrated more clearly in Figure 6.4 which shows that at low amplitudes of oscillation the resonant bubble size corresponds to the largest amplitude of oscillation, but at the higher pressure the smallest bubble has the largest amplitude of oscillation and the largest bubble has the smallest. Therefore it can be reasonably assumed that at higher pressures the majority of the signal detected is from the smaller bubbles in the population, and this is confirmed by the simulation shown in Figure 6.5.

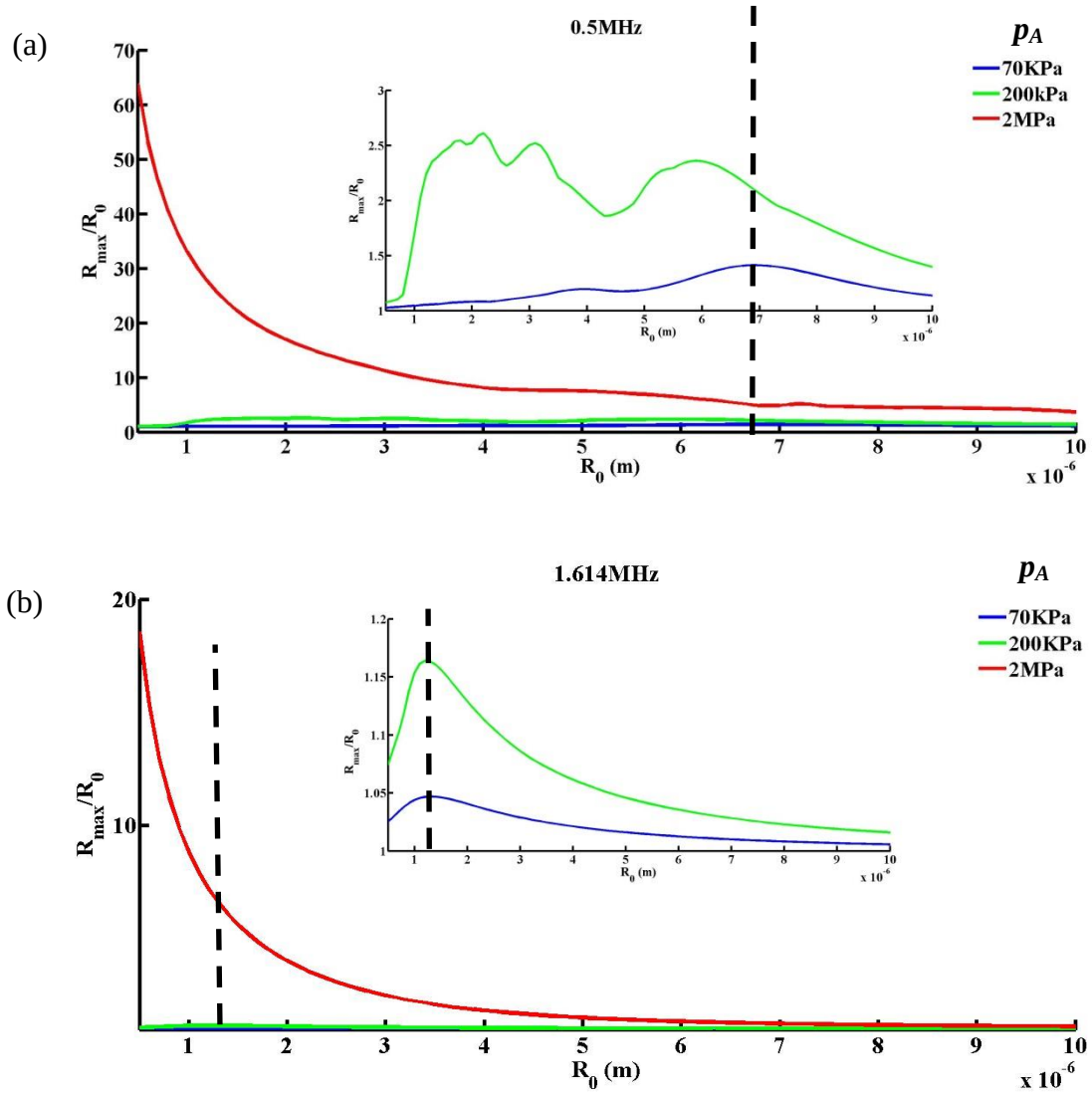

Figure 6.3. Shows the maximum amplitude of oscillation vs. initial bubble size, R_0, for a range of driving pressures and frequencies (a) 0.5MHz and (b) 1.614MHz. The linear resonant bubble size is indicated by the black dotted line and the insert panel shows the results for the lower pressures with a magnified vertical axis.

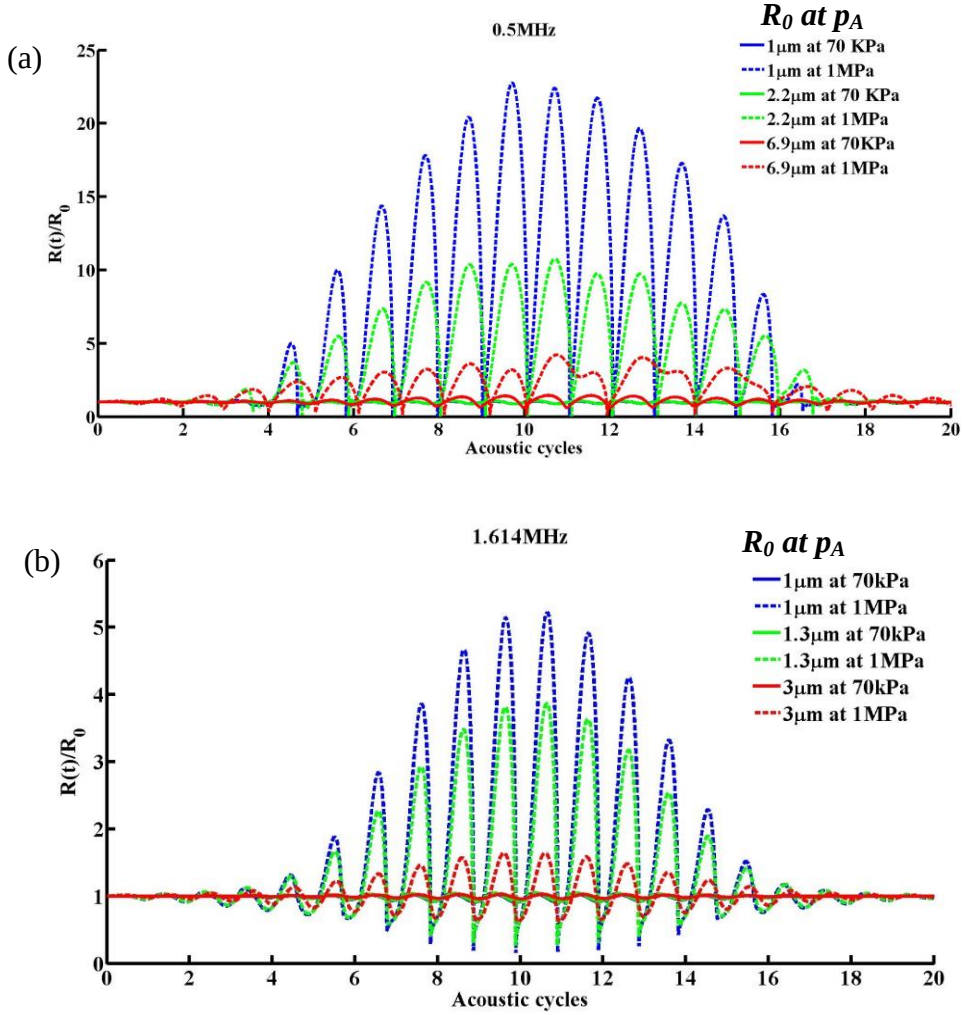

Figure 6.4. Radius-time curves for different bubble sizes and excitation pressure amplitudes at (a) 0.5MHz and (b) 1.614MHz linear resonant bubble size.

(a)

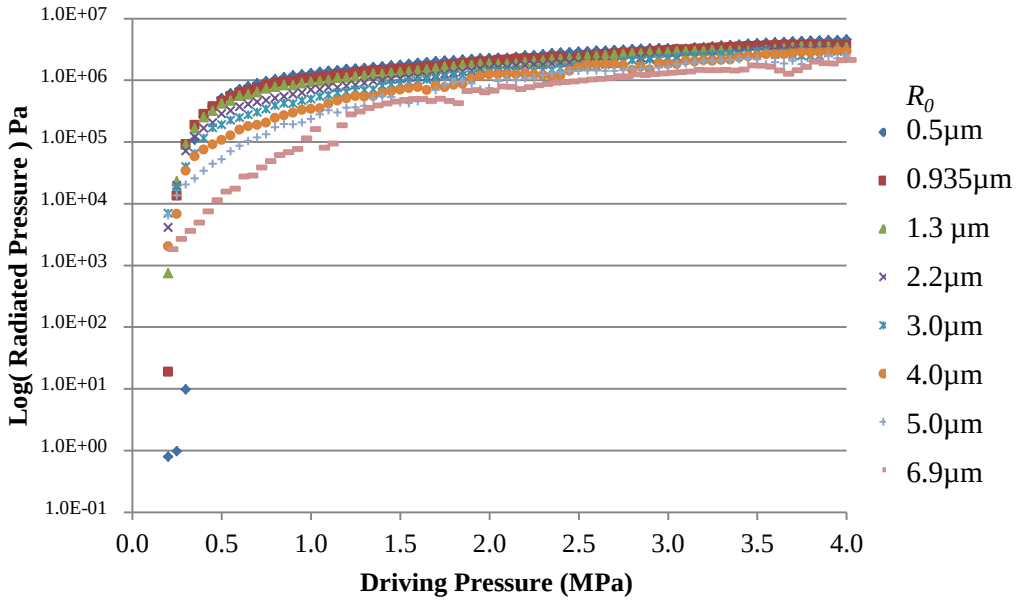

(b)

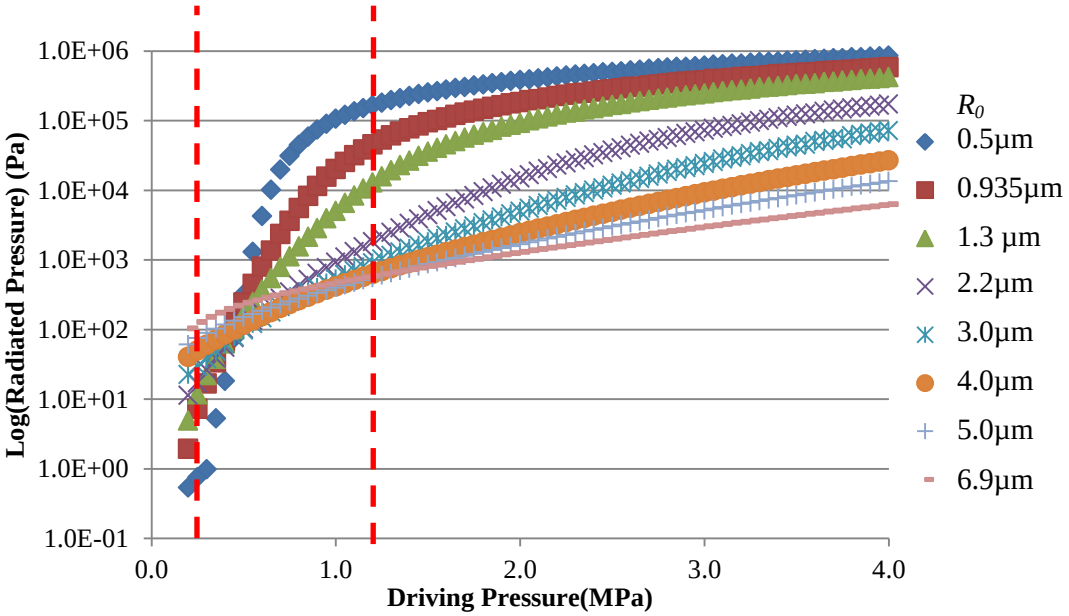

Figure 6.5. Peak negative amplitude Radiated pressure vs. excitation pressure amplitude for different initial bubble radii for (a) 0.5MHz (b) 1.614MHz.where the red dotted lines show the region in which the smaller than resonate size start and eventually all dominate over the resonate bubble size.

The radii chosen for these graphs is discussed in Table 6.2. Figure 6.5 also shows that there is a range of excitation pressures over which the radiation from the smaller bubbles starts to exceed that from the larger bubbles. This change happens over a small range of relatively low driving pressures at 0.5MHz pulse (Figure 6.5(a)), but over a wider range of pressures at 1.614MHz, (Figure 6.5(b)). At the lowest driving pressure, the linear resonant bubble size produces the largest peak P_s^a. As p_A increases to about 0.4MPa a turning point is observed where the maximum P_s^a from smallest bubbles becomes the largest. At ~ 1.5MPa all the bubble sizes represented have a larger maximum P_s^a than the resonant bubble size.

These turning points correspond to the observed behaviour from the experimental data: the rate at which the total energy received was seen to increase with pressure, Figure 6.8, and has been hypothesised to show which bubble sizes are most dominate in these pressures. Below 0.4MPa the low amplitude resonant size and the larger bubbles dominate, in the range 0.4MPa-1.5MPa a mixture of the smallest bubbles and the low amplitude resonate radii dominate, beyond 1.5MPa this signal is purely dominated by the smaller bubbles. This is thought to be due to the fact that the population distribution of bubble size is expected to have a Gaussian profile, while the radiated pressure is expected to have an almost linear distribution, and the convolution for the two to give the bubble size that gives the largest signal is roughly at the mean, hence giving the best correlation, see Figure 6.4. Therefore it is just mere coincidence that in this case that the mean gave a good correlation. It has been shown when investigating this hypothesis that the dominate bubble should be 0.65μm, Figure 6.6, which does not correlate very well to the data, this is possibly due to the delay between assessing the size distribution then performing the experiment meaning that the population probably grew in size.

Average	Pearson Correlation factor for *f*=0.5MHz	Pearson Correlation factor for *f*=1.614MHz
Mode, R_0=0.45μm	0.985208	0.894171
Median, R_0=0.76μm	0.992974	0.925436
Mean, R_0=0.935μm	0.994806	0.951755

Table 6.3 showing the correlation factor for the different averages in the population of the bubbles for each frequency

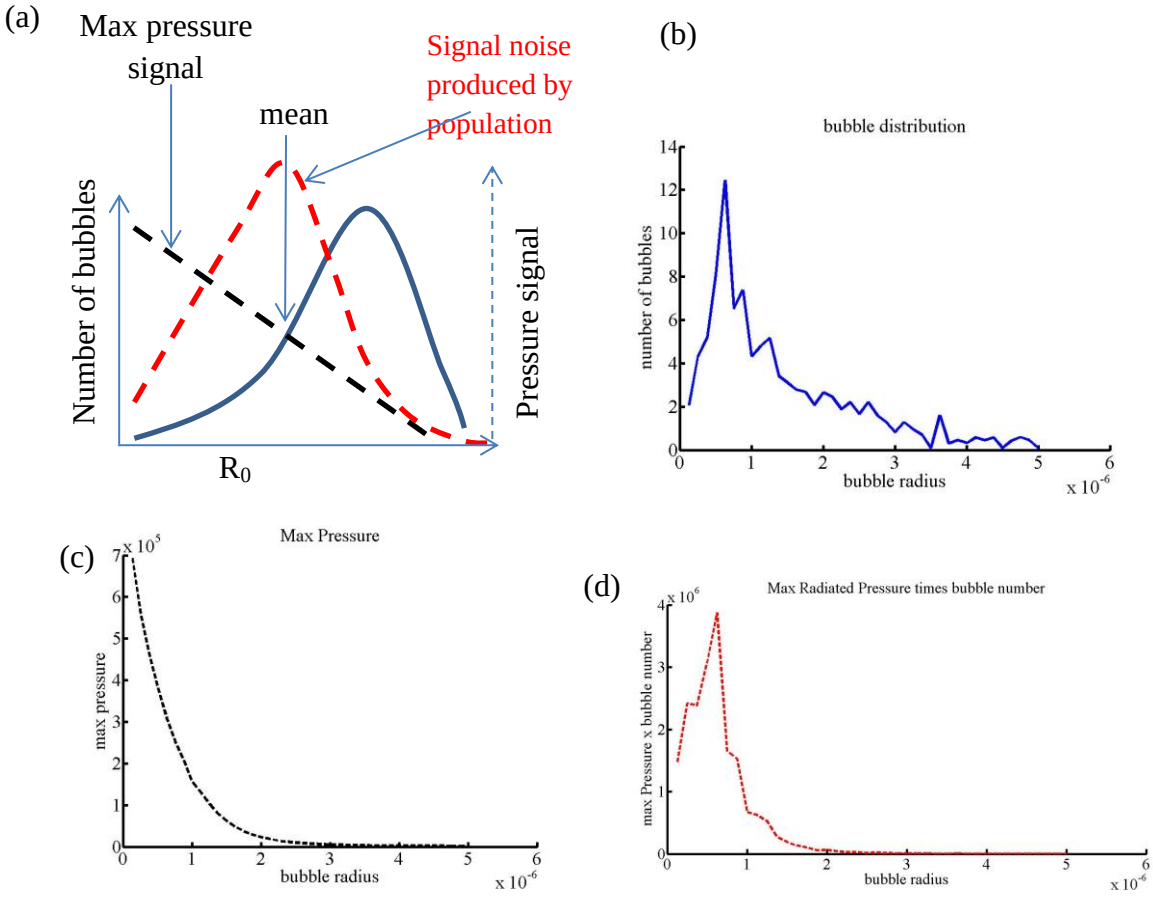

Figure 6.6(a) schematic of theory (b) showing the bubble populations, (c) showing the maximum pressure re-radiated over a number of radii, (d) convolved max pressure and bubble populations, showing that 0.65μm is the prominent bubble signal.

However the question remains which bubble size should be taken to predict when inertial cavitation becomes dominate in the population. It could be argued that the smallest bubble should be used, however this will undergo inertial cavitation first, while the majority of the population is not, therefore underestimating when the signal becomes dominated by inertial cavitation. If modelling with a large bubble then the inertial cavitation limit will be over predicted, as they will undergo inertial cavitation last. This can be seen in Figure 6.7. This could however lead one into thinking that it is the mode of the population that should be modelled. However when comparing the trend of the experimentally total energy received with the theoretical wall Mach number for each pressure, it was found from correlating the mean, median and mode of the SonoVue population that the mean gave the best correlation Table 6.3.

It is therefore evident that the bubble being chosen is not just dependent on the distribution from the population but also on the frequency and pressure being used. However the bubble size used shall be taken from the population after the turning point has occurred, so as to model the higher pressures better.

It should also be noted that in Figure 6.7(a) the behaviour of the 2.2μm radius is peculiar. On further investigation this was seen to be due to the size, frequency and shell parameters chosen and that a radius with behaviour similar to this occurs for each frequency and that it's just by coincidence that it was chosen in this study. Graphs to show that this is not a chaotic region or a numerical error can be found in Appendix D.

(a)

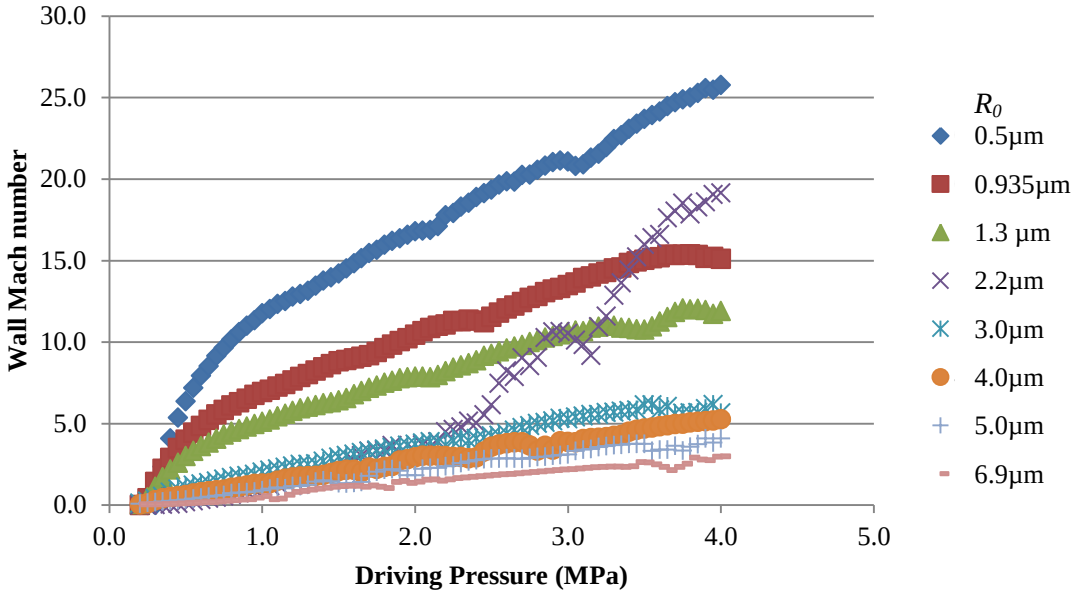

(b)

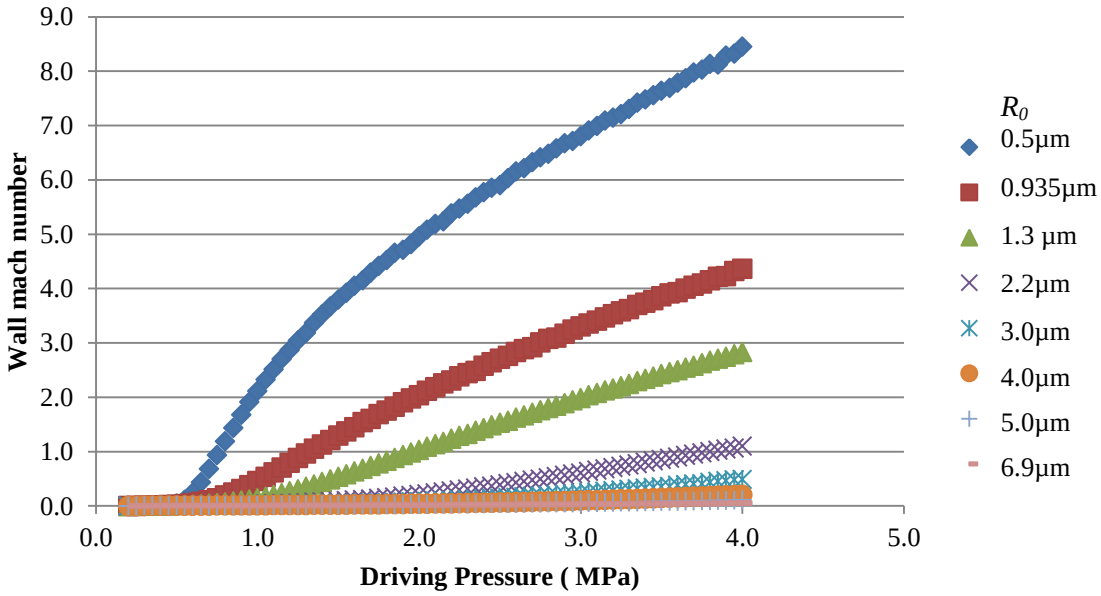

Figure 6.7 showing the wall Mach number for the population (a) here f=0.5MHz and (b) where f=1.614MHz.

6.7 Determination of the Cavitation Threshold

The variation with driving pressure in the total energy emitted from the bubble population measured experimentally was compared with that calculated from the simulations and also the corresponding maximum wall Mach number for each bubble size and driving frequency. Simulations were carried out for both coated and uncoated bubbles

It can be seen from Figure 6.8 and Figure 6.9 that the trend seen in the experimental data is replicated by the simulated results for both frequencies. It can also be seen that there is a large increase with a change in gradient of the graph for the experimental data, when the wall Mach number equals 1, indicating a change in behaviour of the microbubbles, and that inertial cavitation is dominant. The model was run for both a variable surface tension and an uncoated bubble, to assess if including the variable surface tension increased the correlation of the trend seen between the experimental and modelled data. From this, it was found that at the lower frequency of 0.5MHz, the correlation between the experimental data and the two models were equivalent with a Pearson's correlation factor of 0.99. However at the higher frequency of 1.614MHz the variable model was found to have a better correlation with the experimental data having a Pearson's correlation factor of 0.95, compared to the uncoated model which had a Pearson's correlation of 0.91. From this it can be concluded that the variable model gave a better prediction at higher frequencies. Therefore the variable surface tension model should be used to predict where cavitation threshold occurs.

A single model that can predict where in the experiment cavitation threshold should occur is useful as it will cut down on the amount of calibration time during an experiment which would need to occur to find where this point is. This would also allow experimentalists to size the bubble populations and then know which pressure to use to

observe inertially dominated behaviour. This study also indicates that the shell is not completely negligible, as conventional wisdom dictates but does have an effect on the compression stage of the oscillations and should therefore be included in models of large amplitude oscillations. This is due to the bubble having higher viscosity during the compression causing some of the energy in the oscillation to be dissipated and thereby cause smaller expansions with a slower bubble wall velocity.

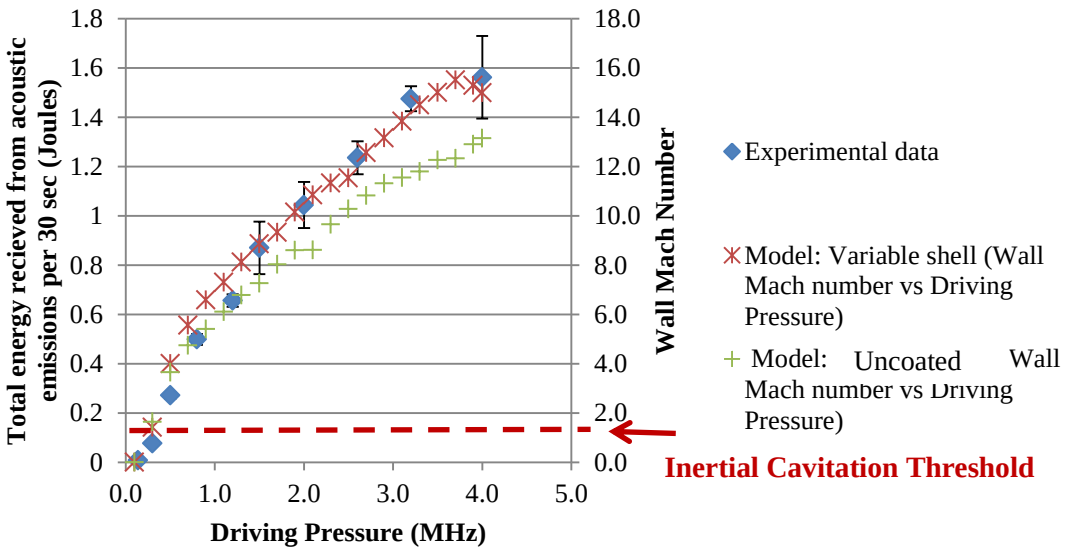

Figure 6.8 Graph comparing the experimentally found Total energy received from the acoustic emissions, (axis on the left hand side), to the modelled Wall Mach number, (axis on the right hand side) for varying pressure at a driving frequency of 0.5MHz. The red dotted line represents where Mach 1 has been reached and therefore inertial cavitation threshold.

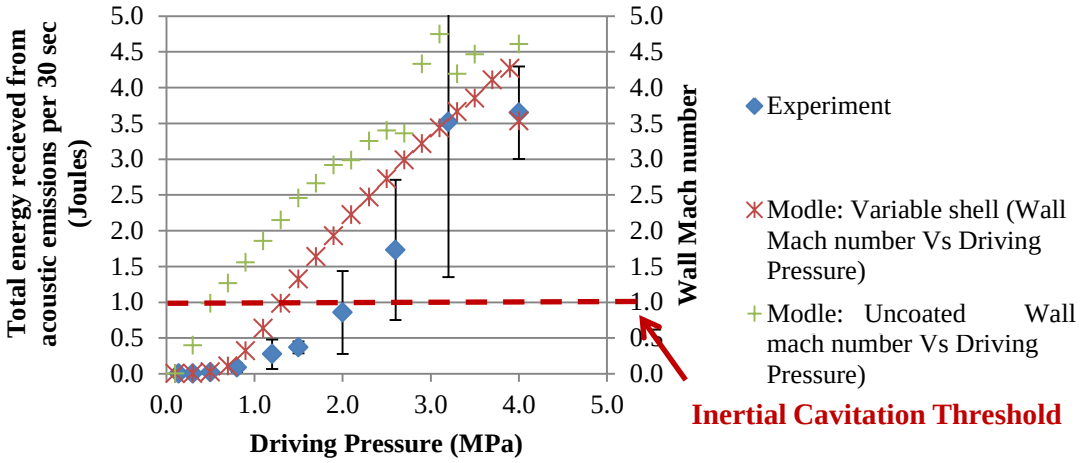

Figure 6.9. Graph comparing the experimental Total energy received from the acoustic emissions, axis on the left hand side), to the modelled Wall Mach number, (axis on the right hand side) for varying pressure at a driving frequency of 1.614MHz. The red dotted line represents Mach 1 has been reached and therefore inertial cavitation threshold.

6.8 Conclusion

In conclusion it has been shown here that the cavitation threshold of a population of bubbles can be predicted using a single microbubble model when using the radii of the population that produces the largest scattering size. As it has been theoretically proven, and confirmed by the experimental data, that as the pressure increases it is the smaller radii bubbles that begin to have the dominant effect on the emissions received experimentally. The trend seen both in the theory and experiment confirms that the inertial cavitation threshold does occur close to where the theoretical wall Mach number equals one. The model presented here and the method of calibration is still in the early stages of development and the author recognises that more data comparison and a more refined model are needed, by incorporating the other shell effects on the bubble, to completely validate this method of as a way to predict the cavitation threshold limit. This shall be discussed more detail in Chapter 9 in the future work section.

6.9 References

1. Pichon, C., et al., *Recent advances in gene delivery with ultrasound and microbubbles.* Journal of Experimental Nanoscience, 2008. **3**(1): p. 17-40.
2. Alexandrov, A.V., *Ultrasound Enhanced Thrombolysis for Stroke.* Seminars in Cerebrovascular Diseases and Stroke, 2005. **5**(2): p. 106-110.
3. Bull, J.L., *The application of microbubbles for targeted drug delivery.* Expert Opinion on Drug Delivery, 2007. **4**(5): p. 475-493.
4. Ferrara, K., Pollard, R., and Borden, M., *Ultrasound microbubble contrast agents: Fundamentals and application to gene and drug delivery.* Annual Review of Biomedical Engineering, 2007. **9**: p. 415-447.
5. Shohet, R.V., et al., *Echocardiographic Destruction of Albumin Microbubbles Directs Gene Delivery to the Myocardium.* Circulation, 2000. **101**(22): p. 2554-2556.
6. Teupe, C., et al., *Vascular Gene Transfer of Phosphomimetic Endothelial Nitric Oxide Synthase (S1177D) Using Ultrasound-Enhanced Destruction of Plasmid-Loaded Microbubbles Improves Vasoreactivity.* Circulation, 2002. **105**(9): p. 1104-1109.
7. Stride, E.P. and Coussios, C.C., *Cavitation and contrast: the use of bubbles in ultrasound imaging and therapy.* Proceedings of the Institution of Mechanical Engineers Part H-Journal of Engineering in Medicine, 2010. **224**(H2): p. 171-191.
8. Chen, W.-S., et al., *Inertial cavitation dose and hemolysis produced in vitro with or without Optison®.* Ultrasound in Medicine & Biology, 2003. **29**(5): p. 725-737.
9. Chen, H., et al., *Preliminary Observations on the Spatial Correlation Between Short-Burst Microbubble Oscillations and Vascular Bioeffects.* Ultrasound in Medicine & Biology, 2012. **38**(12): p. 2151-2162.

10. Chen, W.-S., et al., *The pulse length-dependence of inertial cavitation dose and hemolysis.* Ultrasound in Medicine & Biology, 2003. **29**(5): p. 739-748.
11. Church, C., *The effects of an elastic solid surface layer on the radial pulsations of gas bubbles.* J. Acoust. Soc. Am., 1995. **97**(3): p. 1510.
12. Hoff, L., Sontum, P.C., and Hovem, J.M., *Oscillations of polymeric microbubbles: Effect of the encapsulating shell.* Journal of the Acoustical Society of America, 2000. **107**(4): p. 2272-2280.
13. Herring, C., *Theory of the pulsations of the gas bubble produced by an underwater explosion*. 1941: Columbia Univ., Division of National Defense Research.
14. Trilling, L., *The collapse and rebound of a gas bubble.* Journal of Applied Physics, 1952. **23(1)**: p. 14-17.
15. Gilmore, F.R., *The growth or collapse of a spherical bubble in a viscous compressible liquid.* 1952.
16. Keller, J., *Bubble oscillations of large amplitude.* J.Acoust.Soc.Am., 1980. **68**(2): p. 628.
17. Prosperetti, A., *Nonlinear bubble dynamics.* J.Acoust.Soc.Am., 1988. **83**(2): p. 502.
18. Leighton, T.G., *The Acoustic Bubble*. 1994: Academic Press.
19. Lauterborn, W. and Kurz, T., *Physics of bubble oscillations.* Reports on Progress in Physics, 2010. **73**(10).
20. Church, C.C. and Carstensen, E.L., *"Stable" inertial cavitation.* Ultrasound in Medicine & Biology, 2001. **27**(10): p. 1435-1437.
21. Flynn, H.G., *Cavitation dynamics: II. Free pulsations and models for cavitation bubbles.* The Journal of the Acoustical Society of America, 1975. **58**(6): p. 1160-1170.

22. Noltingk, B.E. and Neppiras, E.A., *Cavitation Produced by Ultrasonics.* Proceedings of the Physical Society of London Section B, 1950. **63**(369): p. 674-685.

23. Webb, I.R., Payne, S.J., and Coussios, C.-C., *The effect of temperature and viscoelasticity on cavitation dynamics during ultrasonic ablation.* The Journal of the Acoustical Society of America, 2011. **130**(5): p. 3458-3466.

24. Webb, I.R., Payne, S.J., and Coussios, C.C., *Effect of temperature on rectified diffusion during ultrasound-induced heating.* J Acoust Soc Am, 2011. **130**(5): p. 3450-7.

25. Collin, J.R. and Coussios, C.C., *Quantitative observations of cavitation activity in a viscoelastic medium.* J Acoust Soc Am, 2011. **130**(5): p. 3289-96.

26. Hilgenfeldt, S., Lohse, D., and Zomack, M., *Response of bubbles to diagnostic ultrasound: a unifying theoretical approach.* The European Physical Journal B - Condensed Matter and Complex Systems, 1998. **4**(2): p. 247-255.

27. Hilgenfeldt, S., Lohse, D., and Zomack, M., *Sound scattering and localized heat deposition of pulse-driven microbubbles.* The Journal of the Acoustical Society of America, 2000. **107**(6): p. 3530-3539.

28. Marmottant, P., et al., *A model for large amplitude oscillations of coated bubbles accounting for buckling and rupture.* Journal of the Acoustical Society of America, 2005. **118**(6): p. 3499-3505.

7 Sensor design

The aim of this chapter is to find a regime in which an encapsulated gas bubble would be a good sensor, to quantitatively assess environmental changes in the liquid, such as hydrostatic pressure, density and viscosity. To restate this thesis is not concerned with the application of bio-sensing, but harnessing bubbles as sensors for other applications, in which conventional measurements cannot be undertaken, but need to be investigated. Therefore to find a regime in which bubbles can be used as sensors the size of the bubbles will no longer be required to be micro.

Thus this chapter investigates and suggests a size and pressure that produces the most stable bubble sensor that can quantitatively detect changes in the dynamic response, both optically and similarly from radiated pressure to calculate ±5% change in the liquid properties surround it.

7.1 Current Issues with Microbubbles

In principle, encapsulated gas bubbles are ideal sensors for the investigation of physical properties at the microscale: they respond strongly to ultrasound and their dynamic response is very sensitive to changes in the surrounding environment. As the results in previous chapters have demonstrated, however, there are a number of practical difficulties in developing a bubble-based sensor. It is very difficult to produce an entirely uniform population of bubbles, i.e. one in which both bubble size and coating properties are identical and defined. Techniques such as microfluidics and coaxial electro hydrodynamic atomisation (CEHDA) can produce a near mono-disperse population, however when their shell properties and dynamic responses are examined it is found that these vary widely over

the population [1, 2]. This represents a significant problem in using them as calibrated sensors.

A further major problem with lipid coated microbubbles is that they can shed their shell when oscillating, which means that their shell properties and hence dynamic response is continually changing both during the course of a pulse and in between pulses [3-5]. This process occurs at different rates depending on the liquid and environment that the bubble is in, as shown previously in Chapter 4, making it a very difficult process to predict, and hence such bubbles are unsuitable for use as sensors (if this mechanism could be understood fully then it could make a good sensor). Even when no acoustic pulse is applied, the population distribution is unstable due to gas diffusion in/out of the bubbles, as discussed in Chapter 3.

Another problem with microbubbles of the size used as ultrasound contrast agents is that they are too small to produce a readily measureable change in their dynamic response corresponding to an alteration in the environment. For uncertainties in experimental equipment to be neglected, a change in radial amplitude of oscillation of at least ±0.5μm is required to be visible under optical video microscopy, and whilst acoustic measurements are typically more sensitive, the uncertainty associated with hydrophone measurements again limits the minimum amplitude of oscillation required to produce an adequate signal. When observing the pressure trace of the signal the difference needs to overcome noise in the signal, leading to a difference in the region of 1kPa or more. However this will depend on how far away from the bubble the hydrophone is and so any changes shall be quantified as a % change in the maximum signal.

7.2 Specifications and Assumptions for an Ideal Sensor

To be used effectively as sensors, bubbles need to meet the following specifications:

- Stable: the bubble properties should not change over the course of the experiment
- Homogeneous: All the bubbles in the population should be identical, in size and mechanical properties.
- Characteristics: the size and coating properties should be well defined
- Acoustically active: the bubble should produce a sufficiently large response to ultrasound excitation to be easily detectable
- Sensitive: the combination of bubble size driving pressure and frequency should be such that changes in the environmental parameters should produce measurable change in the bubble response.

To summarize a stable homogenous population that is acoustically active and large enough to produce an observable change in oscillations corresponding to environmental variations, is required. The environmental parameters being investigated shall be the density, ρ_l, viscosity, μ_l and the hydrostatic pressure, p_0 of the liquid.

A stable homogenous population requires that the bubbles are mono disperse in size possessing identical shell properties that do not change with time, i.e., before, during or after being excited by an acoustic pulse. This means that lipid shedding should be negligible and therefore can be neglected from the model, suggesting that the shell should be made out of a polymer which does not shed, however these bubbles are less echogenic than the lipid coated microbubbles [6]. Therefore for an ideal sensor a polymer bubble with SonoVue type shell properties would be desirable, thus the values from [7] have been used for the bubbles shell parameters in the following simulations, which are shown in Table 7.2.

The change in the radial response needs to be at least +/- 0.5µm to be observable by an optical system this means considering a radius range 10-700µm. This puts a constraint

on the bubble oscillations requiring them to remain stable, this means that no inertial cavitation should occur; this limits the ratio of maximum expansion to $\frac{R_{max}}{R_0} < 2$, where R_{max} is the maximum amplitude of radial oscillation. Also to minimize the uncertainty in the experimental measurements the bubble should be driven at its resonance frequency to produce the largest radial response. The nonlinear response of the bubble could also be exploited here to indicate changes in the dynamic response; however the previous sensitivity study in Chapter 4 indicated that the fundamental response was highly sensitive and always produced the largest change in radial amplitude / radiated pressure.

In order to investigate the optimal parameters of a sensor, Equation (6.13) from Chapter 6 shall be employed. However the range of parameters being investigated here is outside that examined in previous chapters and therefore the validity of the model needs to be verified. The region of interest was from R_0= 10-600μm and pressures from 10–1000kPa. The bubble was assumed to be away from any boundaries and the other bubbles so that no secondary radiation forces can impede on the bubble causing non-spherical oscillations. In this range of sizes surface modes may also occur, these have been assumed to be negligible for the following simulation. Therefore a single bubble model away from the wall, with a variable surface tension ignoring lipid shedding should be used. At these pressures and sizes the Equation (6.13) found in Chapter 6 will be used which incorporates a variable surface tension and is valid for large oscillations which are expected in this range. However before it can be implemented a few checks need to be carried out to ensure that the model is still valid.

The first assumption to check is that the model is still in the range where $c_s/f_0 >> R_0$, still holds. Where c_s is the speed of sound in the liquid and that f_0 is the resonant frequency of the wave. This is proven in Table 7.1, where the equation for f_0 is found in Appendix A .

R_0, μm	f_0, kHz	c_s/f_0 , μm
10	325	4 000
50	65	22 000
100	32	45 000
500	6	229 000
1000	3	459 000

Table 7.1 showing the equilibrium radius, resonate driving frequency and the ratio c_s/f_0 where $c_s=1500ms^{-1}$

As stated previously, in Chapter 6, for the bubble to remain a stable oscillator, the ratio of R_{max}/R_0 <2 must hold, this criterion was chosen as it was an output already needed to investigate the effect of the change in environmental criteria and therefore cut down on the computation time as opposed to calculating $\frac{\dot{R}}{c_s}$ >1 . To check this, the model was run for the parameters stated in Table 7.2 over the range of driving pressures, p_A= 25-1000kPa and equilibrium radii, R_0=10-600µm. It can be seen from Figure 7.1 that all of R_0 range is valid for pressures of 50kPa as the expansion ratio stays below 2. Therefore the reviewed ranges to be investigated are shown in Table 7.3.

However this model does not take into consideration the thermal damping which becomes dominant compared to the other damping terms in this range, see Figure 7.2. The formulas used to calculate these damping constants are found in Appendix A. This should have only a small effect on the results, as it would not be the dominant term in the model, having a magnitude of ~10^9 compared to the most dominant term of ~10^{14}, but it is something that should be considered when looking at the results below. Bubbles of this size can also have observable surface waves, these are waves that occur on the shell and create a dimpled effect like a golf ball, which can affect the spherical nature of the bubble, however for these calculations these effects shall be neglected, as they present no use in the optical or acoustical detection in the change of the response. However it should be noted that for larger bubbles in this range ~1mm in diameter, these effects may become detectable both

optically and acoustically, and could have an effect on the bubbles response via energy being removed from the breathing mode.

Parameter	Value
Liquid density, ρ_l , kg m^{-3}	1000
hydrostatic Pressure, p_0,(kPa)	100
Surface tension of water/air, σ_{water} , (N/m)	0.07
Polytropic constant of gas, γ	1.4
liquid viscosity(bulk) , μ_L,(Pa s)	0.0015
Shell viscosity (dilatational) , k_s, (kg/s)	$15x10^{-9}$
Speed of sound in a liquid, c_s , (ms^{-1})	1500
Shell elasticity, χ, (N/m)	0.3
Number of acoustic cycles, sinusoidal	20

Table 7.2 parameters used to run the simulations

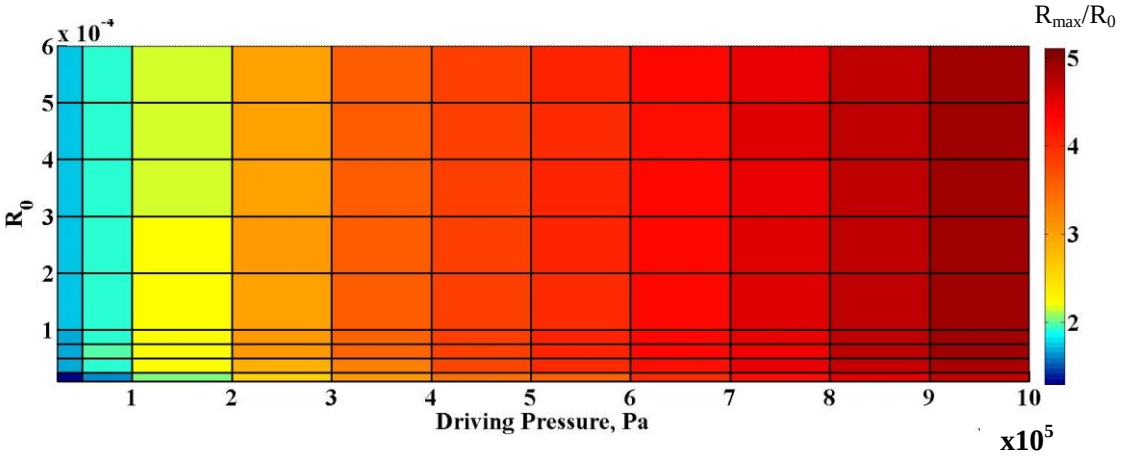

Figure 7.1 Plot showing the ratio of R_{max}/R_0 for a range of pressures and radius, actual values shown in Appendix E.

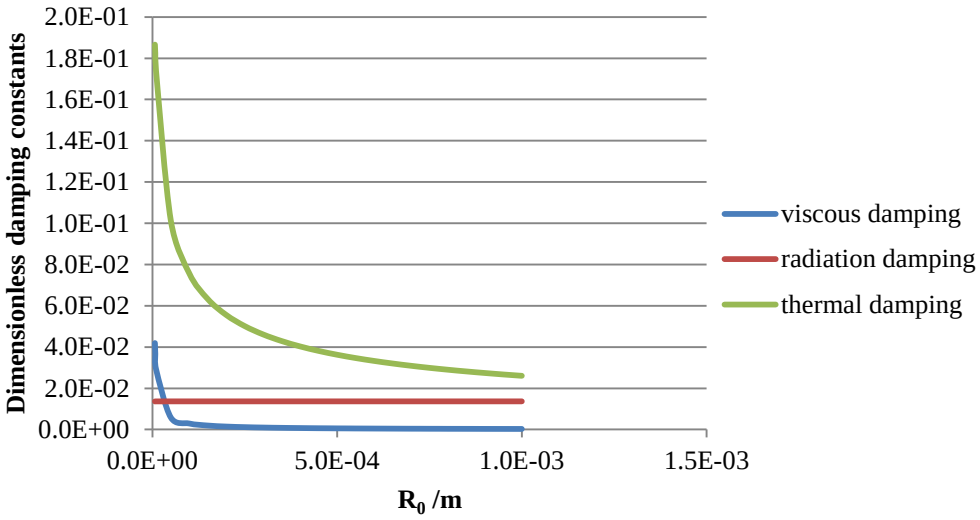

Figure 7.2 Showing the dimensionless damping constants at resonance for the range of R_0 used. This shows that thermal damping is dominating in this range and should be included in the model. These coefficients can be found in Appendix A.

Parameter	Range
R_0, (µm)	50-700 in steps of 65
p_A, (kPa)	10-50 in steps of 5
$p_{0,}$ (kPa)	100±5%
ρ_l, (kg m^{-3})	1000±5%
μ_l ,(Pa s)	0.0015±5%

Table 7.3 Ranges of values being investigated

7.3 Results

The observable differences should correlate to a ±5 % change in the environmental parameter; this change was indicated by the industrial partner as a desirable measurement in sensitivity. The model was run for a 20 cycle sinusoidal pulse, for the parameters stated in Table 7.2 & Table 7.3. The environmental changes investigated were a ±5%, variation in ρ_l, μ_l and p_0 (Table 7.3). When the value was not being varied it was held at its initial value as stated in Table 7.2. The simulations were used to calculate the difference in the maximum radial amplitude, ΔR_{max}, in the oscillation and maximum radiated pressure, $P^a_{s\_max}$, via Equation (6.19) in Chapter 6 (which is measured 1cm away from the bubble) , caused by the change in the environmental parameter.

7.3.1 ±5% Change in ρ_l

First the observable change caused by a ±5% change in liquid density was investigated. The results, see Figure 7.3, show that for a bubble R_0 above 570µm a ΔR_{max} > 1µm is observed, the optimum pressure, (the driving pressure that cause the largest change in response at resonance frequency) appears to be 40kPa. The maximum differences are 1.30 and 1.39 µm for a -/+ 5% change respectively, this corresponds to a ± 0.09 % change in R_{max}, which is quite small. The biggest difference in the $P^a_{s\_max}$ was found for the largest R_0, 700µm and p_A, 50kPa, for both the +/- 5% change. This correlated to a change of 827 and 882 Pa for a -/+ 5% change respectively, which is a +/- 0.5% change in the $P^a_{s\_max}$.

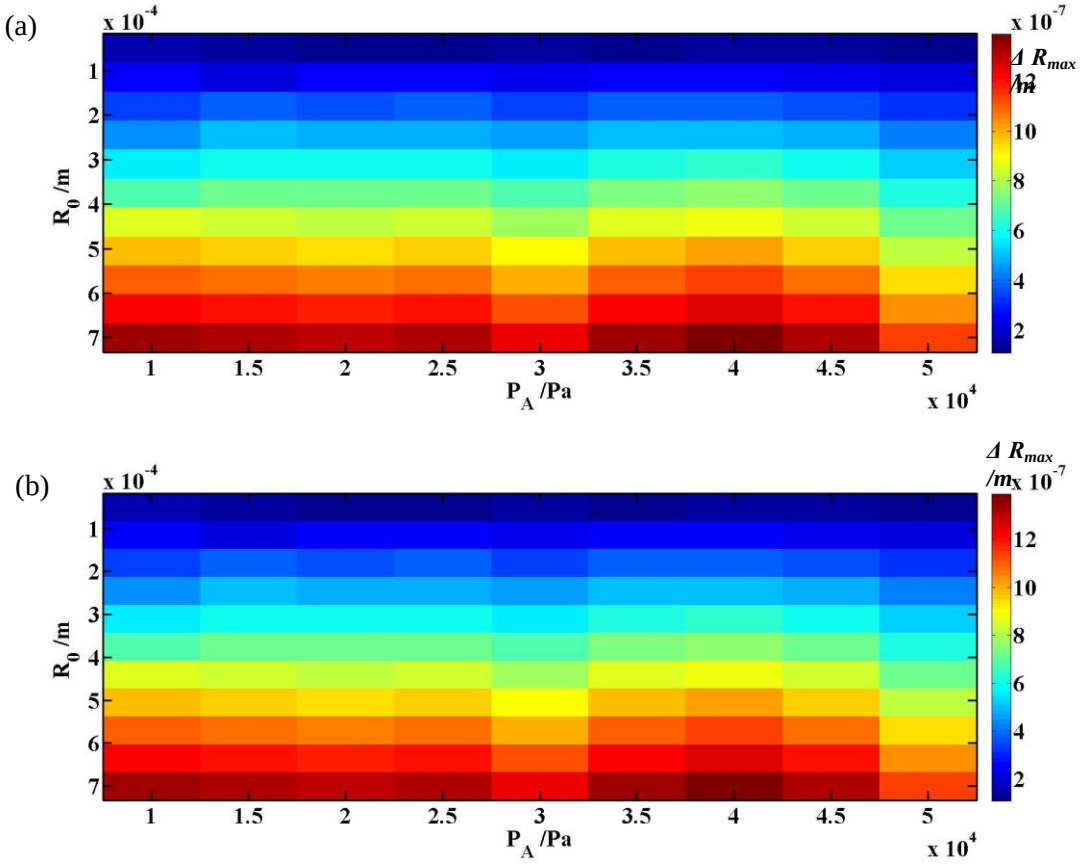

Figure 7.3 Showing the absolute ΔR_{max} for (a) -5% and (b) +5% in ρ_l

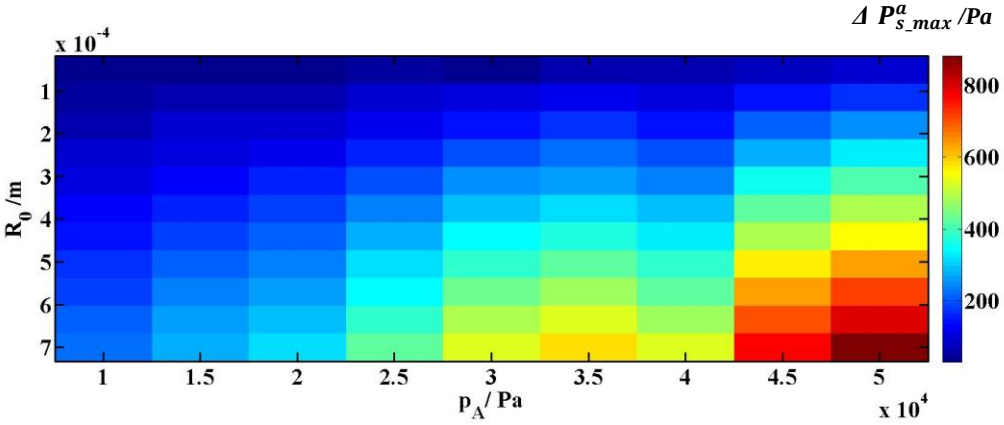

Figure 7.4 Showing the absolute Δ $P^a_{s\_max}$ for a -5% change in ρ_l.

7.3.2 ±5% Change in μ_l

Now investigating the observable change caused by a ±5% change in liquid density. As can be seen from Figure 7.5, ΔR_{max} <1μm for all the radii at all pressures and the ΔR_{max} responses were similar (but with the opposite sign) for both +/-5% change. The maximum difference was observed for R_0 =375μm with a ΔR_{max} =± 6.18x10^{-8} m. When considering the difference in $P^a_{s\_max}$, Figure 7.6, the largest difference is seen for the smallest R_0, 50μm at the largest p_A=50kPa, though this change is only 25Pa and would not be observable. Therefore the use of microbubbles to observe changes in μ_l in this range is not feasible. In this case it can be seen that the trend observed for the largest change observed for the $P^a_{s\_max}$ and ΔR_{max} is reversed. This is because the difference in the radial oscillation is so small that the largest difference for $P^a_{s\_max}$ will be proportional to the driving pressure used. This has though caused a very small difference with a variation of 12Pa over the whole range.

(a)

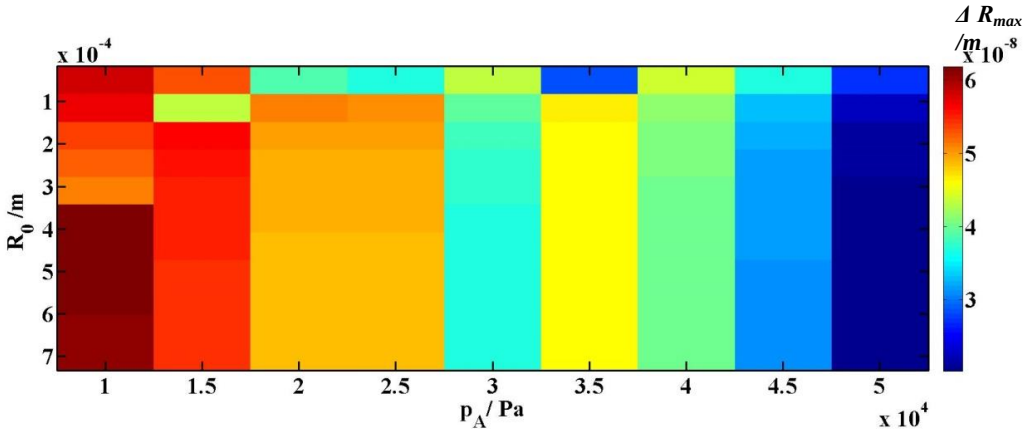

Figure 7.5 *Showing the absolute ΔR_{max} for -5% in μ_l*

(b)

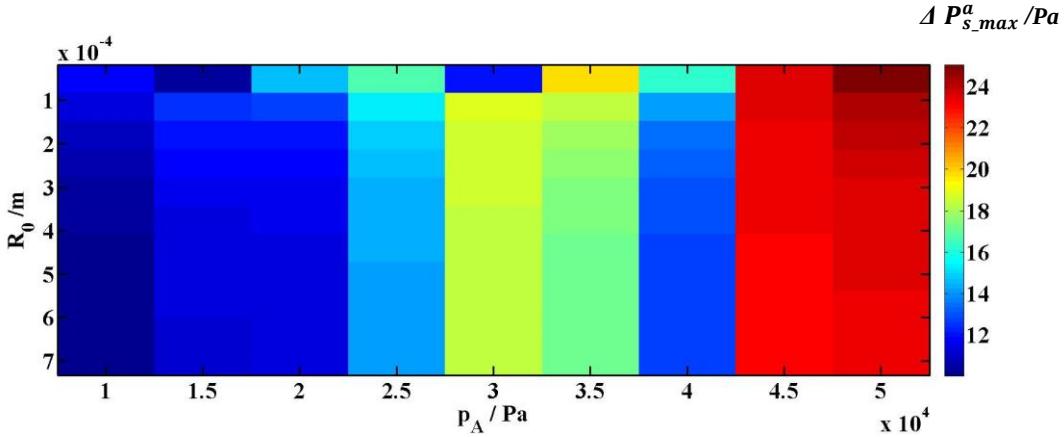

Figure 7.6 Showing the absolute $\Delta P^a_{s\_max}$ -5% in μ_l

7.3.3 ±5% Change in p_0

It can be seen from Figure 7.7 that a ±5% change in p_0 produces a ΔR_{max}>1μm for the majority of the bubbles, except the smallest two radii, R_0<180μm. For Figure 7.7 (b) the +5% it can be seen that the largest pressure produces a noticeably smaller ΔR_{max} than the -5% . However the maximum difference is found when R_0=700μm and p_A=35kPa , where ΔR_{max}=19.8μm for a -/+ 5%, this corresponds to a ± 1.5 % change in the R_{max}, still when compared to the radius of the bubble it is still small. The pressure difference again was larger with the $\Delta P^a_{s\_max}$ output being found at a R_0=700μm and a p_0=40and 45kPa for a -/+ 5% change respectively, at both these pressures the % in $\Delta P^a_{s\max}$ is 3.5-4.5%. Yet when comparing this in real terms this corresponds to a maximum radiated pressure ≈100kPa with a ±1kPa change. Which if the signal to noise ratio is high should be observable.

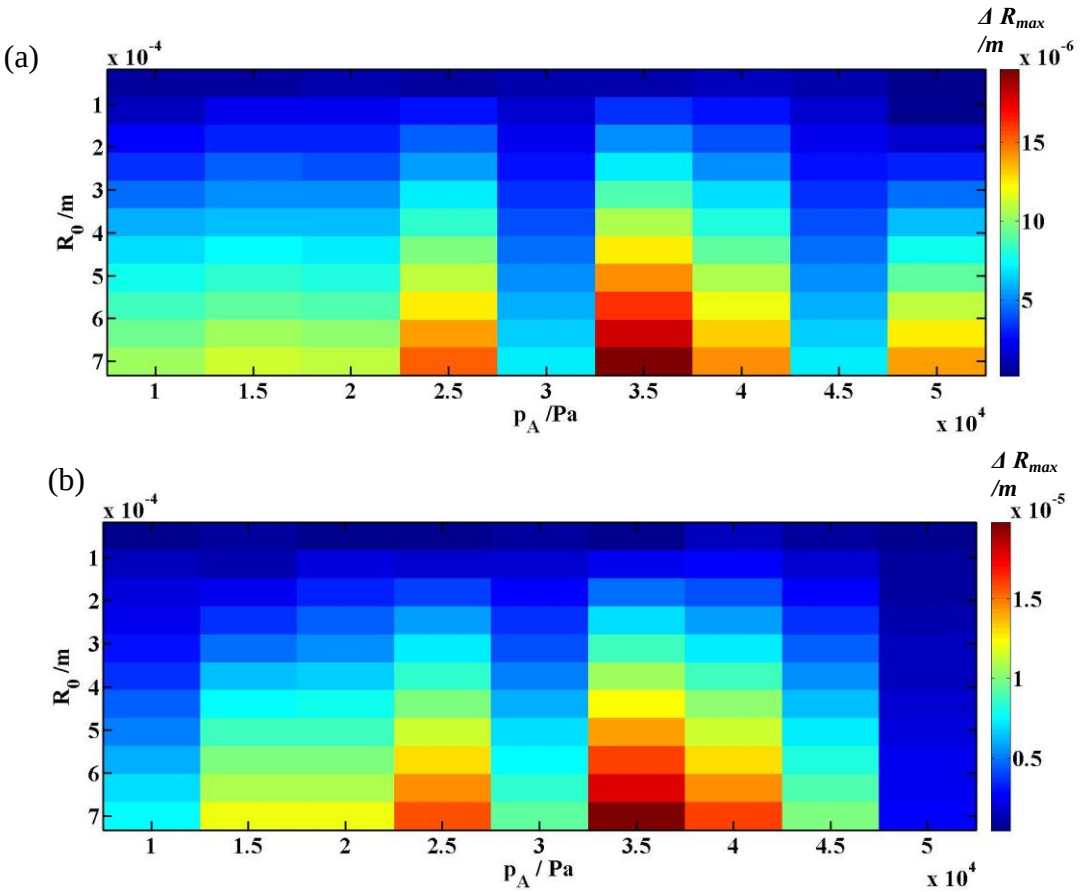

Figure 7.7 *Showing the absolute ΔR_{max} for (a) -5% and (b) +5% in p_0*

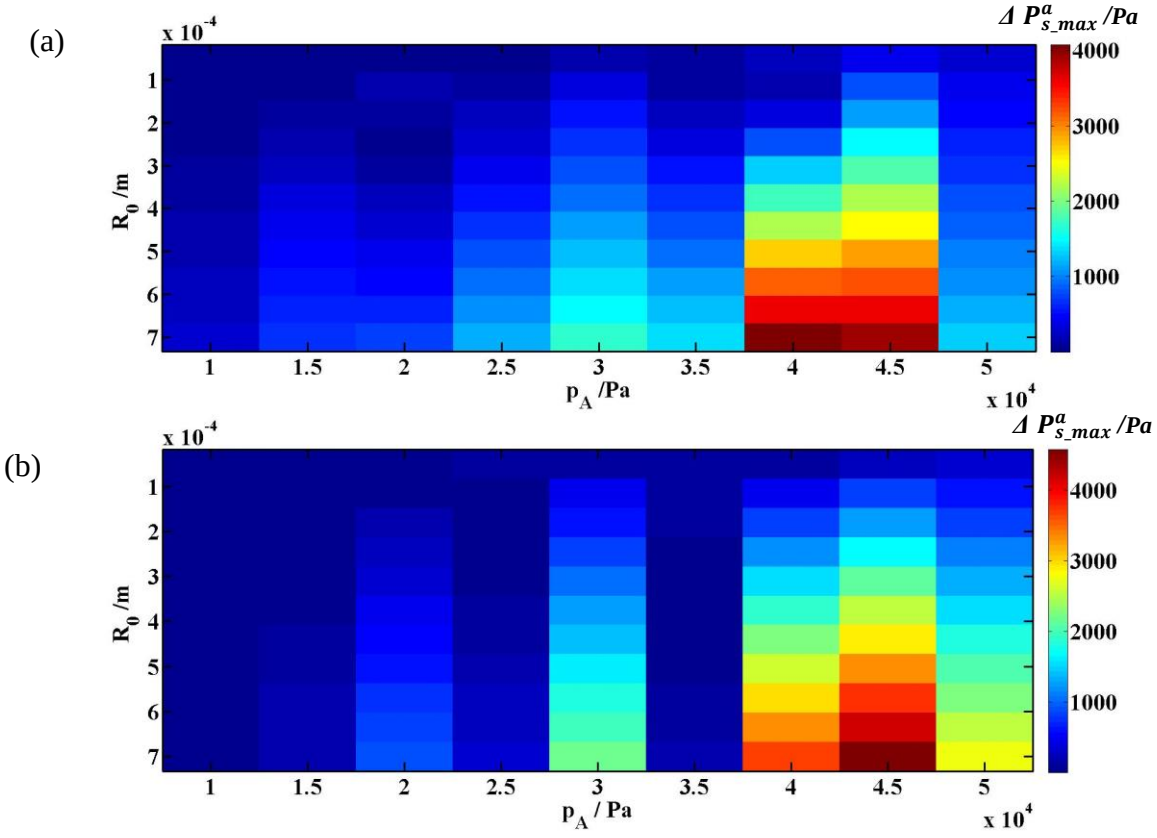

Figure 7.8 Showing the absolute $\Delta P^a_{s\_max}$ for (a) -5% and (b) +5% in p_0

7.4 Discussion

It becomes apparent from these results that the % change in signal is larger for radiated pressure than it is optically. It has also been shown that it is very unlikely that any difference in the bubbles response could be detected either optically or acoustically for a change in liquid viscosity. Those observed due to changes ρ_l are also very small, with the largest difference being in the radiated pressure of 0.5%, which is unlikely to be detectable experimentally unless the signal to noise ratio is exceptionally high. However for hydrostatic pressure, where the majority of bubbles produced a 1μm change and the maximum radial response was found at R_0=700μm with a p_A =35kPa which produced a 1.5% change corresponding to ≈ 20μm which on a maximum expansion of 1275μm should be experimentally observable. The change in pressure amplitude was also larger at -/+3.5-4.5% change in signal, which with an experimental set up, depending on the signal to noise ratio, should also be observable.

The biggest obstacle to using microbubbles as sensors is the requirement that the bubbles should be precisely and repeatable manufactured, to produce a homogenous population. This represents many practical issues which are difficult with the current technology to overcome, with the demands in industry for the manufacturing to be scaled to produce a volume of bubbles in a short period of time. It would be great if it were possible to calibrate a given bubble by determining its resonance frequency before use, in a known environment, then observing any deviation from this response as a change in the environment. However the response is dependent on too many parameters and the range in which bubbles could be used as sensors is too narrow for them to be viable. The bubbles if they were to be produced would need to be manufactured via a lab on chip in a microfluidic

device with the bubbles being used instantly, after finding some way of producing uniform surfactant coated microbubble.

7.5 Summary

In this chapter the criteria for an ideal microbubble sensor were formulated and the corresponding bubble characteristics determined by using the model developed in previous chapters to perform a sensitivity analysis. It was found that the effect upon the bubble response of differences in liquid viscosity and density was too small to be detectable either optically or acoustically for the parameter range examined. The change in dynamic response due to variations in hydrostatic pressure, however, should be detectable provided experimental uncertainties can be minimised and the probability of surface waves in this regime neglected. It was also seen that in all cases the change in radiated pressure was larger than that in radial amplitude, as expected from the underlying equations. Thus, the radiated pressure would be the most appropriate sensing variable, which shall be discussed in more detail in Chapter 8 Section 8.3.

7.6 References

1. Hosny, N.A., et al., *Mapping microbubble viscosity using fluorescence lifetime imaging of molecular rotors.* Proceedings of the National Academy of Sciences, 2013.
2. Postema, M., et al., *Ultrasound-induced encapsulated microbubble phenomena.* Ultrasound in Medicine & Biology, 2004. **30**(6): p. 827-840.
3. Borden, M.A., et al., *Influence of lipid shell physicochemical properties on ultrasound-induced microbubble destruction.* Ultrasonics, Ferroelectrics and Frequency Control, IEEE Transactions on, 2005. **52**(11): p. 1992-2002.
4. O'Brien, J.-P., *Improved Characterisation and Modelling of Microbubbles in Biomedical Applications*, in *Mathematics*2013, University College London: London. p. 193.
5. O'Brien, J.-P., Ovenden, N., and Stride, E., *Accounting for the stability of microbubbles to multi-pulse excitation using a lipid-shedding model.* The Journal of the Acoustical Society of America, 2011. **130**(4): p. EL180-EL185.
6. Kwan, J.J. and Borden, M.A., *Lipid monolayer collapse and microbubble stability.* Advances in Colloid and Interface Science, 2012. **183–184**(0): p. 82-99.
7. Marmottant, P., et al., *A model for large amplitude oscillations of coated bubbles accounting for buckling and rupture.* Journal of the Acoustical Society of America, 2005. **118**(6): p. 3499-3505.

8 Conclusions

8.1 Overview

The overall aim of the work described in this thesis was to improve the theoretical characterisation of microbubbles and to use the results to improve the prediction of their behaviour and to assess their applicability as sensors. The first aim of this chapter is to evaluate the objectives set out in Chapter 1 and assess to what degree they have been accomplished and summarise the contributions of the work. The second is to examine those areas needing additional investigation and to discuss any new problems identified as a result of the work, together with possible means of addressing them.

8.2 Contributions

In this section the achievements of the work will be compared with the list of aims set out in Chapter 1 in order to assess the degree to which new contributions have been made. These aims can be summarised as :

- Reviewing existing theoretical models used to predict the forces involved in optically trapping particles, assessing the models applicability to microbubbles and using the model to determine the trap parameters required to optimise the strength of the trap.
- Reviewing existing theoretical models used to predict the behaviour of microbubbles under ultrasound excitation, deriving a new model for the acoustic response, investigating the models validity in a range of environments (via a sensitivity analysis and comparison to experimental data) and assessing their applicability for a use in designing a sensor.

In Chapter 2 the planned review of previous theoretical models and experimental work on optical trapping was completed. It was demonstrated that the forces involved in

trapping intermediate sized low index particles such as microbubbles were predicted better by the ray optics model than the electric dipole. It also suggested that the most stable trapping position for a particular bubble size does not follow a linear relationship with respect to trapping mode or power, but possesses a more complex behaviour, depending on where the equilibrium trapping position of the bubble is found.

In Chapter 3 the review of previous theoretical models for the excitation of microbubbles via ultrasound was completed. It was found that there was some inconsistency within existing models in terms of the frames of reference used to derive coupled radial and translational microbubble motion. Therefore a new model was derived from first principles. This model also included time dependent effects such as lipid shedding, gas diffusion, variable surface tension and a newly derived variable viscosity.

In Chapter 4 this model was assessed to see which terms became significant under a variety of conditions. The terms found to be negligible under all conditions of interest, were T_B and T_H, which were then neglected in subsequent implementation of the model. It was demonstrated for the first time, that a unique set of parameters describing the shell coating could be derived through fitting between the model and experimental data. This was extremely important in determining the feasibility of a bubble-based sensor given the potentially large number of unknown parameters in the system. A sensitivity analysis was then undertaken to assess which factors affect the bubble dynamic response the most, this included the effect upon lipid shedding, translation and maximum amplitude of oscillation. The results of this analysis indicated that the initial radius of the bubble, R_0 and the driving pressure, p_A, of the acoustic wave were the most significant parameters at any given driving frequency, with the lipid absorption coefficient, k_1, dominating the lipid shedding behaviour. The uncertainty associated with experimental measurements of microbubble dynamics was then considered. Given the maximum accuracy with which R_0 and p_A could be determined

and the sensitivity of the microbubble response to these parameters it was found that measurements of the shell parameters obtained through fitting of experimental to simulated data would be subject to considerable uncertainties.

In Chapter 5 the results from simulations using the new bubble model were compared to experimental data to assess the model's validity. It was found that the new viscosity term did not improve the prediction of microbubble behaviour and that a constant viscosity term actually produced a closer fit. The model was found to describe the occurrence of lipid shedding well, over both single and multiple acoustic pulses. However, there are still some features of the microbubble response not captured by the model and proposals for how these might be addressed are discussed in more detail in the next section.

In Chapter 6 the new model was modified to account for compressibility in the liquid surrounding the microbubble. It was discovered through comparison to experimental data that a single microbubble model, can be used successfully to predict the inertial cavitation threshold of a microbubble population of known size distribution. The change in the rate of total acoustic energy received from the microbubble population experimentally at different driving frequencies and pressures was found to correlate well to the theoretically predicted bubble wall Mach number. It was shown that the inclusion of the variable shell parameters gave a small improvement in correlation, indicating that the bubble coating should not be entirely neglected when considering the large amplitude behaviour of microbubbles. It was also shown that with increasing driving pressure the smaller bubbles in the population contributed proportionally more to the overall acoustic emissions; in contrast to the observed behaviour at lower pressures which was dominated by the resonant bubbles at a given driving frequency.

It was demonstrated in Chapters 4 & 5 that lipid shedding, the size of microbubbles and the inconsistencies of manufacturing and hence lack of uniformity in shell properties make it difficult at present to utilise bubbles as sensors since a given bubble may respond very differently from another to the same acoustic pulse. Therefore in Chapter 7 the requirements for an ideal sensor were formulated and the existence of (a) regime(s) in which microbubble sensors could theoretically be used most effectively was investigated. It was found that a relatively large bubble driven at resonance but at a low pressure could produce detectable changes in response due to changes in its environment. Though the change in acoustic emission was larger than that in radial amplitude, indicating that acoustic rather than optical sensing would be most appropriate. Also, the response to changes in hydrostatic pressure was found to be much more significant than that due to changes in liquid density or viscosity.

8.3 Further work

It was shown in the previous section that each of the aims set out in Chapter 1 has been accomplished and that a number of additional discoveries have also been made as a result of the work. As indicated at several stages throughout the thesis, however, there are many areas requiring additional investigation. The aim of this section is to summarise those areas.

In Chapter 2 the spring constants predicted by the ray optics model incident on a trapped microbubble need to be compared with those obtained experimentally, as do the forces predicted for a scanning optical tweezer set up, in order to assess which trapping technique produces the strongest and most stable trap for manipulating microbubbles.

The model presented in Chapters 3 and 4 also needs to be validated experimentally, to assess how well the predicted translational motion corresponds to observed behaviour. In Chapters 3-5, it became apparent that though the current model does predict the behaviour

of lipid shedding it could be improved with the rate of the term changing at the beginning and the end of consecutive pulses, to allow for the experimentally observed phenomena of over filled lipid shells and the end stable radial size where lipid shedding becomes negligible. An improvement of the variable viscosity term could also be made by allowing the term to change more slowly during compression and expansion, with a different functional dependence on the radius of the bubble than that of the surfactant concentration.

Correspondingly further investigation is needed to understand the mechanism(s) behind lipid shedding and how viscosity in the shell arises. This should be carried out both experimentally and theoretically to assess whether there is, for example, a constant shedding rate over the whole bubbles surface or do certain regions tend to shed more than others due to and/or creating a non-uniform distribution of lipid over the shell. The method of transportation of the lipid from the shell also needs to be investigated further to establish if it is happening during the whole pulse with a uniform loss of molecules or if it is due to droplets forming that reach a certain size detach from the shell and are then propelled away from the bubble or carried away by streaming in the liquid around the bubble as it oscillates.

The model presented in Chapter 6 as a method of characterising inertial cavitation is still in the early stages of development and further comparison is needed with experimental data sets for a variety of frequencies. The model could also be refined by using the sigmoidal surface tension function incorporating lipid shedding and a variable viscosity.

It has been shown in this thesis that for microbubbles to be used successfully as sensors a number of improvements in bubble manufacture are required to produce homogenous monodisperse bubbles. Lipid shedding needs to be eliminated either through the use of new materials or avoiding shedding regimes; or the bubbles manufactured in

such a way that they will all shed at the same rate, thus allowing for the accurate prediction of bubble size change and surfactant loss. In addition, the experimental devices for monitoring bubble response need to improve in resolution in the case of optical techniques, (though ultimately this is limited by diffraction), and sensitivity for the scattered pressure signal.

8.4 Summary

In conclusion the aims and objectives set out in chapter 1 have been achieved. Most notably models have been derived to describe the behaviour of microbubbles under optical trapping and acoustic excitation. In the case of the latter this includes the effects of the bubbles undergoing lipid shedding and translational motion near and far away from a rigid boundary. Good agreement of the model predictions with experimental data has been demonstrated and it has been proven that a unique set of shell parameters can be obtained through fitting the model to experimental measurements. The model has been used to theoretically show that currently commercially available microbubbles are not suitable for use as sensors and the manufacturing requirements and regimes in which they might be suitable have been discussed. Areas for further work have also been outlined in this chapter, including a comparison of optical trapping techniques to understand which produces the most stable traps, a more thorough understanding of the mechanism behind microbubble lipid shedding and the way that the shell dissipates energy, and a closer examination of the regimes in which bubbles might be used as stable calibrated sensors.

Appendix

A. Linearization of the Equation

The linearized version of the code for the radial equation is found via removing the translational coupling parts, using $R=R_0(1-z(t))$.

$$\rho_L\left(R\ddot{R}+\frac{3}{2}\dot{R}^2\right)=\left(p_0+\frac{2\sigma}{R_0}\right)\left(\frac{R_0}{R}\right)^{3\gamma}-\frac{2\sigma}{R}-p_0-P_{ac}-\frac{4\dot{R}\mu_L}{R}-\frac{4\kappa_s\dot{R}}{R^2}$$

$$\rho_L\left(R_0(1-z(t))R_0\ddot{z}+\frac{3}{2}R_0^2\dot{z}^2\right)$$

$$=\left(p_0+\frac{2\sigma}{R_0}\right)(1-z(t))^{3\gamma}-\frac{2\sigma(1-z(t))}{R_0}-p_0-P_{ac}$$

$$-\frac{4R_0\dot{z}\mu_L\,(1-z(t))}{R_0}-\frac{4\kappa_s R_0\,\dot{z}(1-2z)}{R_0^2}$$

Where, R is the radius of the microbubble, where an overdon represents a derivative to time, R_0 is the equilibrium radius, κ_s is the viscosity, σ is the surface tnsion, $P_{ac}= p_A\text{Sin}(\omega t)$, where p_A is the driving pressure of the wave, $\omega=2\pi f$, f is the driving frequency, p_0 is the hydrostatic pressure, μ_L is the liquid viscosity, γ is the polytropic constant, ρ_L is liquid density.

Disregarding higher level terms & simplifying gives:

$$\rho_L R_0\ddot{z}+\left(4\mu_L+4\frac{k_s}{R_0}\right)\dot{z}+\left[3\gamma\left(P_0+\frac{2\sigma}{R_0}\right)-\frac{2\sigma}{R_0}\right]z=P_{ac}$$

Which can be written as $m_b\ddot{z}+b_b\dot{z}+k_bz=P_{ac}$ where:

$$m_b=\rho_L R_0$$

$$b_b=\left(4\mu_L+4\frac{k_s}{R_0}\right)$$

$$k_b = \left[3\gamma\left(P_0 + \frac{2\sigma}{R_0}\right) - \frac{2\sigma}{R_0}\right]$$

Where the natural frequency $\omega_0 = \sqrt{\frac{k_b}{m_b}}$ and the resonant frequency is given by $\omega_r = \omega_0\sqrt{1-2\zeta^2}$, where $\zeta = \frac{b_b}{2\sqrt{m_b k_b}}$.

This gives the linearized numerical version of the code as

$$R(t) = R_0 \frac{(1 - p_{ac}\sin(\omega\, t))}{\sqrt{\left(\left(\frac{k_b}{m_b}\right)^2 - \omega^2\right)^2 + \left(\frac{b_b}{m_b}\right)^2 \omega^2}}$$

Every code written and used for this thesis was compared to the linearized version here to check that it was valid.

The damping coefficents at resonance were found via[1] :

Radiation damping coefficient: $\delta_{rad} = \frac{\omega_0 R_0}{c}$

Viscous damping coeffincet: $\delta_{vis} = \frac{4\kappa_s}{R_0^2 \rho \omega_0}$

Thermal damping coeffiecnt: $\delta_{th} = \frac{2\left(\sqrt{\frac{16}{9(\gamma-1)^2}\frac{G_{th}g}{f_0}} - 3 - \frac{3\gamma-1}{3(\gamma-1)}\right)}{\frac{16}{9(\gamma-1)^2}\frac{G_{th}g}{f_0} - 4}$

Where, $G_{th} = \frac{3\gamma p_0}{4\pi\rho_l D_g}$, D_g is gas diffusion which for air is $2.08\text{x}10^{-5}\text{m}^2\text{s}^{-1}$

and $g = 1 + \frac{2\sigma}{p_0 R_0} - \frac{2\sigma}{3\kappa_s p_0 R_0}$

B. Validation of the Code

Validation of the code in equations (3.36-3.37) for a RNNP style model in the radial via comparison between the numerical and analytical result. Calculated for R_0=1μm, f=0.7MHz, $p_A = 10kPa$, 50 acoustic cycles,$p_0 = 100kPa$, $\mu_s = 2.5\ Pa.s, \mu_l = 8.9 \times 10^{-4} Pa.s, \sigma = 7.2 \times 10^{-2} N.m^{-1}, \rho_l = 998\ Kg.m^{-3}, k_s = 15 \times 10^{-9}, d_s = 1.5nm, c =$

[1] *Leighton, T.G., The Acoustic Bubble. 1994: Academic Press.*

$1500, \rho_g = 1.83\ Kg.m^{-3}, \gamma = 1.4$. These were based on the proposed experimental conditions for the initial calibration of the system.

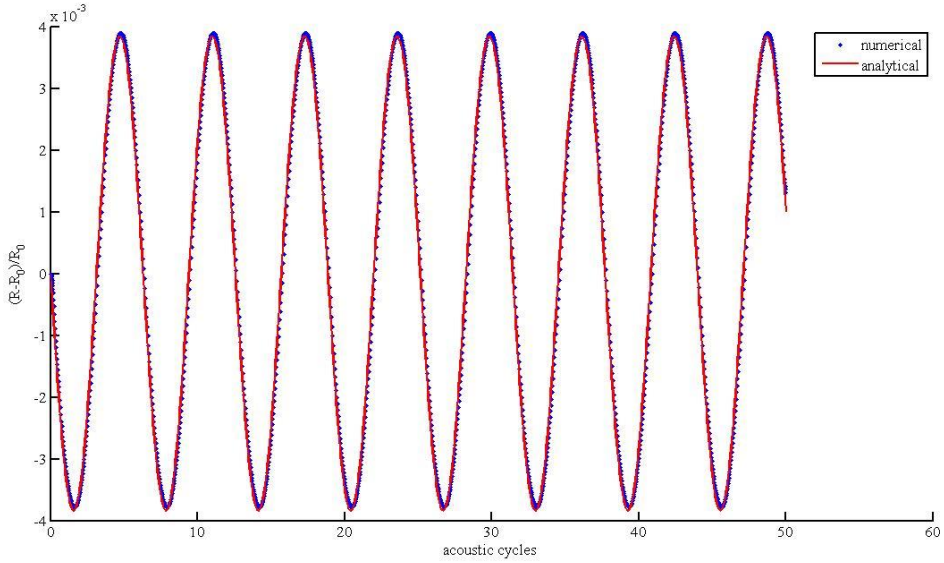

Figure B.1Comparison between the radial motion predicted from a numerical solution of equation and an analytical 1st order solution of the RNNP model. The parameters used given above. This graph was compared for all the codes.

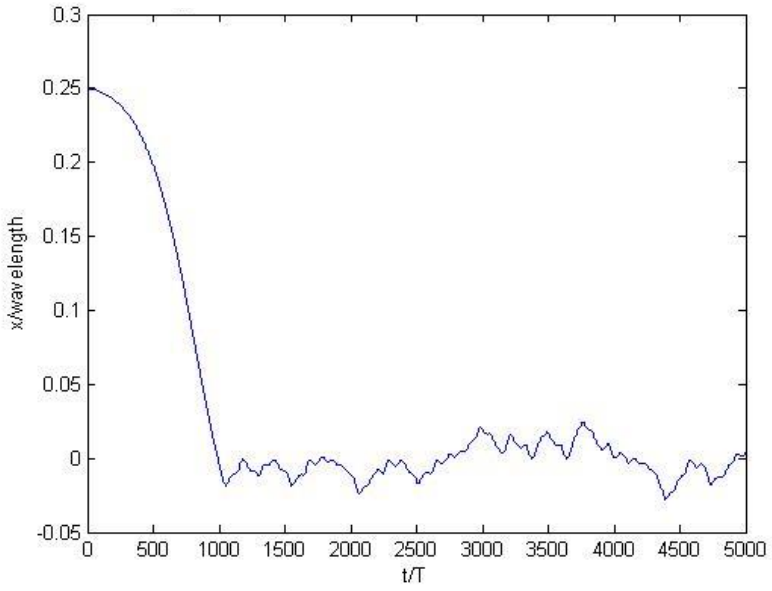

Figure B.2 Showing bubble translation as a function of time for R_0/R_{res}=1which replicates the graph found in Fig. 4 Watanabe & Kukita [2] [1]

[2] *Watanabe, T. and Y. Kukita, Translational and Radial Motions of a Bubble in an Acoustic Standing-Wave Field. Physics of Fluids a-Fluid Dynamics, 1993. 5(11): p. 2682-2688.*

C. Code

C.1 Code used in Chapter 4 &5

```
function jpcode_260214_sense_analysis
clc
clear all
global  M_air1 M_air2 M_pfc1 M_pfc2 fract_surf_1a fract_surf_2a  cs
dmdt1a dmdt1b dmdt2a dmdt2b  accn1 accn2 GAMMA_EQ_a GAMMA_EQ_b
temp_conc1_a temp_conc1_b temp_conc2_a temp_conc2_b d R02 M0_air1 M0_air2
M0_pfc1 M0_pfc2 Alpha_air Alpha_pfc DR0 R0 RHO SIGMA P0 amp mul PV f ks
KAPPA tau K1_a K2_a  K1_b K2_b Csurfbulk GAMMA_RUPT_a GAMMA_RUPT_b
GAMMA_BUCK_a GAMMA_BUCK_b GAMMA_STAR_a GAMMA_STAR_b GAMMA_STAR2_a
GAMMA_STAR2_b SIGMA_STAR2_a SIGMA_STAR2_b GAMMA_SURF1_a GAMMA_SURF1_b
GAMMA_SURF2_a GAMMA_SURF2_b SHELL_ELAST_a SHELL_ELAST_b GAMMA_MAX_a
GAMMA_MAX_b SIGMA_MIN_a SIGMA_MIN_b SIGMA_STAR_a SIGMA_STAR_b Qsig_a
Msig_a Bsig_a vsig_a Qsig_b Msig_b Bsig_b vsig_b Gamma_air Gamma_pfc
Dmin_air D_air Dmin_pfc D_pfc
%temp_conc dmdt accn

DR0=1e-6;                   %bubble radius 1
DR02=1e-6;                  %bubble radius 2
dd=2*5*DR0;                 %the distance between the bubble and the wall(
for bubble-bubble * by 2)

%liquid constants
DRHO=1000;                    %liquid density
Dmul=1e-3;                    %viscosity of the liquid
DP0=1e5;                      %hydrostatic Pressure

%Pulse constants
Damp=100e3;                   %driving Pressure
CYCLES=1;                     %number of repeat cycles
% Df=1e6;                       %frequency of the pulse

ca=1500;                      %Speed of sound in a liquid

%Surfactant  liquid constants
KAPPA=1.4;                    %polytropic constant
DPV=0;                        %vapour Pressure

DSIGMA=7e-2;                  %surface tension (air/water)
fract_surf=1.0;               %fraction of surfactant
DCsurfbulk = 1;               %//Initial bulk surfactant concentration
kg/m^3 = mg/ml
Df=1e6;
% Df=((((DRHO*DR0^2)^(-1))*(3*KAPPA*(DP0+(2*DSIGMA)*DR0^(-1))-
(2*DSIGMA)*DR0^(-1)))^(0.5))/(2*pi)
ks=15e-9/DP0/DR0*(2*pi*Df); % dimensionless constant viscosity if needed
%Surfactant dependent liquid a constants
DSIGMA_MIN_a=0.001;             %minumum surface tension
DK1_a=60000;                  %absorption coefficient
DK2_a=DK1_a*0.05;                 %deabsorption coeficient
% surfactant const needed for morris Surface tension and to find the
equilibrium surface tenison
DSIGMA_STAR_a=0.025;            %star surface tension
DSIGMA_STAR2_a=0.069;           %star 2 surface tension
DGAMMA_STAR_a=3e-8;             %surface concentrations star
DGAMMA_STAR2_a=2.88e-8;         %surface concentrations star 2
% DGAMMA_EQ=3.0e-8
```

```
DGAMMA_EQ_a=(DK1_a*DCsurfbulk*DGAMMA_STAR_a)/(DK1_a*DCsurfbulk+DK2_a); %
Equillibrium surface tenion
DDsurf_a=1e-13;           %DIFFUSIVITY OF SURFACTANT m^2/s
DSHELL_ELASTICITY_a=2.5; %Shell elasticity

%Surfactant dependent liquid B constants
DSIGMA_MIN_b=0.001;           %minumum surface tension
DSIGMA_STAR_b=0.025;          %star surface tension
DSIGMA_STAR2_b=0.069;         %star 2 surface tension
DK1_b=60000;                %absorption coefficient
DK2_b=DK1_b*0.05;              %deabsorption coeficient
%surface concentrations
DGAMMA_STAR_b=3e-8;
DGAMMA_STAR2_b=2.88e-8;
% DGAMMA_EQ=3.0e-8
DGAMMA_EQ_b=(DK1_b*DCsurfbulk*DGAMMA_STAR_b)/(DK1_b*DCsurfbulk+DK2_b);
DDsurf_b=1e-13;           %DIFFUSIVITY OF SURFACTANT m^2/s
DSHELL_ELASTICITY_b=2.5; %Shell elasticity

%Gas constants
B=8.314;                %Universal gas Constant J/K/mol
T=295;                  %Temperature of the liquid K
f_air=1.0;              %fraction of air
DM_air=0.29;            %Molar mass of air Kg/mol
DM_pfc=0.188;           %Molar mass of pfc Kg/mol
Dk_air=3.77e-7;         %Henry's constant air s^2/m^2
Dk_pfc=9.5e-9;          %Henery's constant pfc S^2/m^2
DD_air=2e-9;            %diffusion air m^2/s
DD_pfc=1e-11;           %diffusion pfc m^2/s
DDmin_air=1e-9;         %min Diffusion of air m^2/s
DDmin_pfc=1e-14;        %min Diffusion pfc m^2/s
DLMAX1=6*DR0;           % Max Length m
DLMAX2=6*DR02;          % Max Length m
%Lenths size m
DLENGTH_SIZE=2e-8;
DTIME_SIZE=1e-9;

%dimemsionalizing
R0=DR0/DR0;
R02=DR02/DR0;
d=dd/DR0;
RHO = DRHO *(DR0*2*pi*Df)^2 / DP0;
SIGMA = DSIGMA / (DP0*DR0);

P0 = DP0/DP0;
mul = Dmul*2*pi*Df/DP0;
f = Df/(2*pi*Df);
cs=ca/(DR0*2*pi*Df);
amp = Damp/DP0;
PV = DPV/DP0;
% K1_a=DK1_a/DP0/DR0^2
K1_a=DK1_a*DP0/DR0^2/(2*pi*Df)^3;
K2_a=DK2_a/(2*pi*Df);
% K1_b=DK1_b/DP0/DR0^2;
K1_b=DK1_b*DP0/DR0^2/(2*pi*Df)^3;
K2_b=DK2_b/(2*pi*Df);
%//Initial bulk surfactant concentration kg/m^3 = mg/ml
Csurfbulk = DCsurfbulk*(DR0^2)*(2*pi*Df)^2/DP0;


SIGMA_MIN_a=DSIGMA_MIN_a/(DP0*DR0);
```

```
SIGMA_STAR_a=DSIGMA_STAR_a/(DP0*DR0);
SIGMA_STAR2_a=DSIGMA_STAR2_a/(DP0*DR0);
GAMMA_STAR_a=DGAMMA_STAR_a*(2*pi*Df)^2*DR0/DP0;
GAMMA_STAR2_a=DGAMMA_STAR2_a*(2*pi*Df)^2*DR0/DP0;
% GAMMA_EQ= 2.65e-04
GAMMA_EQ_a=DGAMMA_EQ_a*(2*pi*Df)^2*DR0/DP0;
%Parameters needed for Marmotants modle of surface tension
SHELL_ELAST_a=DSHELL_ELASTICITY_a/(DP0*DR0);
GAMMA_MAX_a=GAMMA_EQ_a/0.6;
GAMMA_BUCK_a=GAMMA_EQ_a*R0*R0*(SIGMA_STAR_a/SHELL_ELAST_a+1);
GAMMA_RUPT_a=GAMMA_BUCK_a/(SIGMA/SHELL_ELAST_a+1);
% Diffusivity of the surfactant
D_surf_a=DDsurf_a/(DR0^2*2*pi*Df);


SIGMA_MIN_b=DSIGMA_MIN_b/(DP0*DR0);
SIGMA_STAR_b=DSIGMA_STAR_b/(DP0*DR0);
SIGMA_STAR2_b=DSIGMA_STAR2_b/(DP0*DR0);
GAMMA_STAR_b=DGAMMA_STAR_b*(2*pi*Df)^2*DR0/DP0;
GAMMA_STAR2_b=DGAMMA_STAR2_b*(2*pi*Df)^2*DR0/DP0;
% GAMMA_EQ= 2.65e-04
GAMMA_EQ_b=DGAMMA_EQ_b*(2*pi*Df)^2*DR0/DP0;
%Parameters needed for Marmotants modle of surface tension
SHELL_ELAST_b=DSHELL_ELASTICITY_b/(DP0*DR0);
GAMMA_MAX_b=GAMMA_EQ_b/0.6;
GAMMA_BUCK_b=GAMMA_EQ_b*R0*R0*(SIGMA_STAR_b/SHELL_ELAST_b+1);
GAMMA_RUPT_b=GAMMA_BUCK_b/(SIGMA/SHELL_ELAST_b+1);
% Diffusivity of the surfactant
D_surf_b=DDsurf_b/(DR0^2*2*pi*Df);
GAMMA_EQ=GAMMA_EQ_a*fract_surf+GAMMA_EQ_b*(1-fract_surf);


%normalizing the gas constants
Alpha_air=(B*T/DM_air)/(DR0*2*pi*Df)^2;
k_air=Dk_air/(DR0*2*pi*Df)^2;
D_air=DD_air/(DR0^2*2*pi*Df);
Dmin_air=DDmin_air/(DR0^2*2*pi*Df);
Lmax1=DLMAX1/DR0;
Lmax2=DLMAX2/DR0;
Length_size=DLENGTH_SIZE/DR0;
TIME_SIZE = DTIME_SIZE*2*pi*Df;
Gamma_air=(3*Alpha_air)/(4*pi*f_air);
Alpha_pfc=(B*T/DM_pfc)/(DR0*2*pi*Df)^2;
k_pfc=Dk_pfc/(DR0*2*pi*Df)^2;
D_pfc=DD_pfc/(DR0^2*2*pi*Df);
Dmin_pfc=DDmin_pfc/(DR0^2*2*pi*Df);
Gamma_pfc=(3*Alpha_pfc)/(4*pi*(1-f_air));


% Constants used for sigmodal surface tension 1
Qsig_a=0.9799;
Bsig_a=138.8;
Msig_a=0.9814;
vsig_a=2.926;

% Constants used for sigmodal surface tension 2
Qsig_b=0.9799;
Bsig_b=138.8;
Msig_b=0.9814;
vsig_b=2.926;
```

```
% Variant on radius
% bubble1
%Mass of a surfactant
DM0surf1_a=4*pi*DR0*DR0*DGAMMA_EQ_a;
DM0surf1_b=4*pi*DR0*DR0*DGAMMA_EQ_b;
%//Initial surf mass given equilibrium surf conc
M0surf1_a = (DM0surf1_a*fract_surf)/DP0/DR0*(2*pi*Df)^2;
M0surf1_a_effec=DM0surf1_a/DP0/DR0*(2*pi*Df)^2;
M0surf1_b = (DM0surf1_b*(1-fract_surf))/DP0/DR0*(2*pi*Df)^2;
%//Initial surf mass given equilibrium surf conc
M0surf1_b_effec = DM0surf1_b/DP0/DR0*(2*pi*Df)^2;
% dimensionless Initial surf mass given equilibrium surf conc
M0_air1=((DP0+2*(nonlin_st_a(GAMMA_EQ_a)*fract_surf+nonlin_st_b(GAMMA_EQ_
b)*(1-
fract_surf))*DP0)*((4/3)*pi*DR0^3*f_air*DM_air/(B*T)*((2*pi*Df)^2)*(DP0*D
R0)^(-1)));     %//Initial  mass of air at equilibrium
C0_air1=k_air*M0_air1*Alpha_air*(3/4)/(pi*DR0^3)*DR0^3;
% Inital concentraion of air
M0_pfc1=((DP0+2*(nonlin_st_a(GAMMA_EQ_a)*fract_surf+nonlin_st_b(GAMMA_EQ_
b)*(1-fract_surf))*DP0)*((4/3)*pi*DR0^3*(1-
f_air)*DM_pfc/(B*T)*((2*pi*Df)^2)*(DP0*DR0)^(-1))); %//Initial  mass of
pfc at equilibrium
C0_pfc1=k_pfc*M0_pfc1*Alpha_pfc*(3/4)/(pi*DR0^3)*DR0^3;
%//Initial  concentraion of pfc

 % bubble2
%Mass of a surfactant
DM0surf2_a=4*pi*DR02*DR02*DGAMMA_EQ_a  ;
DM0surf2_b=4*pi*DR02*DR02*DGAMMA_EQ_b ;
%//Initial surf mass given equilibrium surf conc
M0surf2_a = (DM0surf2_a*fract_surf)/DP0/DR0*(2*pi*Df)^2;  %dimesnionless
Actual mass
M0surf2_a_effec=DM0surf2_a/DP0/DR0*(2*pi*Df)^2;            %
dimensionless effective mass of surfactant Initial surf mass given
equilibrium surf conc
M0surf2_b=(DM0surf2_b*(1-fract_surf))/DP0/DR0*(2*pi*Df)^2;
%//Initial surf mass given equilibrium surf conc
M0surf2_b_effec= DM0surf2_b/DP0/DR0*(2*pi*Df)^2;
M0_air2=((DP0+2*(nonlin_st_a(GAMMA_EQ_a)*fract_surf+nonlin_st_b(GAMMA_EQ_
b)*(1-
fract_surf))*DP0)*((4/3)*pi*DR0^3*f_air*DM_air/(B*T)*((2*pi*Df)^2)*(DP0*D
R0)^(-1)));      %//Initial  mass of air at equilibrium
C0_air2=k_air*M0_air2*Alpha_air*(3/4)/(pi*DR02^3)*DR0^3;
% Inital gas concentraion of air
M0_pfc2=((DP0+(nonlin_st_a(GAMMA_EQ_a)*fract_surf+nonlin_st_b(GAMMA_EQ_b)
*(1-fract_surf))*DP0)*((4/3)*pi*DR0^3*(1-
f_air)*DM_pfc/(B*T)*((2*pi*Df)^2)*(DP0*DR0)^(-1))); %//Initial  mass of
pfc at equilibrium
C0_pfc2=k_pfc*M0_pfc2*Alpha_pfc*(3/4)/(pi*DR0^3)*DR0^3;
%//Initial  concentraion of pfc

%Bulk gas concentraion of air
Cbulk_air=k_air*DP0/DP0;
Cbulk_pfc=k_pfc*DP0/DP0;

if(round(Lmax1/Length_size)<2)
    LENGTH_INT1=2;
else LENGTH_INT1=round(Lmax1/Length_size);
end

if(round(Lmax2/Length_size)<2)
```

```
    LENGTH_INT2=2;
else LENGTH_INT2=round(Lmax2/Length_size);
end

%VARIABLES FOR NONLINEAR viscosity
rstar1=4.5e-6*DR0^(-1);
rstar2=1e-6*DR0^(-1);
ks1=7e-9*2*pi*Df/DR0/DP0;
ks2=1.6e-8*2*pi*Df/DR0/DP0;
syms A B
s1=solve(A*4*pi*rstar1^2+B==ks1, A*4*pi*rstar2^2+B==ks2);
Bcoef=s1.B;
Acoef=s1.A;

%Pulse constants
n=10;                              %number of cycles in the gaussian pulse
tau=n/f/2;                        %gaussian pulse const
dtmax=n*2/(Df);                   %dimensional max time to run raius
tmax=dtmax*2*pi*Df;               %non dimensional time run for the ode(
bubble oscillating)
% period=2e-10*2*pi*Df;            %period of pulse
%

%matrixs
cyc=[0:CYCLES];
% cyc=[0 1 2 3 4 5 6];
   % 5 6 7 8 9 10 11 12 13 14 15 16 17 18 19 20 21 22 23 24 25 26 27 28
29 30];
   cyc2=[1:CYCLES];
% cyc2=[1 2 3 4 5 6];
% 4 5 6 7 8 9 10 11 12 13 14 15 16 17 18 19 20 21 22 23 24 25 26 27 28 29
30];

% bubble 1 matrixs
radii1=zeros(1,(CYCLES+1));

a1=zeros(1,(CYCLES*2+1));        %radius of bubble 1
a2=zeros(1,(CYCLES*2+1));        %accleration of the radius bubble 1
a3=zeros(1,(CYCLES*2+1));        %mass of air in bubble
a4=zeros(1,(CYCLES*2+1));        % mass flux of air in bubble
a5=zeros(1,(CYCLES*2+1));        % effective mass of surfactant A in
bubble 1
a5b=zeros(1,(CYCLES*2+1));        % mass of surfactant A in bubble 1
a6=zeros(1,(CYCLES*2+1));        % mass flux of surfactant A in bubble 1
a13=zeros(1,(CYCLES+1));         %  startign distance of bubble 1
a17=zeros(1,(CYCLES+1));         % mass of pfc in bubble
a18=zeros(1,(CYCLES+1));         % mass flux of pfc in bubble
a21=zeros(1,(CYCLES*2+1));        % mass of surfactant B in bubble 1
a21b=zeros(1,(CYCLES*2+1));       % mass of surfactant B in bubble 1

% bubble 2 matrixes
% a7=radius, a8=acceleration of the radius, a9=mass of air, a10=mass flux
of air, a11=mass of surfactant, a12=mass flux of surfactant
radii2=zeros(1,(CYCLES+1));
a7=zeros(1,(CYCLES*2+1));    % radius in bubble 2
a8=zeros(1,(CYCLES*2+1));    %accelration of radius bubble 2
a9=zeros(1,(CYCLES*2+1));    % mass of air bubble 2
a10=zeros(1,(CYCLES*2+1));   % mass flux of air bubble 2
a11=zeros(1,(CYCLES*2+1));   % mass of surfactant A bubble 2
a11b=zeros(1,(CYCLES*2+1));   % mass of surfactant A bubble 2
a12=zeros(1,(CYCLES*2+1));   % mass flux of surfactant A bubble 2
```

```
a15=zeros(1,(CYCLES+1));    % starting distance bubble 2
a19=zeros(1,(CYCLES+1));    % mass of pfc in bubble 2
a20=zeros(1,(CYCLES+1));    % mass flux of pfc in bubble 2
a22=zeros(1,(CYCLES*2+1));  % mass of surfactant B bubble 2
a22b=zeros(1,(CYCLES*2+1));  % mass of surfactant B bubble 2
fract_surf_1=zeros(1,(CYCLES+1));
fract_surf_2=zeros(1,(CYCLES+1));
conc_air1_now=zeros(1,LENGTH_INT1+1);
conc_air1_old=zeros(1,LENGTH_INT1+1);
conc_air2_now=zeros(1,LENGTH_INT2+1);
conc_air2_old=zeros(1,LENGTH_INT2+1);

conc_pfc1_now=zeros(1,LENGTH_INT1+1);
conc_pfc1_old=zeros(1,LENGTH_INT1+1);
conc_pfc2_now=zeros(1,LENGTH_INT2+1);
conc_pfc2_old=zeros(1,LENGTH_INT2+1);

conc_surf1_a_now=zeros(1,LENGTH_INT1+1);
conc_surf1_a_old=zeros(1,LENGTH_INT1+1);
conc_surf1_b_now=zeros(1,LENGTH_INT1+1);
conc_surf1_b_old=zeros(1,LENGTH_INT1+1);

conc_surf2_a_now=zeros(1,LENGTH_INT1+1);
conc_surf2_a_old=zeros(1,LENGTH_INT1+1);
conc_surf2_b_now=zeros(1,LENGTH_INT1+1);
conc_surf2_b_old=zeros(1,LENGTH_INT1+1);

maxrad1=zeros(1,(CYCLES));
minrad1=zeros(1,(CYCLES));
maxrad2=zeros(1,(CYCLES));
minrad2=zeros(1,(CYCLES));

%setting inital conditions
a1(1)=R0;           % radius 1
a2(1)=0;            % acceleration of radius 1
a3(1)=M0_air1;      % mass of air 1
a4(1)=0;            % mass flux air 1
a5(1)=M0surf1_a_effec;     % mass surfactnat A 1 effective
a5b(1)=M0surf1_a;     % mass surfactnat A 1 effective
a6(1)=0;            % mass flux surfactant A 1
a13(1)=-d/2;           % distance of bubble 1
a17(1)=M0_pfc1;     % mass of pfc 1
a18(1)=0;           % massw flux  pfc
a21(1)=M0surf1_b_effec;   % mass surfactan_B 1 effective
a21b(1)=M0surf1_b ; % mass surfactan_B 1 effective
radii1(1)=R0;       % radius of bubble 1 matrix
tran1(1)=0;       % trans of bubble 1 matrix
a7(1)=R02;          % radius 2
a8(1)=0;            % mass of flux pfc 2
a9(1)=M0_air2;      % mass air 2
a10(1)=0;           % mass flux air bubbl2
a11(1)=M0surf2_a_effec;   % mass of surfatant A 2 effective
a11b(1)=M0surf2_a  ; % mass of surfatant A 2 effective
a15(1)=d/2;           % distance of bubble 2
a19(1)=M0_pfc2;     % mass of pfc
a20(1)=0;           %mass flux pfc
a22(1)=M0surf2_b_effec;   % mass surfactan_B 2 effective
a22b(1)=M0surf2_b ; % mass surfactan_B 2 effective
radii2(1)=R02;      % radius of bubble 2 matrix
fract_surf_1(1)=fract_surf;
fract_surf_2(1)=fract_surf;
```

```
%//Bubble initial conditions
% bub_concair1=C0_air1;
% bub_concair2=C0_air1;

if(GAMMA_EQ==0)
    conc_air1_now(1)=C0_air1;
    conc_air2_now(1)=C0_air2;
    conc_pfc1_now(1)=C0_pfc1;
    conc_pfc2_now(1)=C0_pfc2;
    conc_air1_old(1)=C0_air1;
    conc_air2_old(1)=C0_air2;
    conc_pfc1_old(1)=C0_pfc1;
    conc_pfc2_old(1)=C0_pfc2;

else
    conc_air1_now(1)=Cbulk_air;
    conc_air2_now(1)=Cbulk_air;
    conc_air1_old(1)=Cbulk_air;
    conc_air2_old(1)=Cbulk_air;

    conc_pfc1_now(1)=Cbulk_pfc;
    conc_pfc2_now(1)=Cbulk_pfc;
    conc_pfc1_old(1)=Cbulk_pfc;
    conc_pfc2_old(1)=Cbulk_pfc;

end


for ii=2:1:LENGTH_INT1+1
    conc_air1_now(ii)=Cbulk_air;
    conc_air1_old(ii)=Cbulk_air;
    conc_pfc1_now(ii)=Cbulk_pfc;
    conc_pfc1_old(ii)=Cbulk_pfc;
    conc_surf1_a_now(ii)=Csurfbulk;
    conc_surf1_a_old(ii)=Csurfbulk;
    conc_surf1_b_now(ii)=Csurfbulk;
    conc_surf1_b_old(ii)=Csurfbulk;
end

for iii=2:1:LENGTH_INT2+1
    conc_air2_now(ii)=Cbulk_air;
    conc_air2_old(ii)=Cbulk_air;
    conc_pfc2_now(ii)=Cbulk_pfc;
    conc_pfc2_old(ii)=Cbulk_pfc;
    conc_surf2_a_now(ii)=Csurfbulk;
    conc_surf2_a_old(ii)=Csurfbulk;
    conc_surf2_b_now(ii)=Csurfbulk;
    conc_surf2_b_old(ii)=Csurfbulk;

end

for tt=2:2:(CYCLES*2+1)
    if(tt>1)

        fract_surf_1(tt/2+1)=a5b(tt-1)/(a5b(tt-1)+a21b(tt-1));
        fract_surf_2(tt/2+1)=a11b(tt-1)/(a11b(tt-1)+a22b(tt-1));
      a1(tt)=(a21(tt-1)*(GAMMA_EQ_b*4*pi)^(-1))^(0.5)*(1-
fract_surf_1(tt/2+1))+(a5(tt-1)*(GAMMA_EQ_a*4*pi)^(-
1))^(0.5)*fract_surf_1(tt/2+1);                    % recalculation of
radius 1
```

```
        a7(tt)=(a22(tt-1)*(GAMMA_EQ_b*4*pi)^(-1))^(0.5)*(1-
fract_surf_2(tt/2+1))+(a11(tt-1)*(GAMMA_EQ_a*4*pi)^(-
1))^(0.5)*fract_surf_2(tt/2+1)  ;                    % recalculation of
radius 2  adius 2
        GAMMA_SURF1_a=GAMMA_EQ_a;
% resetting the surface A concentration to equilibrium 1
        GAMMA_SURF2_a=GAMMA_EQ_a;
% resetting the surface A concentration to equilibrium 2
        GAMMA_SURF1_b=GAMMA_EQ_b;
% resetting the surface B concentration to equilibrium 1
        GAMMA_SURF2_b=GAMMA_EQ_b;
% resetting the surface  B concentration to equilibrium 2
        a3(tt)=(a1(tt)^3.0)*Gamma_air^(-
1)*(P0+2*(nonlin_st_a(GAMMA_EQ_a)*fract_surf_1(tt/2+1)+nonlin_st_b(GAMMA_
EQ_b)*(1-fract_surf_1(tt/2+1)))*a1(tt)^(-1)); % recalculation of  air  1
        a9(tt)=(a7(tt)^3.0)*Gamma_air^(-
1)*(P0+2*(nonlin_st_a(GAMMA_EQ_a)*fract_surf_2(tt/2+1)+nonlin_st_b(GAMMA_
EQ_b)*(1-fract_surf_2(tt/2+1)))*a7(tt)^(-1)); % recalculation of air 2
        a17(tt)=(a1(tt)^3.0)*Gamma_pfc^(-
1)*(P0+2*(nonlin_st_a(GAMMA_EQ_a)*fract_surf_1(tt/2+1)+nonlin_st_b(GAMMA_
EQ_b)*(1-fract_surf_1(tt/2+1)))*a1(tt)^(-1));% recalculation of pfc 1
        a19(tt)=(a7(tt)^3.0)*Gamma_pfc^(-
1)*(P0+2*(nonlin_st_a(GAMMA_EQ_a)*fract_surf_2(tt/2+1)+nonlin_st_b(GAMMA_
EQ_b)*(1-fract_surf_2(tt/2+1)))*a7(tt)^(-1));% recalculation of pfc 2


        conc_air1_old(1)=a3(tt)*Gamma_air*(a1(tt)^-
3.0)*k_air*((2*pi*Df*DR0)^2.0); % recalculation of concentration of air
1
        conc_air2_old(1)=a9(tt)*Gamma_air*(a7(tt)^-
3.0)*k_air*((2*pi*Df*DR0)^2.0); % recalculation of concetration of air  2
        conc_pfc1_old(1)=a17(tt)*Gamma_pfc*(a1(tt)^-
3.0)*k_pfc*((2*pi*Df*DR0)^2.0);% recalculation of concentration of pfc  1
        conc_pfc2_old(1)=a19(tt)*Gamma_pfc*(a7(tt)^-
3.0)*k_pfc*((2*pi*Df*DR0)^2.0);% recalculation of concentration of pfc 2

        conc_air1_now(1)=conc_air1_old(1);
        conc_air2_now(1)=conc_air2_old(1);
        conc_pfc1_now(1)=conc_pfc1_old(1);
        conc_pfc2_now(1)=conc_pfc2_old(1);

        a5(tt)=a5(tt-1);   % mass of the surfactant 1 _a effective
        a11(tt)=a11(tt-1); % mass of surfactant 2A  effective
        a21(tt)=a21(tt-1);   % mass of the surfactant 1 _b  effective
        a22(tt)=a22(tt-1); % mass of surfactant 2B effective
         a5b(tt)=a5b(tt-1);   % mass of the surfactant 1 _a
        a11b(tt)=a11b(tt-1); % mass of surfactant 2A
        a21b(tt)=a21b(tt-1);   % mass of the surfactant 1 _b
        a22b(tt)=a22b(tt-1); % mass of surfactant 2B
        rad1(1)=a1(tt);    % radius of 1
        rad2(1)=a7(tt);    % radius of 2
        acc1(1)=0;         % radial acceleration 1
        acc2(1)=0;         % radial acceleration 2
        vel1(1)=acc1(1);
        vel2(1)=acc2(1);

    elseif(GAMMA_EQ==0)
        a3(tt)=(a1(tt-1)^3.0)*Gamma_air^(-
1)*(P0+2*(nonlin_st_a(GAMMA_EQ_a)*fract_surf_1(tt/2+1)+nonlin_st_b(GAMMA_
EQ_b)*(1-fract_surf_1(tt/2+1)))*a1(tt-1)*(-1));
```

```
        a9(tt)=(a7(tt-1)^3.0)*Gamma_air^(-
1)*(P0+2*(nonlin_st_a(GAMMA_EQ_a)*fract_surf_2(tt/2+1)+nonlin_st_b(GAMMA_
EQ_b)*(1-fract_surf_2(tt/2+1)))*a7(tt-1)*(-1));
        a17(tt)=(a1(tt-1)^3.0)*Gamma_pfc^(-
1)*(P0+2*(nonlin_st_a(GAMMA_EQ_a)*fract_surf_1(tt/2+1)+nonlin_st_b(GAMMA_
EQ_b)*(1-fract_surf_1(tt/2+1)))*a1(tt-1)*(-1));
        a19(tt)=(a7(tt-1)^3.0)*Gamma_pfc^(-
1)*(P0+2*(nonlin_st_a(GAMMA_EQ_a)*fract_surf_2(tt/2+1)+nonlin_st_b(GAMMA_
EQ_b)*(1-fract_surf_2(tt/2+1)))*a7(tt-1)*(-1));
    else
        a3(tt) = (a1(tt-1)^3.0)*Gamma_air^(-1)*P0;
        a9(tt) = (a7(tt-1)^3.0)*Gamma_air^(-1)*P0;
        a17(tt) = (a1(tt-1)^3.0)*Gamma_pfc^(-1)*P0;
        a19(tt) = (a7(tt-1)^3.0)*Gamma_pfc^(-1)*P0;
    end
    %//Fluxes equal 0
    a2(tt)=0;
    a4(tt)=0;
    a6(tt)=0;
    a18(tt)=0;

    a8(tt)=0;
    a10(tt)=0;
    a12(tt)=0;
    a20(tt)=0;

    masurf_a(tt/2)=(a5(tt)/a5(tt-1));
    masurf2_a(tt/2)=(a11(tt)/M0surf2_a);
    masurf_b(tt/2)=(a21(tt)/M0surf1_b);
    masurf2_b(tt/2)=(a22(tt)/M0surf2_b);
    radii2(tt/2)=a7(tt)*DR02*2;
    conc_surf1_a_now(1)=Csurfbulk;
    conc_surf2_a_now(1)=Csurfbulk;
    conc_surf1_b_now(1)=Csurfbulk;
    conc_surf2_b_now(1)=Csurfbulk;
    temp_conc1_a =conc_surf1_a_now(1);
    temp_conc2_a =conc_surf2_a_now(1);
    temp_conc1_b =conc_surf1_b_now(1);
    temp_conc2_b =conc_surf2_b_now(1);
    fract_surf_1a=fract_surf_1(tt/2+1);
     fract_surf_2a=fract_surf_2(tt/2+1);
    R0=a1(tt);
    R02=a7(tt);

    M_surf1_a=a5(tt);
    M_surf2_a=a11(tt);
    M_surf1_b=a21(tt);
    M_surf2_b=a22(tt);
    M_air1=a3(tt)
    M_air2=a9(tt);
    M_pfc1=a17(tt);
    M_pfc2=a19(tt);
    x1=a13(tt/2);
    x2=a15(tt/2);
    d=abs(a13(tt/2)-a15(tt/2));
%           options=odeset('MaxStep',period);
    options=odeset('MaxStep',0.01);

    [t,r] =ode45(@jprp2,[0
tmax],[R0,0,R02,0,M_air1,0,M_surf1_a,0,M_air2,0,M_surf2_a,0,x1,0,x2,0,M_p
fc1,0,M_pfc2,0,M_surf1_b,0,M_surf2_b,0],options);
```

```
%
    tm=t/2/pi;
    figure
    plot(tm,r(:,1),'r', tm, r(:,3),'g','linewidth',2);


    r1= r(:,1);
    r2= r(:,2);
    r3= r(:,5);
    r4= r(:,6);
    r5= r(:,7);
    r6= r(:,8);
    r7= r(:,3);
    r8= r(:,4);
    r9= r(:,9);
    r10= r(:,10);
    r11= r(:,11);
    r12= r(:,12);
    r13= r(:,13);
    r14= r(:,14);
    r15= r(:,15);
    r16= r(:,16);
    r17=r(:,17);
    r18=r(:,18);
    r19=r(:,19);
    r20=r(:,20);
    r21=r(:,21);
    r22=r(:,23);
    %  //Now update R, surface concentration and gas conc adjacent to
bubble

    a1(tt+1)=r1(length(r(:,1)));
    a2(tt+1)=r2(length(r(:,2)));
    a3(tt+1)=r3(length(r(:,5)));
    a5(tt+1)=r5(length(r(:,7)));
    a7(tt+1)=r7(length(r(:,3)));
    a8(tt+1)=r8(length(r(:,4)));
    a9(tt+1)=r9(length(r(:,9)));
    a11(tt+1)=r11(length(r(:,11)));
    a13(tt/2+1)=r13(length(r(:,13)));
    a15(tt/2+1)=r15(length(r(:,15)));
    a17(tt+1)=r17(length(r(:,17)));
    a19(tt+1)=r19(length(r(:,19)));
    a21(tt+1)=r21(length(r(:,21)));
    a22(tt+1)=r22(length(r(:,23)));
    % updating real masses
    a5b(tt+1)=((a5(tt+1)/a5(tt))*a5b(tt));
    a11b(tt+1)=((a11(tt+1)/a11(tt))*a11b(tt));
    a21b(tt+1)=((a21(tt+1)/a21(tt))*a21b(tt));
    a22b(tt+1)=((a22(tt+1)/a22(tt))*a22b(tt));

    maxrad1(tt/2)=max(r(:,1))/R0;
    minrad1(tt/2)=min(r(:,1))/R0;

    maxrad2(tt/2)=max(r(:,3))/R0;
    minrad2(tt/2)=min(r(:,3))/R0;

%     mass_1A((tt+2)/2)

    R1=a1(tt+1);
    vel1=a2(tt+1);
```

```
    R2=a7(tt+1);
    vel2=a8(tt+1);
    %     accn=a2(tt+1);
    GAMMA_SURF1_a =
a5(tt+1)*((a5b(tt+1)/(a5b(tt+1)+a21b(tt+1))))*(4*pi*R1*R1)^(-1);
    GAMMA_SURF2_a =
a11(tt+1)*((a11b(tt+1)/(a11b(tt+1)+a22b(tt+1))))*(4*pi*R2*R2)^(-1);
    GAMMA_SURF1_b = a21(tt+1)*(1-
(a5b(tt+1)/(a5b(tt+1)+a21b(tt+1))))*(4*pi*R1*R1)^(-1);
    GAMMA_SURF2_b = a22(tt+1)*(1-
(a11b(tt+1)/(a11b(tt+1)+a22b(tt+1))))*(4*pi*R2*R2)^(-1);

    bub_concair1 = k_air*a3(tt+1)*Alpha_air*(4/3.0*pi*R1^3*(f_air))^(-1);
    bub_concair2 = k_air*a9(tt+1)*Alpha_air*(4/3.0*pi*R2^3*(f_air))^(-1);
    conc_air1_now(1)  = bub_concair1;
    conc_air2_now(1)  = bub_concair2;
    bub_concpfc1 = k_pfc*a17(tt+1)*Alpha_pfc*(4/3.0*pi*R1^3*(1-f_air))^(-
1);
    bub_concpfc2 = k_pfc*a19(tt+1)*Alpha_pfc*(4/3.0*pi*R2^3*(1-f_air))^(-
1);
    conc_pfc1_now(1)  = bub_concpfc1;
    conc_pfc2_now(1)  = bub_concpfc2;
    conc_surf1_a_now(1)= -dmdt1a/(4*pi*R1*R1*Length_size);
    conc_surf2_a_now(1)= -dmdt2a/(4*pi*R1*R1*Length_size);
    conc_surf1_b_now(1)= -dmdt1b/(4*pi*R1*R1*Length_size);
    conc_surf2_b_now(1)= -dmdt2b/(4*pi*R1*R1*Length_size);



%%%%%%%%%%%%%%%%%%%%%%%%%%%%%%%%%%%%%%%%%%%%%%%%%%%%%%%%%%%%%%%%%%%%%%%%%%%%
%%%%%%%%%%%%%%%%%%%%%%%%%%%%%%%
    % bubble 1
    for rr=2:1:LENGTH_INT1


        conc_air1_now(rr)=((D_air*TIME_SIZE)*(rr*Length_size+R1)^(-1))...
            *( conc_air1_old(rr+1)-conc_air1_old(rr-1)*(Length_size)^(-
1)...
            +(rr*Length_size+R1)*(conc_air1_old(rr+1)-
2*conc_air1_old(rr)+conc_air1_old(rr-1))*(Length_size)^(-2))...
            -((R1*(rr*Length_size+R1)^(-1))^(2)-
1)*vel1*TIME_SIZE*(conc_air1_old(rr+1)-conc_air1_old(rr-
1))*((2*Length_size)^(-1))+conc_air1_old(rr);


        conc_pfc1_now(rr)=((D_pfc*TIME_SIZE)*(rr*Length_size+R1)^(-1))...
            *( conc_pfc1_old(rr+1)-conc_pfc1_old(rr-1)*(Length_size)^(-
1)...
            +(rr*Length_size+R1)*(conc_pfc1_old(rr+1)-
2*conc_pfc1_old(rr)+conc_pfc1_old(rr-1))*(Length_size)^(-2))...
            -((R1*(rr*Length_size+R1)^(-1))^(2)-
1)*vel1*TIME_SIZE*(conc_pfc1_old(rr+1)-conc_pfc1_old(rr-
1))*((2*Length_size)^(-1))+conc_pfc1_old(rr);

        conc_surf1_a_now(rr)=((D_surf_a*TIME_SIZE)*(rr*Length_size+R1)^(-
1))...
            *( conc_surf1_a_old(rr+1)-conc_surf1_a_old(rr-
1)*(Length_size)^(-1)...
            +(rr*Length_size+R1)*(conc_surf1_a_old(rr+1)-
2*conc_surf1_a_old(rr)+conc_surf1_a_old(rr-1))*(Length_size)^(-2))...
```

```
            -((R1*(rr*Length_size+R1)^(-1))^(2)-
1)*vel1*TIME_SIZE*(conc_surf1_a_old(rr+1)-conc_surf1_a_old(rr-
1))*(2*Length_size)^(-1)+conc_surf1_a_old(rr);


conc_surf1_b_now(rr)=((D_surf_b*TIME_SIZE)*(rr*Length_size+R1)^(-1))...
            *( conc_surf1_b_old(rr+1)-conc_surf1_b_old(rr-
1)*(Length_size)^(-1)...
            +(rr*Length_size+R1)*(conc_surf1_b_old(rr+1)-
2*conc_surf1_b_old(rr)+conc_surf1_b_old(rr-1))*(Length_size)^(-2))...
            -((R1*(rr*Length_size+R1)^(-1))^(2)-
1)*vel1*TIME_SIZE*(conc_surf1_b_old(rr+1)-conc_surf1_b_old(rr-
1))*(2*Length_size)^(-1)+conc_surf1_b_old(rr);

    end

    %               //Calculate fluxes
    a4(tt+1)=(-3*conc_air1_now(1)+4*conc_air1_now(2)-
conc_air1_now(3))/(2*Length_size);
    a18(tt+1)=(-3*conc_pfc1_now(1)+4*conc_pfc1_now(2)-
conc_pfc1_now(3))/(2*Length_size);

    % #endif

    %               //Move concentration of now to being old for the
start of
    %               the next loop
    for rr=1:1:LENGTH_INT1;
        conc_air1_old(rr) = conc_air1_now(rr);
        conc_pfc1_old(rr) = conc_pfc1_now(rr);
        conc_surf1_a_old(rr) = conc_surf1_a_now(rr);
        conc_surf1_b_old(rr) = conc_surf1_b_now(rr);
    end
        %bubble 2
        for rrr=2:1:LENGTH_INT2

            conc_air2_now(rrr)=((D_air*TIME_SIZE)*(rrr*Length_size+R2)^(-
1))...
                *( conc_air2_old(rrr+1)-conc_air2_old(rrr-
1)*(Length_size)^(-1)...
                +(rrr*Length_size+R2)*(conc_air2_old(rrr+1)-
2*conc_air2_old(rrr)+conc_air2_old(rrr-1))*(Length_size)^(-2))...
                -((R2*(rrr*Length_size+R2)^(-1))^(2)-
1)*vel2*TIME_SIZE*(conc_air2_old(rrr+1)-conc_air2_old(rrr-
1))*(2*Length_size)^(-1)+conc_air2_old(rrr);

            conc_pfc2_now(rrr)=((D_pfc*TIME_SIZE)*(rrr*Length_size+R2)^(-
1))...
                *( conc_pfc2_old(rrr+1)-conc_pfc2_old(rrr-
1)*(Length_size)^(-1)...
                +(rrr*Length_size+R2)*(conc_pfc2_old(rrr+1)-
2*conc_pfc2_old(rrr)+conc_pfc2_old(rrr-1))*(Length_size)^(-2))...
                -((R2*(rrr*Length_size+R2)^(-1))^(2)-
1)*vel2*TIME_SIZE*(conc_pfc2_old(rrr+1)-conc_pfc2_old(rrr-
1))*(2*Length_size)^(-1)+conc_pfc2_old(rrr);


conc_surf2_a_now(rrr)=((D_surf_a*TIME_SIZE)*(rrr*Length_size+R2)^(-1))...
                *( conc_surf2_a_old(rrr+1)-conc_surf2_a_old(rrr-
1)*(Length_size)^(-1)...
```

```
                +(rrr*Length_size+R2)*(conc_surf2_a_old(rrr+1)-
2*conc_surf2_a_old(rrr)+conc_surf2_a_old(rrr-1))*(Length_size)^(-2))...
                -((R2*(rrr*Length_size+R2)^(-1))^(2)-
1)*vel2*TIME_SIZE*(conc_surf2_a_old(rrr+1)-conc_surf2_a_old(rrr-
1))*(2*Length_size)^(-1)+conc_surf2_a_old(rr);


conc_surf2_b_now(rrr)=((D_surf_b*TIME_SIZE)*(rrr*Length_size+R2)^(-1))...
                *( conc_surf2_b_old(rrr+1)-conc_surf2_b_old(rrr-
1)*(Length_size)^(-1)...
                +(rrr*Length_size+R2)*(conc_surf2_b_old(rrr+1)-
2*conc_surf2_b_old(rrr)+conc_surf2_b_old(rrr-1))*(Length_size)^(-2))...
                -((R2*(rrr*Length_size+R2)^(-1))^(2)-
1)*vel2*TIME_SIZE*(conc_surf2_b_old(rrr+1)-conc_surf2_b_old(rrr-
1))*(2*Length_size)^(-1)+conc_surf2_b_old(rr);

        end

        %               //Calculate fluxes
        a10(tt+1)=(-3*conc_air2_now(1)+4*conc_air2_now(2)-
conc_air2_now(3))/(2*Length_size);
        a20(tt+1)=(-3*conc_pfc2_now(1)+4*conc_pfc2_now(2)-
conc_pfc2_now(3))/(2*Length_size);


        %               //Move concentration of now to being old for the
start of
        %               the next loop
        for rrr=1:1:LENGTH_INT2;
            conc_air2_old(rrr) = conc_air2_now(rrr);
            conc_pfc2_old(rrr) = conc_pfc2_now(rrr);
            conc_surf2_a_old(rrr) = conc_surf2_a_now(rrr);
            conc_surf2_b_old(rrr) = conc_surf2_b_now(rrr);
        end
%         (a21(tt-1)*(GAMMA_EQ_b*4*pi)^(-1))^(0.5)*(1-fract_surf)+(a5(tt-
1)*(GAMMA_EQ_a*4*pi)^(-1))^(0.5)*fract_surf ;

        radii1(tt/2+1)=(a21(tt+1)*(GAMMA_EQ_b*4*pi)^(-1))^(0.5)*(1-
(a5b(tt+1)/(a5b(tt+1)+a21b(tt+1))))+(a5(tt+1)*(GAMMA_EQ_a*4*pi)^(-
1))^(0.5)*(a5b(tt+1)/(a5b(tt+1)+a21b(tt+1))) ;
  %    radii2(tt/2+1)=((a11b(tt+1)*(GAMMA_EQ_a)^(-
1)+a22b(tt+1)*GAMMA_EQ_b^(-1))*(4*pi)^(-1))^(0.5);


%   tran1(tt/2+1)=a13(tt+1)-a13(tt);

end
% figure
% hold on
masurf_a(CYCLES+1)=(a5(CYCLES*2+1))/M0surf1_a;
masurf_b(CYCLES+1)=(a21(CYCLES*2+1))/M0surf1_b;
masurf2_a(CYCLES+1)=(a11(CYCLES*2+1))/M0surf2_a;
masurf2_b(CYCLES+1)=(a22(CYCLES*2+1))/M0surf2_b;



figure
subplot(3,1,1); plot(cyc,radii1,'c')
title('resting radius with time')
xlabel('Acoustic cycles');
ylabel('(Radius-R_0)/R_0');
```

```
subplot(3,1,2);
plot(cyc,a13-a13(1),'c')
title('translational distance moved with time')
xlabel('Acoustic cycles');
ylabel('distance moved');
subplot(3,1,3);
plot(cyc2,(maxrad1),'c',cyc2,(minrad1),'c')
title('max and min radius during pulse')
xlabel('Acoustic cycles');
ylabel('(Radius-R_0)/R_0');
title('resting radius with time')
xlabel('Acoustic cycles');
ylabel('(Radius-R_0)/R_0');


end

function [betareturn]=bbeta_a(y)
global GAMMA_STAR_a
if y<0.96*GAMMA_STAR_a
    betareturn= 1.0;
elseif(y>=0.96*GAMMA_STAR_a && y<GAMMA_STAR_a)
    betareturn= 25*(1-y/GAMMA_STAR_a);
else betareturn=0;

end
end

function [betareturn]=bbeta_b(y)
global GAMMA_STAR_b
if y<0.96*GAMMA_STAR_b
    betareturn= 1.0;
elseif(y>=0.96*GAMMA_STAR_b && y<GAMMA_STAR_b)
    betareturn= 25*(1-y/GAMMA_STAR_b);
else betareturn=0;

end
end

function [gg]= nonlin_st_a(ssurfconc)
global SIGMA SIGMA_MIN_a Qsig_a Bsig_a Msig_a vsig_a GAMMA_EQ_a

ff=ssurfconc/GAMMA_EQ_a;
  surface_ten = SIGMA + (SIGMA_MIN_a-SIGMA)/((1+Qsig_a*exp(-Bsig_a*((ff)-
Msig_a)))^(1/vsig_a));
        gg=surface_ten;

end
function [gg]= nonlin_st_b(ssurfconc)
global SIGMA SIGMA_MIN_b Qsig_b Bsig_b Msig_b vsig_b GAMMA_EQ_b

ff=ssurfconc/GAMMA_EQ_b;
  surface_ten = SIGMA + (SIGMA_MIN_b-SIGMA)/((1+Qsig_b*exp(-Bsig_b*((ff)-
Msig_b)))^(1/vsig_b));
        gg=surface_ten;

end

function [dif_pfc]=nonlin_diff_pfc1_a(surfconc)
global Dmin_pfc D_pfc GAMMA_EQ_a
```

```
if(surfconc<GAMMA_EQ_a)
    dif_pfc=(Dmin_pfc-D_pfc)/GAMMA_EQ_a*surfconc + D_pfc;

else  dif_pfc=Dmin_pfc;

end
if dif_pfc<Dmin_pfc
    dif_pfc=Dmin_pfc;
end
end


function [dif_pfc]=nonlin_diff_pfc1_b(surfconc)
global Dmin_pfc D_pfc  GAMMA_EQ_b


if(surfconc<GAMMA_EQ_b)
    dif_pfc=(Dmin_pfc-D_pfc)/GAMMA_EQ_b*surfconc + D_pfc;

else  dif_pfc=Dmin_pfc;

end
if dif_pfc<Dmin_pfc
    dif_pfc=Dmin_pfc;
end
end

function [dif_air]=nonlin_diff_air1_a(surfconc)
global Dmin_air D_air GAMMA_EQ_a
    if(surfconc<GAMMA_EQ_a)
        dif_air=(Dmin_air-D_air)/GAMMA_EQ_a*surfconc + D_air;

    else  dif_air=Dmin_air;

    end
    if dif_air<Dmin_air
        dif_air=Dmin_air;
    end
end

function [dif_air]=nonlin_diff_air1_b(surfconc)
global Dmin_air D_air GAMMA_EQ_b
    if(surfconc<GAMMA_EQ_b)
        dif_air=(Dmin_air-D_air)/GAMMA_EQ_b*surfconc + D_air;

    else  dif_air=Dmin_air;

    end
    if dif_air<Dmin_air
        dif_air=Dmin_air;
    end
end

function dr=jprp2(t,r);
 global  M_air1 M_air2 M_pfc1 M_pfc2 fract_surf_1a fract_surf_2a
GAMMA_EQ_a GAMMA_EQ_b cs dmdt1a dmdt1b dmdt2a dmdt2b accn1 accn2
temp_conc1_a temp_conc1_b temp_conc2_a temp_conc2_b d R02 M0_air1 M0_air2
M0_pfc1 M0_pfc2 Alpha_air Alpha_pfc DR0 R0 RHO SIGMA P0 amp mul PV f ks
KAPPA tau K1_a K1_b K2_a K2_b Csurfbulk GAMMA_RUPT_a GAMMA_RUPT_b
GAMMA_BUCK_a GAMMA_BUCK_b GAMMA_STAR_a GAMMA_STAR_b GAMMA_STAR2_a
```

```
GAMMA_STAR2_b SIGMA_STAR2_a SIGMA_STAR2_b  GAMMA_SURF1_a GAMMA_SURF1_b
GAMMA_SURF2_a GAMMA_SURF2_b SHELL_ELAST_a SHELL_ELAST_b GAMMA_MAX_a
GAMMA_MAX_b SIGMA_MIN_a SIGMA_MIN_b SIGMA_STAR_a SIGMA_STAR_b Qsig_a
Msig_a Bsig_a vsig_a Qsig_b Msig_b Bsig_b vsig_b Gamma_air Gamma_pfc
Dmin_air D_air Dmin_pfc D_pfc

dr=zeros(24,1);

dr(1)=r(2);


dr(2)=((-3/2)*r(2)^(2)*(r(1)^(-1)))...
    +(RHO*r(1))^(-1)...
   *(((4/3)*pi*R0^(3))^(-
1)*(M_air1*Alpha_air+(M_pfc1*Alpha_pfc))*(R0*r(1)^(-1))^(3*KAPPA)...
    +PV-P0-amp*sin(2*pi*(t)*f)...
    -
2*(nonlin_st_a(r(7)/(4*pi*r(1)^(2)))*(fract_surf_1a)+nonlin_st_b(r(21)/(4
*pi*r(1)^2))*(1-fract_surf_1a))*(r(1)^(-1))...
    -4*mul*r(2)*(r(1)^(-1))...
    -4*(kss(r(7)/(4*pi*r(1)^(2))))*r(2)*r(1)^(-2))...
    -(2*r(3)*r(4)^(2)+r(3)^(2)*dr(4))*((r(15)-r(13))*r(1))^(-1)...
    +((r(14)-(amp*(RHO*cs)^(-1))*cos((2*pi*f)*t))^(2)*(4*r(1))^(-1))...
    +(r(3)^(2)*((2*(r(15)-r(13))^(2)*r(1))^(-1)))...
    *(3*r(4)*(r(14)-(amp*(RHO*cs)^(-1))*cos((2*pi*f)*t))...
    +3*r(4)*(r(16)-(amp*(RHO*cs)^(-1))*cos((2*pi*f)*t))...
    +r(3)*(dr(16)+(amp*(2*pi*f*cs^(-1))*r(16)*cos((2*pi*f)*t)*(RHO*cs)^(-
1))+((amp*(2*pi*f))*(RHO*cs)^(-1))*(sin((2*pi*f)*t)))...
    -2*(r(4)*(r(16)-r(14))))...
    -(((3/2)*(r(14)-(amp*(RHO*cs)^(-1))*cos((2*pi*f)*t))+(r(16)-
r(14)))*(((r(16)-(amp*(RHO*cs)^(-1))*cos((2*pi*f)*t))*r(3)^(3))*((r(15)-
r(13))^(3)*r(1))^(-1)));


dr(3)=r(4);

% dr(4)= (RHO*r(3))^(-1);...
% *exp(-4*((t-tau)/tau)^2)


dr(4)=(-3/2)*r(4)^(2)*(r(3)^(-1))...
    +(RHO*r(3))^(-1)...
    *(((4/3)*pi*R02^(3))^(-
1)*(M_air2*Alpha_air+(M_pfc2*Alpha_pfc))*(R02*r(3)^(-1))^(3*KAPPA)...
    +PV-P0-amp*sin(2*pi*(t)*f)...
    -
2*(nonlin_st_a(r(11)/(4*pi*r(3)^2))*(fract_surf_2a)+nonlin_st_b(r(23)/(4*
pi*r(3)^2))*(1-fract_surf_2a))*(r(3)^(-1))...
    -4*mul*r(4)*(r(3)^(-1))...
    -4*kss(r(11)/(4*pi*r(3)^2))*r(4)*r(3)^(-2))...
    -(((r(15)-r(13))*r(3))^(-1))*(2*r(1)*r(2)^(2)+r(1)^(2)*dr(2))...
    +(r(16)-(amp*(RHO*cs)^(-1))*cos((2*pi*f)*t))^2*(4*r(3))^(-1)...
    +(-(3/2)*(r(16)-(amp*(RHO*cs)^(-1))*cos((2*pi*f)*t))+(r(16)-
r(14)))*(((r(14)-(amp*(RHO*cs)^(-
1))*cos((2*pi*f)*t))*r(1)^(3))*(2*(r(15)-r(13))^(3)*r(3))^(-1))...
    -(r(1)^(2)*(2*(r(15)-r(13))^2*r(3))^(-1))...
    *(r(1)*(dr(14)+(amp*(2*pi*f*cs^(-
1))*r(14)*cos((2*pi*f)*t)*(RHO*cs)^(-1))+((amp*(2*pi*f))*(RHO*cs)^(-
1))*(sin((2*pi*f)*t)))...
    +3*r(2)*(r(14)-(amp*(RHO*cs)^(-1))*cos((2*pi*f)*t))...
    +3*r(2)*(r(16)-(amp*(RHO*cs)^(-1))*cos((2*pi*f)*t))...
```

```
    +(r(16)-r(14))*r(2));

dr(5)=(4*pi*r(1)^2)*(nonlin_diff_air1_a(GAMMA_SURF1_a)*fract_surf_1a+nonl
in_diff_air1_b(GAMMA_SURF1_b)*(1-fract_surf_1a))*r(6);

dr(6)=0;

if GAMMA_SURF1_a>GAMMA_STAR_a
    dr(7)=0;
    if dr(7)>0
        dr(7)=0;
    end

elseif GAMMA_SURF1_a>GAMMA_MAX_a
    dr(7)=GAMMA_MAX_a*8*pi*r(1)*r(2);
    if dr(7)>0
        dr(7)=0;
    end

else

dr(7)=(4*pi*r(1)^2*bbeta_a(GAMMA_SURF1_a))*(K1_a*temp_conc1_a*(GAMMA_STAR
_a-r(7)/(4*pi*r(1)^2))-K2_a*r(7)/(4*pi*r(1)^2));
    if dr(7)>0
        dr(7)=0;
    end
end

dr(8)=0;

dr(9)=(4*pi*r(3)^2)*(nonlin_diff_air1_a(GAMMA_SURF2_a)*fract_surf_2a+nonl
in_diff_air1_b(GAMMA_SURF2_b)*(1-fract_surf_2a))*r(10);
% dr(9)=(4*pi*r(3)^2)*nonlin_diff_air1_a(GAMMA_SURF2_a)*r(10);

dr(10)=0;

if GAMMA_SURF2_a>GAMMA_STAR_a
    dr(11)=0;
    if dr(11)>0
        dr(11)=0;
    end

elseif GAMMA_SURF2_a>GAMMA_MAX_a
    dr(11)=GAMMA_MAX_a*8*pi*r(3)*r(4);
    if dr(11)>0
        dr(11)=0;
    end

else

dr(11)=(4*pi*r(3)^2*bbeta_a(GAMMA_SURF2_a))*(K1_a*temp_conc2_a*(GAMMA_STA
R_a-r(11)/(4*pi*r(3)^2))-K2_a*r(11)/(4*pi*r(3)^2));
    if dr(11)>0
        dr(11)=0;

    end
end

dr(12)=0;

dr(13)=r(14);
```

```
dr(13)=r(14);
dr(14)=-((2/3)*pi*RHO*r(1)^(3))*((amp*(2*pi*f*cs^(-
1))*r(14)*cos(2*pi*f*t)*sin((2*pi*f*cs^(-1))*r(13))*(RHO*cs)^(-
1))+((amp*2*pi*f)*(RHO*cs)^(-1))*(sin(2*pi*f*t)*cos((2*pi*f*cs^(-
1))*r(13))))...
    +((((2*pi*f*cs^(-1))*amp)*((RHO*cs)^(-
1)))*(cos(t*2*pi*f)*sin((2*pi*f*cs^(-1))*r(13)))*(r(14)-(amp*(RHO*cs)^(-
1))*cos(2*pi*f*t)*cos((2*pi*f*cs^(-1))*r(13))))...
    -((9*mul*(2*RHO*r(1)^(2))^(-1))*(r(14)-(amp*(RHO*cs)^(-
1))*cos(2*pi*f*t)*cos((2*pi*f*cs^(-1))*r(13))))...
    -3*r(2)*(r(1)^(-1))*(r(14)-(amp*(RHO*cs)^(-
1))*cos(2*pi*f*t)*cos((2*pi*f*cs^(-1))*r(13)))...
    +(2*(2*pi*f*cs^(-1))*amp*(RHO^(-1))*cos((2*pi*f*cs^(-
1))*r(13))*sin(t*2*pi*f))...
    +((3*r(3)^2)*(r(15)-r(13))^(-2))...
    *((((2*pi*f*cs^(-1))*amp*r(3))*(cs*RHO)^(-
1))*cos(t*2*pi*f)*sin((2*pi*f*cs^(-1))*r(13))-(2*r(4)^(2)*r(3)^(-1))-
(3*r(2)*r(4)*(r(1)^(-1)))-dr(4))...
    +(3*r(3)^(3)*(r(15)-r(13))^(-3))...
    *((2*(r(16)-r(14))*r(4)*r(3)^(-1))...
+(dr(16)+(amp*(2*pi*f*cs^(-1))*r(16)*cos(2*pi*f*t)*sin((2*pi*f*cs^(-
1))*r(15))*(RHO*cs)^(-1))+((amp*2*pi*f)*(RHO*cs)^(-
1))*(sin(2*pi*f*t)*cos((2*pi*f*cs^(-1))*r(15))))...
    -((r(16)-(amp*(RHO*cs)^(-1))*cos(2*pi*f*t)*cos((2*pi*f*cs^(-
1))*r(15)))*((2*pi*f*cs^(-1))*amp*cos(t*2*pi*f)*sin((2*pi*f*cs^(-
1))*r(13)))*(cs*RHO)^(-1))...
    +((3*(r(16)-(amp*(RHO*cs)^(-1))*cos(2*pi*f*t)*cos((2*pi*f*cs^(-
1))*r(15))))*((r(2)*r(1)^(-1))+(r(4)*r(3)^(-1)))));


dr(15)=r(16);

dr(16)=-((2/3)*pi*RHO*r(3)^(3))*((amp*(2*pi*f*cs^(-
1))*r(16)*cos(2*pi*f*t)*sin((2*pi*f*cs^(-1))*r(15))*(RHO*cs)^(-
1))+((amp*2*pi*f)*(RHO*cs)^(-1))*(sin(2*pi*f*t)*cos((2*pi*f*cs^(-
1))*r(15))))...
    +((r(16)-(amp*(RHO*cs)^(-1))*cos(2*pi*f*t)*cos((2*pi*f*cs^(-
1))*r(15)))*( (2*pi*f*cs^(-1))*amp*cos(t*2*pi*f)*sin((2*pi*f*cs^(-
1))*r(15)))*(RHO*cs)^(-1))...
    -((9*mul*(2*RHO*r(3)^(2))^(-1))*(r(16)-(amp*(RHO*cs)^(-
1))*cos(2*pi*f*t)*cos((2*pi*f*cs^(-1))*r(15))))...
    -((3*r(3)^(-1))*(r(16)-(amp*(RHO*cs)^(-
1))*cos(2*pi*f*t)*cos((2*pi*f*cs^(-1))*r(15)))*r(4))...
    +(2*(2*pi*f*cs^(-1))*amp*cos((2*pi*f*cs^(-
1))*r(15))*sin(t*2*pi*f)*RHO^(-1))...
    +((3*r(1)^2)*(r(15)-r(13))^(-2))...
    *(dr(2)-((2*pi*f*cs^(-1))*amp*cos(t*2*pi*f)*sin((2*pi*f*cs^(-
1))*r(15))*r(2)*(cs*RHO)^(-1))+(2*r(2)^(2)*r(1)^(-
1))+(3*r(2)*r(4)*r(3)^(-1)))...
    +(3*r(1)^(3)*(r(15)-r(13))^(-3))...
    *((-2*(r(16)-r(14))*r(2)*r(1)^(-1))...
    +(dr(14)+(amp*(2*pi*f*cs^(-1))*r(14)*cos(2*pi*f*t)*sin((2*pi*f*cs^(-
1))*r(13))*(RHO*cs)^(-1))+((amp*2*pi*f)*(RHO*cs)^(-
1))*(sin(2*pi*f*t)*cos((2*pi*f*cs^(-1))*r(13))))...
    -((r(14)-(amp*(RHO*cs)^(-1))*cos(2*pi*f*t)*cos((2*pi*f*cs^(-
1))*r(13)))*( (2*pi*f*cs^(-1))*amp*cos(t*2*pi*f)*sin((2*pi*f*cs^(-
1))*r(15)))*((cs*RHO)^(-1)))...
    +(3*(r(14)-(amp*(RHO*cs)^(-1))*cos(2*pi*f*t)*cos((2*pi*f*cs^(-
1))*r(13)))*((r(2)*r(1)^(-1))+(r(4)*r(3)^(-1)))));
```

```
dr(17)=(4*pi*r(1)^2)*(nonlin_diff_pfc1_a(GAMMA_SURF1_a)*fract_surf_1a+non
lin_diff_pfc1_b(GAMMA_SURF1_b)*(1-fract_surf_1a))*r(17);

dr(18)=0;


dr(19)=(4*pi*r(3)^2)*(nonlin_diff_pfc1_a(GAMMA_SURF2_a)*fract_surf_2a+non
lin_diff_pfc1_b(GAMMA_SURF2_b)*(1-fract_surf_2a))*r(17);

dr(20)=0;

if GAMMA_SURF1_b>GAMMA_STAR_b
    dr(21)=0;
    if dr(21)>0
        dr(21)=0;
    end

elseif GAMMA_SURF1_b>GAMMA_MAX_b
    dr(21)=GAMMA_MAX_a*8*pi*r(1)*r(2);
    if dr(21)>0
        dr(21)=0;
    end

else

dr(21)=(4*pi*r(1)^2*bbeta_b(GAMMA_SURF1_b))*(K1_b*temp_conc1_b*(GAMMA_STA
R_b-r(21)/(4*pi*r(1)^2))-K2_b*r(21)/(4*pi*r(1)^2));
    if dr(21)>0
        dr(21)=0;
    end
end

dr(22)=0;

if GAMMA_SURF2_b>GAMMA_STAR_b
    dr(23)=0;
    if dr(23)>0
        dr(23)=0;
    end

elseif GAMMA_SURF2_b>GAMMA_MAX_b
    dr(23)=GAMMA_MAX_b*8*pi*r(3)*r(4);
    if dr(23)>0
        dr(23)=0;
    end

else

dr(23)=(4*pi*r(3)^2*bbeta_b(GAMMA_SURF2_b))*(K1_b*temp_conc2_b*(GAMMA_STA
R_b-r(23)/(4*pi*r(3)^2))-K2_b*r(23)/(4*pi*r(3)^2));
    if dr(23)>0
        dr(23)=0;

    end
end

dr(24)=0;

dmdt1a=dr(7);
```

```
accn1=dr(2);
dmdt2a=dr(11);
accn2=dr(4);
dmdt1b=dr(21);
dmdt2b=dr(23);
% GAMMA_SURF=r(7)/(4*pi*r(1));
% GASSY=(((4/3)*pi*R0^3)^(-1)*(M0_air1*Alpha_air+(M0_pfc1*Alpha_pfc)))-
P0-2*R0^(-
1)*(nonlin_st_a(GAMMA_EQ_a)*(fract_surf_2a)+nonlin_st_b(GAMMA_EQ_b)*(1-
fract_surf_2a))
end

function [bb]=kss(pp)
global GAMMA_EQ_a GAMMA_MAX_a ks

fff=pp;

if (pp/GAMMA_MAX_a)<1
 visco= ks*tanh(fff/(GAMMA_MAX_a-fff))/tanh(GAMMA_EQ_a/(GAMMA_MAX_a-
GAMMA_EQ_a));
else
%
visco= ks*tanh(GAMMA_MAX_a/(GAMMA_MAX_a-
GAMMA_MAX_a))/tanh(GAMMA_EQ_a/(GAMMA_MAX_a-GAMMA_EQ_a));
end
% if constant
% visco =ks

bb=visco;
end
```

C.2 Code for Chapter 6 &7

```
function Keller_Miskis
% Author Caroline Harfield caroline.harfield@stcatz.ox.ac.uk
% This file runs the code for the Keller-Miskis equation in 3 forms, with
a
% shell (call skel function in ode), with a shell and variable surface
tension (varskel) and without a shell aka an
% uncoated bubble (kel). The Presure wave is in a Guassian form.It is
also
% set up to run multiple radius and pressures.
clear
clc
clear all
global R0 rhol p0 sig0 gamma mul amp f cl  SHELL_ELAST R_buck R_rupt
R_breakup ks tau

% definition of Variables
%Inital bubble Radius range of bubble radii used, goes inital, diffrence
%taken: end value,(m)

% dR0r=[0.81e-6/2 0.9e-6/2 0.99e-6/2 1.57e-6/2 1.87e-6/2 2.17e-6/2 1.18e-
6/2 1.35e-6/2 1.52e-6/2];
% dR0r=[0.5e-6 0.935e-6 1.3e-6 2.2e-6 3e-6 4.e-6 5.0e-6 6.9e-6];
dR0r=1.3e-6;
% start of the radii loop
 for index2=1:length(dR0r)
dR0=dR0r(index2)         %inital radius, m
drhol=1000;                 %density of liquid, kg/m^3
dp0=1e5;                    %hydrostatic pressre, Pa
dsig0=0.07;                 %surface tension (air/water), N/m
```

```
gamma=1.4;                  %Polytropic constant
dmul=0.001;                 %viscosity of the liquid, Pa.s
% df=1.614e6;                   %frequency of the driving wave, Hz
df=0.5e6;
dcl=1500;                   %speed of sound in liquid, m/s
dd=10e-3 ;                  % distance your measuring the radiated
pressure from the bubble, m
dks=15e-9;                  % viscosity of the shell, Kg/s
dampr=[2.4e6 3.8e6 3.95e6];
%Variables for the variable surface tension, based on the Term in
%Marmottant 2005
dR_buck=dR0;                % buckling radii,m
DSHELL_ELASTICITY=0.3;        %Shell elasticity N/m
dR_rupt=dR_buck*(1+dsig0/DSHELL_ELASTICITY)^(1/2); % radi at which
rupture occurs
%number of cycles in pulse ( pulse is in the form of a Guassin wave in
code,
%change to Gussian if preffered
n=20;

% defining memory needed to store outputs
radius=zeros(1,length(dampr));      % This gives the radius of the bubble
R0 to the Spread sheet
wall_v=zeros(1,(length(dampr)));    %This stores the maximum wall
velocity of the run
min_rad=zeros(1,(length(dampr)));   %This stores the minimum radius
max_v=zeros(1,(length(dampr)));     %This stores the Maximum radius
max_pre=zeros(1,(length(dampr)));   %This stores the maximum active
radiated Pressure
min_pre=zeros(1,(length(dampr)));   %This Stores the mimium active
radiated Presure
Ws_radiated=zeros(1,(length(dampr))); %This Stores the radiated power
over the pulse

for index=1:length(dampr)
radius(1)=dR0; % This Puts the resting Readius of the bubble solved for
on the first line of the spread sheet
%non dimesnionalizing
R0=dR0/dR0;
p0=dp0/dp0;
amp=dampr(index)/dp0;
ampy=dampr(index)/1e6
mul=dmul*(2*pi*df)/dp0;
rhol=drhol*(2*pi*df)^2*dR0^2/dp0;
sig0=dsig0/(dp0*dR0);
f=df/(2*pi*df);
cl=dcl/(dR0*2*pi*df);
SHELL_ELAST=DSHELL_ELASTICITY/(dp0*dR0);
d=dd/dR0;
ks=dks/dp0/dR0*(2*pi*df);
R_buck=dR_buck/dR0;
R_rupt=dR_rupt/dR0;

tau=n/f/2;      %gaussian pulse const, uncomment if using a gaussian
pulse
dtmax=n/(df);   %Max time if using a gaussian pulse

tmax=dtmax*2*pi*df;  %max time if using a sin(wt) wave

% Solving the ODE
options=odeset('MaxStep',0.001);
```

```
% change fuunction here variable shell= varskel, shelled=skel,
%no shell= kel ode15s was used as 0de45 took twice as long at this
%specification of time step
[t,r] =ode15s(@varskel,[0 tmax],[R0,0],options);
% re-dimensionalising time for plots
tm=t/(2*pi);

 % calculating the acceleration of the bubble wall as MatLab is stupid
and
% doesn't give it as an output but does caculate it.
c=(r(:,2));
cc=zeros(1,length(r(:,2)));
for i=2:1:length(r(:,2))    % starts from 2 as the inital condition is
zero
    cc(i)=(c(i)-c(i-1))/(t(i)-t(i-1));
end

% caculating the active radiated pressure
active=(rhol.*r(:,1)/d).*(r(:,1).*cc'+2*r(:,2).^2);
% caculating the passive radiated Pressure
passive=1*((3*d*cl^2)^(-1)).*r(:,1).^3.*(-(2*pi*f)^2.*sin((2*pi*f).*t));
% caculating total pressure
ptot=active+passive;
% calculating the power radiated over a pulse
ws= ((4*pi)*(rhol *cl)^(-1))*trapz(t,(d*d.*ptot.*ptot));
%
figure
%%Plots radius
plot(tm,r(:,1))
title(['Radial vs time at pressure',num2str(ampy),'MPa and radius',
num2str(dR0),'freq', num2str(df),'Hz'])
xlabel('Acoustic cycles');
ylabel('non-dimensional Radius');

%redimensionalizing units
wall_v(index)=max(abs(r(:,2)))/cl;
max_rad(index)=max(r(:,1))*dR0;
min_rad(index)=min(r(:,1))*dR0;
max_pre(index)=max(active)*dp0;
min_pre(index)=min(active)*dp0;
Ws_radiated(index)=ws*dp0*(dR0^3)*(df*2*pi);

end

    fx1=[radius;dampr;wall_v;max_rad;
min_rad;max_pre;min_pre;Ws_radiated];
  %excel file please change name for diffrent frequencies
  ffy=df/1e6;
  % actomatically saves file with frequency used
xlswrite(['final_rad_Var_Shell_range_for',num2str(ffy),'MHz_rad_missing13
.xls'],fx1,index2);
end
end

function [gg]= nonlin_st(RR)
%nonlinear surface tension function see marmottant for explination
global SHELL_ELAST R_buck R_rupt sig0

if RR <R_buck
    gg=0;
```

```
elseif RR<R_rupt
    gg=SHELL_ELAST*((RR^2/R_buck^2)-1);

else
    gg=sig0;

end
end

function dr=varskel(t,r);
% keller-Miskis eq with marmontant variables
global R0 rhol p0 sig0 gamma mul amp f cl ks SHELL_ELAST R_buck R_rupt
tau

 dr=zeros(2,1);

 dr(1)=r(2);
 % marmotant variable shell
 dr(2)=(4*mul*rhol^(-1)-r(1)*(r(2)-cl))^(-1)...
     *((1/2)*r(2)^(3)...
     +r(2)*rhol^(-1)*((p0+2*nonlin_st(R0)*R0^(-1))*(R0*r(1)^(-
1))^(3*gamma)-p0)...
     -cl*((3/2)*r(2)^2 ...
     +4*mul*r(2)*(rhol*r(1))^(-1)...
      +2*nonlin_st(r(1))*(rhol*r(1))^(-1)...
      +4*ks*r(2)*r(1)^(-2)...
     -rhol^(-1)*((p0+2*nonlin_st(R0)*R0^(-1))*(R0*r(1)^(-1))^(3*gamma)-
p0))...
     -r(1)*r(2)*rhol^(-1)*(3*gamma*(p0+2*nonlin_st(R0)*R0^(-
1))*(R0*r(1)^(-1))^(3*gamma)*r(1)^(-1))...
    +((1+r(2)*cl^(-1))*(amp)*cl*rhol^(-1)*sin((2*pi*f)*(t+(r(1)*cl^(-
1))))*exp(-4*((t-tau)/tau)^2)));

end

function dr=skel(t,r);
% keller-Miskis eq with shell
global R0 rhol p0 sig0 gamma mul amp f cl ks SHELL_ELAST R_buck R_rupt
tau

 dr=zeros(2,1);

 dr(1)=r(2);
 % non variable shell
 dr(2)=(4*mul*rhol^(-1)-r(1)*(r(2)-cl))^(-1)...
     *((1/2)*r(2)^(3)...
     +r(2)*rhol^(-1)*((p0+2*sig0*R0^(-1))*(R0*r(1)^(-1))^(3*gamma)-p0)...
     -cl*((3/2)*r(2)^2 ...
     +4*mul*r(2)*(rhol*r(1))^(-1)...
      +2*sig0*(rhol*r(1))^(-1)...
      +4*ks*r(2)*r(1)^(-2)...
               -rhol^(-1)*((p0+2*sig0*R0^(-1))*(R0*r(1)^(-1))^(3*gamma)-
p0))...
     -r(1)*r(2)*rhol^(-1)*(3*gamma*(p0+2*sig0*R0^(-1))*(R0*r(1)^(-
1))^(3*gamma)*r(1)^(-1))...
    +((1+r(2)*cl^(-1))*(amp)*cl*rhol^(-1)*sin((2*pi*f)*(t+(r(1)*cl^(-
1))))*exp(-4*((t-tau)/tau)^2)));
end
function dr=kel(t,r);
% keller-Miskis eq with no shell
```

```
global R0 rhol p0 sig0 gamma mul amp f cl ks SHELL_ELAST R_buck R_rupt
tau

 dr=zeros(2,1);

 dr(1)=r(2);
 % no shell
  dr(2)=(4*mul*rhol^(-1)-r(1)*(r(2)-cl))^(-1)...
     *((1/2)*r(2)^(3)...
     +r(2)*rhol^(-1)*((p0+2*sig0*R0^(-1))*(R0*r(1)^(-1))^(3*gamma)-p0)...
     -cl*((3/2)*r(2)^2 ...
     +4*mul*r(2)*(rhol*r(1))^(-1)...
     -rhol^(-1)*((p0+2*sig0*R0^(-1))*(R0*r(1)^(-1))^(3*gamma)-p0))...
     -r(1)*r(2)*rhol^(-1)*(3*gamma*(p0+2*sig0*R0^(-1))*(R0*r(1)^(-
1))^(3*gamma)*r(1)^(-1))...
    +((1+r(2)*cl^(-1))*(amp)*cl*rhol^(-1)*sin((2*pi*f)*(t+(r(1)*cl^(-
1))))*exp(-4*((t-tau)/tau)^2)));
end

end
```

D. Anomaly in Chapter 6

The 2.2µm being driven at 0.5 MHz was not in a chaotic regime as can be seen from Figure D.1.

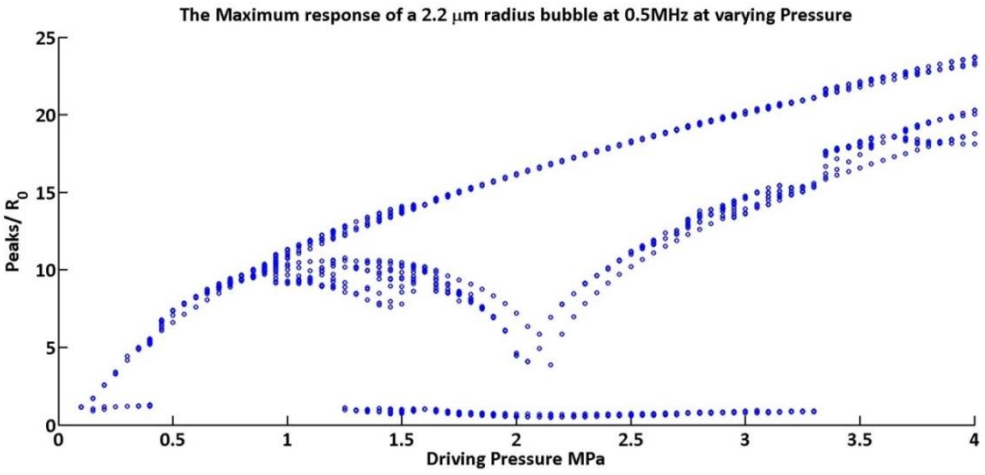

Figure D.1 Birfuractation diagram of the peaks found for a 50 cycle pulse for a range of pressures.

It can also be seen from the figures in Figure D***.2*** that it was not due to a numerical error.

Radial oscillation for *f=0.5*MHz at 4MPa

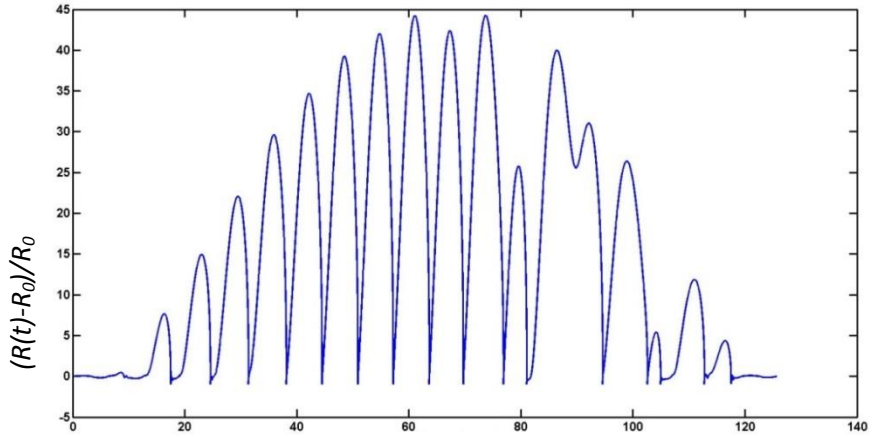

Radial oscillation for *f=0 .5*MHz at 2.5MPa

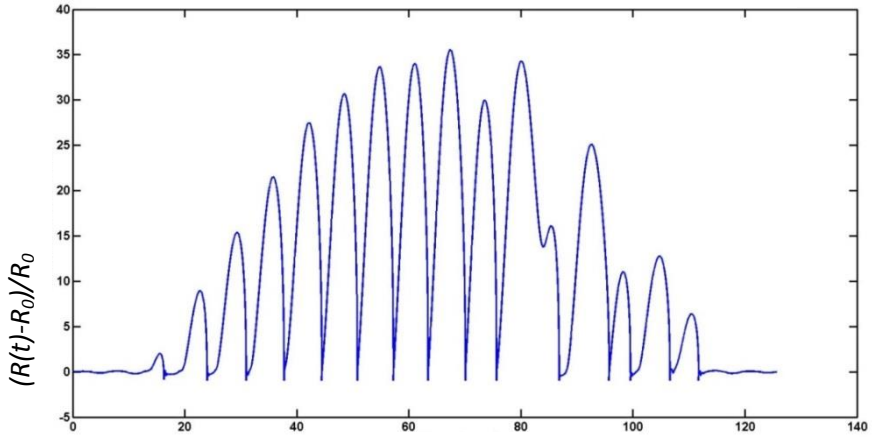

Radial oscillation for *f=0.5*MHz at 1.5MPa

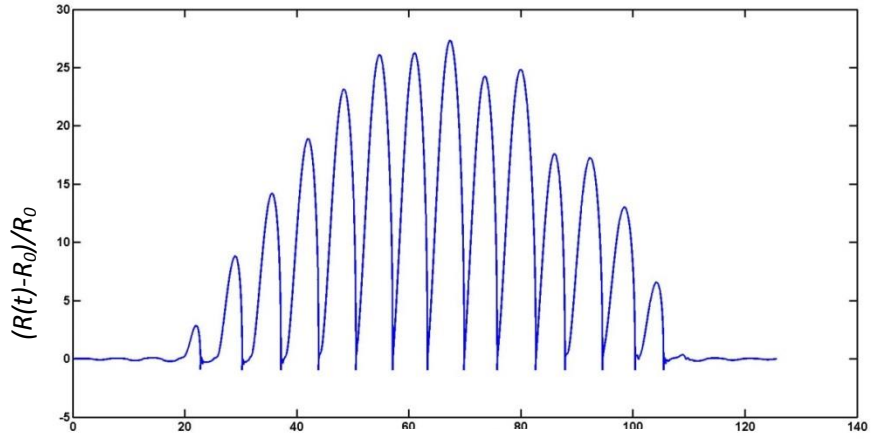

Figure D.2Figures showing the radial time curves of 2.2μm bubble at a driving frequency of 0.5MHz for a range of pressures, as it can be seen no numerical instability is visible

E. Table of Data for Chapter 7

Driving Pressure kPa/ Radius µm	25.00	50.00	100.00	200.00	300.00	400.00	500.00	600.00	700.00	800.00
10.00	1.29	1.64	2.02	2.56	3.05	3.40	3.56	4.02	4.24	4.45
25.00	1.67	1.93	2.24	2.89	3.29	3.78	4.00	4.26	4.47	4.67
50.00	1.71	1.95	2.22	3.03	3.51	3.82	4.05	4.28	4.44	4.71
75.00	1.71	1.95	2.21	3.03	3.51	3.83	4.08	4.30	4.50	4.71
100.00	1.71	1.94	2.20	3.01	3.57	3.83	4.03	4.31	4.52	4.71
200.00	1.72	1.94	2.19	3.04	3.57	3.83	4.08	4.31	4.53	4.70
300.00	1.72	1.94	2.19	2.96	3.58	3.83	4.05	4.32	4.49	4.72
400.00	1.72	1.93	2.19	2.96	3.58	3.83	4.03	4.26	4.53	4.71
500.00	1.72	1.93	2.18	2.96	3.58	3.83	4.09	4.32	4.48	4.70
600.00	1.72	1.93	2.18	2.97	3.58	3.83	4.08	4.25	4.45	4.68

Table E.1 showing the values of the radius found in chapter 7. To demonstrate that 50kPa is the largest pressure that can be used without the expansion $R(t)/R_0$ going above 2

F. List of Footnotes

Chapter 2

The terms Gaussian and Laguerre-Gaussian refer to the mathematical functions that describe the beam intensity profile. 13

Chapter 4

High speed fluorescence microscopy footage of single bubbles undergoing lipid shedding was kindly provided by colleagues at Erasmus University, Rotterdam, The Netherlands 3.Gelderblom, E.C., *Ultra-high-speed fluorescence imaging*, 2012: Enschede. p. 144.. 128

Appendix A

Leighton, T.G., The Acoustic Bubble. 1994: Academic Press. 198

Appendix B

Watanabe, T. and Y. Kukita, Translational and Radial Motions of a Bubble in an Acoustic Standing-Wave Field. Physics of Fluids a-Fluid Dynamics, 1993. 5(11): p. 2682-2688. 199